Dynamic-Shield Intensity Modulated Brachytherapy for Prostate Cancer

Gabriel Famulari

Department of Physics
McGill University

A thesis submitted to McGill University in partial fulfillment of the requirements of the degree of
Doctor of Philosophy

August 2020

ABSTRACT

Intensity modulated brachytherapy (IMBT) is a brachytherapy technique which incorporates static or dynamic shielded applicator(s) or source(s) to provide a highly directional dose distribution. In the case of prostate cancer, IMBT is desirable to reduce the dose delivered to organs at risk, such as the urethra, or allow for dose escalation without an associated increase in urethral dose. However, the implementation of IMBT requires an appropriate radiation source and delivery system. The aim of this thesis was to investigate a feasible method to deliver dynamic-shield IMBT for the treatment of prostate cancer. A Monte Carlo (MC) treatment planning system for brachytherapy applications (RapidBrachyMCTPS) based on the Geant4 simulation toolkit was developed with the capabilities to perform IMBT treatment planning. The MC dose calculation engine was benchmarked against previously validated MC codes and measurements using Gafchromic$^{\mathrm{TM}}$ film. An intermediate-energy source such as ^{169}Yb is desirable for IMBT since the transmission can easily be modulated with a small amount of shielding material. A microdosimetric analysis based on track structure simulations using Geant4-DNA predicted that ^{169}Yb has a relative biological effectiveness of $\sim$1.1 relative to ^{192}Ir for high dose rate brachytherapy (HDR BT). A dose calculation study in heterogeneous media was also performed to assess the importance of accounting for tissue heterogeneities for accurate dosimetry in bony structures with ^{169}Yb. Next, we designed and developed an ^{169}Yb source and delivery system (AIM-Brachy) that can enable dynamic-shield IMBT for prostate cancer. The AIM-Brachy system is a portable device that dynamically controls the rotation of thin platinum shields inserted within interstitial catheters for prostate HDR BT. A treatment planning study was then carried out to demonstrate the superiority of ^{169}Yb-based IMBT compared to conventional ^{192}Ir-based HDR BT for prostate cases. The IMBT plans achieved a significantly lower urethra D_{10} (by 13% on average) without affecting other plan quality indices. The urethra-sparing properties are desirable to minimize the occurrence and severity of genitourinary toxicity or, alternatively, to escalate the dose delivered to the target maintaining a similar level of toxicity. Finally, this work involved the development and characterization of a new source model. The dosimetric parameters for the ^{169}Yb source model were calculated using RapidBrachyMCTPS. Then, the dose distribution around the source with/without the shielded applicator was experimentally validated in water with good agreement using a multipoint plastic scintillator detector. The ^{169}Yb source coupled with the AIM-Brachy system is a promising technique to deliver dynamic-shield IMBT.

RÉSUMÉ

La curiethérapie avec modulation d'intensité (IMBT) est une technique de curiethérapie qui utilise des applicateurs ou des sources blindés statiques ou dynamiques pour fournir une distribution de dose directionnelle. Dans le cas du cancer de la prostate, l'IMBT est souhaitable pour réduire la dose délivrée aux organes à risque, tels que l'urètre, ou permettre une augmentation de la dose sans augmentation associée de la dose urétrale. Cependant, la mise en œuvre de l'IMBT nécessite une source de rayonnement et un système de délivrance appropriés. Le but de cette thèse était d'étudier une méthode réalisable pour délivrer l'IMBT dynamique pour le traitement du cancer de la prostate. Un système de planification de traitement Monte Carlo (MC) pour les applications de curiethérapie basé sur l'outil Geant4 (RapidBrachyMCTPS) a été développé avec les capacités d'effectuer la planification de traitement IMBT. Le moteur de calcul de la dose MC a été comparé aux codes MC précédemment validés et aux mesures de la dose par film Gafchromic$^{\text{TM}}$. Une source d'énergie intermédiaire telle que ^{169}Yb est souhaitable pour l'IMBT car la transmission peut facilement être modulée avec une petite quantité de matériau de blindage. Une analyse microdosimétrique basée sur l'outil Geant4-DNA a prédit que l'^{169}Yb a une efficacité biologique relative de $\sim$1,1 par rapport à l'^{192}Ir pour la curiethérapie à haut débit de dose (HDR BT). Une étude de calcul de dose en milieu hétérogène a également été réalisée pour évaluer l'importance de tenir compte des hétérogénéités tissulaires pour une dosimétrie précise dans les structures osseuses avec l'^{169}Yb. Ensuite, nous avons conçu et développé une source d'^{169}Yb et un système de délivrance (AIM-Brachy) qui peut delivrer l'IMBT dynamique pour le cancer de la prostate. Le système AIM-Brachy est un appareil portable qui contrôle dynamiquement la rotation des écrans de platine minces insérés dans les cathéters interstitiels pour la curiethérapie de la prostate. Une étude de planification de traitement a ensuite été réalisée pour démontrer la supériorité de l'IMBT avec l'^{169}Yb par rapport à la HDR BT conventionnelle avec l'^{192}Ir pour les cas de prostate. Les plans IMBT ont atteint une D_{10} de l'urètre nettement inférieure (de 13% en moyenne) sans affecter les autres indices de qualité du plan. Les propriétés de conservation de l'urètre sont souhaitables pour minimiser l'apparition et la gravité de la toxicité génito-urinaire, ou encore, pour augmenter la dose délivrée à la cible en maintenant un niveau de toxicité similaire. Enfin, ce travail a impliqué le développement et la caractérisation d'un nouveau modèle de source. Les paramètres dosimétriques du modèle de source d'^{169}Yb ont été calculés à l'aide de RapidBrachyMCTPS. Ensuite, la distribution de la dose autour de la source avec/sans écran a été validée expérimentalement dans l'eau avec un bon accord en utilisant un détecteur à scintillateur plastique multipoint. La source d'^{169}Yb couplée au système AIM-Brachy est une technique prometteuse pour delivrer l'IMBT dynamique.

ACKNOWLEDGEMENT

I would like to thank my supervisor, Dr. Shirin A. Enger, for guidance, encouragement and support throughout my academic studies. I would like to acknowledge all the help I have received from my co-authors: Dr. Piotr Pater, Dr. Marc-André Renaud, Dr. Christopher M. Poole, Dr. Michael D. C. Evans, Dr. Jan Seuntjens, Dr. Joanne Alfieri, Dr. Té Vuong, Haydee M. Linares Rosales, Justine Dupere, Dr. David C. Medich, Dr. Luc Beaulieu, and Dr. Shirin A. Enger. I would like to thank my supervisory committee, Dr. Steve Davis, Dr. Kari Tanderup and Dr. Jean-François Carrier, for their guidance and input towards this project. I would like to acknowledge financial support by the Alexander Graham Bell Doctoral Canada Graduate Scholarship (CGS-D) from the Natural Sciences and Engineering Research Council of Canada (NSERC), Schulich Graduate Scholarship, NSERC CREATE Medical Physics Research Training Network grant (number 432290), Collaborative Health Research Projects grant (number 523394-18) and NSERC Discovery grant (number 241018). I would like to thank everyone in the Medical Physics Unit, who have influences me greatly over the years, for all the fruitful discussions and for providing such a wonderful environment to perform research. Finally, I would like to express my gratitude to my wife Karina and my parents Marisa and Joe for their unwavering support and for allowing me to pursue my dream.

CONTRIBUTION OF AUTHORS

The core work of this thesis consists of 5 articles, including 4 published peer-reviewed articles and 1 manuscript under review. These articles consist of original work and distinct contributions to knowledge. As the primary author, I designed and carried out the experiments and the simulations, performed the data analysis and wrote the manuscripts. The contributions of the co-authors to each article are highlighted below.

The first article (chapter 5), "Microdosimetric evaluation of current and alternative brachytherapy sources - a Geant4 simulation study", Gabriel Famulari, Piotr Pater, Shirin A. Enger, presents work conducted by Gabriel Famulari. Piotr Pater assisted in the formulation of the methodology and provided the analysis code. Shirin A. Enger provided general guidance and supervision.

The second article (chapter 6), "RapidBrachyMCTPS: a Monte Carlo-based treatment planning system for brachytherapy applications", Gabriel Famulari, Marc-André Renaud, Christopher M. Poole, Michael D. C. Evans, Jan Seuntjens, Shirin A. Enger, presents work conducted by Gabriel Famulari. Marc-André Renaud and Christopher M. Poole were involved in software development. Michael D. C. Evans assisted with the measurements. Jan Seuntjens and Shirin A. Enger provided general guidance and supervision.

The third article (chapter 7), "Can intermediate energy sources result in elevated bone doses for prostate and head & neck high dose rate brachytherapy?", Gabriel Famulari, Joanne Alfieri, Marie Duclos, Té Vuong, Shirin A. Enger, presents work conducted by Gabriel Famulari. Joanne Alfieri provided clinical insight. Marie Duclos and Té Vuong provided sets of patient imaging and treatment data. Shirin A. Enger provided general guidance and supervision.

The fourth article (chapter 8), "A novel ^{169}Yb-based dynamic-shield intensity modulated brachytherapy system for prostate cancer", Gabriel Famulari, Marie Duclos, Shirin A. Enger, presents work conducted by Gabriel Famulari. Marie Duclos provided clinical insight. Shirin A. Enger provided general guidance and supervision.

The fifth article (chapter 9), "Monte Carlo dosimetric characterization of a new high dose rate ^{169}Yb brachytherapy source and experimental validation using a multipoint plastic scintillator detector", Gabriel Famulari, Haydee M. Linares Rosales, Justine Dupere, David C. Medich, Luc Beaulieu, Shirin A. Enger, presents work conducted by Gabriel Famulari and Haydee M. Linares Rosales. Haydee M. Linares Rosales was involved with the measurements, data analysis and writing. Justine Dupere assisted with the measurements. David C. Medich provided access to facilities and equipment to perform the measurements. Luc Beaulieu and Shirin A. Enger provided general guidance and supervision.

Table of contents

List of figures

List of tables

LIST OF ABBREVIATIONS

AAPM	**A**merican **A**ssociation of **P**hysicists in **M**edicine
AIM-BRACHY	**A**nisotropic **I**ntensity **M**odulated **BRACHY**therapy
AISI	**A**merican **I**ron and **S**teel **I**nstitute
ASCII	**A**merican **S**tandard **C**ode for **I**nformation **I**nterchange
BT	**B**rachy**T**herapy
BED	**B**iologically **E**ffective **D**ose
CFSA	**C**arrier-**F**ree **S**pecific **A**ctivity
CCS	**C**ollapsed **C**one **S**uperposition
CERN	**C**onceil **E**uropéen pour la **R**echerche **N**ucléaire
CNSC	**C**anadian **N**uclear **S**afety **C**ommission
COIN	**CO**nformity **IN**dex
CPE	**C**harged **P**article **E**quilibrium
CPU	**C**entral **P**rocessing **U**nit
CSDA	**C**ontinuous **S**lowing **D**own **A**pproximation
CT	**C**omputed **T**omography
CTV	**C**linical **T**arget **V**olume
DD	**D**ose **D**ifference
DICOM	**D**igital **I**maging and **CO**mmunications in **M**edicine
DMBT	**D**ynamic **M**odulated **B**rachy**T**herapy
DNA	**D**eoxyribo**N**ucleic **A**cid
DSB	**D**ouble **S**trand **B**reak
DTA	**D**istance **T**o **A**greement
DVH	**D**ose-**V**olume **H**istogram
EBRT	**E**xternal **B**eam **R**adio**T**herapy
EGS	**E**lectron **G**amma **S**hower
ENSDF	**E**valuated **N**uclear **S**tructure **D**ata **F**ile
EQD2	**EQ**uivalent **D**ose in **2** Gy fractions
ESTRO	**E**uropean **S**ocie**T**y for **R**adiotherapy and **O**ncology
GBBS	**G**rid **B**ased **B**oltzmann **S**olver
GDCM	**G**rassroots **D**i**C**o**M**
GEANT4	**GE**ometry **AN**d **T**racking **4**
GEC-ESTRO	**G**roupe **E**uropéen de **C**uriethérapie - **E**uropean **S**ocie**T**y for **R**adiotherapy and **O**ncology

GI	**G**astro**I**ntestinal
GNRT	**G**old **N**anoparticle-**Aided** **T**herapy
GPU	**G**raphics **P**rocessing **U**nit
GU	**G**enito**U**rinary
GUI	**G**raphical **U**ser **I**nterface
HDR	**H**igh **D**ose **R**ate
HI	**H**omogeneity **I**ndex
HU	**H**ounsfield **U**nit
HVL	**H**alf-**V**alue **L**ayer
ICRP	**I**nternational **C**ommission on **R**adiological **P**rotection
ICRU	**I**nternational **C**ommission on **R**adiation **U**nits and measurements
IMBT	**I**ntensity **M**odulated **B**rachy**T**herapy
IMRT	**I**ntensity **M**odulated **R**adio**T**herapy
IPSA	**I**nverse **P**lanning **S**imulated **A**nnealing
KERMA	**K**inetic **E**nergy **R**eleased per unit **MA**ss
LBTE	**L**inear **B**oltzmann **T**ransport **E**quation
LDR	**L**ow **D**ose **R**ate
LET	**L**inear **E**nergy **T**ransfer
LQ	**L**inear **Q**uadratic
MBDCA	**M**odel-**B**ased **D**ose **C**alculation **A**lgorithm
MC	**M**onte **C**arlo
MCPT	**M**onte **C**arlo **P**hoton **T**ransport
MCTS	**M**onte **C**arlo **T**rack **S**tructure
MLC	**M**ulti-**L**eaf **C**ollimator
MRI	**M**agnetic **R**esonance **I**maging
mPSD	**m**ultipoint **P**lastic **S**cintillator **D**etector
NIST	**N**ational **I**nstitute of **S**tandards and **T**echnology
NRC	**N**ational **R**esearch **C**ouncil of Canada
OAR	**O**rgan **A**t **R**isk
OD	**O**ptical **D**ensity
PDR	**P**ulsed **D**ose **R**ate
PENELOPE	**P**enetration and **ENE**rgy **LO**ss of **P**ositrons and **E**lectrons
PMMA	**P**oly**M**ethyl **M**eth**A**crylate
PMT	**P**hoto**M**ultiplier **T**ube

PSD	**P**lastic **S**cintillator **D**etector
PTV	**P**lanning **T**arget **V**olume
RBE	**R**elative **B**iological **E**ffectiveness
RSBT	**R**otating **S**hield **B**rachy**T**herapy
RTOG	**R**adiation **T**herapy **O**ncology **G**roup
SI	**S**ystème **I**nternational
SLAC	**S**tanford **L**inear **A**ccelerator **C**enter
SNR	**S**ignal-to-**N**oise **R**atio
SSD	**S**ource-**S**urface **D**istance
STL	**ST**ereo**L**ithography
TCPE	**T**ransient **C**harged **P**article **E**quilibrium
TEPC	**T**issue **E**quivalent **P**roportional **C**ounter
TG	**T**ask **G**roup
TIFF	**T**agged **I**mage **F**ile **F**ormat
TPS	**T**reatment **P**lanning **S**ystem
TRUS	**T**rans**R**ectal **U**ltra**S**ound
TVL	**T**enth-**V**alue **L**ayer
US	**U**ltra**S**ound
VTK	**V**isualization **T**ool**K**it
WAFAC	**W**ide-**A**ngle **F**ree-**A**ir **C**hamber

Chapter 1

Introduction

1.1 Cancer

A tumour begins when healthy cells change and grow uncontrollably, forming a mass. A tumour can be malignant (cancerous) or benign. A malignant tumour can grow and spread, or metastasize, to other parts of the body [1]. A benign tumour means the tumour can grow but will not spread. A benign tumour usually can be removed without it causing much harm.

The majority of cancers (90-95% of cases) are due to environmental factors [2]. The remaining cancers are due to inherited genetics. Common environmental factors that contribute to cancer include tobacco, diet and obesity, infections, radiation, stress, lack of physical activity and environmental pollutants.

The Canadian Cancer Society [3] estimates that 45% of men and 42% of women are expected to develop cancer during their lifetimes. More importantly, 29% of men and 24% of women are expected to die from cancer, making cancer the leading cause of death in Canada. In 2020, an estimated 225 800 Canadians will be diagnosed with cancer, and 83 300 Canadians are expected to die from cancer. Lung (29 800), breast (27 700), colorectal (26 900) and prostate (23 300) cancer are the most common types of cancer in Canada, as they account for almost half (48%) of all new cancer diagnoses. Although the number of newly diagnosed cancer cases in Canada is steadily increasing, survival rates are also increasing. This is largely due to improvements in prevention, screening, detection and treatment. Development of imaging modalities has made it possible to detect cancer early, accurately diagnose it and improve the definition of target volumes or healthy tissue at risk. Due to scientific and technological advances in the last decades, we have access to better tools and techniques to provide effective treatments, and new treatment options are now available. Most common cancer types with solid tumours can be treated with radiation therapy in some way. Radiation therapy alone or in combination with chemotherapy, hormone therapy, immunotherapy and surgery, is used to treat cancer patients with intent to cure (curative therapy), to prevent tumour recurrence after surgery (adjuvant therapy), and to manage symptoms when cure is not possible (palliative care). The increasing number of clinical trials has also led to more targeted therapies and improved understanding of treatment efficacy.

1.2 Radiation therapy

Radiation therapy, or radiotherapy, refers to therapy using ionizing radiation, generally as part of cancer treatment to control or kill malignant cells. Radiation therapy uses ionizing radiation to damage the DNA of cancer cells by causing breaks in the DNA molecule. The goal of this DNA damage is to disrupt the cell's ability to function properly, grow and replicate, and thereby induce cell death. Cells have mechanisms for repairing single-strand and double-stranded DNA damage. However, double-stranded breaks (DSB) are much more difficult to repair, and thus are more likely to lead to cell death.

Radiation therapy may be curative in a number of types of cancer if they are localized to one area of the body. Radiation therapy can be divided into two general categories: external beam radiotherapy (EBRT) and brachytherapy. The amount of absorbed radiation dose in radiation therapy is specified in units of gray (Gy). The treatment modality and prescription dose generally depends on the tumour type, location and stage.

The aim of radiation therapy is to deliver an appropriate amount of radiation to the tumour to obtain a high probability of tumour control, while sparing as much normal tissue as possible to avoid serious short- and long-term complications (toxicities). Local control of a tumour refers to the total disappearance of the primary tumour and neighboring metastases without any local recurrence. While local control is certainly important to increase disease-free survival, managing radiotherapy toxicity can result in a better quality of life for the patient. This concept is referred to as the therapeutic ratio. Figure 1.1 illustrates an example of tumour control probability (TCP) and normal tissue complication probability (NTCP) as a function of absorbed dose. In this example, a dose of 60-70 Gy maximizes the therapeutic ratio (very high TCP and very low NTCP). For typical treatments, TCP should be greater than 0.5 and NTCP should be lower than 0.05.

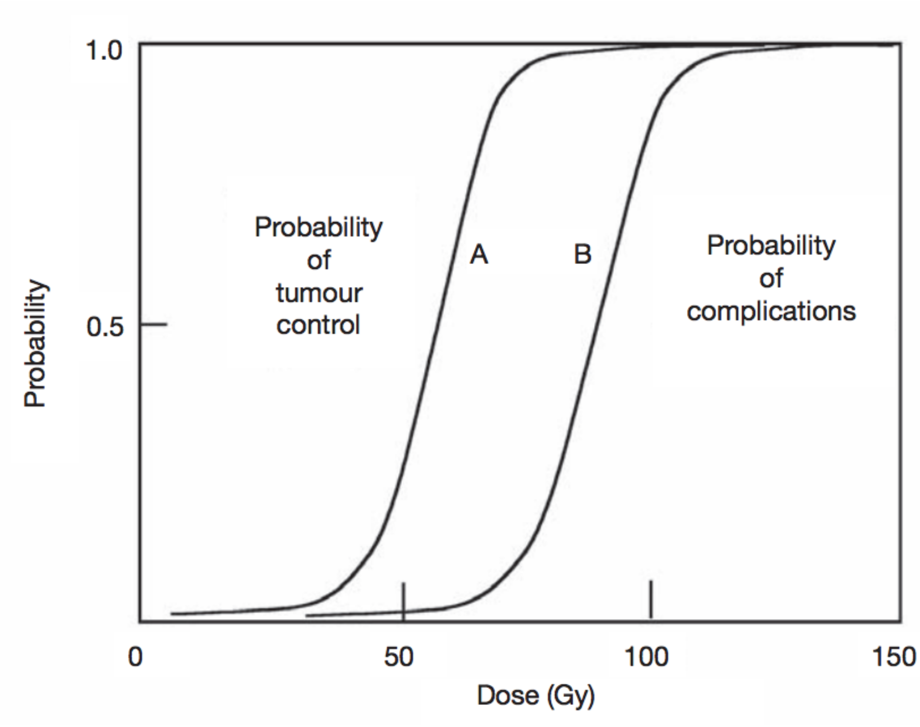

Figure 1.1: The principle of therapeutic ratio. Tumour control probability (TCP) and normal tissue complication probability (NTCP) are indicated in curves A and B, respectively. Figure reproduced from [4].

EBRT is the most common form of radiation therapy [4]. The patient sits or lies on a couch and a beam of ionizing radiation is directed to the tumour site. EBRT is typically delivered using linear accelerators. Megavoltage photon and electron beams are by far the most widely used sources for EBRT. The aim of radiation therapy is to give an adequate radiation absorbed dose to the volumes containing malignant cells while minimizing the dose to healthy tissue.

Intensity modulated radiation therapy (IMRT) is an advanced radiotherapy technique used to minimize the amount of normal tissue being irradiated in the treatment field [5]. The intensity modulation is achieved by moving the leaves in the multi-leaf collimator (MLC) during the course of treatment, thereby delivering a radiation field with a non-uniform intensity. Each leaf in the MLC is aligned parallel to the radiation field and can be moved independently to block part of the field. By adjusting the position of the leaves, the radiation field can be matched to the shape of the tumour. Today, the majority of patients receiving radiation therapy undergo IMRT.

Brachytherapy is a form of radiation therapy that uses radiation sources (most commonly photon-emitting radionuclides) that are permanently or temporarily placed inside or near the tumour, giving a high radiation dose to the target volume while maintaining a low dose to surrounding healthy tissues. Radiation can be delivered in a brief treatment session, as in high dose rate (HDR) brachytherapy, or over a long period of time, as in low dose rate (LDR) brachytherapy. Brachytherapy requires the positioning of catheters (interstitial), tubes (intraluminal) or site-specific applicators (intracavitary) into body cavities and tissues to guide the radiation source to the treatment site.

The physical advantage of brachytherapy treatments compared with EBRT is the improved localized delivery of dose to the target volume of interest since the photons emitted from brachytherapy sources are low energetic, with short interaction distance and deposit most of their energy in the target. However, brachytherapy can only be used in cases where the tumour is well localized and relatively small. In a typical radiotherapy department, about 10-20% of all radiotherapy patients are treated with brachytherapy [4]. Its invasiveness compared to EBRT explains why it is a less frequently performed treatment, but its popularity is rising. Within all brachytherapy procedures, the main tumour sites are: gynaecology, prostate, breast, bronchus and head & neck cancer [6]. Essential to the success of brachytherapy is an accurate dose calculation and administration.

1.3 The role of brachytherapy in prostate cancer treatment

In order to improve biochemical control while limiting long-term complications, brachytherapy has been incorporated into radiation therapy treatment for prostate cancer, either alone (monotherapy) or in combination with EBRT (boost). Regardless of the treatment technique, disease-free survival rates are consistently high (>90%) [7], hence long-term complications play a large role in the selection of the appropriate treatment technique since these may impact the quality of life of patients.

The brachytherapy boost (HDR or LDR) is a recommended method of dose escalation for intermediate- and high-risk prostate cancer [8]. HDR brachytherapy combined with EBRT appears to be superior in terms of efficacy compared to EBRT alone [9, 10]. The most common dose regimen is 15 Gy in a single treatment session (or fraction), followed by 37.5 Gy in 15 fractions of EBRT. Long-term genitourinary (GU) toxicity is typically avoided by limiting the dose delivered to the urethra during brachytherapy. However, the rate of severe GU complications, such as urethral strictures, is significantly higher for patients that received the boost compared to those who received EBRT alone [11]. Many techniques to generate urethra sparing plans have been proposed to reduce the risk and severity of GU toxicities [12, 13].

Alternatively, further escalation of the brachytherapy dose, while maintaining similar urethral doses, would allow for a reduction in the total dose delivered through EBRT, which may result in lower GU toxicity than the conventional approach while achieving a similar rate of biochemical control [14].

The use of brachytherapy as a monotherapy has been demonstrated to be safe and effective for patients with low- and favorable/intermediate-risk prostate cancer [7]. One of the benefits of brachytherapy monotherapy, compared with surgery and EBRT, is the reduction in long-term toxicity such as incontinence, erectile dysfunction, and proctitis. HDR monotherapy in 2 or 3 fractions is emerging as a viable alternative to LDR brachytherapy with less toxicity [7]. The potential to deliver HDR monotherapy in a single fraction presents many advantages in terms of patient inconvenience, workflow and treatment cost. While a single fraction of 19 Gy seems to be well tolerated, the rate of biochemical control is lower than expected [15, 16]. Further dose escalation to 21 Gy or 23 Gy [17] may be beneficial to increase the long-term efficacy of the treatment.

1.4 Limitations of brachytherapy techniques

Brachytherapy sources generally provide a near-isotropic radiation intensity distribution. For most brachytherapy applications, there are two main parameters that can be varied to modulate the dose distribution: the position of the source and the time spent at each position. This effectively limits the ability to conform the dose distribution to the shape of the target in many situations where dose escalation is limited due to proximity to radiation sensitive tissues. A technique that can provide an asymmetric radiation emission distribution could provide an additional degree of freedom to modulate the dose distribution.

1.5 Thesis motivation and objectives

Intensity modulated brachytherapy (IMBT) has the potential to improve the therapeutic ratio by providing an asymmetric radiation emission distribution. However, the clinical implementation of IMBT requires an appropriate radiation source and collimation system, as well as an advanced treatment planning system coupled to an accurate dose calculation engine that can account for the attenuation of radiation by the collimation system. Currently, there are no commercial products that can deliver IMBT for prostate cancer. The purpose of this work is to develop a feasible method to deliver IMBT for the treatment of prostate cancer.

The main objectives of this thesis can be summarized as follows:

1. Develop and validate a platform that can enable fast and accurate patient-specific dose calculation and treatment planning for conventional brachytherapy and IMBT applications.
2. Perform a series of simulation studies using the platform to evaluate the potential benefits and limitations of IMBT for prostate cancer. Determine whether tissue heterogeneity effects and radiobiological effects need to be considered in the planning process for the proposed radiation source.
3. Design, develop and construct a prototype source and delivery system to validate the simulation results through a series of measurements.

1.6 Published work

1.6.1 Thesis publications

The following articles are considered the core work of this thesis:

1. **Famulari G**, Pater P, Enger SA. Microdosimetric evaluation of current and alternative brachytherapy sources - a Geant4-DNA simulation study. Int J Radiat Oncol Biol Phys. 2018;100(1):270-277.
2. **Famulari G**, Renaud M, Poole CM, Evans MDC, Seuntjens J, Enger SA. RapidBrachyMCTPS: a Monte Carlo-based treatment planning system for brachytherapy applications. Phys Med Biol. 2018;63(17):175007.
3. **Famulari G**, Alfieri J, Duclos M, Vuong T, Enger SA. Can intermediate-energy brachytherapy sources lead to elevated bone doses for prostate and head & neck brachytherapy? Brachytherapy. 2020;19(2):255-263.
4. **Famulari G**, Duclos M, Enger SA. A novel ^{169}Yb-based dynamic-shield intensity modulated brachytherapy delivery system for prostate cancer. Med Phys. 2020;47(3):859-868.
5. **Famulari G**, Linares Rosales HM, Dupere J, Medich DC, Beaulieu L, Enger SA. Monte Carlo dosimetric characterization of a new high dose rate ^{169}Yb brachytherapy source and experimental validation using a multipoint plastic scintillator detector. Med Phys. 2020;47(9):4563-4573.

1.6.2 Other publications

The following articles were published during the course of my studies. These articles adopted the methodology and algorithms developed in this thesis and applied them to various applications outside of the specific focus of this thesis.

1. Barberio M, Scisciò M, Vallières S, Cardelli F, Chen SN, **Famulari G**, Gangolf T, Revet G, Schiavi A, Senzacqua M, Antici P. Laser-accelerated particle beams for stress testing of materials. Nat Commun. 2018;9(1):372.

2. Shoemaker T, Vuong T, Glickman H, Kaifi S, **Famulari G**, Enger SA. Dosimetric considerations for ytterbium-169, selenium-75 and iridium-192 radioisotopes in high-dose-rate endorectal brachytherapy. Int J Radiat Oncol Biol Phys. 2019;105(4):875-883.

3. Lund CM, **Famulari G**, Montgomery L, Kildea J. A microdosimetric analysis of the interactions of mono-energetic neutrons with human tissue. Phys Med. 2020;73:29-42.

1.7 Thesis outline

This thesis is organized as follows. Chapter 2 introduces the concepts in radiation physics, dosimetry and microdosimetry that are relevant to brachytherapy applications. Chapter 3 presents clinical and physical aspects of brachytherapy. This chapter introduces the concept of IMBT, and presents a literature review on the various applications of IMBT. The review discusses the differences between static vs. dynamic shielding techniques, and shielded-source vs. shielded-applicator techniques. Chapter 4 introduces the current brachytherapy dosimetry formalism, as well as the introduction and application of model-based dose calculation algorithms. A summary of the Monte Carlo radiation transport codes and techniques adopted in the simulation components of this thesis are also presented. This chapter introduces experimental dosimetry techniques relevant to the work of this thesis, including film dosimetry and plastic scintillator dosimetry. Finally, a review of clinical brachytherapy uncertainties is included. Chapter 5 presents a study that evaluates the relative biological effectiveness for various photon-emitting brachytherapy sources using microdosimetry concepts and Monte Carlo track structure simulations. Chapter 6 presents a study that describes and validates a fast Monte Carlo-based treatment planning system for brachytherapy applications. Chapter 7 presents a study that evaluates the impact of patient heterogeneities on the dose distribution for various photon-emitting brachytherapy sources. Chapter 8 presents a study that proposes a system design that can enable dynamic-shield IMBT for prostate cancer and evaluates the benefit of IMBT for prostate cancer patients. Chapter 9 presents a study that calculates the dosimetric parameters for the bare source and experimentally validates the dose distribution emitted from the bare/shielded source. Finally, Chapter 10 discusses future directions for this project and outlook for the field of IMBT in general.

References

[1] WHO. Cancer Fact sheet No 297; 2014. Retrieved 10 June 2014.

[2] Anand P, Kunnumakkara AB, Sundaram C, Harikumar KB, Tharakan ST, Lan OS, et al. Cancer is a preventable disease that requires major lifestyle changes. Pharm Res. 2008;25(9):2097–2116.

[3] Society CC. Canadian Cancer statistics at a glance; 2020. Retrieved 4 March 2020.

[4] IAEA. Radiation oncology physics: a handbook for teachers and students. Podgorsak EB, editor. Vienna, Austria; 2005.

[5] ICRU. Prescribing, recording, and reporting intensity-modulated photon-beam therapy (IMRT). ICRU Report. 2010;83.

[6] Guedea F, Ventura M, Mazeron JJ, Torrecilla JL, Bilbao P, Borràs JM. Overview of brachytherapy resources in Europe: A survey of patterns of care study for brachytherapy in Europe. Radiother Oncol. 2007;82:52–54.

[7] Mendez LC, Morton GC. High dose-rate brachytherapy in the treatment of prostate cancer. Transl Androl Urol. 2018;7(3):357–370.

[8] Chin J, Rumble RB, Kollmeier M, Heath E, Efstathiou J, Dorff T, et al. Brachytherapy for Patients With Prostate Cancer: American Society of Clinical Oncology/Cancer Care Ontario Joint Guideline Update. J Clin Oncol. 2017;35:1737–1743.

[9] Hoskin PJ, Rojas AM, Bownes PJ, Lowe GJ, Ostler PJ, Bryant L. Randomised trial of external beam radiotherapy alone or combined with high-dose-rate brachytherapy boost for localised prostate cancer. Radiother Oncol. 2012;103:207–222.

[10] Spratt DE, Zumsteg ZS, Ghadjar P, Kollmeier MA, Pei X, Cohen G, et al. Comparison of high-dose (86.4 Gy) IMRT vs combined brachytherapy plus IMRT for intermediate-risk prostate cancer. BJU Int. 2014;114(3):360–367.

[11] Hsu IC, Bae K, Shinohara K, Pouliot J, Purdy J, Ibbott G, et al. Phase II trial of combined high-dose-rate brachytherapy and external beam radiotherapy for adenocarcinoma of the prostate: preliminary results of RTOG 0321. Int J Radiat Oncol Biol Phys. 2010;78(3):751–758.

[12] Cunha JAM, Pouliot J, Weinberg V, Wang-Chesebro A, Roach M, Hsu IC. Urethra low-dose tunnels: validation of and class solution for generating urethra-sparing dose plans using inverse planning simulated annealing. Brachytherapy. 2012;11(5):348–353.

[13] Kunogi H, Cunha JAM, Chang AJ, Gadzinski AJ, Shinohara K, Hsu IC. A novel urethral sparing technique for high-dose-rate prostate brachytherapy after transurethral resection of the prostate. Brachytherapy. 2017;16(6):1113–1118.

[14] Dahn HM, Oliver PAK, Allen S, Cherpak A, Syme A, Patil N, et al. Individualized dose-escalation of HDR prostate brachytherapy implant to decrease required external beam radiation dose: a retrospective feasibility study. Adv Rad Oncol. 2019;4:641–648.

[15] Prada PJ, Cardenal J, Blanco AG, Anchuelo J, Ferri M, Fernández G, et al. High-dose-rate interstitial brachytherapy as monotherapy in one fraction for the treatment of favorable stage prostate cancer: toxicity and long-term biochemical results. Radiother Oncol. 2016;119(3):411–416.

[16] Mendez LC, Ravi A, Chung H, Tseng CL, Wronski M, Paudel M, et al. Pattern of relapse and dose received by the recurrent intraprostatic nodule in low- to intermediate-risk prostate cancer treated with single fraction 19 Gy high-dose-rate brachytherapy. Brachytherapy. 2018;17(2):291–297.

[17] Gay HA, Michalski JM, Baumann B, DeWees T. A Phase I/II Study Evaluating the Safety and Efficacy of 21 Gy for High Dose Rate (HDR) Prostate Brachytherapy. Identifier No. NCT03424850;. Retrieved from https://clinicaltrials.gov/ct2/show/NCT03424850.

Chapter 2

Radiation physics and dosimetry

2.1 Radioactivity[1]

2.1.1 Radioactive decay

Radioactive decay occurs when an unstable parent radionuclide decays into a daughter nuclide. During this process, the unstable nucleus loses energy (in terms of rest mass) through the emission of radiation. A description of common modes of radioactive decay is presented in section 2.1.2. Radioactive decay is a stochastic process at the level of a single atom. A key assumption in the universal law of radioactive decay is that the probability for a single atom to decay remains constant over time. However, the radioactive decay process for a collection of atoms is governed by the Poisson distribution and can be characterized using decay constants. The mathematics of Poisson processes reduce to the law of exponential decay for the collection of atoms. The number of radioactive atoms $N(t)$ as a function of time t is defined using the following relation:

$$N(t) = N(0)e^{-\lambda t} \tag{2.1}$$

where $N(0)$ is the initial number of radioactive atoms and λ is the decay constant. The decay constant λ is related to the half-life $T_{1/2}$ of the radionuclide as follows:

$$\lambda = \frac{\ln 2}{T_{1/2}} \tag{2.2}$$

---

[1] The information in this section is based on [1] and [2].

The activity A of a radioactive material at a time t is defined as the product of the decay constant λ and the number of radioactive nuclei N:

$$A(t) = \lambda N(t) = \lambda \frac{m(t) N_A}{w} \tag{2.3}$$

where m is the mass of the radionuclide, N_A is Avogadro's constant (6.022×10^{23} mol^{-1}) and w is the atomic weight of the element. The SI unit for activity is the "Becquerel" (Bq), defined as one decay per second. The historical unit of activity is the "Curie" (Ci), defined as 3.7×10^{10} Bq. The specific activity a is the ratio of the activity A per unit mass m of radioactive nuclide or element:

$$a = \frac{A}{m} \tag{2.4}$$

The specific activity achieved in practice is generally lower than the carrier-free specific activity (CFSA) because the source contains stable nuclei in addition to radioactive nuclei.

2.1.2 Decay modes

In the radioactive decay process, the radioactive parent P of atomic number Z and atomic mass A is converted into a daughter D, releasing either an alpha particle (α), beta particles (β^-, β^+), electrons (e^-), gamma-rays (γ), X-rays, (anti-)neutrinos (ν_e, $\bar{\nu}_e$), etc. The α particles consist of a positively charged helium nucleus (He^{2+}). The γ, β^- and β^+ particles are defined as photons, electrons and positrons, respectively, that originate from radioactive decay processes. The common modes of decay relevant to brachytherapy are described in this section.

Alpha decay

Alpha decay occurs when a heavy nucleus disintegrates and emits an α particle:

$${}^{A}_{Z}P \longrightarrow {}^{A-4}_{Z-2}D + \alpha \tag{2.5}$$

Beta decay

Two types of beta decay exist: β^- decay and β^+ decay. β^- decay occurs when a nucleus disintegrates, converts a neutron into a proton and emits an electron and an electron antineutrino:

$${}^{A}_{Z}P \longrightarrow {}_{Z+1}^{\;\;A}D + \beta^- + \bar{\nu}_e \tag{2.6}$$

β^+ decay occurs when a nucleus disintegrates, converts a proton into a neutron and emits an positron and an electron neutrino:

$$^{A}_{Z}P \longrightarrow {}^{A}_{Z-1}D + \beta^+ + \nu_e \tag{2.7}$$

β^- decay generally occurs in nuclei that have excessive neutrons, while β^+ decay generally occurs in nuclei that have excessive protons.

Gamma decay

Gamma decay occurs when an excited nucleus returns to the ground state and emits a γ:

$$^{A}_{Z}P^* \longrightarrow {}^{A}_{Z}P + \gamma \tag{2.8}$$

Electron capture

Electron capture occurs when an inner atomic electron is captured by the proton in the nucleus. This process converts the proton into a neutron and emits an electron neutrino:

$$^{A}_{Z}P + e^- \longrightarrow {}^{A}_{Z-1}D + \nu_e \tag{2.9}$$

Internal conversion

Internal conversion occurs when an excited nucleus returns to the ground state and emits an orbital inner shell electron:

$$^{A}_{Z}P^* \longrightarrow {}^{A}_{Z}P + e^- \tag{2.10}$$

Characteristic X-rays or Auger electrons may be emitted when an electron from an outer shell fills the inner shell vacancy.

2.1.3 Neutron activation

Neutron activation is the process by which neutron radiation induces radioactivity in materials. It occurs when nuclei capture free neutrons, become heavier and enter excited states. The excited nucleus often decays immediately by emitting radiation such as gamma rays or beta particles through (n,γ) or (n,$\beta^\pm$) reactions, respectively. The process of neutron capture often results in the formation of an unstable activation product.

Basic activation model

Activation of nuclides occurs when a stable parent nuclide P is bombarded with neutrons in a nuclear reactor and transforms into a radioactive daughter D that subsequently decays. The system of differential equations that describe radionuclide production is given by:

$$\frac{dN_P}{dt}(t) = -\phi\sigma_P N_P(t) \tag{2.11}$$

$$\frac{dN_D}{dt}(t) = \phi\sigma_P N_P(t) - \lambda_D N_D(t) \tag{2.12}$$

where N_P and N_D represent the number of parent and daughter nuclides at a given time t, respectively, dN_P/dt and dN_D/dt are the rates of change in the number of parent and daughter nuclides, respectively, at a given time t, ϕ is the flux of neutrons in the reactor, σ_P is the activation cross section of the parent nuclide, and λ_D is the decay constant of the daughter radionuclide. Assuming there is no flux depression, the activity of the daughter A_D can be expressed as follows:

$$A_D(t) = \frac{\phi\sigma_P\lambda_D}{\lambda_D - \phi\sigma_P} N_P(0) \left(e^{-\phi\sigma_P t} - e^{-\lambda_D t}\right) \tag{2.13}$$

where $N_P(0)$ is the initial number of parent nuclei [3]. The activity A_D reaches a maximum saturation level after a time t_{max}:

$$t_{max} = \frac{\ln\left(\lambda_D/\phi\sigma_P\right)}{\lambda_D - \phi\sigma_P} \tag{2.14}$$

Long-term activation

In the long term irradiation of targets with high neutron activation cross sections, the achievable activity may be limited by activation of the daughter D itself. Considering corrections for activation of the radioactive daughter D, the system of differential equations need to be modified accordingly:

$$\frac{dN_P}{dt}(t) = -\phi\sigma_P N_P(t) \tag{2.15}$$

$$\frac{dN_D}{dt}(t) = \phi\sigma_P N_P(t) - \lambda_D N_D(t) - \phi\sigma_D N_D(t) \tag{2.16}$$

This differential equation can be generalized to any situation by stating that the rate of change in the number of nuclides is equivalent to the sum of the rate of production minus the sum of the rate of loss through radioactive decay and/or neutron activation processes. The activity of the daughter A_D can be expressed in a similar fashion:

$$A_D(t) = \frac{\phi\sigma_P(\lambda_D + \phi\sigma_D)}{(\lambda_D + \phi\sigma_D) - \phi\sigma_P}\, N_P(0)\, (e^{-\phi\sigma_P t} - e^{-(\lambda_D + \phi\sigma_D)t}) \tag{2.17}$$

. The saturation activity t_{max} is defined as:

$$t_{max} = \frac{\ln\,((\lambda_D + \phi\sigma_D)/\phi\sigma_P)}{(\lambda_D + \phi\sigma_D) - \phi\sigma_P} \tag{2.18}$$

Neutron temperature

The neutron flux ϕ and neutron activation cross section σ adopted in the activation equations are generally specified for thermal neutrons (E_K = 0.025 eV), and exclude higher energy neutrons such as epithermal, resonance, intermediate, and fast neutrons, which are also produced in the nuclear reactor. This approximation provides a good estimate since the neutron capture cross section is typically much greater for thermal neutrons than it is for higher energy neutrons, except in the resonance peak region. In order to avoid discrepancies, production rates are usually estimated in a highly thermalized flux.

2.2 Radiation physics[2]

2.2.1 Photon interactions

Photon beam attenuation

Photon beams are attenuated as they pass through matter, since photons can be scattered and absorbed in matter. The intensity of a narrow beam of monoenergetic photons in a homogeneous medium is described as follows:

$$I = I_0\, e^{-\mu x} \tag{2.19}$$

where μ is the linear attenuation coefficient, which depends on photon energy $h\nu$ and atomic number Z of the medium. The μ is expressed in units of cm^{-1}. The coefficient describes the

---

[2] The information in this section is based on [1] and [2].

probability that a photon will interact in the medium per unit path length. The mass attenuation coefficient is defined as the ratio of μ by the density ρ. The mass attenuation coefficient μ/ρ is typically expressed in units of cm^2 g^{-1}.

The half-value layer (HVL), tenth value layer (TVL) and mean free path (MFP) are defined as the thickness of the material that attenuates the photon beam intensity, or air kerma rate, to one half (50%), one tenth (10%) and $1/e$ (36.8%) of its maximum value, respectively:

$$\mathrm{HVL} = \frac{\ln 2}{\mu} \tag{2.20}$$

$$\mathrm{TVL} = \frac{\ln 10}{\mu} \tag{2.21}$$

$$\mathrm{MFP} = \frac{1}{\mu} \tag{2.22}$$

The HVL, TVL and MFP are typically expressed in units of cm or mm of target material. One TVL is equivalent to roughly 3.32 HVL. The MFP is the average distance a photon travels between collisions with atoms of the target medium.

Types of photon interactions

Photons may undergo various possible interactions with the atoms of a medium. The probability or cross section for each interaction depends on the energy $h\nu$ of the photon and on the atomic number Z of the medium. The photon interactions may be with a tightly bound electron, with the field of the nucleus or with a free orbital electron. During the interaction, the photon may scatter (either coherently or incoherently) or it may be completely absorbed.

Rayleigh scattering

In Rayleigh (coherent) scattering, the photon interacts with a 'bound' orbital electron and is scattered at a small angle, without losing kinetic energy. Since no energy transfer occurs, Rayleigh scattering contributes to the attenuation coefficient but does not result in an energy transfer to charged particles. The mass attenuation coefficient for Rayleigh scattering is proportional to $Z/(h\nu)^2$. The importance of Rayleigh scattering compared to other photon interactions is relatively small in the photon energy range for brachytherapy.

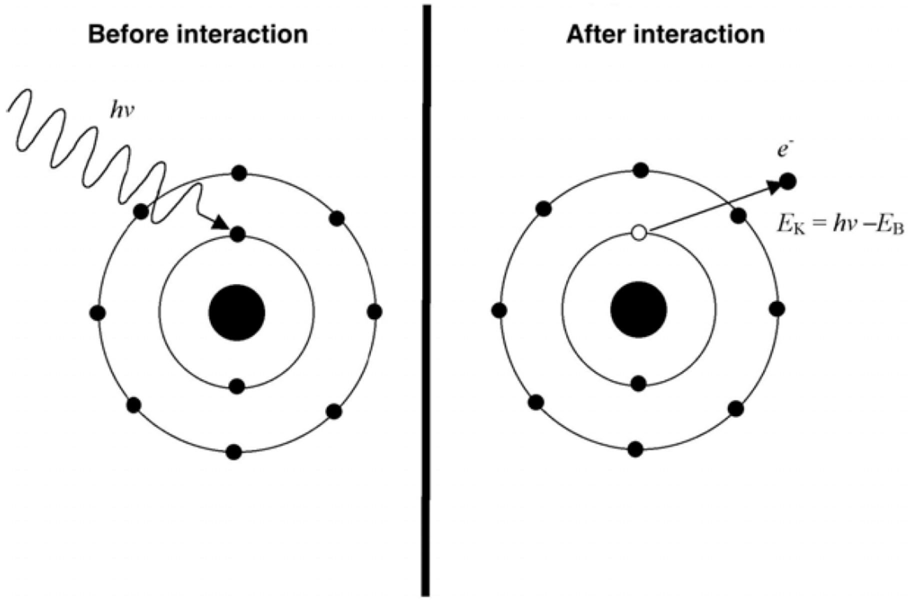

Figure 2.1: Schematic diagram for the photoelectric effect. Figure reproduced from [2].

Photoelectric effect

In the photoelectric effect, the photon interacts with a ’tightly bound’ orbital electron and is absorbed, while the orbital electron is ejected from the atom as a photoelectron with a kinetic energy E_K:

$$E_K = h\nu - E_B \tag{2.23}$$

where $h\nu$ is the initial photon energy and E_B is the binding energy of the electron (Figure 2.1). The mass attenuation coefficient for the photoelectric effect is approximately proportional to $Z^3/(h\nu)^3$. For $h\nu < E_B$ for a particular electronic shell, photons cannot undergo the photoelectric effect with electrons in that particular shell. This result in sharp discontinuities (absorption edges) in the plot of photoelectric attenuation coefficient as a function of photon energy $h\nu$.

Compton scattering

In Compton (incoherent) scattering, the photon interacts with a ’free and stationary’ orbital electron, transfers some of its energy to a recoil electron, and is scattered at an angle θ (Figure 2.2). The scattered photon energy $h\nu'$ and the kinetic energy of the recoil electron E_K are given

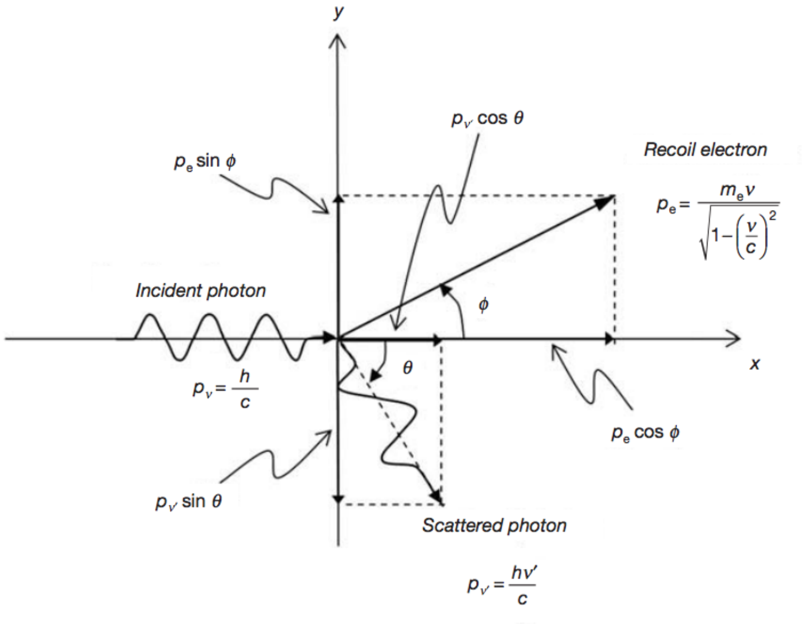

Figure 2.2: Schematic diagram for Compton scattering. Figure reproduced from [1].

by the following relations:

$$h\nu' = h\nu \, \frac{1}{1+\varepsilon(1-\cos\theta)} \tag{2.24}$$

$$E_K = h\nu \, \frac{\varepsilon(1-\cos\theta)}{1+\varepsilon(1-\cos\theta)} \tag{2.25}$$

where $h\nu$ is the initial photon energy, $\varepsilon = \frac{h\nu}{m_e c^2}$ is the normalized incident photon energy, m_e is the electron rest mass and c is the speed of light. The scattering angle θ and the recoil angle ϕ are related by:

$$\cot\phi = (1+\varepsilon)\tan(\theta/2) \tag{2.26}$$

In general, as the initial photon energy increases, the angular distributions of the scattered photon and recoil electron become more forward peaked. The mass attenuation coefficient for Compton scattering is mostly independent of Z (proportional to Z/A) and decreases with increasing photon energy $h\nu$ in the relevant range for brachytherapy (Figure 2.4).

Pair production and triplet production

In pair production, the photon interacts with the field of a nucleus, is completely absorbed and an electron-positron pair is produced (Figure 2.3). The minimum energy threshold for pair production is $2m_ec^2$ = 1.022 MeV. In triplet production, the photon interacts with the field of an orbital electron, disappears, produces an electron-positron pair and transfers kinetic energy to an orbital electron. The minimum energy threshold for triplet production is 4 m_ec^2 = 2.044 MeV. The mass attenuation coefficients for pair and triplet production are roughly proportional to Z, and increase with increasing photon energy $h\nu$. Pair production and triplet production are followed by the annihilation of the positron with a 'free and stationary' electron, producing two annihilation photons, most commonly with energies of m_ec^2 = 0.511 MeV each and emitted at about 180° from each other to satisfy the conservation of momentum and energy.

Relative predominance of interactions

The probability of a photon to undergo any one of these interactions depends on the photon energy $h\nu$ and the atomic number Z of the medium. The contribution of each photon interaction to the total mass attenuation coefficient μ/ρ is shown as a function of photon energy $h\nu$ in Figure 2.4 for carbon and lead. The absorption edges are present for lead, while the absorption edges for carbon are not visible since they occur at energies lower than 1 keV.

The regions of relative predominance of the three main photon interactions are shown as a function of photon energy $h\nu$ and atomic number Z in Figure 2.5. In general, the photoelectric effect dominates at low photon energies $h\nu$ and high atomic numbers Z, Compton scattering dominates at intermediate photon energies $h\nu$ and low atomic numbers Z, and pair (triplet) production dominates at very high photon energies $h\nu$ and high atomic numbers Z. In the case of liquid water (Z_{eff} = 7.4) and soft tissue, the photoelectric effect dominates for energies below 20 keV, Compton scattering dominates in the 20 keV to 20 MeV energy range, and pair production dominates for energies above 20 MeV.

Energy transfer and absorption

Two other related coefficients are used to describe the characteristics of a photon beam. The mass-energy transfer coefficient μ_{tr}/ρ and mass-energy absorption coefficient μ_{en}/ρ describe the energy transferred from photons to charged particles and the energy absorbed by the medium, respectively. The mass-energy transfer coefficient μ_{tr}/ρ at a photon energy $h\nu$ is related to the

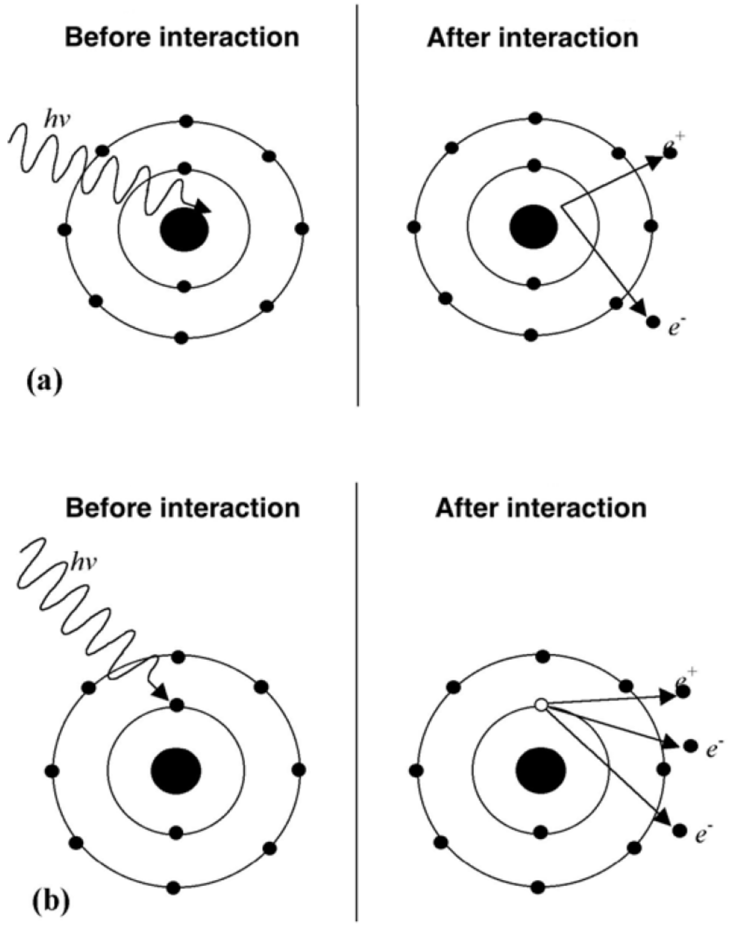

Figure 2.3: Schematic diagram for (a) pair and (b) triplet production. Figure reproduced from [2].

mass attenuation coefficient μ/ρ as follows:

$$\frac{\mu_{tr}}{\rho} = \frac{\mu}{\rho}\,\frac{\overline{E}_{tr}}{h\nu} \tag{2.27}$$

where $\overline{E}_{tr}$ is the average energy transferred to charged particles in the medium. The mass-energy absorption coefficient μ_{en}/ρ at the photon energy $h\nu$ is related to the mass attenuation coefficient μ/ρ as follows:

$$\frac{\mu_{en}}{\rho} = \frac{\mu}{\rho}\,\frac{\overline{E}_{en}}{h\nu} \tag{2.28}$$

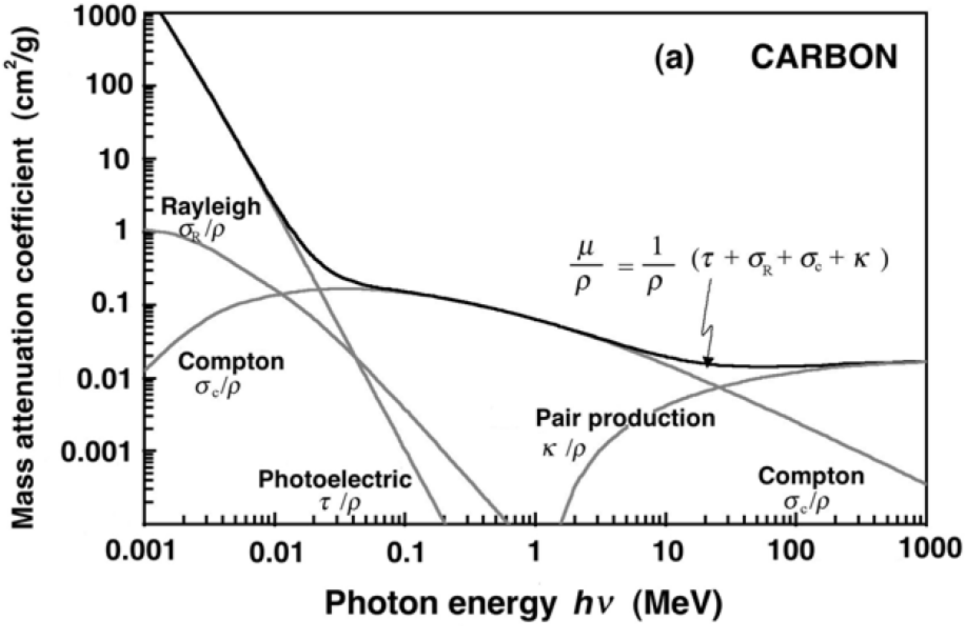

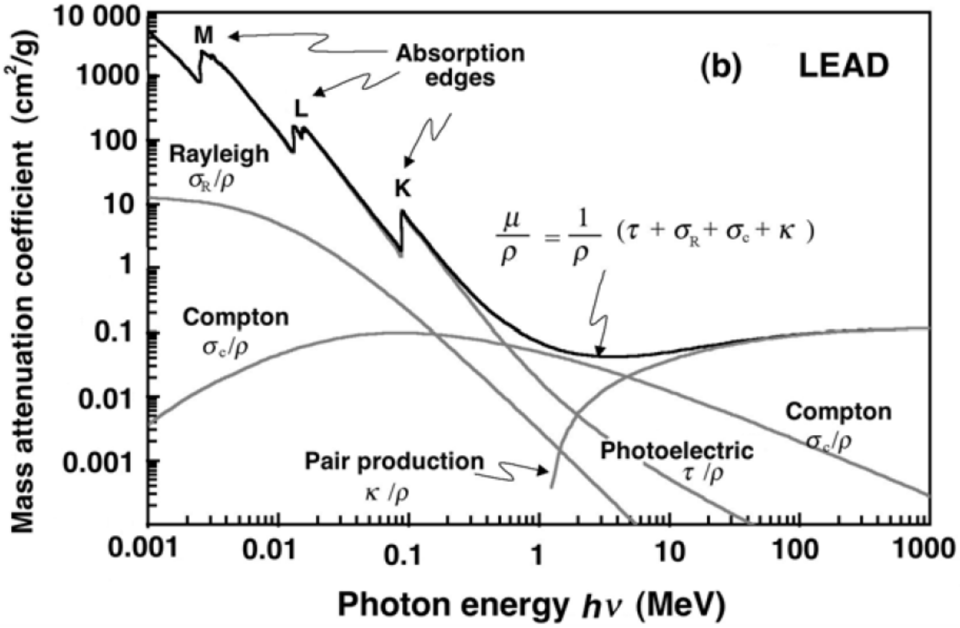

Figure 2.4: Mass attenuation coefficient μ/ρ against photon energy $h\nu$ for (a) carbon and (b) lead. The individual coefficients for Rayleigh scattering, photoelectric effect, Compton scattering, and pair/triplet production are also shown. Figure reproduced from [2].

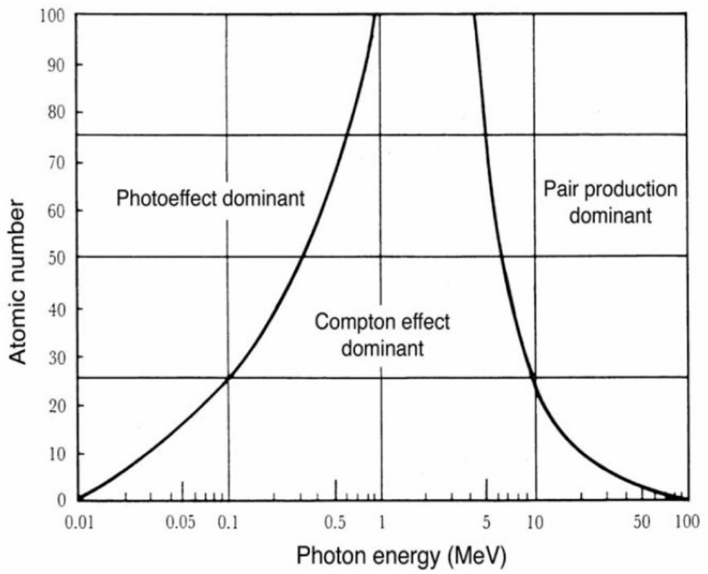

Figure 2.5: Relative predominance of photon interactions as a function of atomic number Z and photon energy $h\nu$. Figure reproduced from [1].

where $\overline{E}_{en}$ is the average energy deposited by charged particles in the medium. The relation between mass-energy absorption coefficient $\frac{\mu_{en}}{\rho}$ and mass-energy transfer coefficient $\frac{\mu_{en}}{\rho}$ is expressed as follows:

$$\frac{\mu_{en}}{\rho} = \frac{\mu_{tr}}{\rho} \left(1 - \overline{g}\right) \tag{2.29}$$

where $\overline{g}$ is the average fraction of the energy transferred to secondary charged particles that is lost through radiative processes. As an example, the radiative fraction $\overline{g}$ is approximately 0.3% for electrons produced by ^{60}Co γ-rays in air [2]. The radiative fraction $\overline{g}$ increases with increasing photon energy $h\nu$ and atomic number Z, and is negligible for photon energies below 1 MeV.

The mass attenuation coefficient μ/ρ, mass-energy transfer coefficient μ_{tr}/ρ and mass-energy absorption coefficient μ_{en}/ρ are shown as a function of photon energy $h\nu$ for carbon and lead in Figure 2.6. At photon energies of a few keV, where the photoelectric effect dominates; most of the energy is transferred to electrons which deposit their energy locally and thus $\mu/\rho \approx \mu_{tr}/\rho \approx \mu_{en}/\rho$. At higher photon energies up to a few MeV, Compton scattering dominates; μ_{tr}/ρ diverges from μ/ρ because only a fraction of the energy is transferred to electrons and $\mu_{tr}/\rho \approx \mu_{en}/\rho$ because of complete absorption of recoil electrons. At photon energies above 10 MeV, pair/triplet production dominates; $\mu/\rho \approx \mu_{tr}/\rho$ because most of the energy is transferred to charged particles and μ_{en}/ρ diverges from μ_{tr}/ρ because of the higher radiative losses at higher energies. With an increasing photon energy $h\nu$ and atomic number Z, the radiative fraction g increases and so does the difference between μ_{en}/ρ and μ_{tr}/ρ.

Production of vacancies in atomic shells

In the photoelectric effect, the Compton effect and triplet production, vacancies are produced in the atomic shells through the ejection of orbital electrons. When a core electron is removed, leaving a vacancy in the atomic shell, an electron from a higher energy level may fall into the vacancy, resulting in a release of energy. This can either result in the emission of characteristic X-rays or through the ejection of a Meitner-Auger electron.

2.2.2 Electron interactions

Types of electron interactions

As an energetic electron traverses matter, it interacts with matter through Coulomb interactions with atomic orbital electrons and atomic nuclei. In general, the electron experiences a large number of interactions before its kinetic energy goes down to zero. Through these collisions, the electrons may scatter or lose their kinetic energy through collision and radiative losses. Electrons with kinetic energy E_K can lose energy up to $E_K/2$ in individual ionizing collisions and energy up to E_K in individual radiative collisions.

Electron-orbital electron interactions

Coulomb interactions between the incident electron and orbital electrons result in ionizations and excitations of the absorber atoms, through soft or hard collisions. Soft collisions occur when the electron interacts with the whole atom and transfers a small amount of energy to orbital electrons. Hard collisions occur when the electron interacts with an orbital electron and transfers a large amount of energy to orbital electrons. Ionization refers to the ejection of an orbital electron, while excitation refers to the transfer of an orbital electron to a higher atomic shell.

Electron-nucleus interactions

Coulomb interactions between the incident electron and nuclei of the absorber atom result in electron scattering and energy loss of the electron through bremsstrahlung (photon) production.

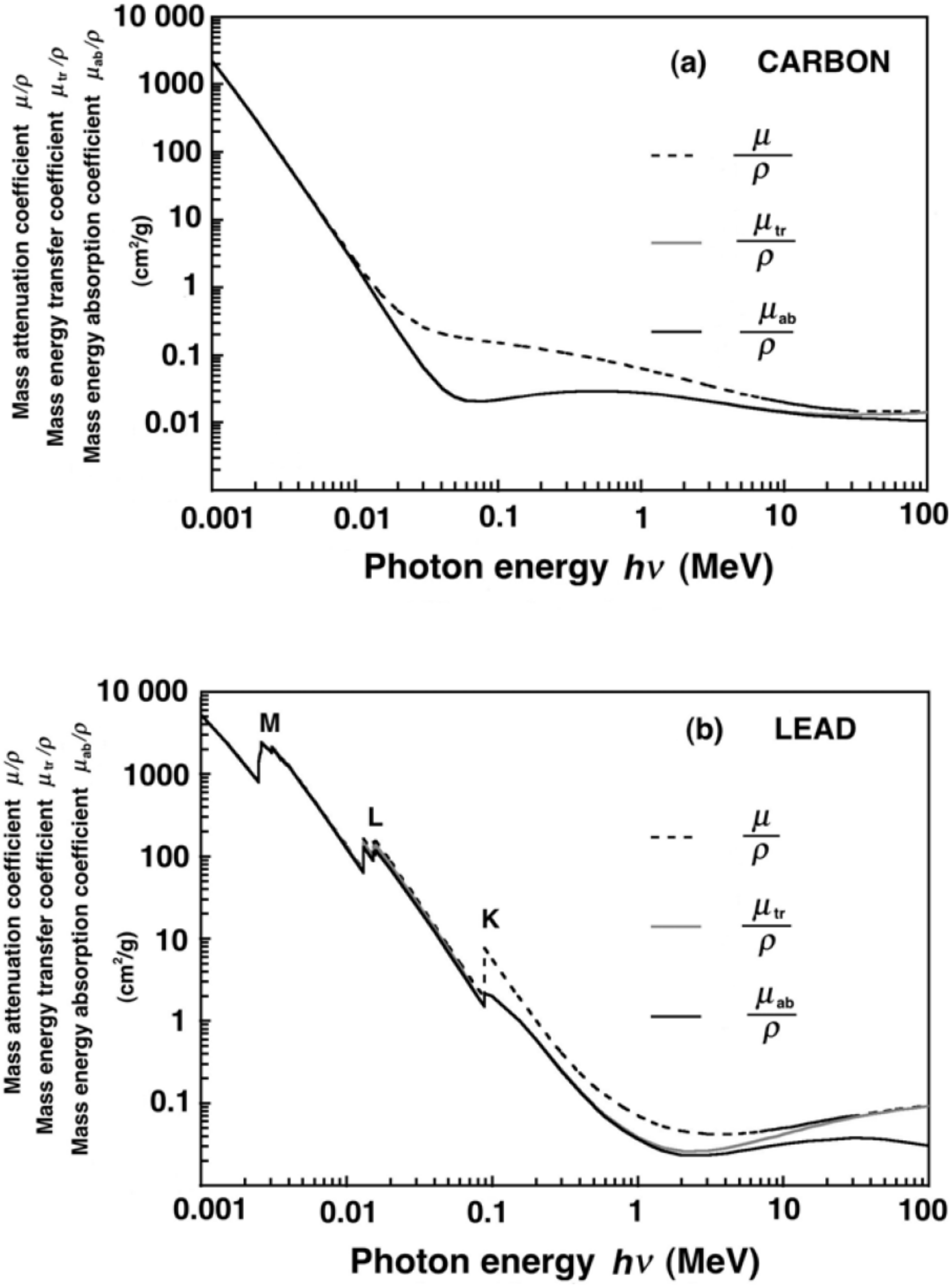

Figure 2.6: Mass attenuation coefficient μ/ρ, mass-energy transfer coefficient μ_{tr}/ρ and mass-energy absorption coefficient μ_{en}/ρ against photon energy $h\nu$ for (a) carbon and (b) lead. Figure reproduced from [2].

The radiative yield increases with the kinetic energy E_K of the incident electrons and the atomic number Z of the medium.

Stopping power

Stopping power S describes the inelastic energy losses by an electron traversing through a medium:

$$S = \frac{dE_K}{dl} \tag{2.30}$$

where dE_K is the kinetic energy loss per unit path length dl. Stopping power is typically expressed in units of MeV cm^{-1}. The mass stopping power is the ratio of S by the density ρ of the medium. The mass stopping power S/ρ is given in units of MeV cm^{-1} g^{-1}.

The total stopping power is divided into two components: the collision stopping power S_{col} and the radiative stopping power S_{rad}. The collision stopping power S_{col} is the part of stopping power that relates to electron-orbital electron interactions. The radiative stopping power S_{rad} is the part of stopping power that relates to electron-nucleus interactions. The total mass stopping power, mass collision stopping power and mass radiative stopping power are shown as a function of the electron kinetic energy E_K for water, aluminum and lead in Figure 2.7. The mass collision stopping power S_{col}/ρ is generally independent of kinetic energy E_K in the MeV range, but decreases with decreasing energy for kinetic energies E_K less than 1 MeV. It depends largely on the atomic number Z of the medium, as it decreases with increasing Z. On the other hand, the mass radiative stopping power S_{rad}/ρ increases with increasing kinetic energy E_K and Z. The mass radiative stopping power S_{rad}/ρ is negligible compared to the total mass stopping power for kinetic energies E_K below 1 MeV.

The stopping power can be used to calculate the electron range, calculated according to the continuous slowing down approximation (CSDA). The CSDA range for an electron is expressed as follows:

$$R_{CSDA} = \int_0^{E_{K_i}} \frac{1}{(S/\rho)}\, dE_K \tag{2.31}$$

where E_{K_i} is the initial kinetic energy of the electron. Range is typically expressed in units of cm. The CSDA range is a good approximation for the average path length travelled by a charged particle as it slows down to rest in a medium. However, this definition neglects scattering, energy loss fluctuations along the track, and energy loss straggling (variation in range due to statistical nature of ionization and excitation events). Therefore, the CSDA range R_{CSDA} represents an upper limit on the actual range R that a charged particle can travel. Figure

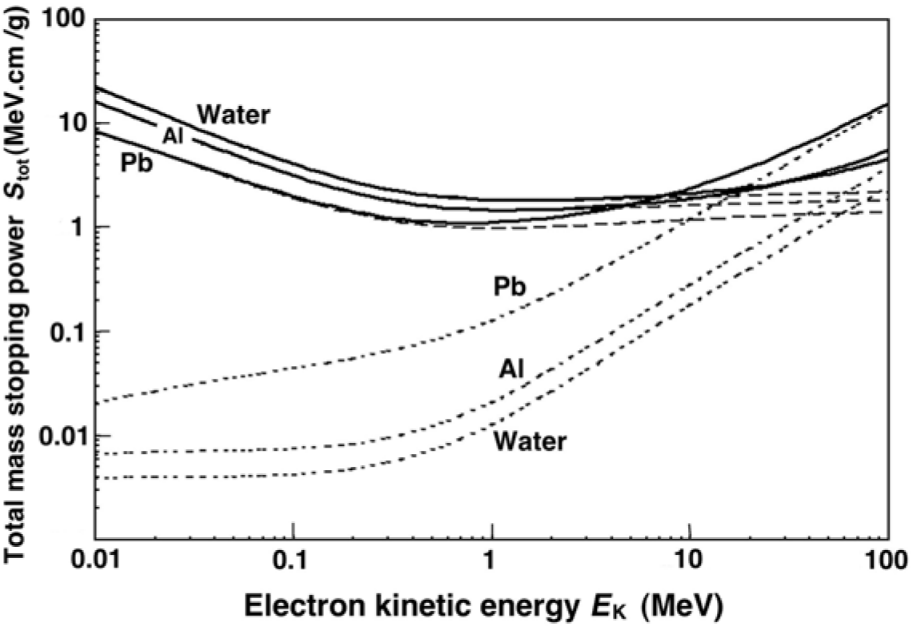

Figure 2.7: Total mass stopping power S/ρ for electrons in water, aluminum and lead against the electron kinetic energy E_K shown with solid curves. The mass collision stopping power S_{col}/ρ and mass radiative stopping power S_{col}/ρ are shown with dashed and dotted curves, respectively. Figure reproduced from [2].

2.8 shows a schematic that highlights the difference between the CSDA range R_{CSDA} and the penetration range R for a light charged particle such as an electron.

The restricted collision stopping power L_Δ accounts for the fraction of the collisional stopping power S_{col} involving transfer energies smaller than a cutoff value Δ:

$$L_\Delta = \frac{dE_\Delta}{dl} \tag{2.32}$$

where dE_Δ is the energy lost by a charged particle due to soft and hard collisions in traversing a distance dl minus the total kinetic energy of the charged particles released with kinetic energies in excess of Δ. The restricted stopping power excludes secondary electrons (delta-rays) with energies larger than a threshold value Δ and that carry energy far from the primary track.

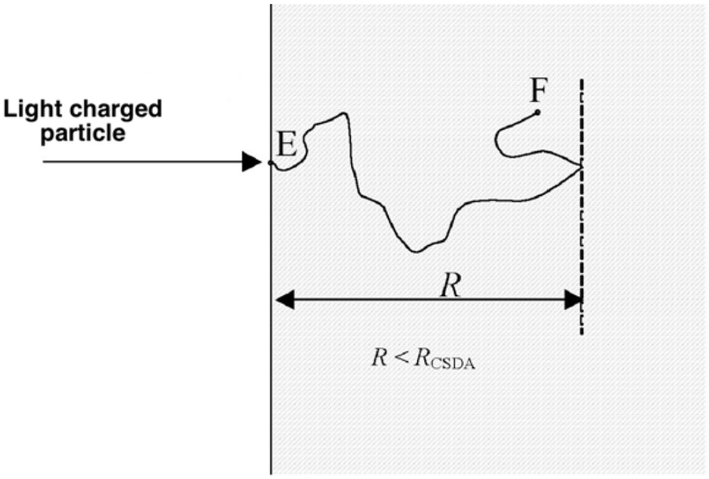

Figure 2.8: Schematic diagram of a light charged particle (e.g. electron) penetration into a medium. Figure reproduced from [2].

Linear energy transfer

The linear energy transfer (LET) describes the average energy an ionizing particle transfers to the medium per unit distance. The LET is typically expressed in units of keV μm^{-1}. LET depends on the type and energy of the radiation as well as the radiological properties of the medium. LET generally increases with decreasing kinetic energy of the charged particle and, therefore, varies along the charged particle track. Two quantities are commonly reported: track-averaged LET and dose-averaged LET. The track-averaged LET represents the average LET assuming equal weight to each unit of track length. The dose-averaged LET assigns a weight to each unit of track length that is proportional to the energy deposited within each interval. Heavy charged particles (e.g. alpha particles, heavy ions) are considered to have high LET (densely ionizing), while light charged particles (e.g. electrons, protons) are considered to have low LET (sparsely ionizing). While indirectly ionizing radiation (e.g. photons, neutrons) cannot be described by LET, LET values are still reported for these particles; these values refer to the LET of the secondary charged particles released from the interaction of the indirectly ionizing radiation. LET helps explain why certain radiation qualities are more effective at producing biological damage than other radiation qualities for the same absorbed dose. High LET radiation is expected to cause more complex DNA damage that is difficult to repair than low LET radiation.

2.3 Dosimetry concepts[3]

2.3.1 Fluence and flux

The fluence Φ is defined as the number of incident particles crossing a plane per unit cross-sectional area:

$$\Phi = \frac{dN}{dA} \tag{2.33}$$

where dN represent the number of particles incident on a sphere of cross-sectional area dA [4]. The SI unit for fluence is m^{-2}. The energy fluence Ψ is the ratio of the radiant energy dE crossing a plane per unit cross-sectional area dA:

$$\Psi = \frac{dE}{dA} = \frac{dN}{dA}\,E = \Phi\,E \tag{2.34}$$

The energy fluence can be related to the fluence using this relation. The SI unit for energy fluence is J m^{-2}.

These quantities are defined for monoenergetic beams. However, realistic radiation beams are almost always polyenergetic. For polyenergetic beams, the concept of fluence spectrum and energy fluence spectrum need to be introduced:

$$\Phi_E(E) = \frac{d\Phi}{dE}(E) \tag{2.35}$$

$$\Psi_E(E) = \frac{d\Psi}{dE}(E) = \frac{d\Phi}{dE}(E)\,E \tag{2.36}$$

where $\Phi_E(E)$ and $\Psi_E(E)$ represent the fluence spectrum and energy spectrum differential in energy E, respectively.

The flux ϕ, or fluence rate, is the ratio of the fluence $d\Phi$ by the time interval dt:

$$\phi = \frac{d\Phi}{dt} \tag{2.37}$$

The SI unit for flux is m^{-2} s^{-1}. Note that fluence (and flux) are defined at a point, however any measurement or simulation scores these quantities in a finite volume V. An alternative definition based on path lengths [5] is often adopted in Monte Carlo (MC) simulations of individual particle tracks (see Section 4.3). The fluence can be defined as the ratio of l/V, where l is the average total length of particle track segments contained within a finite volume V. This

---

[3] The information in this section is based on [1] and [2].

definition allows the calculation of fluence in macroscopic volumes, and does not assume that particle tracks inside the sampling volume are straight lines.

2.3.2 Kerma

Kerma (acronym for "kinetic energy released per unit mass") quantifies the average amount of energy transferred from indirectly ionizing radiation (such as photons and neutrons) to directly ionizing radiation (such as electrons, protons, and heavy ions):

$$K = \frac{d\overline{E}_{tr}}{dm} \tag{2.38}$$

where $d\overline{E}_{tr}$ is the mean energy transferred from the indirectly ionizing radiation to charged particles in the medium per unit mass dm in a finite volume V [4]. Note that this quantity only takes into account the energy transferred to the medium, not the energy absorbed in the medium. The SI unit of kerma is Gy (or J kg^{-1}).

Total kerma can be separated into two components: collision kerma K_{col} and radiative kerma K_{rad}. The collision kerma K_{col} is the part of the total kerma that leads to the production of secondary charged particles that dissipate their energy as ionization in or near the particle tracks in the medium. The radiative kerma K_{rad} is the part of the total kerma that leads to the production of radiative photons as the secondary charged particles slow down and interact in the medium. The relation between collision kerma K_{col} and total kerma K is expressed as follows:

$$K_{col} = K\,(1 - \overline{g}) \tag{2.39}$$

where $\overline{g}$ is the radiative fraction.

For monoenergetic photons, the total kerma K and collision kerma K_{col} are related to the energy fluence Ψ as follows:

$$K = \Psi \left(\frac{\mu_{tr}}{\rho}\right) \tag{2.40}$$

$$K_{col} = \Psi \left(\frac{\mu_{en}}{\rho}\right) \tag{2.41}$$

where (μ_{tr}/ρ) and (μ_{en}/ρ) are the mass-energy transfer coefficient and mass-energy absorption coefficient, respectively, for the medium at a given energy E. For polyenergetic beams, the spectrum-averaged mass-energy transfer coefficients and mass–energy absorption coefficients can be used in conjunction with total energy fluence Ψ to obtain the total kerma K and collision kerma K_{col}:

$$K = \int_0^{E_{max}} \Psi_E(E) \left(\frac{\mu_{tr}}{\rho}\right)(E)\, dE = \Psi \left(\frac{\overline{\mu}_{tr}}{\rho}\right) \tag{2.42}$$

$$K_{col} = \int_0^{E_{max}} \Psi_E(E) \left(\frac{\mu_{en}}{\rho}\right)(E)\, dE = \Psi \left(\frac{\overline{\mu}_{en}}{\rho}\right) \tag{2.43}$$

The kerma rate $\dot{K}$ is the ratio of the kerma dK by the time interval dt:

$$\dot{K} = \frac{dK}{dt} \tag{2.44}$$

The SI unit of kerma rate is Gy s^{-1}.

2.3.3 Dose

The absorbed dose D is defined as the mean energy imparted $d\overline{E}$ by ionizing radiation per unit mass dm in a finite volume V:

$$D = \frac{d\overline{E}}{dm} \tag{2.45}$$

The energy imparted is the sum of all energy entering the volume minus all the energy leaving the volume [4]. The SI unit of absorbed dose is Gy. This quantity is applicable to both directly ionizing (electrons, protons, heavy ions) and indirectly ionizing (photons, neutrons) radiation. For indirectly ionizing radiation, energy is deposited by transferring energy to secondary charged particles, which then transfer their energy to the medium. Note that because secondary charged particles travel in the medium and deposit energy along their tracks, this absorption of energy does not necessarily take place at the same location as the transfer of energy described by kerma.

For monoenergetic charged particles, the absorbed dose D in a uniform medium of density ρ is related to the charged particle fluence Φ as follows:

$$D = \Phi \left(\frac{S_{col}}{\rho}\right) \tag{2.46}$$

where (S_{col}/ρ) is the collision stopping power for the medium at a given energy E. For polyenergetic beams, the spectrum-averaged collision stopping power can be used in conjunction with total fluence Φ to obtain the absorbed dose D:

$$D = \int_0^{E_{max}} \Phi_E(E) \left(\frac{S_{col}}{\rho}\right)(E)\, dE = \Phi \left(\frac{\overline{S}_{col}}{\rho}\right) \tag{2.47}$$

This relationship is valid under the conditions that secondary charged particles deposit their energy locally and radiative particles escape the volume of interest.

The dose rate $\dot{D}$ is the ratio of the dose dD by the time interval time dt:

$$\dot{D} = \frac{dD}{dt} \tag{2.48}$$

The SI unit of dose rate is Gy s^{-1}.

2.3.4 Charged particle equilibrium

In general, the transfer of energy from indirectly ionizing particles to charged particles at a particular location does not lead to the absorption of energy by the medium at the same location. This is due to the finite range of the secondary charged particles released through indirectly ionizing particle interactions. The dose D is related to the collisional kerma K_{col} through the parameter β:

$$D = \beta\, K_{col} \tag{2.49}$$

Since radiative photons mostly escape the volume of interest and thus do not contribute to the absorbed dose in the volume of interest, a valid assumption is that $\beta \approx 1$.

Charged particle equilibrium (CPE) occurs when the number of charged particles of a given type and energy leaving a volume is equal to the number of identical particles entering the volume. When CPE exists in a medium, the absorbed dose in the volume is equal to the collision kerma (β = 1). This is valid irrespective of radiative losses. To guarantee that CPE conditions are met, the medium must be homogeneous in both atomic composition and mass density, and the photon field must be homogeneous in the volume considered (negligible attenuation through the volume). Common causes for CPE failure include: proximity to the radiation source, proximity to a boundary of inhomogeneity in the medium, and high energy radiation. These common causes will be addressed here.

Consider a volume V which contains a smaller volume of interest v, whose boundaries are separated by at least the maximum range of the released secondary charged particles (Figure 2.9). First, if the volume V is too close to the source of indirectly ionizing radiation, then the

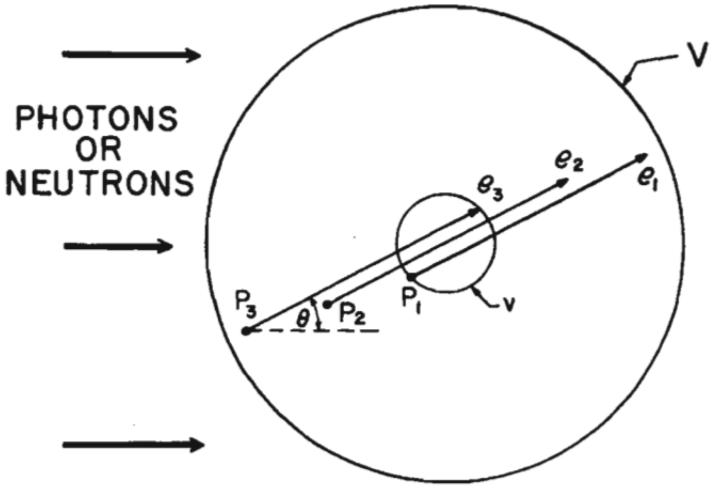

Figure 2.9: Charged particle equilibrium (CPE) conditions for an external source. The volume V contains a homogeneous medium, uniformily irradiated throughout by indirectly ionizing radiation. Secondary charged particles are produced uniformily throughout V. If the minimum distance separating the boundaries of V and smaller volume v is greater than the maximum range of the secondary charged particles, CPE exists in v. Figure reproduced from [6].

energy fluence will be significantly non-uniform within V, and there will be more secondary charged particles entering the volume than leaving the volume, thus loss of CPE may occur in v. Second, if the volume V is separated by a boundary between non-homogeneous media, the fluence of charged particles arriving at v will likely be different than that for a homogeneous medium, thus loss of CPE may occur in v. This difference may be due to change in the production of secondary charged particle and/or change in the range or scattering properties of secondary charged particles. Third, as the energy of indirectly ionizing radiation increases, the range of the secondary charged particles increases more rapidly than the mean free path of the primary radiation. As a result, for very high energy radiation, where the penetrating power of the primary and secondary charged particles are comparable, it becomes important to consider the attenuation of the primary radiation within V. This leads to a difference in the charged particle fluence entering and leaving the volume of interest v. The degree of CPE failure becomes progressively larger at higher energies.

The concept of CPE is best illustrated in an example for a broad, clean beam (i.e. no contamination) of indirectly ionizing radiation. Figure 2.10 shows the relation between collisional kerma K_{col} and absorbed dose D for a typical high-energy photon beam as a function of depth

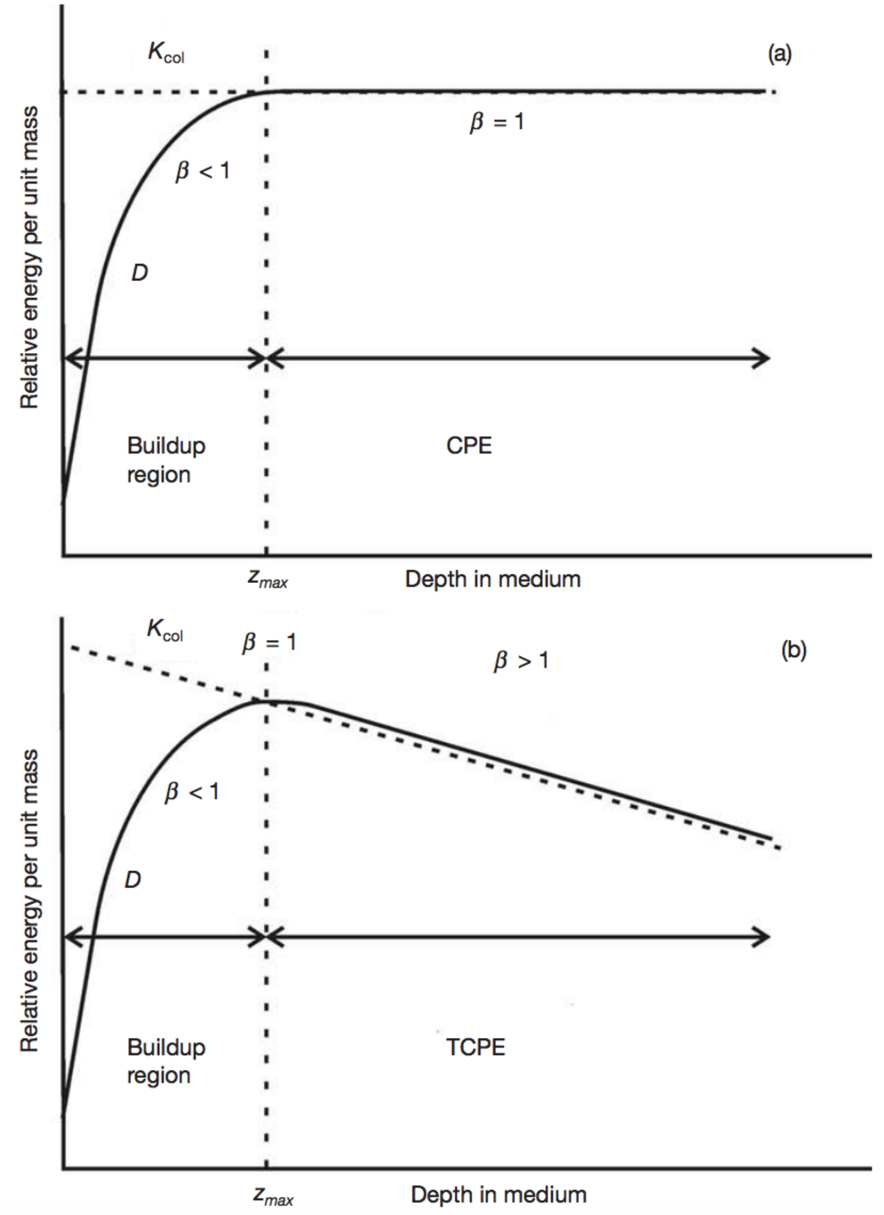

Figure 2.10: Collision kerma and absorbed dose as a function of depth in a medium irradiated by a high energy photon beam for (a) the hypothetical case of no photon attenuation or scattering and for (b) the realistic case. Figure reproduced from [1].

under two scenarios: a) the photon fluence is constant and b) the photon fluence is attenuated by the medium.

In the case where photon attenuation and scattering are considered negligible (Figure 2.10a), the collisional kerma K_{col} remains constant with depth. Initially, at small depths in the medium, there is a build-up region for the dose, where the electron fluence and thus the absorbed dose D increase as a function of depth until the depth of maximum dose z_{max}, which is similar to the range of the secondary charged particles in the medium. The build-up region ($\beta < 1$) is followed by a region where complete CPE exists ($\beta = 1$).

When attenuation and scattering are not negligible (Figure 2.10b), the photon fluence and collisional kerma K_{col} decrease exponentially with depth. The build-up region ($\beta < 1$) is followed by a region where absorbed dose is larger than collisional kerma ($\beta > 1$), since the absorbed dose is due to electrons liberated by the photon fluence upstream that is slightly larger than the photon fluence downstream. In this region, transient charged particle equilibrium (TCPE) exists as β is essentially constant with depth and is greater than unity, since the average range of the secondary electrons does not vary considerably with depth. In this scenario, conditions of true CPE ($\beta = 1$) exist only at the depth of maximum dose z_{max}, where the rising slope due to the build-up of charged particles is balanced by the descending slope due to the attenuation of the photon beam. However, the existence of a proportional relationship between absorbed dose and collisional kerma ($D \sim K_{col}$) under TCPE conditions is valuable for high-energy photon beams.

2.4 Microdosimetry concepts[4]

2.4.1 Introduction to microdosimetry

Ionizing radiation causes a variety of biological effects after it interacts with biological targets such as individual cells or subcellular structures. The detailed understanding of the mechanisms by which these effects are induced are related to the patterns of energy deposition in microscopic regions called domains. The concept of average absorbed dose D to a macroscopic volume (as an approximation to dose at a point) is not sufficient to adequately characterize the energy deposition, since this quantity ignores the random fluctuations of the energy imparted on the scale of these microscopic domains. The fluctuations are most substantial for low absorbed doses, small volumes and densely ionizing radiation. In these cases, the energy imparted to a microscopic domain may span several orders of magnitude or may even be zero. The concept of average LET (track-average or dose-average) ignores many stochastic effects that influence

---

[4] The information in this section is based on [7] and [8].

track structure, such as the fluctuation of energy loss along the track (energy loss straggling), the finite range of the particles and the variation of LET along the track, and the lateral extension of the track due to delta rays and scattering. These limitations of the absorbed dose D and LET illustrate the need for additional concepts and quantities that are based on random variables instead of average or expectation values.

Microdosimetry is the theoretical and experimental investigation of the imparted energy probability distributions in a small, microscopic volume of matter that is crossed by single ionizing particles [8]. The small, microscopic volume is meant to represent the volume of the critical target of radiation damage. Microdosimetric distributions describe the spatial pattern of energy deposition along the charged particle track, the fluctuations of energy imparted in microscopic domains and the biological effectiveness of different radiation qualities. The microdosimetric quantities are related to the absorbed dose D and LET, but will also take into consideration all the related stochastic effects that are disregarded in those concepts.

2.4.2 Microdosimetric quantities

Specific energy z represents the stochastic analog of the absorbed dose D and is defined as:

$$z = \frac{\varepsilon}{m} \tag{2.50}$$

where ε is the energy imparted to a small volume of mass m [9]. Specific energy is expressed in units of Gy. In microscopic dimensions, where the fluctuation in energy deposition becomes of increasing importance, specific energy z is the appropriate description of energy deposition instead of average absorbed dose D. The specific energy varies with the absorbed dose D and is defined for multiple events. An event essentially consists of an individual interaction of a charged particle track with a target volume. An event denotes the interaction of statistically correlated particles, including secondary particles, that deposit energy within the target volume. The passage of a charged particle through the site without any energy deposition event is therefore not counted as an event. In a multiple-event spectrum, there are several events that contribute to the total energy imparted. Both the number of events n and the energy imparted ε in each event are governed by Poisson statistics. The frequency distribution of specific energy z for an average absorbed dose D can be described by a compound Poisson process:

$$f(z,D) = \sum_{\nu=0}^{\infty} \frac{e^{-n} n^{\nu}}{\nu!} f_{\nu}(z) \tag{2.51}$$

where n represents the mean number of events per site and $f_\nu(z)$ represents the probability of obtaining a specific energy z in exactly ν events. The mean specific energy $\bar{z}$ is the microdosimetric equivalent of absorbed dose:

$$\bar{z} = \int_0^\infty z\, f(z,D)\, dz \tag{2.52}$$

At larger doses, the distribution tends to a normal distribution with average value D. The specific energy distributions can also be defined for single events. The single-event frequency mean and dose mean specific energy, $\bar{z}_F$ and $\bar{z}_D$, respectively, are defined as:

$$\bar{z}_F = \int_0^\infty z\, f_1(z)\, dz \tag{2.53}$$

$$\bar{z}_D = \int_0^\infty z\, d_1(z)\, dz = \frac{\int_0^\infty z^2\, f_1(z)\, dz}{\int_0^\infty z\, f_1(z)\, dz} = \frac{\overline{z_F^2}}{\bar{z}_F} \tag{2.54}$$

where $f_1(z)$ and $d_1(z)$ represent the normalized frequency and dose distributions of specific energy for single events, respectively. The dose average is always greater than the frequency average since large energy deposition events contribute more to the energy imparted than low energy deposition events. To account for the overlap of multiple tracks m in the scoring volumes at large doses D, the multiple-track distribution $f(z,D)$ can be obtained by performing the convolution of the single-track distribution $f_1(z)$ with itself m times.

Lineal energy y represents the stochastic analog of LET and is defined for single events only:

$$y = \frac{\varepsilon}{\bar{l}} \tag{2.55}$$

where ε is the energy imparted in a single event and $\bar{l}$ is the mean chord length of the object under mean free path (μ) randomness, which means all tracks intersecting the sphere originate uniformly from random points in space, are isotropically distributed and travel in a straight line [7]. The mean chord length $\bar{l}$ is equal to $\frac{4V}{S}$ for a convex site of volume V and surface area S. For spherical sites with diameter d, the mean chord length $\bar{l}$ is equal to $\frac{2d}{3}$. Lineal energy is expressed in units of keV μm^{-1}. The single-event frequency mean and dose mean lineal energy, $\bar{y}_F$ and $\bar{y}_D$, respectively:

$$\bar{y}_F = \int_0^\infty y\, f(y)\, dy \tag{2.56}$$

$$\bar{y}_D = \int_0^\infty y\, d(y)\, dy = \frac{\int_0^\infty y^2\, f(y)\, dy}{\int_0^\infty y\, f(y)\, dy} = \frac{\overline{y_F^2}}{\bar{y}_F} \tag{2.57}$$

where $f(y)$ and $d(y)$ represent the normalized frequency and dose distributions of lineal energy for single events, respectively. As previously discussed, the dose mean lineal energy $\bar{y}_D$ (analog to dose-averaged LET) is always greater than the frequency mean lineal energy $\bar{y}_F$ (analog to track-averaged LET). The single-event frequency and dose distributions of lineal energy are independent of the absorbed dose D and are characteristic of the radiation quality itself. Lineal energy distributions are typically displayed by plotting $y\, d(y)$ as a function of y on a semi-logarithmic axis. In this type of display, equal areas under the curve between two values of y represent equal fractional doses.

The fundamental difference between quantities like absorbed dose D and specific energy z, or LET and lineal energy y, is their relation to the stochastic nature of the energy imparted. Absorbed dose and LET are macroscopic quantities defined by average energy depositions, while specific and lineal energy are stochastic quantities described by distributions of energy deposition events. If the probability of damage in a given domain is related to the energy imparted in the volume, then it might be better described by the microdosimetric distributions for that particular domain volume than by the absorbed dose D and LET. While LET depends on the energy cutoff and is defined over a small distance compared to the range of the charged particle, lineal energy y depends on the size and shape of the target volume and can be valid for target volumes larger than the range.

2.4.3 Application of microdosimetry to radiation quality

Microdosimetry has been used extensively to characterize radiation quality in radiation therapy and radiation protection [10]. While LET is an average quantity that is difficult to measure in practice, lineal energy distributions are measurable quantities in general. Microdosimetric distributions can typically be measured using tissue-equivalent proportional counters (TEPCs) or simulated using Monte Carlo track structure (MCTS) codes (see Section 4.3.2). Systematic microdosimetric measurements are faster and cheaper to perform than radiobiological experiments. The dose mean lineal energy $\bar{y}_D$ is a recommended quantity for the evaluation of radiation quality [11]. Historically, the dose mean lineal energy $\bar{y}_D$ in micrometer-sized target volumes have most often been reported to quantify radiation quality [12]. This was mainly due to technical reasons, since the tissue-equivalent diameter of TEPCs is typically on the order of 1 μm. However, lineal energy distributions can vary significantly with the size and shape of the scoring volumes used. Indeed, it may be of interest to study the energy deposition patterns in sites comparable to the size of biologically relevant DNA structures, such as DNA segments

($\sim$2 nm), nucleosomes ($\sim$10 nm) and chromatin fibres ($\sim$30 nm). For nanometer-sized target volumes, MCTS simulations are typically preferred over TEPC measurements, due to the relatively high uncertainties in these measurements [13]. Recently, Lindborg et al. [14, 15] determined that the dose mean lineal energy $\bar{y}_D$ in a volume with a diameter on the order of 10 nm can provide a strong indication of the relative effectiveness of the radiation in fractionated radiation therapy applications, for a variety of endpoints taken from *in vivo* experiments with animals and *in vitro* experiments with cell lines. This relationship was consistently observed for low LET and high LET radiation, including photon, proton, neutron and heavy ion therapy beams. Thus, in some cases, microdosimetry can provide a quantitative relationship between the spatial pattern of energy deposition and the biological effects of radiation.

References

[1] IAEA. Radiation oncology physics: a handbook for teachers and students. Podgorsak EB, editor. Vienna, Austria; 2005.

[2] Podgorsak EB. Radiation physics for medical physicists. 3rd ed. Berlin, Germany: Springer-Verlag; 2010.

[3] Hetherington ELR, Wood NR. The production of ytterbium-169 radiography sources in a high flux reactor. Lucas Heights, Australia: Australian Atomic Energy Commission; 1974.

[4] ICRU. Fundamental quantities and units for ionising radiation (revised). ICRU Report. 2011;11(1).

[5] Papiez MJ, Battista JJ. Radiance and particle fluence. Phys Med Biol. 1994;39:1053–1062.

[6] Attix FH. Introduction to radiological physics and radiation dosimetry. Madison: Wiley-VCH; 2005.

[7] Kellerer AM. Fundamentals of microdosimetry. Harcourt Brace Jovanovich; 1985.

[8] Rossi HH, Zaider M. Microdosimetry and its applications. Berlin: Springer-Verlag; 1995.

[9] ICRU. Microdosimetry. vol. ICRU Report 36. Bethesda, MD: International Commission on Radiation Units & Measurements; 1983.

[10] ICRP. The 2007 recommendations of the International Commission on Radiological Protection. ICRP publication 103. Ann ICRP. 2007;37(2-4):1–332.

[11] Nikjoo H, Lindborg L. RBE of low-energy electrons and photons. Phys Med Biol. 2010;55(10):65–109.

[12] ICRU. The quality factor in radiation protection. vol. ICRU Report 40. Bethesda, MD: International Commission on Radiation Units & Measurements; 1986.

[13] Lillhök JE, Grindborg JE, Lindborg L, Gudowska I, Alm Carlsson G, Söderberg J, et al. Nanodosimetry in a clinical neutron therapy beam using the variance-covariance method and Monte Carlo simulation. Phys Med Biol. 2007;52(16):4953–4966.

[14] Lindborg L, Hultqvist M, Tedgren AC, Nikjoo H. Lineal energy and radiation quality in radiation therapy: model calculations and comparison with experiment. Phys Med Biol. 2013;58(1):3089–3105.

[15] Lindborg L, Hultqvist M, Tedgren AC, Nikjoo H. Nanodosimetry and RBE values in radiotherapy. Radiat Prot Dosimetry. 2015;166(1-4):339–342.

Chapter 3

Brachytherapy

3.1 Types of brachytherapy[1]

3.1.1 Implantation techniques

Brachytherapy treatments can be classified by the type of implant used. Brachytherapy can be administered by placing radioactive sources into body cavities close to the tumour volume (intracavitary), over the tissue to be treated (surface), in a lumen (intraluminal), or into arteries (intravascular). Sources can also be implanted within the tumour volume (interstitial) or during surgery (intraoperative). In general, the two most common types of brachytherapy treatments are interstitial and intracavitary.

3.1.2 Source loading

Brachytherapy sources can be loaded through hot loading, where the applicator is preloaded and contains the radioactive sources at the time of placement into the patient, or through afterloading, where the applicator is first placed into the region of interest and the radioactive sources are loaded later, either by hand (manual afterloading) or by a machine (remote afterloading). The use of remote afterloading devices offers several practical advantages over manual procedures, such as increased patient treatment capacity, consistent and reproducible treatment delivery and reduced radiation exposure of staff. Hot loading is not performed in the clinic for radiation safety of the patient and staff.

---

[1] The information in this section is based on [1].

3.1.3 Treatment time

Brachytherapy treatments can be categorized with respect to the treatment time. Radioactive sources can be implanted permanently or temporarily inside the patient. In a temporary implant, the dose is delivered over a short period of time and is removed afterwards. In a permanent implant, the dose is delivered over the lifetime of the source until it decays completely.

3.1.4 Dose rate

Brachytherapy treatments can also be classified based on their dose rates [2]. Low dose rate (LDR) brachytherapy refers to a treatment with a dose rate of 0.4-2 Gy h^{-1}. The main isotopes used in conventional LDR brachytherapy is ^{125}I. This is compatible with either conventional manual or automatic afterloading techniques. High dose rate (HDR) brachytherapy refers to a treatment a dose rate greater than 12 Gy h^{-1}. In practice, HDR treatments are given with a substantially higher dose rate than that given by the lower limit of 12 Gy h^{-1}. The main isotope used in conventional HDR brachytherapy is ^{192}Ir. This is compatible with remote afterloading technology only, because of the high source activity.

Compared to LDR brachytherapy, HDR brachytherapy allows for the optimization of dose distribution, delivers outpatient treatments, and eliminates the radiation exposure to the staff. However, there are some disadvantages that should also be considered, such as the potential for serious accidents and the need for increased staff commitment.

The process of delivering pulsed-dose-rate (PDR) brachytherapy is similar to HDR, but radiation is delivered in short pulses over several hours. PDR combines the practical advantages of HDR brachytherapy (dose optimization, outpatient treatment and radiation safety) with the radiobiological advantages of LDR brachytherapy [3]. PDR brachytherapy is administered using a remote afterloader.

3.2 Photon-emitting brachytherapy sources

Sealed photon-emitting brachytherapy sources are most commonly available as radioactive seeds. Brachytherapy sources are usually encapsulated to contain the activity, to reduce beta contamination and to provide rigidity to the source. The brachytherapy source photon fluence spectrum consists of γ-rays, characteristic X-rays and bremsstrahlung that originate either in the source core or in the capsule.

Table 3.1: Physical properties of photon-emitting radionuclides.

Radionuclide	Decay mode	Half-life	Mean photon energy (keV)	HVL (mm Pb)
^{60}Co	β^-	5.3 y	1250	11.0
^{137}Cs	β^-	30.2 y	662	5.5
^{192}Ir	β^- (95%), EC (5%)	73.8 d	380	2.5
^{75}Se	EC	118.5 d	210	1.0
^{57}Co	EC	272 d	114	0.6
^{169}Yb	EC	32.0 d	93	0.48
^{153}Gd	EC	240.4 d	60	0.12
^{131}Cs	EC	9.7 d	30	0.030
^{125}I	EC	59.5 d	28	0.025
^{103}Pd	EC	17.0 d	21	0.008

Table 3.1 lists the physical properties of various clinical and hypothetical photon-emitting brachytherapy sources. The choice of an appropriate photon-emitting radionuclide for a specific brachytherapy application depends on several relevant characteristics, such as the average photon energy, the half-life, the specific activity (or dose rate), and the cost of production. The main production mode for the listed radionuclides is through neutron activation in a nuclear reactor, except for ^{57}Co which is mainly produced using a cyclotron. Photon-emitting radionuclides can be classified based on the average energy E_{avg} of the emitted photons. Sources belonging to the same energy category have similar dosimetric characteristics in terms of attenuation and scatter in tissue. The average photon energy E_{avg} mainly influences the penetration in tissue and shielding material (e.g. HVL, TVL, MFP), which dictate the dose distribution in tissue and the shielding requirements for the treatment room.

3.2.1 Low-energy sources

Low-energy sources ($E_{avg} < 50$ keV) do not penetrate very far in tissue and are typically used in interstitial LDR brachytherapy. Over the last few years, ^{125}I and ^{103}Pd have been extensively used for permanent prostate brachytherapy implants [4]. Recently, ^{131}Cs sources were also introduced for this purpose [5]. While the average energy of the sources are roughly equivalent, the shorter half-lives of ^{103}Pd and ^{131}Cs may present logistic and radiobiological advantages compared to ^{125}I.

3.2.2 Intermediate-energy sources

Intermediate-energy sources (50 keV $< E_{avg} <$ 200 keV) penetrate further in water or tissue but can easily be attenuated by high-Z material such as lead. They are desirable to reduce shielding requirements for the treatment room or to spare healthy tissues. Various designs of ^{169}Yb sources have been proposed and/or developed over the years for LDR [6] and HDR [7–9] brachytherapy applications as well as for a new treatment technique called gold nanoparticle-aided therapy (GNRT) [10]. ^{153}Gd has been proposed as a source to deliver IMBT for prostate cancer [11–14]. However, the low maximum specific activity [15] limits the feasibility of the technique. ^{57}Co has been proposed as a hypothetical HDR brachytherapy source due to its high specific activity and long half-life [16]. However, the production costs related to irradiation using a cyclotron are too elevated for clinical use.

3.2.3 High-energy sources

High-energy sources ($E_{avg} >$ 200 keV) penetrate deep into water or tissue. ^{192}Ir is the most common radioisotope used in HDR brachytherapy. ^{60}Co offers logistic and economic advantages due to its longer half-life, however additional shielding is required for the treatment room [17]. ^{137}Cs sources have been used for several decades in LDR brachytherapy but have been discontinued [18]. ^{75}Se has traditionally been used as a radiation source in industrial radiography, but has physical and dosimetric characteristics that make it an interesting radionuclide for HDR brachytherapy [19]. Its longer half-life would allow for fewer source exchanges, while its lower energy would lower shielding requirements for the room and would improve the effectiveness of shielded intracavitary applicators [20].

3.2.4 Electronic brachytherapy sources

Electronic brachytherapy (eBT) uses miniature x-ray sources, which operate between 50 and 100 kVp, to deliver radiation at very high dose rates to shallow depth and are typically used for skin brachytherapy and intraoperative brachytherapy. Currently, there exists several eBT systems on the market: Intrabeam (Zeiss, Jena, Germany), Xoft (iCAD, Nashua, New Hampshire), Papillon (Ariane Medical Systems, Alfreton, England), Photoelectric Therapy (Xstrahl, Suwanee, USA), Esteya (Elekta Brachytherapy, Veenendaal, The Netherlands) and SRT 100 (Sensus Healthcare, Boca Raton, USA). Advantages of eBT sources include reduced dose to organs at risk, minimal dose to staff, no leakage radiation during off-treatment times, minimal shielding requirements and no radioactive waste. However, eBT sources cannot be used for interstitial brachytherapy due to the source dimensions that are larger than the diameter of interstitial catheters, in addition to the limited range of the photons.

3.3 Radiobiology

3.3.1 Direct and indirect effects of radiation

When cells are exposed to ionizing radiation, the physical effects between radiation and atoms or molecules in those cells occur in a first stage, while the biological effects which may affect cell function occur in a later stage. The biological effects of radiation result mainly from damage to the DNA molecule, which is the most critical target within the cell. DNA double-strand breaks (DSB) are widely accepted as the key driver of radiobiological effects in cells.

Typically, radiation damage is characterized as either direct or indirect effects. In direct action, the radiation interacts directly with the critical target in the cell such as DNA. The atoms of the target itself may be ionized or excited through Coulomb interactions, leading to the chain of physical and chemical events that eventually produce the biological damage. Direct action is the dominant process for high LET particles since densely ionizing radiation is more likely to interact directly with the critical target. In indirect action, the radiation interacts with other molecules and atoms within the cell to produce free radicals, which can, through diffusion in the cell, damage the critical target within the cell. About two thirds of the biological damage by low LET radiation is due to indirect action.

Radiation damage can be classified in three categories: lethal, sublethal or potentially lethal lesions. Lethal lesions refers to damage that is irreversible, irreparable and leads to cell death. Sublethal lesions refer to damage that is either repaired within a few hours or that eventually leads to lethal damage if additional sublethal damage occurs during that timeframe. Potentially lethal lesions refer to damage that can be manipulated by repair when cells are allowed to remain in a non-dividing state.

3.3.2 Linear-quadratic model

A cell survival curve describes the relationship between the surviving fraction of irradiated cells and the absorbed dose. The linear-quadratic (LQ) model assumes that there are two components to cell killing by radiation. The first component is proportional to the absorbed dose (αD), while the second component is proportional to the square of the dose (βD^2). The expression for the cell survival curve can then be described by the following equation:

$$S = e^{-(\alpha D + \beta D^2)} \tag{3.1}$$

where S is the surviving fraction at a given dose D, α is the initial slope of the cell survival curve and β is the quadratic component of the cell survival curve. An intuitive interpretation of these two contributions to cell killing is that the linear component represents cell killing from lethal damage caused by a single particle track, while the quadratic component represents cell killing resulting from the interaction of sublethal lesions caused by different particles tracks leading to lethal damage. The α/β ratio gives the dose at which the linear and quadratic components of cell killing are equal. This is often referred to as the shoulder region of the dose-response curve. In general, both the linear and quadratic components of cell killing are observed for low LET particles, while for high LET particles, the linear component dominates the dose response curve (Figure 3.1). The latter is due to the fact that multiple tracks of high LET radiation are unlikely to intersect or damage the same critical target at the doses relevant to radiation therapy (few Gy).

A tissue expresses response to radiation damage either as an early (acute) effect or as a late (chronic) effect. Early effects occur during or shortly after the treatment, mainly affect rapidly proliferating tissues and can be manageable and/or reversible in many cases. Late effects, on the other hand, occur months or years after the treatment, can be permanent and may negatively impact the quality of life of patients. The cell survival curves for late responding tissues, which have a low α/β ratio, are more curved than those for early responding tissues, which have a high α/β ratio. Early responding tissues see a relatively constant rate of cell killing with increasing dose, while late responding tissues demonstrate increased survival at lower doses but significantly greater toxicity at higher doses. Most tumours are rapidly growing and have a high α/β ratio. The linear and quadratic components of cell killing are equal at $\alpha/\beta \approx 10$ Gy for early responding normal tissues and tumours and $\alpha/\beta \approx 3$ Gy for late responding normal tissues, respectively. A well known exception is prostate cancer tissue, which has an α/β ratio of 1.5 Gy, even lower than that of the surrounding late responding healthy tissue. This explains why HDR brachytherapy, which can deliver a high dose to the prostate, is an effective treatment for prostate cancer. The α/β ratios for early and late reactions in human tissues are relatively consistent with results from experimental animal models [21].

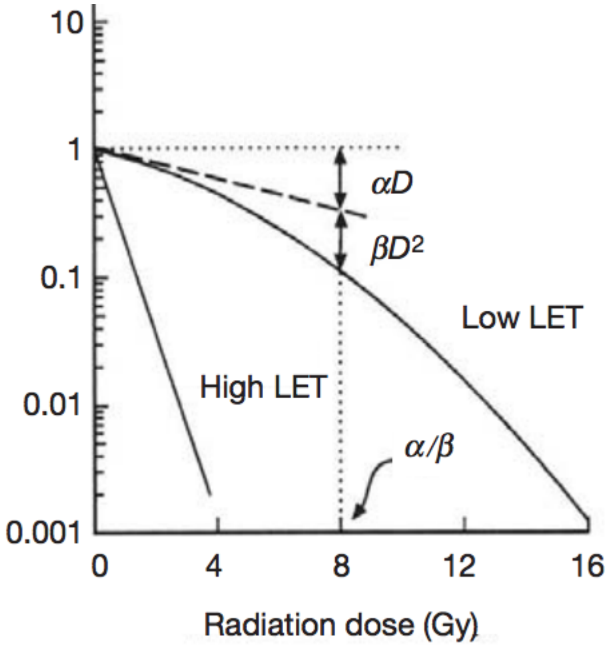

Figure 3.1: Hypothetical survival curve for high LET and low LET radiation according to the linear-quadratic model. α and β represent the linear and quadratic components to cell killing. Figure reproduced from [1].

3.3.3 Dose, dose rate and fractionation

In general, radiation therapy is delivered in several, low doses over a period of several days or weeks (e.g. EBRT, HDR brachytherapy). When the total absorbed dose D is divided into n fractions with a dose per fraction d, there is enough time to allow full repair of sublethal lesions between the fractions. The survival fraction S for a fractionated treatment can then be derived assuming that each fraction provides an independent biological effect:

$$S = \left(e^{-(\alpha d + \beta d^2)}\right)^n = e^{-n(\alpha d + \beta d^2)} = e^{-D(\alpha + \beta d)} \tag{3.2}$$

When a treatment is fractionated, the shoulder of the survival curve has to be repeated many times and, as a result, the quadratic component of cell killing is reduced (as $Dd < D^2$). Typically, a low dose per fraction (few Gy) is selected to reduce normal tissue complications (late effects) while improving the cell killing effect in the tumour (early effects). The time interval between radiation fractions preferentially allows normal cells to repair sublethal damage. It also allows the repopulation of normal healthy cells, reassortment of tumour cells into more radiosensitive phases of the cell cycle and perfusion of oxygen into hypoxic regions of tumours. The underlying

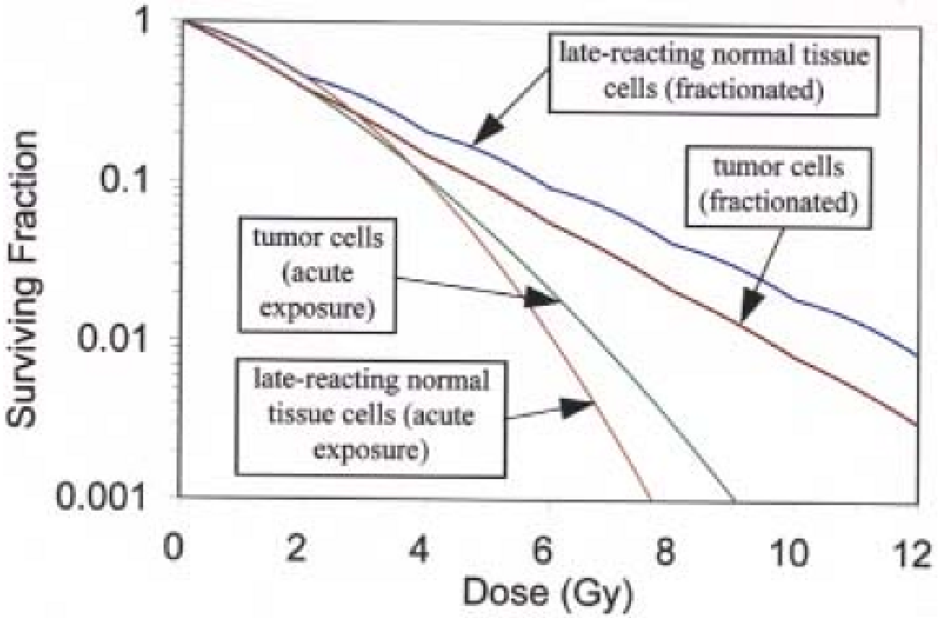

Figure 3.2: Surviving fraction for early (tumour) and late responding cells as function of the absorbed dose delivered in a single fraction (acute exposure) or multiple 2 Gy fractions (fractionated). Figure reproduced from [22].

goal of fractionation is to optimize the dose per fraction to produce the maximum separation between the early responding tumours and late responding tissue curves (Figure 3.2).

The biologically effective dose (BED) is a quantity based on the linear-quadratic model that characterizes the biological effect for fractionated radiation therapy:

$$\mathrm{BED} = D\left(1 + \frac{d}{\alpha/\beta}\right) \tag{3.3}$$

The BED can thus be separated into two factors, where the first factor is the total dose and the second factor represents the relative effectiveness of that total dose. Another useful method to compare the biological effectiveness between fractionation schedules is to express the effective dose as if it were given with a standard dose per fraction d of 2 Gy. The equivalent dose in 2 Gy fractions (EQD2) is defined as follows:

$$\mathrm{EQD2} = D\,\frac{\left(1 + \frac{d}{\alpha/\beta}\right)}{\left(1 + \frac{2\ \mathrm{Gy}}{\alpha/\beta}\right)} \tag{3.4}$$

This leads to the use of a common quantity that has been very practical to compare different fractionation schedules. It has also simplified the dose summation when brachytherapy is combined with external beam to provide dose escalation.

In LDR brachytherapy, the total dose D is delivered over a period of days or weeks at a very low dose rate. The same dose delivered in LDR brachytherapy may produce less cell killing than that, say, for HDR brachytherapy, because a significant repair of sublethal damage occurs during the delivery. The BED can be defined for LDR brachytherapy taking into account sublethal damage repair:

$$\mathrm{BED} = D\left(1 + \frac{2D}{(\alpha/\beta)\,\mu T}\left[1 - \frac{1}{\mu T}(1 - e^{-\mu T})\right]\right) \tag{3.5}$$

where T is the duration of the treatment, $\mu = \frac{\ln 2}{T_{1/2}}$ is the parameter associated to the half-time of repair $T_{1/2}$ for sublethal lesions. The BED generally decreases with decreasing dose rate in the dose rate range relevant to LDR brachytherapy (0.4-2 Gy h^{-1}).

3.3.4 Radiation quality

The relative biological effectiveness (RBE) is defined as the ratio of the absorbed dose for a reference radiation D_{ref}, such as ^{60}Co γ-rays, and a given type of radiation D_X that result in the same biological effect:

$$\mathrm{RBE} = \frac{D_{ref}}{D_X} \tag{3.6}$$

The RBE depends on factors such as the dose, dose rate, fractionation schedule, radiation quality, and biological endpoint. Biological endpoints can include cell death, chromosome aberrations, mutations, induction of DSB and carcinogenic transformations.

The RBE varies with radiation quality or LET because of the differences in the spatial pattern of energy deposition. Figure 3.3 shows a general trend of RBE as a function of LET. As LET increases, the RBE increases slowly at first and then more rapidly as the LET increases beyond 10 keV $\mu\mathrm{m}^{-1}$. Over 100 keV $\mu\mathrm{m}^{-1}$, the RBE starts to fall as LET increases. The LET at which the RBE reaches a peak is consistent for a wide range of mammalian cells. It is believed that this peak in efficiency is reached when the clustering of energy deposition events matches the average distance between strands (2 nm) in the DNA molecule. At higher LET values, more energy is deposited between the strands without an increase in biological damage since the energy depositions are concentrated in such a limited volume.

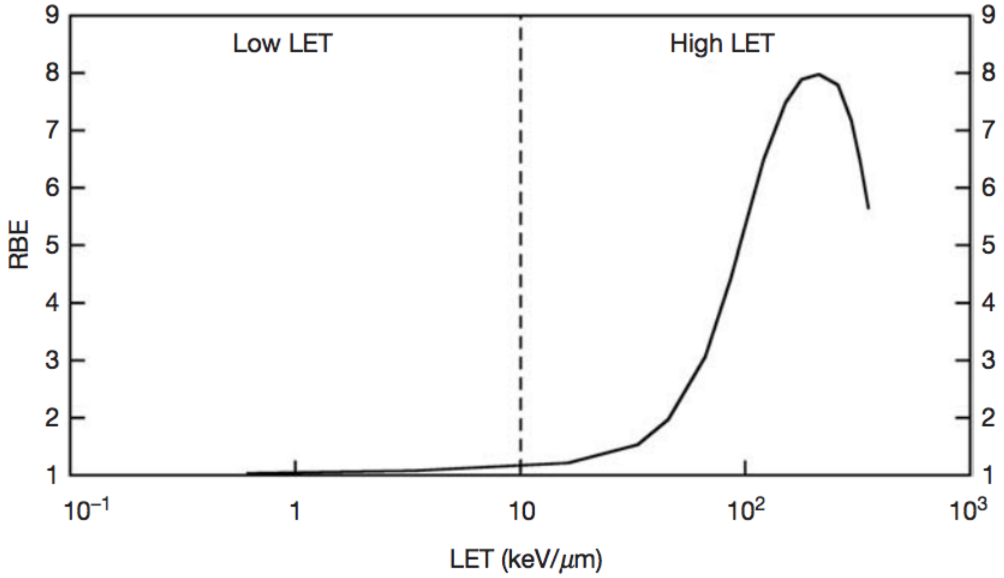

Figure 3.3: Variation of RBE as a function of LET for a typical mammalian cell. The dashed line shows a separation in regions between low LET and high LET radiation. Figure reproduced from [1].

The ICRP recommends the use of radiation weighting factors to account for the radiation quality effect [23]. The weighting factor for a given radiation quality converts an absorbed dose into a biological equivalent dose. However, a radiation weighting factor of 1 is applied to all photon-emitting sources. Thus, the impact of radiation quality on RBE has effectively been ignored in brachytherapy clinical practice. However, many studies have shown that low-energy brachytherapy sources and X-ray sources have RBE values that are greater than unity for various endpoints.

In practice, there is no therapeutic advantage associated with using a radiation source with a higher or lower RBE, unless there is a differential effect between normal tissue and tumour. However, it is important to consider in the assignment of prescription doses to ensure that the same biological effect is delivered from different radiation qualities.

3.4 HDR brachytherapy treatment workflow

3.4.1 Applicator implantation

The catheters, tubes and/or applicators need to be inserted inside the patient to guide the source to the treatment site. Catheter, tube and/or applicator implantation is generally performed under real-time image guidance with the patient under general anesthesia. Interstitial catheters may be inserted according to a needle placement template (Figure 3.4). Intracavitary applicators may need to be stabilized. For pelvic applications, a Foley catheter, a thin flexible tube, is inserted through the urethra and into the bladder to drain urine, and is also used to define the urethral position.

3.4.2 Imaging, contouring and catheter localization

The planning images are then acquired using the same patient positioning that will be used during treatment delivery (Figure 3.4). These images are necessary for identification of the catheters and fiducial markers, as well as volume delineations for the target volume and sensitive structures. In current practice, the common imaging modalities used for catheter localization and treatment planning include computed tomography (CT), magnetic resonance imaging (MRI) and transrectal ultrasound (TRUS). Dummy catheters, radiopaque markers and/or contrast solution may be used to improve the visibility of the catheters.

The images are sent to the treatment planning system for contouring. The target, organs at risk (OARs) and other structures of interest are contoured on the planning images. There are several definitions of the target that need to be defined. The gross tumor volume (GTV) corresponds to the gross palpable, visible, or clinically demonstrable tumour growth. The clinical target volume (CTV) contains the GTV and includes regions where subclinical malignant disease may be present. The planning target volume (PTV) surrounds the CTV with a margin to compensate for the uncertainties in treatment delivery. These uncertainties can be due to physiological motion and variations in size, shape, and position of the CTV during therapy or for uncertainties in the patient setup during irradiation. In general, the PTV is equal to the CTV in most brachytherapy applications because there is minimal risk of setup errors.

Applicator reconstruction is required to define the source pathway in three dimensions for each channel and to determine the tip-end of each channel in order to establish the most distal source position. The source pathway determines the possible positions where the source can dwell and the orientation of the source at each position. The tip-end of each channel must be

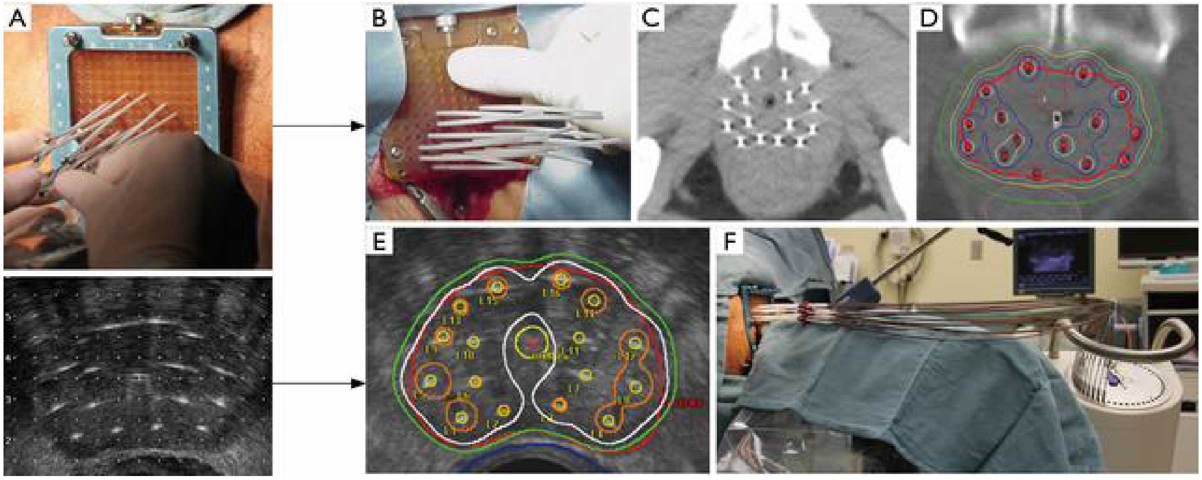

Figure 3.4: Example workflow for prostate HDR brachytherapy. (A) Insertion of catheters into the prostate under TRUS guidance. For CT-based planning: (B) the template is locked and sutured to the perineum, (C) a CT image set is obtained, and (D) a treatment plan is generated using the planning CT. For TRUS-based planning: (E) a treatment plan is generated using the TRUS images and (F) the patient is treated in the same position. Figure reproduced from [24].

identified so that the treatment unit knows how far to send the source out when the treatment plan is exported to the treatment console.

3.4.3 Treatment planning optimization

A treatment plan consists of a set of dwell positions for the source and the amount of time that the source will dwell in each of these, referred to as dwell times. Each catheter provides a set of possible dwell positions. While the source position can be defined along a continuous curve, a discrete number of available dwell positions is defined before a plan is created. Typically, the available dwell positions are set by defining a constant step size between positions (e.g. 2-5 mm). A plan can be created by either forward planning or inverse planning.

Forward planning

In forward planning, the treatment plan is constructed manually using graphical tools available in treatment planning systems. Dwell times are assigned to each available dwell position and the resulting dose distribution is created. The resulting dose distribution is evaluated according to clinical criteria for the volumes of interest, and repeatedly adjusted until it fulfills or comes close enough to the plan evaluation criteria.

Anatomy-based inverse planning

The inverse planning approach can be defined as a method of treatment planning where one starts with clinical objectives and then determines the treatment parameters that will achieve it. The dose constraints, assigned to the target and OAR volumes or to a set of defined points, constitute the starting point of the optimization process. The main benefit of the inverse planning approach is that all clinical requirements are simultaneously and automatically taken into account in the planning process. Inverse planning becomes a trial-and-error process in the search for proper dose constraints that result in a plan that fulfills or comes close enough to the plan evaluation criteria. Therefore, the plan quality is highly dependent on the selection of dose constraints.

The goal of optimization in HDR brachytherapy is to seek the optimal combination of dwell positions and dwell times that best fulfills the treatment objectives. The optimizer uses a linear least squares technique to determine the dwell time at each dwell position that produces the final dose distribution. The dose inside each voxel can be represented as the sum of the dose contributions from each dwell position:

$$D_i = \sum_j d_{ij} t_j \tag{3.7}$$

where

- D_i: Dose at voxel i.
- d_{ij}: Dose rate contribution from dwell position j to voxel i.
- t_j: Dwell time at dwell position j.

The optimization problem can be solved mathematically as an objective function minimization problem. The objective function is a measure of the plan quality in reference to the objectives. Lower and upper dose limits for each structure are used as inputs to the model and the model then penalizes values below or above these limits, respectively. Multiple objectives can be formulated as a single objective function with each objective assigned a relative importance factor (or weight). This is referred to as a single-objective problem. A general objective function F of this type is written as follows:

$$F = \sum_{s \in S} \frac{1}{|N_s|} \sum_{i \in N_s} \left[w_s^L \, H(D_s^L - D_i) \, (D_s^L - D_i)^p + w_s^U \, H(D_i - D_s^U) \, (D_i - D_s^U)^p \right] \tag{3.8}$$

where

- S: Set of structures.
- N_s: Set of dose-calculation points in structure s.
- D_i: Dose at voxel i.
- w_s^L, w_s^U: Weight for underdosage and overdosage for structure s.
- D_s^L, D_s^U: Lower and upper dose limit for structure s.
- p: Model parameter.
- $H(x)$: Heaviside function. $H(x) = 1$ if $x \geq 0$, $H(x) = 0$ if $x < 0$

Many objective functions applied to HDR brachytherapy applications use the general model with linear penalties (p = 1) [25, 26] or quadratic penalties (p = 2) [27–29]. Essentially, the model penalizes dose values to each voxel in a structure that are above/below the upper/lower limits, respectively. The objective function is normalized by the number of voxels in the structure to remove any bias towards the volume of the structure. The objective function can also include dose limits for the surface of a structure [25, 26], which means that penalties are only assigned to points along the surface of a structure. An alternative approach is to incorporate realistic treatment goals (e.g. dose-volume parameters) as inputs to the optimizer [30–33], since a certain portion of the volume for a given structure is almost always expected to receive a dose that lies outside of the acceptable dose range. In this approach, penalties are only assigned to dose in voxels when a certain proportion of the volume receives more/less than the dose limits. Several constraints can then be applied to each structure to better tailor the dose distribution. The dose-volume approach has many benefits, since the inputs to the optimizer are directly linked to the clinical goals that are used to evaluate plan quality. While clinical objectives, optimization constraints and plan evaluation metrics should be the same in an ideal situation, this may not always be the case in practice. Tuning of the optimization weights and constraints is therefore a trial-and-error process in the search for an acceptable plan.

Many algorithms have been investigated for HDR brachytherapy treatment planning, including stochastic (simulated annealing [25], evolutionary algorithm [34]) and deterministic methods (gradient-based [27, 28], linear programming [35, 26], mixed integer programming [31], column generation [36]). The most prominent tools that have been incorporated in commercial treatment planning systems are inverse planning simulated annealing (IPSA) [25] and hybrid inverse planning and optimization (HIPO) [27]. While IPSA has been shown to be

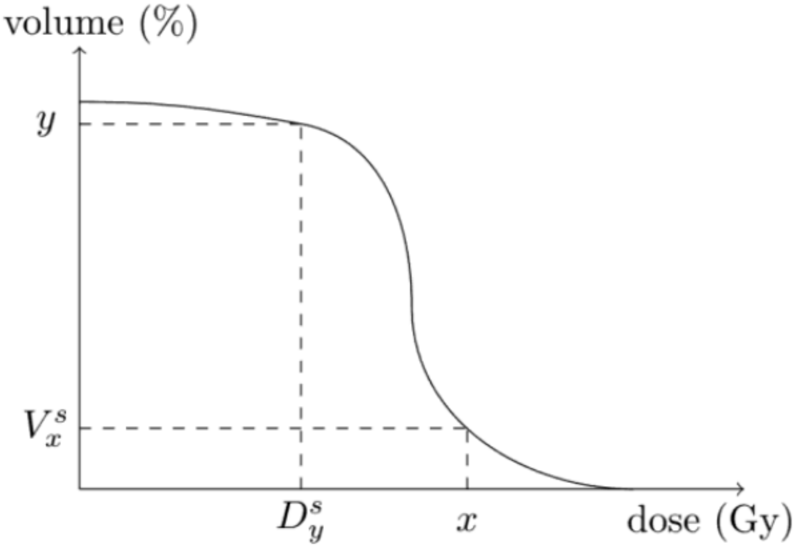

Figure 3.5: Example of a cumulative DVH. Figure reproduced from [37].

effective method, HIPO can produce a more uniform dwell time distribution by minimizing the dwell time variations between adjacent dwell positions. In addition, HIPO can also be used to optimize the catheter positions in addition to the dwell times at each position. After optimization, if target coverage is not satisfied, graphical optimization is used to normalize the dose distribution by manually dragging the isodose curves until acceptable target coverage is achieved.

3.4.4 Clinical treatment evaluation

Dose at points and isodose curves

The dose distribution can be visualized by superimposing the dose distribution over the planning images (Figure 3.4). The plan can be evaluated by slice-by-slice visualization of the target coverage. The dose at specific points of interest can be calculated [2]. In addition, hot and cold spots can be identified using the isodose curves (or colorwash). In an ideal case, the reference isodose should be perfectly aligned with the contour of the PTV (or CTV).

Dose-volume histogram

The dose-volume histogram (DVH) is a histogram which relates radiation dose D to contoured volume V in radiation therapy planning. Essentially, it summarizes a three-dimensional dose distribution in a series of two-dimensional plot of D (in Gy) as a function of V (in %) for each structure. The clinical DVH usually includes all contoured tissues or organs in the treatment plan, including target volumes, OAR volumes, external body contour and other arbitrary structures which may have been used for treatment planning. The DVH can be visualized as either a differential DVH (less common) or a cumulative DVH (more common). In the cumulative DVH (Figure 8.3), the value of the y-axis at a given dose D_y^s represents the percent volume of the structure s receiving at least D_y^s. The term DVH in the rest of this thesis refers to the cumulative DVH.

For the tumour, the portion of its volume that receives at least the prescription dose is of interest, while for the OARs, it is rather the portion that receives at most a dose limit of interest. The D_y^s represents the minimum dose delivered to the hottest y% (or y cm^3) of the structure volume. The D_y^s is either expressed in Gy or in % of the prescription dose. The V_x^s represents the volume that receives at least x% of the prescription dose (or x Gy). The V_x^s is either expressed in cm^3 or in % of the structure volume.

For many brachytherapy applications, the clinical dose-volume metrics of interest to evaluate target coverage and homogeneity are the PTV (or CTV) D_{90}, V_{100}, V_{150} and V_{200}. Clinical treatment guidelines recommend that V_{100} should be above 95% in general and above 90% in worst cases. For OARs, the dose-volume metrics that are most commonly reported are the D_{2cc}, D_{1cc} and $D_{0.1cc}$ (cc = cm^3).

There are other plan evaluation tools that are commonly used in brachytherapy to identify the dose homogeneity within the target and the conformality of the dose distribution to the target. The homogeneity index (HI) [38] is defined as the fraction of the target volume receiving between 100% and 150% of the prescription dose:

$$\mathrm{HI} = \frac{V_{100}^{PTV} - V_{150}^{PTV}}{V_{100}^{PTV}} \tag{3.9}$$

The HI is a practical index to assess the homogeneity of the dose distribution within the target. The conformal index (COIN) [39] is defined as the ratio of the target V_{100} and the target volume times the ratio of the target V_{100} and the 100% isodose volume:

$$\mathrm{COIN} = \frac{V_{100}^{PTV}}{V^{PTV}} \frac{V_{100}^{PTV}}{V_{100}} \tag{3.10}$$

The first component describes the fraction of the target volume that is covered by the 100% isodose volume. The second component describes the fraction of the 100% isodose volume that is covered by the target volume. The COIN evaluates how well the prescription dose covers the target and how much normal tissue is covered by the prescription dose.

An advantage of the DVH methodology is that DVH metrics correlate strongly with outcomes and toxicities. A limitation of the DVH methodology is that it offers no spatial information, since the location, size and shape of hot spots or cold spots are unknown. Therefore, it is recommended that the plan is evaluated using a combination of the spatial dose distribution and the DVH. Sector analysis (dividing a region into various sectors) is another method to include some aspects of the spatial distribution in the dose-volume analysis [40].

3.4.5 Treatment delivery

Once the treatment plan is approved, the transfer tubes are connected to each applicator channel or catheter. A series of quality assurance steps are performed to verify the treatment setup and identify possible sources of error. The treatment plan is then exported to the treatment console. Before the active source is sent out, a dummy source with the exact same dimensions as the radioactive source is sent out through each channel to check that there is no obstruction in the source path. During treatment delivery, the source is sent out through each channel once. For each channel, the afterloader sends the source to the most distal dwell position at first, then successively retracts the source to the other dwell positions. After the source spends the required dwell time at each source position, the source is retracted back into the afterloader. The applicator and/or interstitial catheters are then removed and the patient undergoes recovery.

3.5 Intensity modulated brachytherapy

3.5.1 Theoretical concept

Radiation sources used in conventional brachytherapy have generally provided radially symmetric dose distributions. If sources could deliberately provide asymmetric radiation emissions,

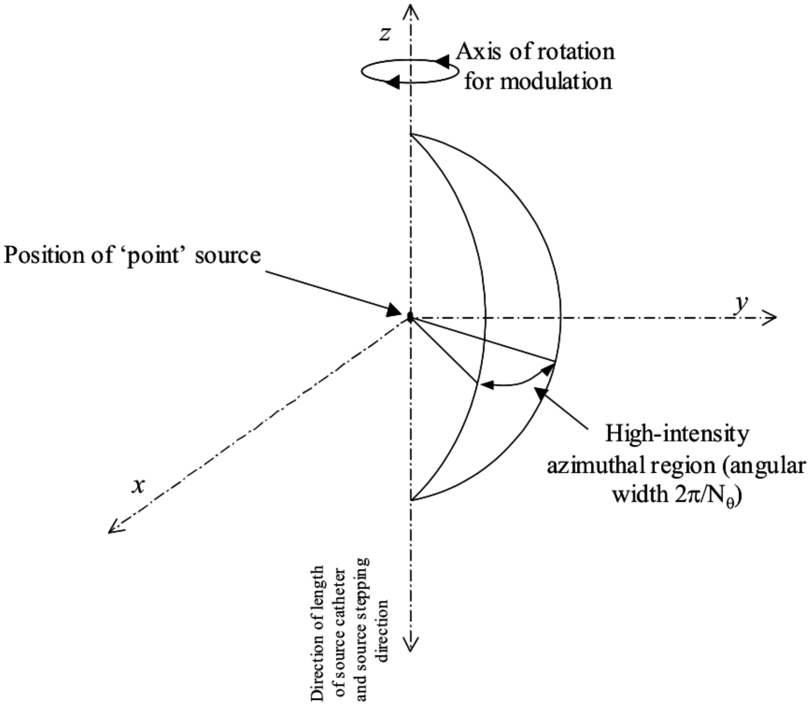

Figure 3.6: Coordinate system defining the high-intensity region around an anisotropic source and the axis of rotation for modulation. Figure reproduced from [42].

then the orientation of the radiation beam at each dwell position could provide additional degrees of freedom to the optimization algorithm. By controlling the dwell time and orientation at each dwell position, one could most likely achieve a more conformal dose distribution. The concept of using sources that provide anisotropic emissions to achieve IMBT was first investigated by Ebert [41, 42]. IMBT would have the potential to enhance the dose in particular regions, such as the tumour, and decrease the dose delivered to adjacent healthy tissues.

Consider a source with an anisotropic emission delivered through some form of shielding or collimation system. The emissions can then be separated into two components: a high-intensity region (the primary beam) and a low-intensity region (attenuated emission). To achieve intensity modulation, it would be necessary to rotate the high-intensity region. If the source longitudinal axis is along the z-axis, with the source emission collimated in azimuthal angle, intensity modulation is achieved via rotation of the source about its axis. In this case, collimation in the polar angle is not included.

Ebert [41, 42] evaluated the limitations in dose modulation resulting from probable constraints on the characteristics of an anisotropic radiation source. Using a simplified model, two

(a) No transmission (b) 10% transmission (c) 30% transmission

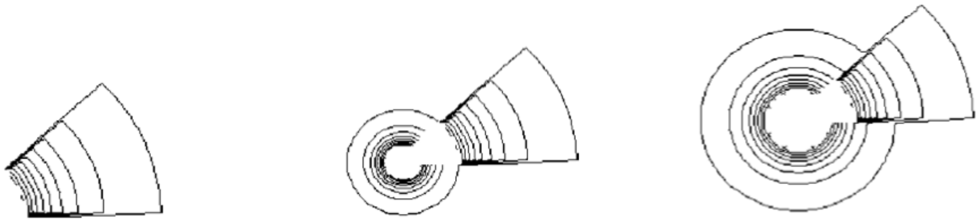

(d) 50% transmission (e) 90% transmission

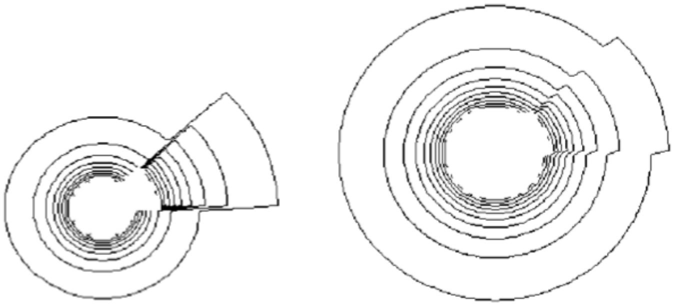

Figure 3.7: Effect of minimum transmission T_{min} through the low-intensity region on the resulting dose distribution around an anisotropic source with a high-intensity region of $\pi/4$. Figure reproduced from [41].

parameters were investigated for a single-source dose distribution: the minimum transmission through the low-intensity region (T_{min}) and the number of possible angular orientations (N_θ). As the minimum transmission T_{min} through the low-intensity region increases, the dose contribution from the attenuated emission becomes more important to consider (Figure 3.7).

The number of possible angular orientations N_θ is inversely proportional to the angular width of the high-intensity region ($2\pi/N_\theta$), assuming a discrete number of orientations with non-overlapping regions. As the width of the high-intensity region decreases, the resolution of modulation increases, but the number of discrete positions of the source required to produce a given high-intensity region increases, and the contribution of the minimum transmission T_{min} becomes of greater importance (Figure 3.8). As shown in Figure 3.9, the large number of superpositions of the low-intensity region leads to smoothing of the intensity modulation. Thus, there must be a set of parameters N_θ and T_{min} that produce an optimal dose distribution for a given treatment situation.

(a) Single source orientation. Source has $\pi/4$ high-intensity region ($N_\theta = 8$)

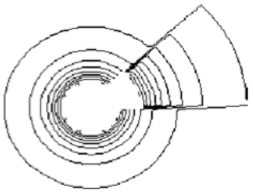

(b) Four source orientations. Source has $\pi/16$ high-intensity region ($N_\theta = 32$)

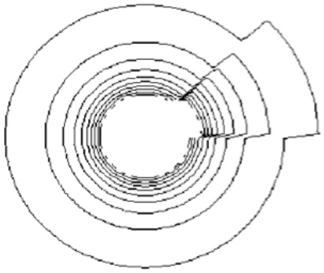

Figure 3.8: Dose distribution around anisotropic source in a sufficient number of orientations to give an emission angle of $\pi/4$ using a source with a high-intensity region of (a) $\pi/4$ (one angular orientation) and (b) $\pi/16$ (four angular orientations). The minimum transmission T_{min} through the low-intensity region is 30% in both cases. (a) Figure reproduced from [41].

Ebert [42] evaluated the benefits and limitations of IMBT in the context of prostate HDR brachytherapy. Two cases were investigated: a two-dimensional example and a three-dimensional example. In the two-dimensional example, the dose contributions to a given slice must result from source positions located within that same slice. This simulates a source which has collimation in azimuthal angle and polar angle. In the three-dimensional example, dose contributions to all slices are taken into account from source positions on all slices. This simulates a source which has collimation in azimuthal angle, but no collimation in polar angle.

Ebert [42] further defined an objective function to evaluate the benefit of IMBT compared to conventional HDR brachytherapy. The objective function takes into account plan conformality (target coverage and normal tissue sparing) and overall treatment time. Given this defined objective function, an optimal plan would provide a uniform dose to the target, negligible dose to normal tissues and would be delivered in a minimal treatment time. Figure 3.10 shows the objective function as a function of the number of orientations N_θ and the minimum transmission T_{min} for the three-dimensional prostate HDR brachytherapy case. Two main conclusions were drawn from this example (similar conclusions were observed in the two-dimensional prostate

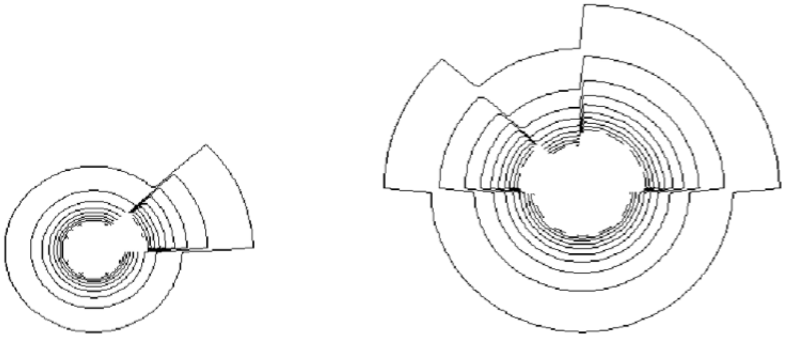

(a) One source orientation (b) Three source orientations

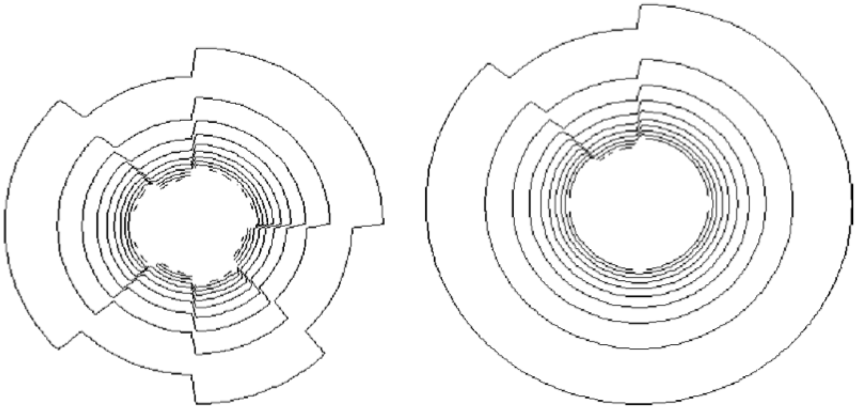

(c) Five source orientations (d) Seven source orientations

Figure 3.9: Effect of multiple angular orientations N_θ for a source with a high-intensity region of $\pi/4$ and a minimum transmission T_{min} through the low-intensity region of 30%. Figure reproduced from [41].

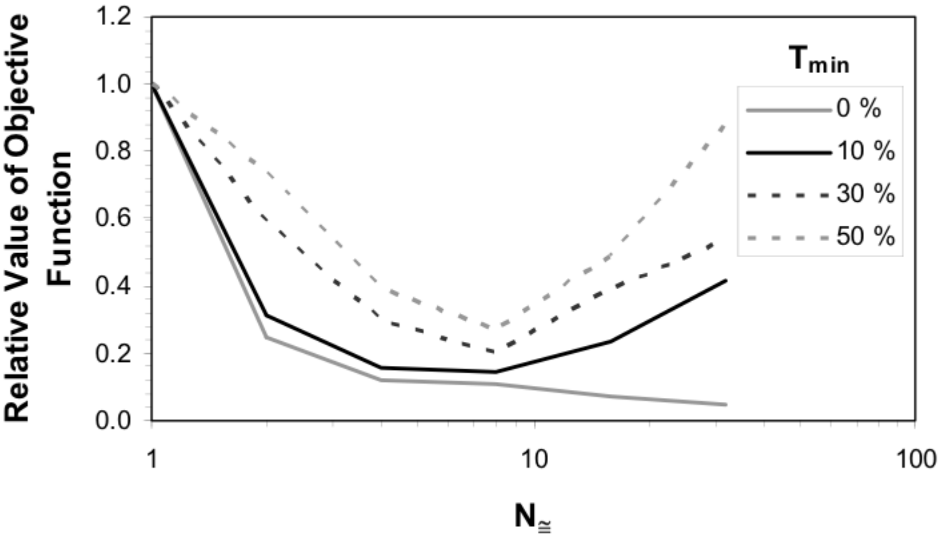

Figure 3.10: Variation of the objective function value for the prostate HDR brachytherapy example. The objective function evaluates target coverage, normal tissue sparing and overall irradiation time. Figure reproduced from [42].

HDR brachytherapy case). First, there is a rapid increase in benefit from IMBT as the minimum transmission T_{min} through the low-intensity region decreases. The decrease in the objective function is mainly due to an increase in plan conformality. Second, there is a rapid increase in benefit from IMBT as the number of angular orientations N_θ increases (or the angular width decreases). The decrease in the objective function is mainly due to an increase in plan conformality. However, a minimum in the objective function is reached at about $N_\theta = 8$. As N_θ continues to increase past this point, the objective function increases rapidly as the overall treatment time increases while plan conformality tends to either reach a plateau or decrease due to the increased contribution from unwanted emissions (refer again to Figures 3.8 and 3.9). Indeed, a realistic, non-zero value for the minimum transmission T_{min} puts a limit on the benefit in plan conformality from using a very fine angular resolution. In addition, for an optimal angular resolution, there is little benefit in decreasing the T_{min} below 10%. Thus, an angular opening of $\pi/4$ or 45° (representing 8 orientations) and a minimum transmission T_{min} of 10% provide an optimal solution.

In addition to investigating the potential advantages of IMBT, Ebert also identified the potential issues that need to be addressed related to the practical implementation of the treatment approach. First, the physical form of the source and collimation system needs to be identified.

Several options include shielded source or shielded applicator, centered or off-centered source, single- or multiple-channeled applicator, single- or multiple-source delivery, and design and material selection for shielding. Second, an appropriate radiation source (e.g. radionuclide or eBT source) needs to be selected. Important characteristics include the energy spectrum, the half-life and the amount of material required to appropriately reduce the minimum transmission through the low-intensity region. Third, a method of orienting the source at a given dwell position and a method to verify those orientations need to be identified. The delivery can be performed using a step-and-shoot approach or a continuous source/shield motion approach with constant or variable speed. Fourth, the dose distribution around the source needs to be well characterized at each dwell position and orientation and the impact of positioning errors should be investigated. Regarding treatment planning, the delivery can be restricted to a discrete number of dwell positions and orientations or the dwell positions and orientations can follow a continuous trajectory. The possibility to overlap multiple high-intensity regions may reduce the impact of positioning errors by providing a smoother distribution. Transit time may need to be considered in the dose calculation for the former. Fifth, the combination of symmetric and asymmetric sources could be considered to improve treatment times. It could be possible to replace sources located inside the target and away from radiation sensitive organs with conventional symmetric sources. Sixth, the possibility of adding even more degrees of freedom by allowing source collimation in the polar angle may provide additional benefits at the expense of increased treatment time. These practical considerations will have substantial impact on many aspects related to IMBT, including plan quality, treatment times, robustness to delivery errors, optimization/planning times, treatment costs and workload for staff.

3.5.2 Practical applications

Over the years, various IMBT delivery systems have been proposed, investigated, built, tested and, in some cases, commercialized [43]. The various designs of IBMT sources and applicators are illustrated in Figure 3.11. The IMBT techniques are divided into two main categories: static or dynamic. Static techniques include any shielded technique in which the shield does not move relative to the source or surrounding tissues during brachytherapy delivery. Dynamic techniques include any technique where the shield translates or rotates during treatment relative to the source or surrounding tissues. Each of the two main categories are divided into two subcategories (shielded source or shielded applicator). Shielded source refers to techniques

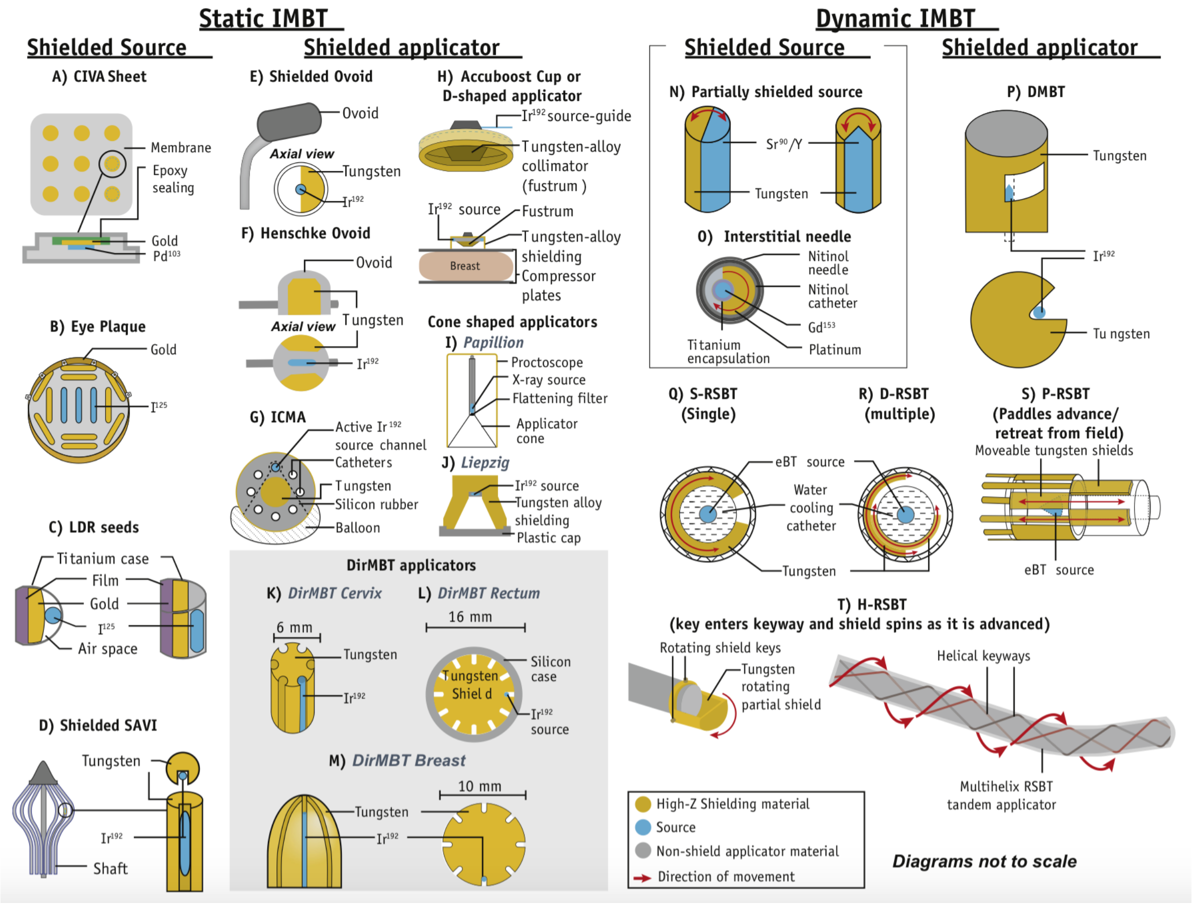

Figure 3.11: Illustration of IMBT techniques. Figure reproduced from [43].

where the shield is directly associated with the source. Shielded applicator refers to techniques where the shield is included in the applicator.

IMBT approaches for static-shielded sources incorporate low-energy photon-emitting sources (^{103}125 or ^{103}Pd) as LDR implants for breast cancer, prostate cancer, ocular melanoma or intra-operative brachytherapy for pancreatic, abdominopelvic, and colorectal cancer. IMBT approaches for static-shielded applicators use primarily high-energy photon-emitting sources (^{192}Ir) combined with tungsten or tungsten-alloy shielding for cervical, colorectal, skin and breast HDR brachytherapy. Dynamic-shielded sources have been investigated for intravascular brachytherapy using a tungsten-shielded ^{90}Sr/^{90}Y source and prostate HDR brachytherapy using a platinum-shielded ^{153}Gd source. Dynamic-shielded applicators incorporate either ^{192}Ir or eBT sources for HDR brachytherapy, and include the "dynamic modulated brachytherapy"

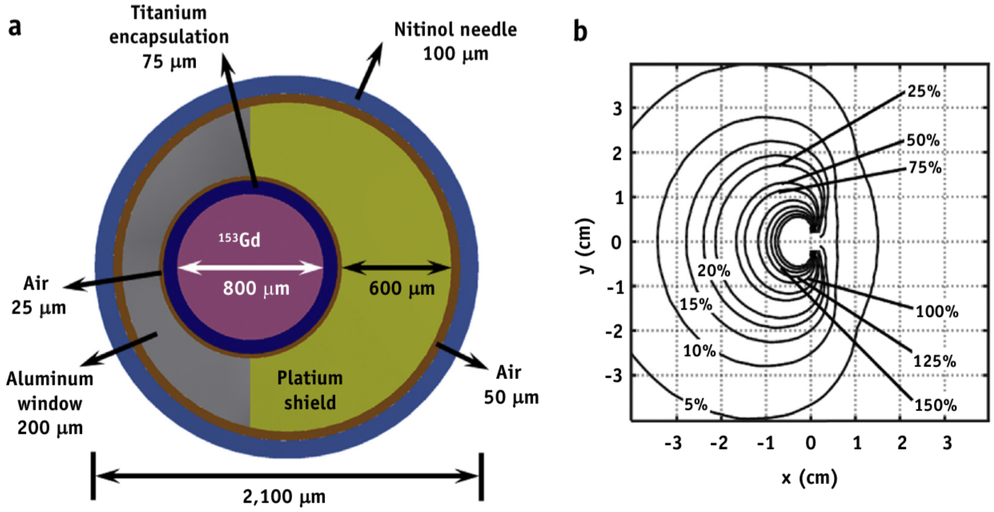

Figure 3.12: (a) Needle-source system with an off-centered ^{153}Gd source and a platinum shield used as the brachytherapy source in the multisource rotating shield brachytherapy apparatus. (b) Dose rate distribution from the shielded source, normalized to 100% at 1 cm from the source. Figure reproduced from [13].

(DMBT) applicator for colorectal cancer and various "rotating shield brachytherapy" (RSBT) applicators for cervical cancer.

Prostate cancer

Adams et al. [12] proposed a needle, source and shield system to deliver interstitial RSBT for prostate cancer (Figure 3.12a). The ^{153}Gd source was partially shielded by a platinum shield with a maximum thickness of 0.6 mm and an emission window of 180°. The platinum shield reduced the dose on the shielded side at 1 cm to about 7% of the dose on the unshielded side (Figure 3.12b). Given similar PTV coverage, RSBT reduced urethral $D_{0.1cc}$ by 29% to 44% relative to conventional HDR brachytherapy, depending on the size of the margin around the urethra (0 to 5 mm, respectively). The average treatment time to deliver 20 Gy to the PTV with 10 ^{153}Gd sources (62 GBq) was 154 mins.

Due to the lower dose rate of ^{153}Gd compared to ^{192}Ir, a multisource system was proposed by Dadkhah et al. [13] to enable clinical delivery (Figure 3.13). The multisource system controls the longitudinal position and orientation of up to 20 shielded ^{153}Gd sources. Given equal PTV coverage, RSBT reduced urethral $D_{0.1cc}$ by 31% compared to conventional HDR

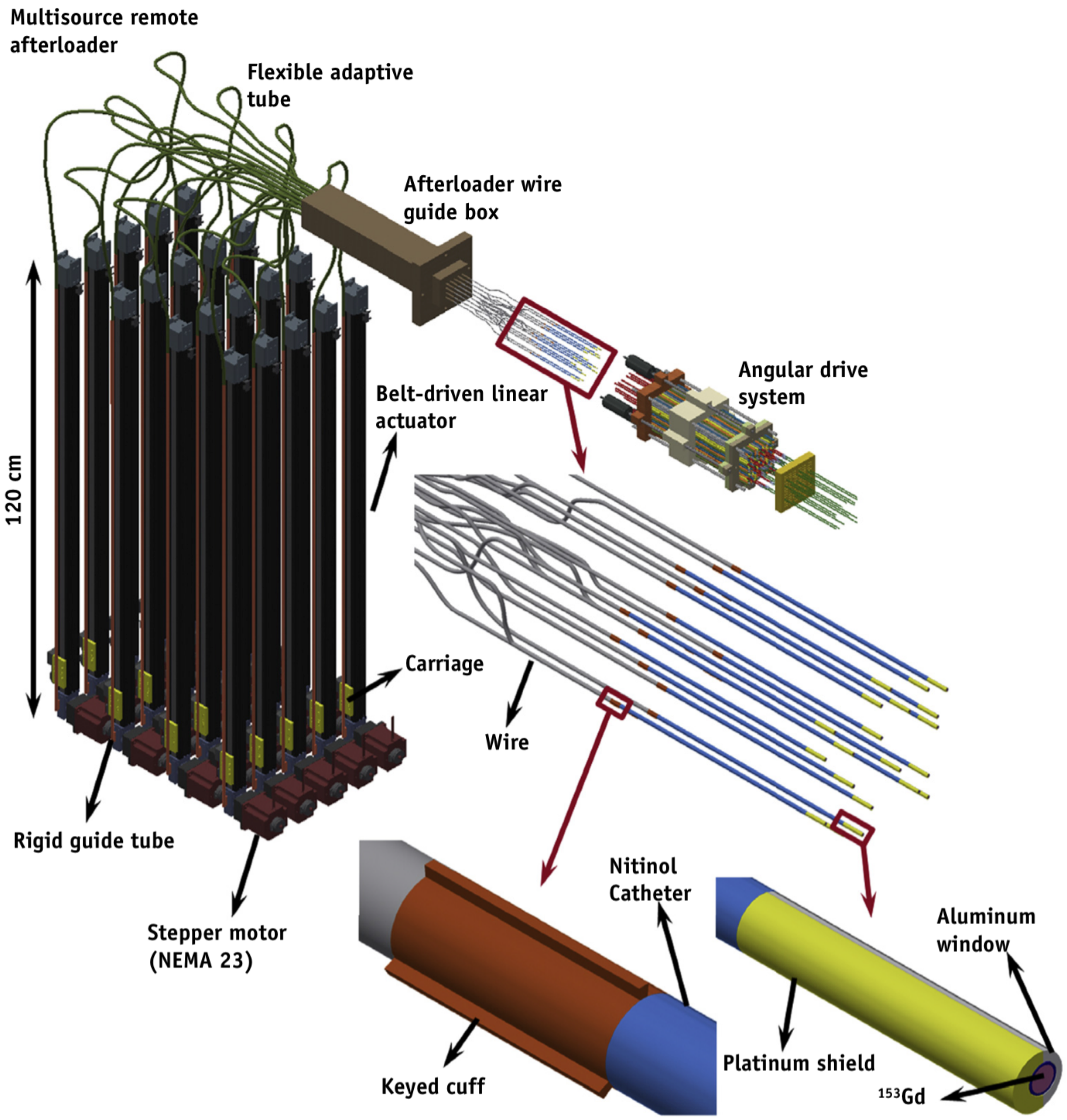

Figure 3.13: Multisource remote afterloader to deliver RSBT for prostate cancer. Each needle, implanted through the patient template, is coupled to the catheter-mounted afterloader wire through a keyed connector (red), which passes through a rotating shaft. The catheter is rigidly attached to a proximal keyed cuff that enables the angular orientation of the shielded source to be fixed and known at all times during treatment. All shafts are locked at the same angular orientation at a given time by the moving template, which when translated, simultaneously rotates all the shafts. The moving template is translated by redundant motors that are attached to lead screws, and the shaft angular positions are known based on the position of the template. Figure reproduced from [13].

brachytherapy given a urethral margin of 3 mm. The average treatment time to deliver 20 Gy to the PTV with 19 ^{153}Gd sources (62 GBq) was 122 mins.

The previous studies did not consider expected radiobiological effects due to substantial variations in dose rate or radiation quality between both techniques. In a following study, Adams et al. [14] incorporated dose rate effects ($T_{1/2}$ = 114 mins, α/β = 3.41 Gy) and RBE (1.00 for ^{192}Ir and 1.15 for ^{153}Gd) into the plan comparison of ^{153}Gd-based RSBT and ^{192}Ir-based HDR brachytherapy. For urethra sparing plans, RSBT decreased the urethral D_{10} (EQD2) by 26.0%±3.4% for fresh sources and 20.2%±4.8% after one half-life. For dose escalation, RSBT increased the urethral D_{10} (EQD2) by 42.5%±8.4% for fresh sources and 20.5%±9.1% after one half-life. The average treatment time to deliver 15 Gy (urethra sparing) and 19 Gy (dose escalation) to the PTV with 20 ^{153}Gd sources (91 GBq) was 217 mins and 134 mins, respectively.

RSBT with the proposed multisource apparatus has the potential to deliver urethra sparing plans without decreasing PTV dose for boost cases, or dose escalation without increasing urethral dose for monotherapy cases. However, this approach has several limitations that put into question the clinical feasibility of the technique. First, the long delivery times ($>$2 h) compared to conventional HDR brachytherapy ($\sim$15 mins) would increase staff workload and, as a result, treatment cost. The elevated risk of patient motion resulting in catheter displacement during treatment may also be of concern. Second, the additional costs required for the handling of multiple ^{153}Gd sources, as well as the multisource apparatus, would likely be substantial. Clinical adoption of RSBT (or IMBT in general) will depend on whether the benefits outweigh the risks and the increased costs for source production and exchange, delivery system hardware and software, quality assurance and workload. Thus, a solution which handles a single source, keeps treatment times reasonable and remains compatible with existing commercial remote afterloading technology would increase the likelihood that IMBT would be adopted in a clinical setting.

References

[1] IAEA. Radiation oncology physics: a handbook for teachers and students. Podgorsak EB, editor. Vienna, Austria; 2005.

[2] ICRU. Recommended dose and volume specification for reporting interstitial brachytherapy. ICRU Report. 1985;38.

[3] Brenner DJ, Hall EJ. Conditions for the equivalence of continuous to pulsed low dose rate brachytherapy. Int J Radiat Oncol Biol Phys. 1994;20:181–190.

[4] Zelefsky MJ, Kuban DA, Levy LB, Potters L, Beyer DC, Blasko JC. Multi-institutional analysis of long-term outcome for stages T1-T2 prostate cancer treated with permanent seed implantation. Int J Radiat Oncol Biol Phys. 2007;67:327–333.

[5] Kehwar TS. Use of Cesium-131 radioactive seeds in prostate permanent implants. J Med Phys. 2009;34(4):191–193.

[6] Currier B, Munro III JJ, Medich DC. Dosimetric characterization of the GammaClip^{TM} ^{169}Yb low dose rate permanent implant brachytherapy source for the treatment of nonsmall cell lung cancer postwedge resection. Med Phys. 2013;40(8):080701.

[7] Medich DC, Tries MA, Munro III JJ. Monte Carlo characterization of an ytterbium-169 high dose rate brachytherapy source with analysis of statistical uncertainty. Med Phys. 2006;33(1):163–172.

[8] Cazeca MJ, Medich DC, Munro III JJ. Monte Carlo characterization of a new Yb-169 high dose rate source for brachytherapy application. Med Phys. 2010;37(3):1129–1136.

[9] Flynn RT, Adams QE, Hopfensperger KM, Wu X, Xu W, Kim Y. Efficient ^{169}Yb high-dose-rate brachytherapy source production using reactivation. Med Phys. 2019;46:2935–2943.

[10] Reynoso FJ, Munro III JJ, Sho SH. Technical note: Monte Carlo calculations for the AAPM TG-43 brachytherapy dosimetry parameters for the titanium-encapsulated Yb-169 source. Med Phys. 2017;18:193–199.

[11] Enger SA, Fisher DR, Flynn RT. Gadolinium-153 as a brachytherapy source. Phys Med Biol. 2013;58(4):957–964.

[12] Adams QE, Xu J, Breitbach EK, Enger SA, Rockey WR, Kim Y, et al. Interstitial rotating shield brachytherapy for prostate cancer. Med Phys. 2014;41(5):051703.

[13] Dadkhah H, Hopfensperger KM, Kim Y, Wu X, Flynn RT. Multisource rotating shield brachytherapy apparatus for prostate cancer. Int J Radiat Oncol Biol Phys. 2017;99(3):719–728.

[14] Adams QE, Hopfensperger KM, Kim Y, Wu X, Xu W, Shukla H, et al. Effectiveness of rotating shield brachytherapy for prostate cancer dose escalation or urethra sparing. Int J Radiat Oncol Biol Phys. 2018;102(5):1543–1550.

[15] Famulari G, Urlich T, Armstrong A, Enger SA. Practical aspects of ^{153}Gd as a radioactive source for use in brachytherapy. Appl Radiat Isot. 2017;130:131–139.

[16] Enger SA, Lundqvist H, D'Amours M, Beaulieu L. Exploring ^{57}Co as a new isotope for brachytherapy applications. Phys Med Biol. 2012;39(5):2342–2345.

[17] Strohmaier S, Zwierzchowski G. Comparison of ^{60}Co and ^{192}Ir sources in HDR brachytherapy. J Contemp Brachytherapy. 2011;3:199–208.

[18] Meigooni AS, Wright C, Koona RA, Awan SB, Granero D, Perez-Calatayud J, et al. TG-43 U1 based dosimetric characterization of model 67-6520 Cs-137 brachytherapy source. Med Phys. 2009;36(10):4711–4719.

[19] Weeks KJ, Schulz RJ. Selenium-75: A potential source for use in high-activity brachytherapy irradiators. Med Phys. 1986;13(5):728–731.

[20] Shoemaker T, Vuong T, Glickman H, Kaifi S, Famulari G, Enger SA. Dosimetric considerations for ytterbium-169, selenium-75, and iridium-192 radioisotopes in high-dose-rate endorectal brachytherapy. Int J Radiat Oncol Biol Phys. 2019;105(4):875–883.

[21] Thames HD, Bentzen SM, Turesson I, Overgaard M, Van den Bogaert W. Time-dose factors in radiotherapy: a review of the human data. Med Phys. 1990;19(3):219–235.

[22] Orton CG. Fractionation: radiobiological principles and clinical practice. In: Khan FM, editor. Treatment planning in radiation oncology. 2nd ed. Philadelphia, PA: Lippincott Williams & Wilkins; 2007. p. 268–280.

[23] ICRP. RBE for deterministic effects. ICRP publication 58. Ann ICRP. 1990;20(4).

[24] Mendez LC, Morton GC. High dose-rate brachytherapy in the treatment of prostate cancer. Transl Androl Urol. 2018;7(3):357–370.

[25] Lessart E, Pouliot J. Inverse planning anatomy-based dose optimization for HDR-brachytherapy of the prostate using fast simulated annealing algorithm and dedicated objective function. Med Phys. 2001;28(5):773–779.

[26] Alterovitz R, Lessard E, Pouliot J, Hsu IC, O'Brien JF, Goldberg K. A hybrid evolutionary algorithm for multi-objective anatomy-based dose optimization in high-dose-rate brachytherapy. Med Phys. 2006;33(11):4012–4019.

[27] Milickovic N, Lahanas M, Papagiannopoulou M, Zamboglou N, Baltas D. Multiobjective anatomy-based dose optimization for HDR-brachytherapy with constraint free deterministic algorithms. Phys Med Biol. 2002;47(13):2263–2280.

[28] Lahanas M, Baltas D, Giannouli S. Global convergence analysis of fast multiobjective gradient-based dose optimization algorithms for high-dose-rate brachytherapy. Phys Med Biol. 2003;48:599–617.

[29] Webster MJ, Devic S, Vuong T, Han DY, Park JC, Scanderbeg D, et al. Dynamic modulated brachytherapy (DMBT) for rectal cancer. Med Phys. 2013;40(1):011718.

[30] Siauw T, Cunha A, Atamtürk A, Hsu I, Pouliot J, Goldberg K. IPIP: A new approach to inverse planning for HDR brachytherapy by directly optimizing dosimetric indices. Med Phys. 2011;38(7):4045–4051.

[31] Gorissen BL, den Hertog D, Hoffmann AL. Mixed integer programming improves comprehensibility and plan quality in inverse optimization of prostate HDR brachytherapy. Phys Med Biol. 2013;58(4):1041–1057.

[32] Holm A, Larsson T, Tedgren A. A linear programming model for optimizing HDR brachytherapy dose distributions with respect to the mean dose in the DVH-tail. Med Phys. 2013;40(8):081705.

[33] Antaki M, Deufel C, Enger SA. Fast mixed integer optimization (FMIO) for high dose rate brachytherapy. Phys Med Biol. 2020;65(21):215005.

[34] Lahanas M, Baltas D, Zamboglou N. A hybrid evolutionary algorithm for multi-objective anatomy-based dose optimization in high-dose-rate brachytherapy. Phys Med Biol. 2003;48(3):399–415.

[35] Jozsef G, Streeter OE, Astrahan MA. The use of linear programming in optimization of HDR implant dose distributions. Med Phys. 2003;30(5):751–760.

[36] Renaud M, Famulari G, Seuntjens J, Enger SA. OC-0256: Column generation-based Monte Carlo treatment planning for rotating shield brachytherapy. Radiother Oncol. 2016;119:S118.

[37] Morén B. Mathematical modelling of dose planning in high dose-rate brachytherapy. Linköping University; 2019.

[38] Wu A, Ulin K, Sternick ES. A dose homogeneity index for evaluating 192Ir interstitial breast implants,. Med Phys. 1988;15(1):104–107.

[39] Baltas D, Kolotas C, Geramani K, Mould RF, Ioannidis G, Kekchidi M, et al. A conformal index (COIN) to evaluate implant quality and dose specification in brachytherapy. Int J Radiat Oncol Biol Phys. 1998;40(2):515–524.

[40] Bice Jr WS, Prestidge BR, Sarosdy MF. Sector analysis of prostate implants. Med Phys. 2001;28(12):2561–2567.

[41] Ebert MA. Possibilities for intensity-modulated brachytherapy: technical limitations on the use of non-isotropic sources. Phys Med Biol. 2002;47:2459–2509.

[42] Ebert MA. Potential dose-conformity advantages with multi-source intensity-modulated brachytherapy (IMBT). Australas Phys Eng Sc Med. 2006;29(2):165–171.

[43] Callaghan CM, Adams Q, Flynn RT, Wu X, Xu W, Kim Y. Systematic review of intensity-modulated brachytherapy (IMBT): static and dynamic techniques. Int J Radiat Oncol Biol Phys. 2019;105(1):206–221.

Chapter 4

Brachytherapy dosimetry

4.1 TG-43 dosimetry protocol[1]

Brachytherapy dose calculations are based on the American Association of Physicists in Medicine (AAPM) Task Group No. 43 (TG-43) protocol [1, 2]. The protocol uses a combination of air-kerma rate measurements, performed in the clinic, and published datasets in the reports for existing source models, to calculate 2D dose distributions in water. The general 2D dose rate equation described by the TG-43 formalism is given as:

$$\dot{D}(r,\theta) = S_K\,\Lambda\,\frac{G_L(r,\theta)}{G_L(r_0,\theta_0)}\,g_L(r)\,F(r,\theta) \tag{4.1}$$

where r denotes the distance from the center of the active source to the point of interest, r_0 = 1 cm denotes the reference distance, θ denotes the polar angle of the point of interest relative to the source longitudinal axis, and θ_0 = 90° denotes the reference angle. The coordinate system is shown in figure 4.1. The parameters introduced by the formalism will be described below.

4.1.1 Air-kerma strength

The air-kerma strength S_K is the air-kerma rate $\dot{K}_\delta(d)$ *in vacuo* at a distance d due to photons of energy greater than δ multiplied by the square of the distance from the source:

$$S_K = \dot{K}_\delta(d)\,d^2 \tag{4.2}$$

---

[1] The information in this section is based on [1] and [2].

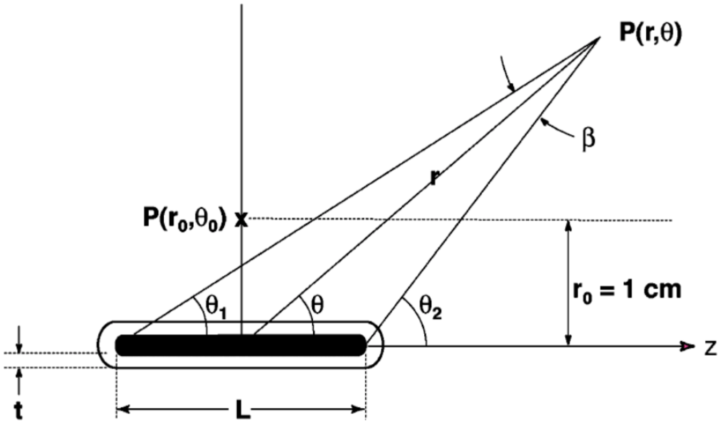

Figure 4.1: Coordinate system for calculation of dosimetric parameters defined in the TG-43 formalism. Figure reproduced from [2].

The unit of air-kerma strength is U = cGy cm^2 h^{-1}. The air-kerma rate measurements are typically performed at 1 m from the source center, ensuring the distance is large compared to the linear dimensions of the source and detector. The energy cut-off δ is intended to exclude low-energy photons that increase the air-kerma rate, but do not contribute significantly to dose at distances greater than 1 mm in water. The value is typically 5 keV and 10 keV for low-energy and high-energy brachytherapy sources, respectively.

4.1.2 Dose rate constant

The dose rate constant Λ is the ratio of the dose rate at the reference position $\dot{D}(r_0, \theta_0)$ and the air-kerma strength S_K:

$$\Lambda = \frac{\dot{D}(r_0, \theta_0)}{S_K} \tag{4.3}$$

The dose rate constant is expressed in units of cGy h^{-1} U^{-1}. The dose rate constant essentially converts a kerma rate in air to a dose rate in water, and is dependent on the source isotope and model.

4.1.3 Geometry function

The geometry function $G_L(r, \theta)$ provides an approximate estimate of the dose rate variation as a function of position based on a line source approximation of the distribution of radioactivity within the source:

$$G_L(r,\theta) = \begin{cases} \frac{\beta}{Lr\ \sin\theta} & \text{if } \theta \neq 0^{\circ} \\ \frac{1}{r^2 - L^2/4} & \text{if } \theta = 0^{\circ} \end{cases}$$

where L is the active length of the source and $\beta = 2\arctan\ (l/2r)$ is the angle subtended by the tips of the line source with respect to the point of interest. The unit of the geometry function is cm^{-2}. The geometry function neglects the effects of scattering and attenuation. It is independent of the source isotope and model (only the active length is required).

4.1.4 Radial dose function

The radial dose function $g_L(r)$ accounts for dose fall-off on the transverse plane due to photon scattering and attenuation, in addition to the fall-off predicted by the geometry function:

$$g_L(r) = \frac{\dot{D}(r,\theta_0)}{\dot{D}(r_0,\theta_0)} \frac{G_L(r_0,\theta_0)}{G_L(r,\theta_0)} \tag{4.4}$$

The radial dose function is equal to unity at the reference distance r_0 = 1 cm.

4.1.5 Anisotropy function

The 2D anisotropy function $F(r,\theta)$ describes the variation in dose rate as a function of polar angle θ and distance r due to photon scattering and attenuation, in addition to the fall-off predicted by the geometry function:

$$F(r,\theta) = \frac{\dot{D}(r,\theta)}{\dot{D}(r,\theta_0)} \frac{G_L(r,\theta_0)}{G_L(r,\theta)} \tag{4.5}$$

The 2D anisotropy function is equal to unity at the reference angle θ_0 = 90°. $F(r,\theta)$ is generally displayed as a function of θ for various depths r.

4.2 Model-based dose calculation algorithms for brachytherapy dosimetry[2]

4.2.1 Heterogeneity effects

The TG-43 algorithm assumes that the medium is composed of homogeneous water with full scattering conditions. However, there exists various sources of heterogeneities in brachytherapy applications. Common sources include tissue heterogeneities, finite patient dimensions (patient-specific scatter conditions), applicator heterogeneities and interseed attenuation. For high-energy brachytherapy sources, the photon interaction processes are dominated by Compton scattering. The Compton scattering cross section depends mostly on the electron density of the medium and is generally independent of the material. As the photon energy decreases, the photoelectric cross section, which strongly depends on the atomic number Z, also increases. For low-energy brachytherapy sources, the photon interaction processes are dominated by the photoelectric effect, and scattering is limited. Thus, dose calculation accuracy is highly dependent on the scatter conditions (at high and intermediate energies) and the photoelectric absorption relative to water (at low and intermediate energies).

4.2.2 Overview of model-based dose calculation algorithms

Collapsed-cone superposition algorithm

The collapsed-cone superposition (CCS) algorithm [5–8] is based on the primary and scatter separation (PSS) formalism [9] for source characterization. The algorithm requires knowledge of two components using precalculated data in a homogeneous water phantom: (1) the distribution of the energy released per mass by primary and scattered photons, and (2) the energy deposition kernels representing the spatial distribution of the absorbed dose around a photon interaction site to model the transport of the released energy. The algorithm assumes CPE conditions, does not consider electron transport, and reports collision kerma to the local medium.

The basic quantity calculated by the algorithm is the dose D per unit of emitted radiant energy R_{prim}. The total dose can be separated into three components:

$$\frac{D}{R_{prim}} = \frac{D_{prim}}{R_{prim}} + \frac{D_{1sc}}{R_{prim}} + \frac{D_{msc}}{R_{prim}} \tag{4.6}$$

---

[2] The information in this section is based on [3] and [4].

where D_{prim} is the dose from primary photons, D_{1sc} is the dose from single-scattered photons, and D_{msc} is the dose from multiple-scattered photons. Here, primary photons refer to photons that leave the source encapsulation and deposit energy in their first interaction outside the source encapsulation. The primary dose is obtained using ray-tracing techniques, while a successive scattering approach is used to calculate the single- and multiple-scattered dose [10]. Overall, the algorithm requires precalculated data for the primary dose distribution (source-specific), the primary photon spectrum (source-specific), the single- and multiple-scatter photon spectra (isotope-specific), and the single- and multiple-scatter energy deposition kernels (isotope-specific) in a large, homogeneous water phantom. Ray-tracing techniques are used to scale the dose distributions and energy deposition kernels for heterogeneities based on a density scaling theorem [11, 12].

Systematic uncertainties may arise from the use of angular discretization in the calculation of the energy deposition kernels combined with a finite grid. A fine angular resolution may lead to exceedingly long computation times. The algorithm may also suffer from ray-tracing artifacts in regions where the scatter component dominates. The CCS algorithm has been integrated into the Oncentra® Brachy ACE (Advanced Collapsed-Cone Engine) (Elekta Brachytherapy, Veenendaal, The Netherlands).

Grid-based Boltzmann equation solvers

The grid-based Boltzmann equation solver (GBBS) [13–17] solves the linear Boltzmann transport equation (LBTE) [18] for neutral particles through the discretization of phase space variables (position, direction, energy) on a spatially variable Cartesian grid. The algorithm systematically discretizes spatial (e.g. finite element methods), angular (e.g. discrete ordinates method), and energy variables (e.g. multigroup approximation). The algorithm defines an LBTE at each voxel in the geometry for a finite number of directions and energies. The resulting linear system of equations is then iteratively solved using the source iteration method [18].

The GBBS provides an approximate, deterministic solution for the entire computational domain that converges to the true solution in the limit of very fine phase-space mesh spacing. The accuracy of the algorithm depends on the resolution of the phase space variables. Systematic uncertainties arise from spatial, angular, and energy discretization due to use of a finite grid. The algorithm requires precalculated data for the angular-dependent primary photon spectrum (source-specific). The primary photon fluence is obtained using ray-tracing techniques. Scattering sources are represented using spherical harmonics and cross sections are expanded using Legendre polynomials [18]. Heterogeneities are directly taken into account in the LBTE. The GBBS algorithm has been integrated into the BrachyVision$^{\text{TM}}$ (BV) Acuros$^{\text{TM}}$ engine (Varian Medical Systems, Palo Alto, CA, USA).

Fast Monte Carlo simulations

The MC simulations solve the linear LBTE by random sampling [19]. The MC method is considered the gold standard for computational dosimetry. Fundamental physical processes are modeled to accurately simulate particle transport and energy deposition in heterogeneous media. The details of general purpose MC codes are presented in section 4.3. Several MC dose calculation engines are currently available for brachytherapy applications such as BrachyDose [20] and egs_brachy [21] based on EGSnrc [22], ALGEBRA [23] and RapidBrachyMCTPS[3] [24] based on Geant4 [25, 26], HDRMC [27] and BrachyGuide [28] based on MCNP [29], and MCPI [30] based on PTRAN [31]. However, MC-based dose calculation algorithms are not currently available in commercial brachytherapy TPS.

MC methods are typically associated with long computation times. Different approaches have been implemented to improve the efficiency of MC methods for brachytherapy applications. For most brachytherapy applications, dose can be approximated by collisional kerma using a track length estimator [31]. The track length estimator scores the energy fluence differential in energy in each voxel and calculates collisional kerma by combining this estimate with mass-energy absorption coefficients (see equation 2.43). Each photon passing through a voxel contributes to the scoring of photon fluence (and hence, dose), which makes it more efficient than analog estimates where a photon interaction is required in a given voxel to provide a dose contribution. Precalculated phase-space files, which store the position, angle and energy of photons exiting the source, may be used for source characterization to speed up calculation times. Phase-space files avoid the need to repeat the simulation of particle transport within the source geometry. Finally, MC simulations can also be accelerated using graphics processing unit (GPU) platforms [32–34].

4.2.3 Dose specification and medium selection

Historically, dose calculations for photon-emitting brachytherapy sources have been based on dose to water in water ($D_{w,w}$). The TG-43 formalism describes dose deposition around a single source in a large spherical water phantom (representing infinite scatter conditions) with uniform density (0.998 g cm^{-3}). In commercial treatment planning systems, total dose computation

---

[3] Introduced in Chapter 6.

is performed by superposition of these precalculated single-source dose distributions (defined using MC) according to the dwell positions and dwell times defined in the plan. While this method is fast, reproducible and practical, it effectively ignores tissue heterogeneities, applicator heterogeneities, interseed attenuation and finite patient dimensions. The rationale for reporting $D_{w,w}$ is that clinical experience is based on this quantity. The TG-186 report [3] distinguishes between $D_{w,w}$ and $D_{w,w/\text{appl/air}}$. $D_{w,w/\text{appl/air}}$ represents a major improvement over $D_{w,w}$ since applicator heterogeneities, interseed attenuation and finite patient dimensions are considered.

Dose to medium in medium ($D_{m,m}$) can be reported to account for tissue heterogeneities. In this case, radiation transport and dose scoring is reported in the local medium. While $D_{m,m}$ can be viewed as the natural choice for dose reporting for MBDCAs, it requires accurate knowledge of the elemental composition and density of tissues. The rationale for calculating $D_{m,m}$ is that the macroscopic dose dominates the response of tissues to radiation (tumour control and normal tissue complications).

An alternative is to report dose to water in medium ($D_{w,m}$). In this case, radiation transport is carried out in medium, but dose is scored in a mass of water embedded within the medium. In most studies, the dose is scored using a conversion method from cavity theory, which depends on the cavity dimensions relative to the range of the secondary electrons [35, 7, 36]. In brachytherapy dose calculation, the water cavity has dimensions similar to the treatment planning voxel (on the order of 1 mm). For photon energies relevant to most brachytherapy applications ($<$300 keV), CPE conditions can be assumed for the cavity and the dose can be converted using the (water/medium) ratios of mass-energy absorption coefficients (large cavity theory). Applying this approximation for ^{60}Co, however, leads to a dosimetric error of approximately 0.1%, 2.5% and 5% for muscle, adipose and bone, respectively [7]. While the conversion from $D_{m,m}$ to $D_{w,m}$ may add additional uncertainties, $D_{w,m}$ is less sensitive to the elemental composition assigned the local medium while providing a more realistic representation of the fluence energy spectrum surrounding the cavity. The rationale for calculating $D_{w,m}$ has been that clinical knowledge is based on dose reporting to water. Another argument in support of $D_{w,m}$ is that biological targets of interest consist mainly of water and are likely to vary less between tissue types due to their functional similarity than the average tissue composition [3].

4.2.4 Imaging and patient modeling

In current practice (based on TG-43), the CT images are used only for contouring of the anatomy and catheter localization. The CT images contain input data that are critical for the accuracy of the dose distribution generated with MBDCAs. The CT scan outputs data on the Hounsfield scale, a quantitative scale that describes the attenuation properties of each voxel. The Hounsfield unit (HU) from the CT scan is defined as follows:

$$\text{HU} = 1000\,\frac{\mu - \mu_{water}}{\mu_{water} - \mu_{air}} \tag{4.7}$$

where μ_{water} and μ_{air} represent the linear attenuation coefficient for water and air, respectively. Since the attenuation coefficient of air is nearly zero, one HU represents a variation in attenuation of 0.1% relative to water. The HU for water and air are 0 and -1000, respectively. MBDCAs require that mass (or electron) density and material composition be assigned to all voxels. Tissue density can be extracted from CT images using a calibration curve which relates HU to mass (or electron) density [37]. A calibration curve is generated using a phantom containing tissue substitutes with known composition and density (Figure 4.2).

The TG-186 report recommends to assign a uniform material composition to each contoured organ and density on a voxel-by-voxel basis based on the HU-to-density curve. Regions of low density (air) and high density (bone, calcification) can also be identified within contoured organs. In the case where contours are missing, a second approach is to assign both material composition and density on a voxel-by-voxel basis based on the HU-to-density curve alone. This method uses the CT information directly and avoids the need for segmentation. In the case where CT images are not available (MRI- or US-based planning), a third approach is to assign material composition and nominal density based on the contoured organs alone, effectively ignoring density variations.

The presence of metallic objects, such as implants and markers, in a CT scan may lead to streaking artifacts that can degrade image quality. These artifacts can lead directly to dose calculation inaccuracies, especially if it results in incorrect material assignment. The TG-186 report recommends to remove visible artifacts using a simple approach, such as a manual override of the tissue composition and density to a single material with uniform density (nominal density or average density of neighboring voxels).

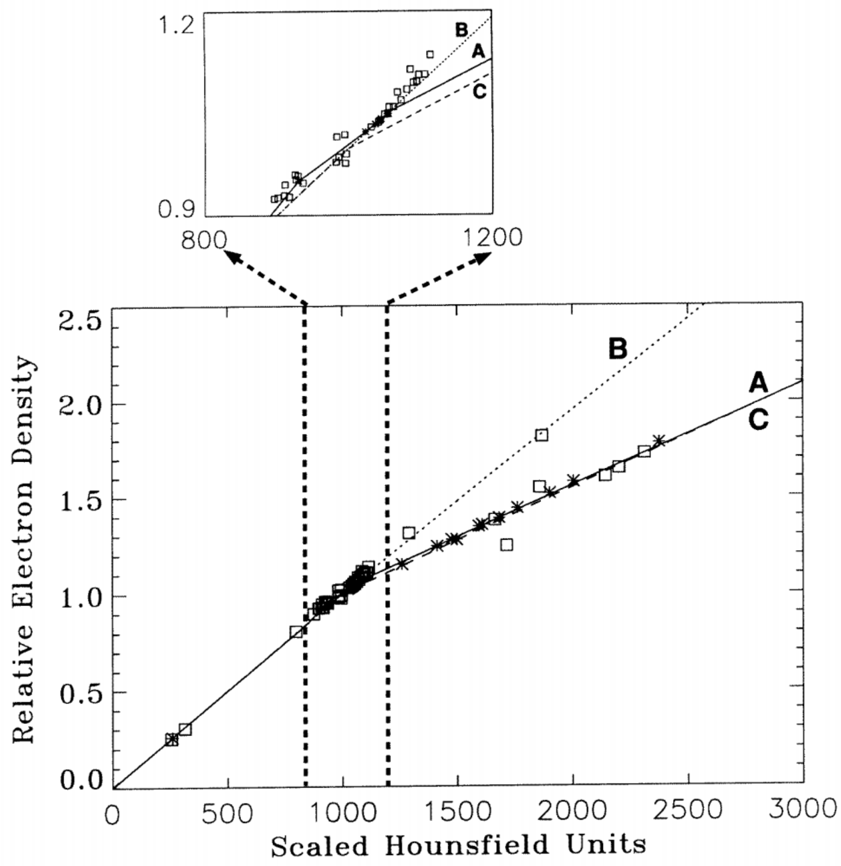

Figure 4.2: Calibration curves for the conversion of Hounsfield units (HU) into relative electron density. The solid line shows the stoichiometric calibration for biological tissues (stars). The dotted and dashed lines shows two different calibrations for tissue substitutes (squares). Figure reproduced from [37].

4.3 Monte Carlo methods

4.3.1 Basics of Monte Carlo simulations

The transport of particles in matter can be solved in an exact manner by the MC method [19]. Particles are generated according to the source energy, spatial and angular distributions. These particles travel a certain distance (determined by a probability distribution) to an interaction site and scatter into another direction, deposit energy and/or release secondary particles. This procedure is repeated until the particle is completely absorbed or leaves the geometry under consideration.

The principles of a general purpose MC code for particle transport can be summarized as a three step process, where each step requires a random number generator to sample from a probability distribution [19]. First, the step length of the particle is determined by sampling the total interaction cross section, and the particle is transported to a new position. Second, the type of interaction event occurring after the step is determined by sampling the relative magnitude of the interaction cross sections. Third, the energy and/or direction of the primary and secondary particles (if secondary particles are ejected) are obtained by sampling the angular differential cross section for the given interaction.

Quantities of interest can be calculated by averaging over a given set of particle histories N. In general, the statistical uncertainty (σ) is inversely proportional to the square root of the number of histories ($\sqrt{N}$). The efficiency (ε) of a MC calculation is defined as follows:

$$\varepsilon = \frac{1}{\sigma^2 T} \tag{4.8}$$

where σ^2 is the estimated variance of the quantity of interest and T is the computation time on a central processing unit (CPU). Since T is proportional to N and σ^2 is inversely proportional to N, ε is independent of N for a given algorithm.

MC simulations are generally computationally expensive and this may lead to very long computation times. In order to improve the efficiency of the simulation, variance reduction techniques can be performed to allow the user to tune the part of the simulation to the part of the problem space (particle type, energy, position, direction) most relevant to the application. Variance reduction techniques should be implemented correctly to avoid introducing systematic errors. Examples of variance reduction techniques include bremsstrahlung splitting, interaction forcing, range rejection, Russian roulette, correlated sampling, photon cross section enhancement and track length estimation [38].

Electron transport can also lead to issues with regards to computation time. During the slowing-down process, electrons may undergo hundreds of thousands of collisions, where most of these collisions only slightly modify the electrons direction and energy. Condensed history techniques [39], which are based on multiple scattering theory [40], use the fact that individual collisions between electrons and atoms generally have an extremely small effect on an electron's direction and energy. Condensed history techniques approximate a group of individual collisions by a larger collision in a single step, which describes the cumulative effect of a large number of physical interactions. These techniques reduce the number of simulated collisions, which improve the computational efficiency of the algorithm.

MC track structure (MCTS) codes handle particle transport in an event-by-event manner. MCTS algorithms simulate the full slowing-down of lower-energy charged particles down to a cutoff energy of about 10 eV. The availability of MCTS codes makes it possible to investigate energy deposition patterns down to the nanometre scale in simple environments such as water. MCTS simulations have become an important tool in biophysical modelling of radiation damage on the level of cellular and sub-cellular structures.

4.3.2 Geant4

Geant4 [25, 26] is an open-source MC toolkit for simulating the passage of particles through matter. It includes a complete range of functionality including tracking, geometry, physics models and scoring. The set of physics models include electromagnetic, hadronic and optical processes, for a large variety of particles, materials and elements, over a very wide energy range (from 250 eV to 1 PeV, depending on the particle type). It has been designed to handle the implementation of complex geometry into the system, the materials involved, the generation of primary particles, the physics processes governing particle interaction and production, the storage of events and tracks, the scoring of sensitive detector components, and the visualisation of the geometry and particles track, using object-oriented technology implemented in the C++ programming language. Each component of the simulation is implemented in a separate class, to allow the easy adaptation for optimal use. Application areas include high energy, nuclear, medical, accelerator and space physics. Geant4 is developed at the European Organization for Nuclear Research (CERN) as an international collaborative project. The dose calculation engine presented in chapter 6 is based on Geant4.

Geant4-DNA

The Geant4 toolkit is continuously being extended with physical, chemical and biological models in order to simulate radiation interaction with matter. The Geant4-DNA [41, 42] physics processes and models can simulate event-by-event interactions of particles (photons, electrons, protons, neutrons, heavy ions) in liquid water down to the eV scale. The Geant4-DNA processes simulate explicitly every interaction without relying on condensed history techniques. The electron interaction processes are based on a combination of semi-empirical models and on the plane-wave Born approximation. The Geant4-DNA processes for electrons include elastic scattering (Champion model), electronic excitation and ionisation of the water molecule (Born approximation), dissociative electron attachment (Sanche model), and vibrational excitation of the molecule (Melton model). Photon interactions are based on the Livermore model. By using Geant4-DNA, damage induced by ionizing radiation on the cellular and subcellular scale can be calculated. The MCTS simulations in chapter 5 were performed using Geant4-DNA.

4.3.3 EGSnrc

EGSnrc [22] is a general-purpose, open-source software toolkit to perform MC simulations of radiation transport through matter. The software models the propagation of photons, electrons and positrons with kinetic energies between 1 keV and 10 GeV. EGSnrc is an extension of the EGS4 ("Electron Gamma Shower") software package developed and maintained by the joint collaboration between the National Research Council of Canada (NRC) and the Stanford Linear Accelerator Center (SLAC). The EGSnrc implementation improves the accuracy of condensed history techniques for charged particle transport and lower-energy scattering cross section data. Various physics models and cross section data are available to simulate electromagnetic processes. The software also contains a C++ geometry library which defines the geometry of complex simulation environments and particle sources. EGSnrc is particularly well-suited for medical physics purposes, such as radiation detection, medical imaging, radiation therapy, nuclear medicine and radiation protection.

The EGSnrc toolkit contains a series of user codes that are designed to handle common types of applications. The user can select the appropriate simulation parameters using the input file and run simulations without having to write a new program. Each user code provides a number of variance reduction techniques that may be suitable for the given application, depending on the simulation parameters. The user codes that are relevant to brachytherapy dose calculations include BrachyDose [20] and egs_brachy [21]. The user code *g* calculates quantities such as (μ_{en}/ρ), (μ_{tr}/ρ) or $\bar{g}$ for a homogeneous medium with a given elemental composition. A library of (μ_{en}/ρ) values (see chapter 6) is required to implement track length estimation in brachytherapy MC simulations.

4.4 Experimental dosimetry

4.4.1 Well-type ionization chamber

The source calibration is an essential component of quality assurance for clinical brachytherapy dosimetry. The source calibration procedure at the clinic consists of measuring the brachyther-

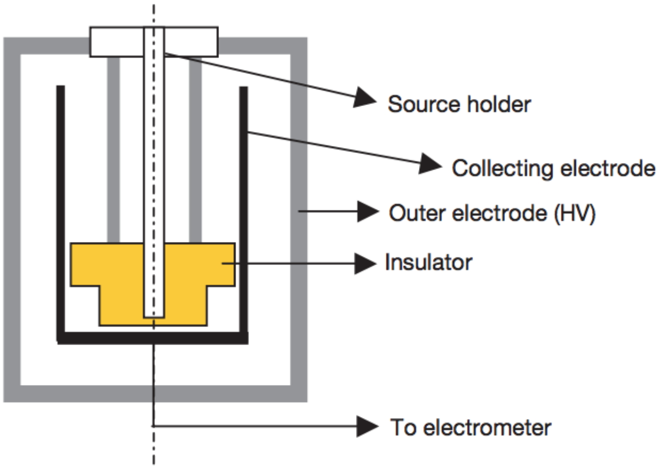

Figure 4.3: Schematic design of a typical well-type ionization chamber. Figure reproduced from [45].

apy source strength to independently verify the value stated on the vendor's source calibration certificate. The air kerma strength S_K is the recommended quantity to specify source strength [43]. Therefore, the calibration of a brachytherapy source consists of an air kerma rate measurement in free space. Well-type ionization chambers are recommended for the routine calibration of brachytherapy sources [44].

A well-type ionization chamber consists of a gas-filled cavity surrounded by an outer electrode and a collecting electrode that are separated by an insulator [45]. A schematic design of a well-type ionization chamber is illustrated in Figure 4.3. When exposed to radiation, the ions produced in the gas are swept from the chamber volume by the electric field between the electrodes. The current in the collecting electrode is read out using an electrometer. A well is included to place the sample inside the detector. The well-type ionization chamber is highly sensitive, has low leakage, and provides close to 4π sampling geometry. The well-type ionization chamber is relatively insensitive to variations in source construction and positioning.

Each well-type ionization chamber is provided with a calibration coefficient for a particular radiation quality (e.g. ^{137}Cs, ^{192}Ir, ^{60}Co, 250 kVp x-rays). This calibration coefficient is derived by traceable calibration to the NRC primary standard or secondary standard for the reference radiation. The air kerma strength S_K is determined as follows:

$$S_K = N_K^R \, I_{max} \, k_{TP} \, k_{ion} \, k_{dec} \tag{4.9}$$

where N_K^R is the air kerma strength calibration coefficient for reference radiation R, I_{max} is the maximum measured ionization current, k_{TP} corrects for deviations in temperature and pressure compared to reference conditions, k_{ion} corrects for ion recombination losses, and k_{dec} accounts for radioactive decay between time of measurement and reference time.

4.4.2 Radiochromic film

Principle of operation

Radiochromic film is a type of film that is commonly used for radiation therapy treatment verification and quality assurance [46]. Radiochromic film consists of a radiation sensitive component (diacetylene monomers) embedded in a water-soluble polymer matrix. Upon exposure to ionizing radiation, the sensitive layer of the film changes colour due to a polymerization process that results in formation of a blue coloured polymer. The change in colour due to ionizing radiation exposure depends on the energy deposited within the radiation sensitive volume of the film. Radiochromic films are self-developing (no need for dark room) and do not require chemical processing after irradiation. In addition, the films can be scanned using typical flatbed scanners (e.g. Epson).

Radiochromic films are commonly used as 2D dosimeters for radiation fields with high dose gradients. These films have been shown to be suitable for various dosimetry application, including megavoltage beams (photons, electrons, hadrons) [46, 47], brachytherapy [48, 49] and diagnostic radiology [50]. The main advantages of radiochromic film as a dosimeter include its high spatial resolution, energy independence (above 100 keV), tissue equivalence, extended dose range, water resistance, relative insensitivity to room light and low cost. Limitations include a small temperature and humidity dependence, energy dependence below 100 keV, and directional dependence of the film response.

Cutting and labeling

The most convenient way of cutting films is to use the paper cutter with a ruler and presser. It is important to make sure that a clear straight cut is performed to avoid unreliable measurements close to the edges of the film piece. Rectangular film pieces are recommended to keep track of film orientation and to provide a labeling section outside of the square measuring area to mark useful information. In general, it is good practice to handle the films using gloves to avoid fingerprints and to minimize the amount of distortion. The films should be stored in a dark, dry area to limit background darkening of film over a long period of time and ideally should be kept in their packaging to avoid accumulation of dust.

Scanning and image processing

When film pieces are placed in the scanner, it is important that the film pieces are placed with the same positioning and orientation before and after irradiation. Maintaining a reproducible position within the scanner bed minimizes the impact of the non-uniform response of the scanner. Rotation of the film pieces on the scanner bed can impact the measured response, since film behaves as a polarizer and exhibits a directional dependence. Film rotation can also introduce unnecessary averaging of adjacent pixels.

Prior to scanning film pieces, the colour bit-depth and scanning resolution need to be determined. Auto-correction imaging filters should also be turned off. The most optimal use of flatbed document scanner is the use of RGB (Red, Green, Blue) scanning mode. Scanned color images, most commonly saved in Tagged Image File Format (TIFF) in RGB mode, represent three images corresponding to each colour channel. It is common practice to use 16-bit deep images per colour [51]. All three color channels can be incorporated to perform triple-channel film dosimetry [52]. The simultaneous acquisition of all three channels improves the accuracy of the dose response. The images should be scanned at a slightly higher resolution than the desired spatial resolution of the dose distribution [51]. The raw data from a particular colour channel over a certain region of interest (ROI) can then be defined by an average pixel value (PV) with its associated standard deviation (σ_{PV}) (Figure 4.4). Once the scanned images are imported and digitized, defective pixels can be identified and removed using the blank scans over predefined scanning ROI [53]. A Wiener filter is then applied to remove the noise from the scanned images caused by the inherent scanner noise and the non-uniformity of the active layer.

The time interval between irradiation and scanning must be kept constant in a given radiochromic film dosimetry protocol. The rate of polymerization is quite high in the first few hours after irradiation, but it gradually stabilizes afterwards [54]. In practice, a waiting period of 24 h is commonly adopted due to its convenience and stability in response.

Net optical density

Consider a light source and a detector which measures either the transmitted light intensity (transmission mode) or the reflected light intensity (reflection mode). The optical density (OD)

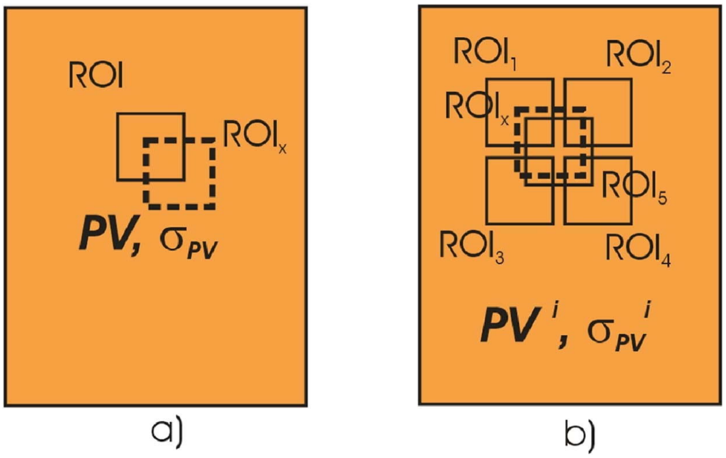

Figure 4.4: Average pixel value (PV) and associated standard deviation (σ_{PV}) (a) over a single ROI and (b) over multiple (five) ROI. The solid lines indicate the ROI used to create the calibration curve(s), while the dashed lines indicate the ROI$_x$ that is used to determine the absolute error in calibration. Figure reproduced from [51].

is a common quantity to define the film's response to ionizing radiation:

$$OD = -\log \frac{I}{I_0} \tag{4.10}$$

where I_0 is the light intensity from the light source and I is the light intensity collected by the detector. In transmission mode, the ratio in intensity is called the transmittance ($T = I^{trans}/I_0^{trans}$). In reflection mode, the ratio in intensity is called the reflectance ($R = I_0^{refl}/I^{refl}$). The selection of measurement mode (transmission or reflection) generally depends on whether the film model is transparent or opaque. The main difference between transmission and reflection mode is that the light has to pass through the active layer twice in reflection mode but only once in transmission mode, which increases the sensitivity of the film's response. The ratios in intensity can be quantified using the pixel value PV in the scanned image.

Regardless of the quantity used to quantify the film's response, it is recommended to measure the change in this quantity for each film piece before and after irradiation. The net optical density ($netOD$) refers to the change in optical density that occurs from an irradiation:

$$netOD = OD_{after} - OD_{before} = \log \frac{PV_{before} - PV_{bkgd}}{PV_{after} - PV_{bkgd}} \tag{4.11}$$

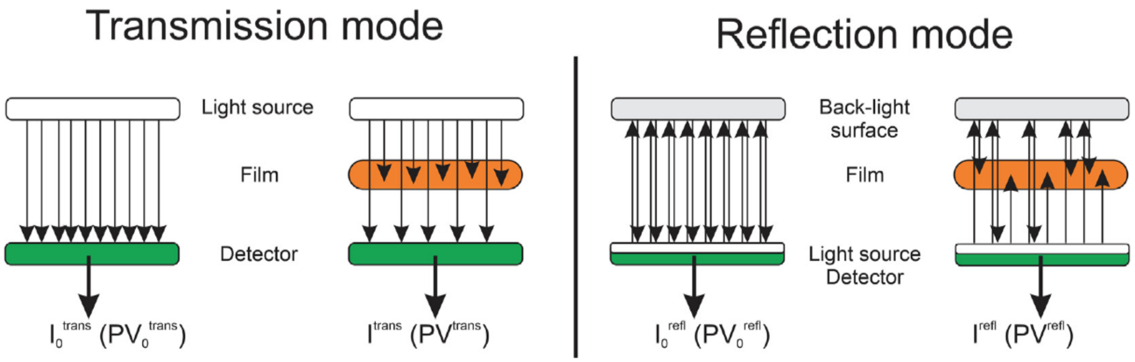

Figure 4.5: Measured raw data using flatbed scanner in transmission and reflection mode. Figure reproduced from [49].

where OD_{before} and OD_{after} represent the optical density before and after the irradiation, respectively, PV_{before} and PV_{after} represent the pixel value before and after the irradiation, respectively, and PV_{bkgd} represents the pixel value of the background signal. The background signal can be measured by covering the scanner bed with an opaque sheet.

A control film is recommended to measure the change in total net optical density caused by irradiation alone [55]. The control film represents a film piece that has not been irradiated and any change in the absorbance for this film piece reflects the film response due to environmental conditions (e.g. temperature, humidity, exposure to UV light or scanning light). If the control film is used, the net optical density of the control film should be subtracted from the measured net optical density as follows:

$$\Delta(netOD) = netOD - netOD^{ctrl} = \log \frac{PV_{before} - PV_{bkgd}}{PV_{after} - PV_{bkgd}} - \log \frac{PV^{ctrl}_{before} - PV_{bkgd}}{PV^{ctrl}_{after} - PV_{bkgd}} \quad (4.12)$$

Calibration

Radiochromic film has a non-linear dose response curve, where the measured signal (e.g. net optical density) is plotted as a function of dose (left side of Figure 4.6). A calibration curve is necessary to relate the net optical density to absorbed dose. The calibration curve must be established by irradiating film pieces to known doses and evaluating the net optical density at each dose value. Plotting a calibration curve where dose is defined as a function of net optical density, and determining an analytical expression for this curve, allows for the conversion of a measured net optical density into a dose (right side of Figure 4.6). Devic et al. [53] suggests a

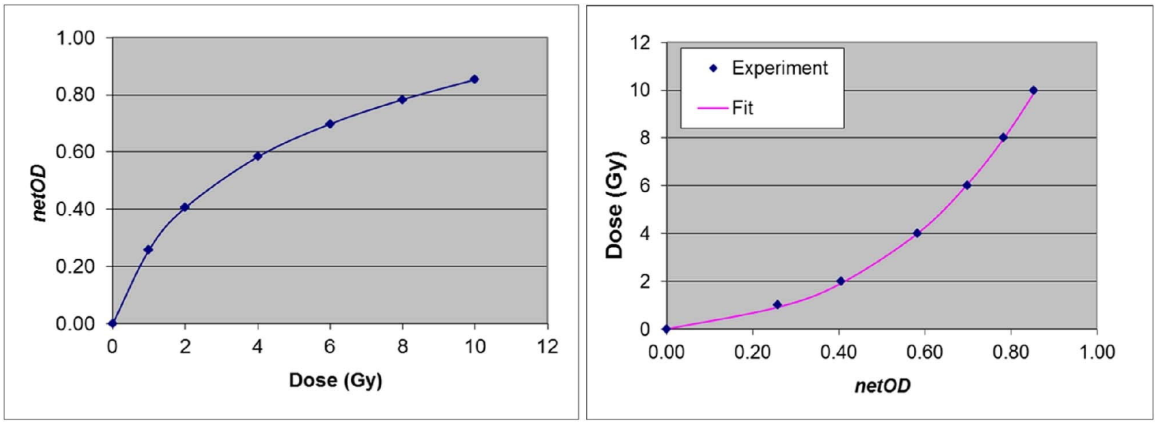

Figure 4.6: Film response curve (left) and calibration curve (right) to relate dose (D) to net optical density ($netOD$). Figure reproduced from [51].

polynomial fitting function of the form:

$$D = b\;(netOD) + c\;(netOD)^n \tag{4.13}$$

where b, c and n are fitting parameters. In general, it is good practice to have more calibration points at very low doses due to the higher sensitivity of the film response. The calibration curve must be established for each film batch, due to the variable response of each film batch. For high-energy photon-emitting brachytherapy sources, the calibration film pieces can be irradiated using a megavoltage photon beam. For low- and intermediate-energy photon-emitting brachytherapy sources, it is important to select a reference beam with a similar beam quality as in the experiment. It is generally good practice to perform the output verification of the photon beam before any irradiation of the calibration film pieces.

To establish the calibration curve, the average pixel values PV and corresponding standard deviations (σ_{PV}) can be calculated either for a single ROI (Figure 4.4a) or for multiple ROI (Figure 4.4b). The advantage of using multiple ROI is that a set of calibration curves can be obtained, and these can be averaged to improve the robustness of the calibration. In addition to ROI sampled for the creation of the calibration curve, another region of interest (ROI$_x$) should be sampled to determine the difference between the delivered dose and the dose calculated using pixel values sampled over ROI$_x$ using the calibration. Since the delivered dose is known during the calibration process, this difference will represent the calibration error, which should be compared to the estimated uncertainty for a given dosimetry protocol [53, 51].

Table 4.1: Film models with useful dose ranges and effective Z (Z_{eff}) of active layer.

Film model	Dose range	Z_{eff}
EBT-2	0.01-30 Gy	7.46
EBT-3	0.01-30 Gy	7.46
EBT-XD	0.04-40 Gy	7.46
MD-V3	1-100 Gy	7.63
HD-V2	10-1000 Gy	7.63
XR-QA2	0.1-20 cGy	55.2

Types of radiochromic film

The most widely used commercial product for dosimetry is Gafchromic$^{\text{TM}}$ film (Ashland ISP, Wayne, NJ, USA). Table 4.1 summarizes the useful dose range of commonly used Gafchromic$^{\text{TM}}$ film models. The active layer of Gafchromic$^{\text{TM}}$ films for radiation therapy applications are near water-equivalent as shown in Table 4.1.

The EBT-2 and EBT-3 films are designed for most radiation therapy applications with dynamic dose range of 0.01-30 Gy. The EBT-2 film model (Figure 4.7a) is asymmetric and contains a 28 μm active layer with a 25 μm pressure-sensitive adhesive layer and 50 μm and 175 μm clear polyester substrate layers. A yellow dye is introduced into the active layer to correct for small variations in the thickness of the active layer. The EBT-3 film model (Figure 4.7b) is symmetric and consists of a 28 μm active layer between two 125 μm matte polyester layers. The matte polyester substrate is treated with microscopic silica particles to prevent the formation of ring patterns when the film is scanned.

The EBT-XD film model (Figure 4.7c) is designed to extend the dynamic range to higher doses (up to 40 Gy) for hypofractionated treatments. It contains a smaller sensitive layer than the previous models. The MD-V3 (Figure 4.7d) and HD-V2 (Figure 4.7e) are designed to further extend the dynamic dose range to 100 Gy and 1000 Gy, respectively.

The XR-QA2 film model (Figure 4.7f) is designed specifically for radiology applications (very small doses). It is designed to be used in the energy range of 20-200 kVp and its dynamic dose range is 0.1-20 cGy.

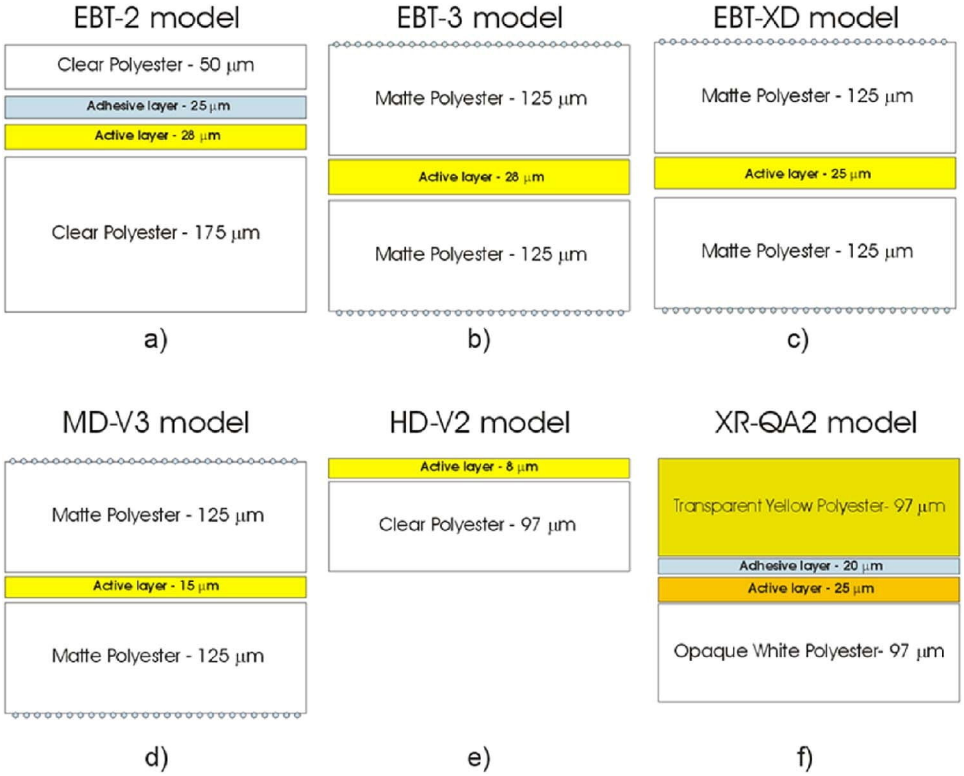

Figure 4.7: Gafchromic film design for various models: (a) EBT-2, (b) EBT-3, (c) EBT-XD, (d) MD-V3 (e) HD-V2, (f) XR-QA2. Figure reproduced from [51].

4.4.3 Plastic scintillator detector

Principle of operation

A scintillator is a material that exhibits scintillation (emission of the absorbed energy in the form of visible light) when excited by ionizing radiation [56]. Two main categories of scintillation detectors exist: organic scintillators and inorganic crystals. This section focuses on organic scintillators. When ionizing radiation interacts with an organic scintillator, orbital electrons are excited to higher energy levels, lose some energy through internal conversion and vibrational excitation, and return to the ground state, emitting a visible photon with higher wavelength (or lower energy) than the absorbed photon. The Stokes shift refers to the difference in wavelength (or energy) between the peaks of the absorption and emission spectra for a given electronic transition. Thus, organic scintillators are transparent to their own emission. Organic scintillating detectors are typically made of crystal, liquid or plastic. The biggest advantage of plastic scintillators is their ability to be molded into various shapes.

A plastic scintillator detector (PSD) consists of three components: a scintillating probe, an optical guide and a photodetector [56]. The intensity of the scintillation light is assumed to be proportional to the energy deposited. The visible light produced in the scintillator travels through internal reflection inside the scintillator and through the optical guide. Optical fibers are commonly used as the optical guide due to their water-equivalence, flexibility and low amount of attenuation through the fiber. The output of the light guide is then captured by a photodetector. The voltage pulse produced by the photodetector is assumed to be proportional to the intensity of the scintillation light. The photodetector may consist of a photomultiplier tube (PMT), photodiode, silicon photomultiplier or charged-coupled device.

Plastic scintillating detectors (PSDs) are suitable as a radiation dosimeter for megavoltage photon beams and brachytherapy [57, 58, 56]. The main advantages of PSDs include their high spatial resolution, fast response, water-equivalence, linear dose response, and independence to dose rate and energy. However, some disadvantages include the stem effect and temperature dependence. The stem effect relates to the Cerenkov radiation and, to a lesser extent, the fluorescence emitted by the optical guide itself. Various algorithms have been proposed and implemented to remove the Cerenkov radiation in PSDs [57, 59, 58].

Multipoint plastic scintillating detectors (mPSD) consist of a series of scintillators attached to a single optical chain [60–62]. The hyperspectral formalism proposed by Archambault et al. [63] allows each scintillator to have an independent signal. The formalism is based on the hypothesis that the recorded signal is a linear superposition of the emission spectra from each light-emitting component. Such an arrangement allows for simultaneous dose rate measurements at multiple points. The focus of this section is on the mPSD developed and characterized by Linares Rosales et al. [62] since this was the detector adopted in Chapter 9.

mPSD configuration

The mPSD consists of three scintillators: BCF-10, BCF-12 and BCF-60 (Saint Gobain Crystals, Hiram, OH, USA). The scintillators are separated by each other by 1 cm of clear optical fiber. A clear optical fiber also conducts the scintillation light to the surface of the photodetector. This optical fiber section is enclosed in a lightproof black jacket. The scintillating fibers and optical fibers have a diameter of 1.0 mm and the tube containing the fibers has an outer diameter of 1.2 mm, which fits within typical brachytherapy catheters.

The individual emission spectra with intensities normalized to a 1 mm segment of scintillator are shown in Figure 4.8. The scintillation intensity was strongest in the BCF-10 scintillator, whereas the BCF-60 scintillator had the weakest scintillation intensity. In addition, the peak

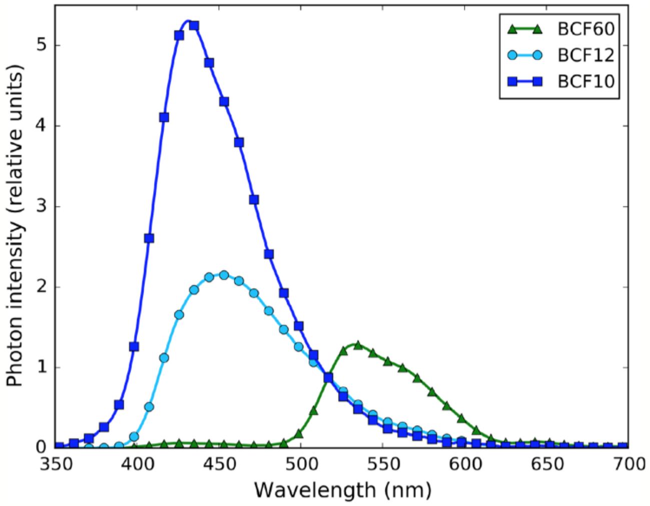

Figure 4.8: Individual scintillator emission spectra for BCF-10, BCF-12 and BCF-60 normalized to a scintillator with 1 mm length. Figure reproduced from [62].

scintillation wavelength was 430 nm for BCF-10, 450 nm for BCF-12 and 530 nm for BCF-60. The optimal configuration of scintillators within an mPSD is based on two factors: the position of each scintillator within the fiber and the length of each scintillator.

Since the absorption spectrum has a lower wavelength range than the emission spectrum, the scintillators should be placed in an order that avoids that the more proximal scintillators will absorb the light emitted by the more distal scintillators (self-absorption), which leads to further excitation of the more distal scintillators (cross-excitation). Indeed, Linares Rosales et al. [62] demonstrated that the shorter wavelength scintillator should be placed closer to the photodetector and the longer wavelength scintillator in the distal position. Thus, for an optimal configuration, BCF-10 should be placed at the proximal position, BCF-12 should be placed in the center position and BCF-60 should be placed at the distal position.

The hyperspectral approach [63] requires a balanced signal contribution from each scintillator to the overall light collection. The intensity of the light depends on the scintillator size, the fiber dimensions and the coupling method. However, the spatial resolution is also dependent on the scintillator size and is certainly an important factor to consider. Linares Rosales et al. [62] proposed an optimal configuration where the lengths of the BCF-10, BCF-12 and BCF-60 scintillators were 3 mm, 6 mm and 7 mm, respectively. This configuration provided a balance in signal contribution from each scintillator and minimized variations in scintillator length to provide similar spatial resolution for each scintillator.

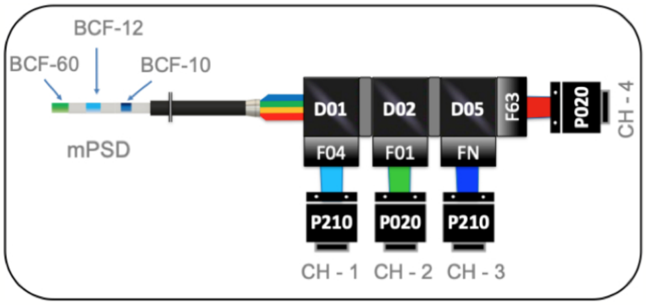

Figure 4.9: Schematic of the light collection system for the mPSD. The light collection system consists of a collection of dichroic mirrors (D), filters (F) and PMTs (P). Figure reproduced from [62].

Light detection system

The optical fiber is connected to a light collection system with components from Hamamatsu Photonics (Hamamatsu, Japan). The light collection system consists of an assembly of PMTs (series H10722) coupled to dichroic mirrors (series A10033) and filters (series A10034) that deconvolve the scintillation light into spectral bands, as shown in Figure 4.9. A channel is defined as an assembly composed of a dichroic mirror, filter and PMT. The components of the channels were selected based on the emission spectrum and light yield, the transmission and attenuation of the optical components reported by the manufacturers, and the PMT noise determined through experiments. Four channels are required to analyze the signal contributions from the three scintillators. The additional channel is included to take into account the stem effect, which needs to be removed from the measured signal.

This assembly filters the total emission spectrum from the mPSD to produce a filtered spectrum entering each PMT. Figure 4.10 shows the total emission spectrum of the scintillation light generated by the mPSD and each channel's filtered spectrum. The dose rate measurement is based on the assumption that the total emission spectrum $\mathbf{m}$ results from the linear superposition of spectra from each light-emitting component:

$$\mathbf{m} = \mathbf{r}_{BCF10}\, x_{BCF10} + \mathbf{r}_{BCF12}\, x_{BCF12} + \mathbf{r}_{BCF60}\, x_{BCF60} + \mathbf{r}_{stem}\, x_{stem} \tag{4.14}$$

where $\mathbf{r}_i$ and x_i represents the normalized emission spectrum and measured intensity of the signal from light-emitting component i, respectively. Once the light emission of each component at different wavebands is characterized, the hyperspectral approach [63] decouples the total

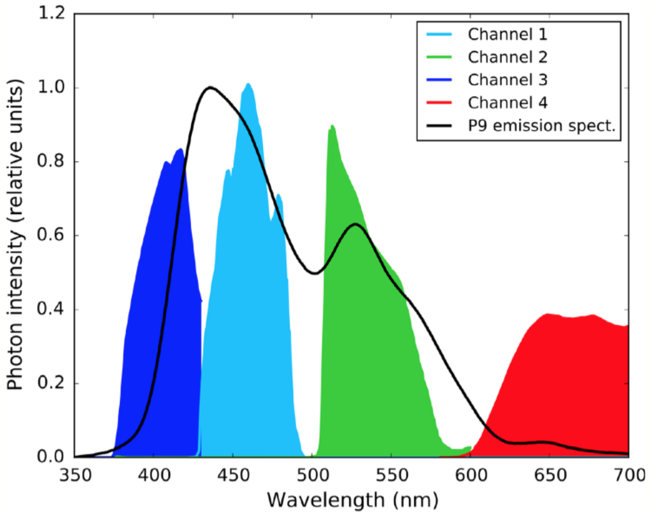

Figure 4.10: Emission and filtered spectra produced by the mPSD. The filtered spectra for each channel were obtained by applying optical filtration to the light entering each PMT. Figure reproduced from [62].

recorded signal **m** and solves the system of equations for the signal fraction x_i contributed by each scintillator.

Calibration

The dose absorbed by the scintillator is directly proportional to the number of scintillation photons detected (assuming no losses due to coupling, self-absorption and cross-excitation). However, a calibration factor is required to convert the measured signal contribution into an absorbed dose. The dose is obtained by performing an irradiation with a known dose to each scintillator:

$$d_i = \frac{x_i}{x_{i,calib}} \, d_{i,calib} \tag{4.15}$$

where $x_{i,calib}$ and $d_{i,calib}$ represent the signal intensity and dose for light-emitting component i under calibration, respectively, and x_i and d_i represent the signal intensity and dose for light-emitting component i during measurement.

Performance of mPSD in HDR brachytherapy

The experimental setup for dose rate measurements in HDR brachytherapy is shown in Figure 4.11. In this setup, the catheters are positioned parallel to each other at fixed distances from

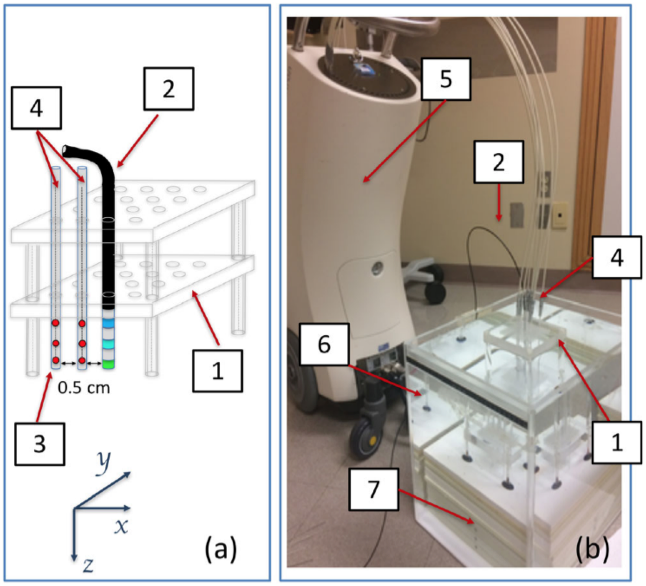

Figure 4.11: (a) Schematic of the PMMA phantom constructed for HDR brachytherapy measurements with an multipoint plastic scintillator detector (mPSD). The catheter positioning allowed source displacement parallel to the mPSD. (b) Experimental setup for HDR brachytherapy measurements. (1) PMMA phantom, (2) mPSD, (3) ^{192}Ir source, (4) 30-cm catheters, (5) Flexitron HDR afterloader unit, (6) water tank, (7) solid-water slabs. Figure reproduced from [62].

each other using a PMMA phantom. The mPSD can be inserted into one of these catheters for dose rate measurements. The transfer tubes are connected to the other catheters to allow the source to dwell at certain positions within these catheters.

To properly differentiate a signal pulse from noise, the Rose criterion states that a signal-to-noise ratio (SNR) of at least 5 is typically required. Linares Rosales et al. [62] reported that the SNR was sufficient (above 5) at a dose rate above 22 mGy s^{-1} for BCF-60 and above a few mGy s^{-1} for BCF-10 and BCF-12. The mPSD was able to measure the dose within 5% at distances within 6.5 cm from the ^{192}Ir HDR source.

4.4.4 Gamma analysis

The commissioning of a TPS routinely requires the comparison of measured and calculated dose distributions. A qualitative comparison can be performed by superimposing the isodose distributions and visually inspecting the overlapped. This can highlight regions of agreement and disagreement, but do not provide a quantitative measure to evaluate the dose calculation algorithm.

The gamma index (γ) is a tool for the quantitative comparison of dose distributions [64, 65]. In clinical practice, the gamma index has traditionally been used to compare measured and calculated dose distributions (1D or 2D). The gamma index is calculated for each point of interest using pre-determined dose difference (DD) and distance to agreement (DTA) criteria.

The DD describes the difference between the measured dose and calculated dose at each point. The DD is most relevant to compare the dose distributions in low dose gradient regions. The DD can be specified as either global or local. The global gamma index calculates the DD relative to the maximum dose in the distribution, while the local gamma index calculates the DD relative to the dose at each evaluated point.

The DTA describes the distance between a measured point and the nearest point in the calculated dose distribution with equal dose. The DTA is most useful to evaluate the agreement in high dose gradient regions, where a small error in distance can result in a large dose deviation. The DTA in high dose gradient regions is less sensitive to misalignments of the dose distributions.

In summary, the criteria for acceptable agreement are generally defined as a DD in regions of low dose gradients and DTA in regions of high dose gradients. These two distributions provide complementary information that are relevant for different regions. Instead of evaluating whether each point exceeds the tolerance in DD and DTA separately, a composite quantity allows for a more general comparison between calculation and measurement that can be displayed in a convenient manner.

Figure 4.12 shows a representation of a composite acceptance criterion that considers both DD and DTA. Given a measurement point $\mathbf{r}_m$ and calculation point $\mathbf{r}_c$, the DTA is represented by $|\mathbf{r}_c - \mathbf{r}_m|$ and the difference between the measured $D_m(\mathbf{r}_m)$ and calculated $D_c(\mathbf{r}_c)$ dose is indicated by $\delta(\mathbf{r}_m, \mathbf{r}_c)$. The DD and DTA criteria are ΔD_M and Δd_M, respectively. The gamma index is defined for the measurement point $\mathbf{r}_m$ as follows:

$$\gamma(\mathbf{r}_m) = \min\{\Gamma(\mathbf{r}_m, \mathbf{r}_c)\}\forall(\mathbf{r}_c) \tag{4.16}$$

where

$$\Gamma(\mathbf{r}_m, \mathbf{r}_c) = \sqrt{\frac{r^2(\mathbf{r}_m, \mathbf{r}_c)}{\Delta d_M^2} + \frac{\delta^2(\mathbf{r}_m, \mathbf{r}_c)}{\Delta D_M^2}}, \tag{4.17}$$

$$r(\mathbf{r}_m, \mathbf{r}_c) = |\mathbf{r}_c - \mathbf{r}_m|, \tag{4.18}$$

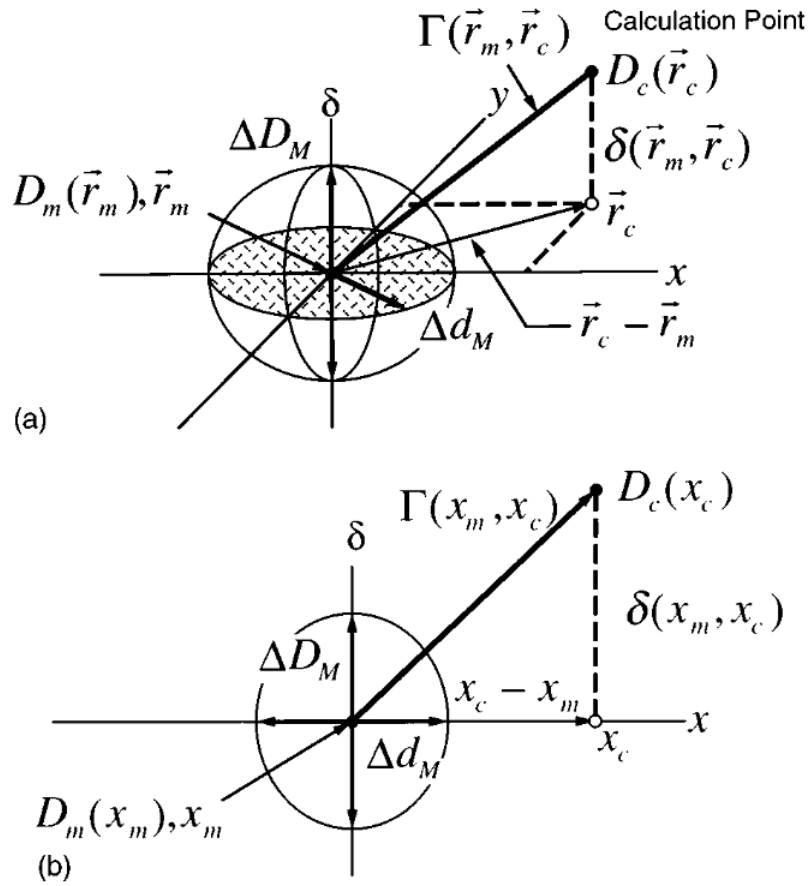

Figure 4.12: Geometric representation of the dose distribution evaluation criteria using DD and DTA in (a) 2D and (b) 1D. Figure reproduced from [64].

$$\delta(\mathbf{r}_m,\mathbf{r}_c)=D_c(\mathbf{r}_c)-D_m(\mathbf{r}_m) \tag{4.19}$$

In equation 4.17, the first term represents the DTA relative to Δd_M and the second term represents the DD relative to ΔD_M. The gamma index evaluation for the measurement point $\mathbf{r}_m$ searches for the calculation point $\mathbf{r}_c$ that minimizes the multidimensional distance $\Gamma(\mathbf{r}_m,\mathbf{r}_c)$ with weighting in DD and DTA defined by ΔD_M and Δd_M, respectively. The passing criterion is $\gamma \leq 1$. Essentially, all calculation points within the ellipsoid (2D) or ellipse (1D) will pass, while those outside will fail.

The DD/DTA criteria for a given application are determined empirically based on clinical experience and measurement uncertainties. Examples of commonly used DD/DTA criteria for IMRT and HDR brachytherapy dose distributions are 2%/2 mm and 3%/3 mm [66, 67]. A cut-off dose can be introduced to limit the evaluation to points that contain at least a certain percentage of the maximum dose (e.g. 20%) [68]. Typically, the clinically acceptable gamma passing rates are on the order of 90% or 95%.

In clinical application, it has become general practice to use the passing percentage of gamma index (the percentage of gamma values where $\gamma \leq 1$ for a set of DD/DTA) to determine whether there is overall agreement between the measured and calculated distributions. The advantage of the gamma passing rate is that it provides a single number which allows for rapid evaluation of plan agreement quality. However, the gamma passing rate has several limitations. First, the gamma passing rate ignores the spatial distribution of the passing and failing points, which can be used to identify errors in setup or delivery. Second, the gamma passing rate may also depend on the type of dosimeter and the associated measurement uncertainties. Third, the gamma passing rate depends on the field of view and the spatial resolution of the 2D dose distribution. Fourth, the gamma passing rate does not provide information on whether the failing points are just above unity or much greater than unity, so the level of disagreement cannot be identified with the gamma passing rate alone. In practice, the gamma distribution should always be visually inspected in addition.

4.5 Uncertainties in brachytherapy dosimetry[4]

4.5.1 Measurement uncertainties

There are a number of uncertainties involved in brachytherapy dose measurements. The most important components of uncertainty are presented in this section.

Source-to-detector positioning

The dose distribution around a brachytherapy source in a phantom is described, to first-order approximation, according to the inverse square law. This means that the relative uncertainty varies strongly with distance. Thus, the uncertainties in the source-to-detector positioning should be estimated as a function of the source-to-detector distance.

---

[4] The information in this section is based on [69].

Dosimeter characteristics

Dosimeters are typically characterized in terms of their reproducibility, sensitivity, relevant dose range, dose rate dependence, energy dependence, spatial resolution and water-equivalency. Each of these components contains an associated uncertainty. Calibration of the dosimeter in various irradiation conditions (e.g. energy, dose, dose rate, temperature/pressure, detector positioning) is a common method to reduce these uncertainties and perform accurate dosimetry. Sources of uncertainty that may be important to consider include, but are not limited to: reproducibility, volume averaging, self-attenuation, energy dependence of the dose response, uniformity, signal-to-noise ratio and calibration fit.

Total uncertainties

DeWerd et al. [69] estimate that the total standard uncertainties ($k = 1$) associated with dose measurements are about 3.0% and 3.6% for high-energy and low-energy brachytherapy sources, respectively.

4.5.2 Monte Carlo uncertainties

While MC methods are considered the gold standard for brachytherapy dosimetry, there are both random (type A) and systematic (type B) uncertainties associated with the simulation process that must be taken into account. A description of the components of uncertainty that arise from MC-based source characterization are presented in this section.

Source geometry

The source geometry used as an input for simulation typically includes the active core, the encapsulation and a small segment of the cable. The source manufacturer typically provides nominal dimensions as well as uncertainties on the dimensions for each component. In addition, there may be internal components which have the potential to change position (e.g. air gaps). Finally, while a uniform activity distribution is usually assumed, the distribution may be heterogeneous to a certain extent. The uncertainties due to variations of each of these individual components (source dimensions, dynamic internal components, activity distribution) should be assessed by simulating an appropriate range of possible source configurations.

Source emissions

The radioactive emission spectrum contains uncertainties related to both the energies and the emission intensities at each energy. The radiation spectra from the National Nuclear Data Center (NNDC) [70] is recommended for brachytherapy simulations. However, the influence of an inaccurate spectrum on the dose distribution should be estimated. In practice, since the precision in emission probabilities is often exaggerated (very low uncertainties), a more meaningful method is to evaluate how the dose distribution is affected by the choice of spectrum from available datasets [71]. In addition, the effect of long-lived radioactive contaminants on the dose distribution should be assessed.

Phantom geometry and composition

Phantom size and composition can have a significant effect on the dose distribution and dosimetric parameters. Source characterization based on TG-43 requires that the phantom geometry provides full scattering conditions (infinite phantom) or, more realistically, sufficient scatter conditions for the range of relevant positions. Systematic errors can arise due to lack of full scattering conditions and should be estimated if the phantom size is not appropriate. Liquid water has a well known composition and mass (or electron) density. However, if the MC simulation aims to simulate the geometry of a physical experiment where the phantom is not liquid water, the uncertainties related to the atomic composition and mass (or electron) densities of the physical phantom should be considered in the uncertainty budget.

Radiation transport code

All MC codes include approximations and assumptions in the simulation of radiation transport. For brachytherapy applications, these may include the implementation of transport or production cuts, electron binding effects, electron transport algorithm, coupled photon-electron transport, bremsstrahlung production and atomic/molecular scattering form factors. The uncertainties related to the physics implementation with radiation transport algorithms should be included in the uncertainty budget.

Interaction and scoring cross sections

The mass attenuation coefficients (μ/ρ) and mass-energy absorption coefficients (μ_{en}/ρ) are required for accurate simulation of photon transport and dose scoring, respectively. These uncertainties are typically considered separately, since dose can be scored in a different medium than that used for photon transport. Ali et al. [72] estimates that the uncertainty ($k = 1$) in both (μ/ρ) and (μ_{en}/ρ) is on the order of ∼0.5% for photons in the energy range of 100 keV to 25 MeV. The influence of the interaction and scoring cross sections on the dose distribution should be assessed in the uncertainty budget.

Scoring algorithms and uncertainties

The scoring algorithm used to determine the dose distribution also presents considerable uncertainties. For large numbers of histories, the type A (statistical) uncertainties in the scored quantities are inversely proportional to the square root of the number of particle histories (Poisson statistics). Typically, dose is scored in a finite volume (voxel) and this provides an estimate for dose at a point. If dose is scored based on energy deposition, the type A uncertainties will be inversely proportional to the square root of the voxel volume. If collisional kerma is scored using a track length estimator, the type A uncertainties will be relatively independent of the voxel thickness but will decrease as the solid angle subtended by the voxel increases. The finite voxel size may lead to volume averaging uncertainties. Voxel size effects can be mitigated by using a track length estimator and decreasing the voxel thickness. Note that the voxel size may also affect the accuracy if the dose is scored using cavity theory. The width of energy bins for energy-weighted tallies and energy thresholds can also result in systematic uncertainties.

Total uncertainties

DeWerd et al. [69] estimates that the total standard uncertainties ($k = 1$) associated with MC dose estimates are about 1.6% and 1.7% for high-energy and low-energy brachytherapy sources, respectively.

4.5.3 Clinical uncertainties

The important sources of uncertainty related to the clinical practice of photon-emitting brachytherapy are presented in this section. The impact of these uncertainties on the overall uncertainty in the dose delivered to the patient are estimated for some typical applications [73].

Air kerma strength calibration

Source strength for photon-emitting brachytherapy sources is typically specified using the air kerma strength S_K. There are systematic uncertainties associated with the primary standard calibration, the transfer of the calibration coefficient to the secondary standards and source manufacturers (well-type ionization chamber), and the source calibrations performed in the clinic (well-type ionization chamber). The combined uncertainty ($k = 1$) in air kerma strength calibration is estimated as 1.5% for high-energy sources and 1.3% for low-energy sources [69].

Treatment planning

Treatment planning systems (TPS) incorporate precalculated dosimetric datasets for each source model. The uncertainties on the consensus dosimetric parameters, mostly determined using MC methods (section 4.5.2), should be included in the uncertainty budget. Another source of uncertainty is the interpolation of the tabulated dosimetric data, calculated in a spherical geometry, onto the voxelized patient geometry.

Dosimetric corrections

Since treatment planning in current clinical practice is performed according to TG-43 protocol, the dosimetric effects due to patient and applicator heterogeneities (section 4.2) can be considered as systematic uncertainties. The incorporation of MBDCAs in clinical practice has the potential to reduce these uncertainties.

Dose delivery

Dose delivery accuracy depends on the consistency of the position of the source inside the applicator and the applicator position inside the patient. For most remote afterloaders, the manufacturers specify a source positioning precision of ±1 mm [74]. The source position in the patient geometry will depend on the curvature of the applicator. Another source of uncertainty is the source position and orientation inside the applicator. It is possible to minimize these uncertainties by reconstruction of the source path during applicator commissioning.

The temporal accuracy and precision of the afterloader should also be of concern. The difference between the measured and calculated dwell time can exceed 60 ms [75]. The transit dose (delivered during source movement) is also not explicitly included in the final dose calculation. However, the manufacturers of the afterloaders may implicitly compensate for the impact of transit dose by reducing the dwell times in the treatment plan [76]. Another potential issue is the rounding error introduced when exporting the treatment plan to the treatment console. The temporal round-off uncertainty is typically under 1% [73].

Imaging

Imaging (CT, US, MRI) allows registration of the dose distribution to the patient anatomy. This process includes aligning the applicator and source path, or the outer applicator surface and patient anatomy, such that the dose distribution can be matched to points and/or volumes reconstructed from the planning images. There are uncertainties related to the reconstruction of the source path [77, 78] and the reconstruction of 3D volumes from 2D contours on sectional slices with a finite slice thickness [79]. Other sources of uncertainties that should be considered include target contouring uncertainties [80] and image fusion uncertainties [81].

Anatomical variations

Variations in the anatomy may occur between fractions (interfraction variations) or within the time of delivery of a single fraction (intrafraction variations). Due to the high dose gradients, small changes in the position/shape of a structure relative to the applicator(s) could lead to large changes in the dose received by a structure. This is especially relevant when one treatment plan is used for multiple fractions, or when organ motion occurs between imaging/treatment planning and dose delivery [82]. Frequent imaging and plan adaptation before each fraction can reduce the impact of major interfraction variations.

Total uncertainties

Kirisits et al. [73] estimates that the total standard uncertainties ($k = 1$) are about 5%, 8%, 12% and 13% for prostate, vaginal, cervical and breast HDR brachytherapy, respectively. The total standard uncertainty ($k = 1$) for prostate LDR brachytherapy is about 11%.

References

[1] Nath R, Andersson LL, Luxton G, Weaver KA, Williamson JF, Meigooni AS. Dosimetry of interstitial brachytherapy sources: Recommendations of the AAPM Radiation Therapy Committee Task Group No. 43. Med Phys. 1995;22(1):209–234.

[2] Rivard MJ, Coursey BM, DeWerd LA, Hanson WF, Huq MS, Ibbott GS, et al. Update of AAPM Task Group No. 43 Report: A revised AAPM protocol for brachytherapy dose calculations. Med Phys. 2004;31(3):633–674.

[3] Beaulieu L, Carlsson Tedgren A, Carrier JF, Davis SD, Mourtada F, Rivard MJ, et al. Report of the Task Group 186 on model-based dose calculation methodsbin brachytherapy beyond the TG-43 formalism: current status and recommendations for clinical implementation. Med Phys. 2012;39(10):6208–6236.

[4] Enger SA, Vijande J, Rivard MJ. Model-based dose calculation algorithms for brachytherapy dosimetry. Semin Radiat Oncol. 2020;30:77–86.

[5] Ahnesjö A. Collapsed cone convolution of radiant energy for photon dose calculation in heterogenous media. Med Phys. 1989;16:577–592.

[6] Carlsson Tedgren AK, Ahnesjö A. Optimization of the computational efficiency of a 3D collapsed cone dose calculation algorithm for brachytherapy. Med Phys. 2008;35:1611–1618.

[7] Carlsson Tedgren A, Alm Carlsson G. Specification of absorbed dose to water using model-based calculation algorithms for treatment planning in brachytherapy. Phys Med Biol. 2013;58(8):2561–2579.

[8] Ahnesjö A, van Veelen B, Carlsson-Tedgren A. Collapsed cone dose calculations for heterogeneous tissues in brachytherapy using primary and scatter separation source data. Comput Methods Programs Biomed. 1989;139:17–29.

[9] Russell KR, Ahnesjö A, Carlsson Å K. Brachytherapy source characterization for improved dose calculations using primary and scatter dose separation. Med Phys. 2005;32:2739–2752.

[10] Carlsson AK, Ahnesjö A. The collapsed cone superposition algorithm applied to scatter dose calculations in brachytherapy. Med Phys. 2000;27(10):2320–2332.

[11] O'Connor JE. The variation of scattered x-rays with density in an irradiated body. Phys Med Biol. 1957;1:352–369.

[12] Carlsson Tedgren AK, Ahnesjö A. Accounting for high Z shields in brachytherapy using collapsed cone superposition for scatter dose calculation. Med Phys. 2003;30:2206–2217.

[13] Gifford KA, Price MJ, Wareing TA, Horton JL, Mourtada F. Optimization of deterministic transport parameters for the calculation of the dose distribution around a high dose-rate 192Ir brachytherapy source. Med Phys. 2006;35(6):2279–2285.

[14] Zourari K, Pantelis E, Moutsatsos A, Petrokokkinos L, Karaiskos P, Sakelliou L, et al. Dosimetric accuracy of a deterministic radiation transport based ^{192}Ir brachytherapy treatment planning system. Part I: Single sources and bounded homogeneous geometries. Med Phys. 2010;37(2):649–661.

[15] Petrokokkinos L, Zourari K, Pantelis E, Moutsatsos A, Karaiskos P, Sakelliou L, et al. Dosimetric accuracy of a deterministic radiation transport based ^{192}Ir brachytherapy treatment planning system. Part II: Monte Carlo and experimental verification of a multiple source dwell position plan employing a shielded applicator. Med Phys. 2011;38(4):011712.

[16] Zourari K, Pantelis E, Moutsatsos A, Petrokokkinos L, Sakelliou L, Georgiou E, et al. Dosimetric accuracy of a deterministic radiation transport based ^{192}Ir brachytherapy treatment planning system. Part III. Comparison to Monte Carlo simulation in voxelized anatomical computational models. Med Phys. 2013;40(1):011712.

[17] Papagiannis P, Pantelis E, Karaiskos P. Current state of the art brachytherapy treatment planning dosimetry algorithms. Br J Radiol. 2014;87(1041):20140163.

[18] Lewis EE, Miller WF. Computational methods of neutron transport. New York, NY, USA: Wiley; 1984.

[19] Andreo P. Monte Carlo techniques in medical radiation physics. Phy Med Biol. 1991;36(7):861–920.

[20] Taylor REP, Yegin G, Rogers DWO. Benchmarking BrachyDose: Voxel based EGSnrc Monte Carlo calculations of TG-43 dosimetry parameters. Med Phys. 2007;34(2):445–457.

[21] Chamberland MJP, Taylor REP, Rogers DWO, Thomson RM. egs_brachy: a versatile and fast Monte Carlo code for brachytherapy. Phys Med Biol. 2016;61(23):8214–8231.

[22] Kawrakow I. Accurate condensed history Monte Carlo simulation of electron transport. I. EGSnrc, the new EGS4 version. Med Phys. 2000;27(3):485–498.

[23] Afsharpour H, Landry G, D'Amours M, Enger S, Reniers B, Poon E, et al. ALGEBRA: ALgorithm for the heterogeneous dosimetry based on GEANT4 for BRAchytherapy. Phys Med Biol. 2012;57(11):3273–3280.

[24] Famulari G, Renaud M, Poole CM, Evans MDC, Seuntjens J, Enger SA. RapidBrachyMCTPS: a Monte Carlo-based treatment planning system for brachytherapy applications. Phys Med Biol. 2018;63(17):175007.

[25] Agostinelli S, Allison J, al Amako K, Apostolakis J, Araujo H, Arce P, et al. Geant4 - a simulation toolkit. Nucl Inst Meth Phys Res A. 2003;506(3):250–303.

[26] Allison J, Amako K, Apostolakis J, Araujo H, Dubois PA, Asai M, et al. Geant4 developments and applications. IEEE Trans Nucl Sci. 2006;53(1):270–278.

[27] Chibani O, C-M Ma C. HDRMC, an accelerated Monte Carlo dose calculator for high dose rate brachytherapy with CT-compatible applicators. Med Phys. 2014;41(5):051712.

[28] Pantelis E, Peppa V, Lahanas V, Pappas E, Papagiannis P. BrachyGuide: a brachytherapy-dedicated DICOM RT viewer and interface to Monte Carlo simulation software. J Appl Clin Med Phys. 2015;16(1):208–218.

[29] Team X-MC: MCNP—A General Monte Carlo N-Particle Transport Code, Version 5, Volume I: Overview and Theory. Los Alamos, NM, USA: Los Alamos National Laboratory; 2003.

[30] Chibani O, Williamson JF. MCPI: a sub-minute Monte Carlo dose calculation engine for prostate implants. Med Phys. 2005;32(12):3688–3698.

[31] Williamson JF. Monte Carlo evaluation of kerma at a point for photon transport problems. Med Phys. 1987;14:567–576.

[32] Hissoiny S, Ozell B, Després P, Carrier JF. GPUMCD: A new GPU-oriented Monte Carlo dose calculation platform. Med Phys. 2011;38(7):4101–4107.

[33] Lemaréchal Y, Bert J, Falconnet C, Després P, Valeri A, Schick U, et al. GGEMS-Brachy: GPU GEant4-based Monte Carlo simulation for brachytherapy applications. Phys Med Biol. 2012;60(30):4987–5006.

[34] Bonenfant E, Magnoux V, Hissoiny S, Ozell B, Després P, Beaulieu L. Fast GPU-based Monte Carlo simulations for LDR prostate brachytherapy. Phys Med Biol. 2015;60(13):4973–4982.

[35] Enger SA, Ahnesjö A, Verhaegen F, Beaulieu L. Dose to tissue medium or water cavities as surrogate for the dose to cell nuclei at brachytherapy photon energies. Phys Med Biol. 2012;57:4489–4500.

[36] Fonseca G, Carlsson Tedgren A, Reniers B, Nilsson J, Persson M, Yoriyaz H, et al. Dose specification for ^{192}Ir high dose rate brachytherapy in terms of dose-to-water-in-medium and dose-to-medium-in-medium. Phys Med Biol. 2015;60:4565–4579.

[37] Schneider U, Pedroni E, Lomax A. The calibration of CT Hounsfield units for radiotherapy treatment planning. Phys Med Biol. 1996;41:111–124.

[38] Gualdrini G, Ferrari P. Monte carlo variance reduction techniques: an overview with some practical examples. Radiat Prot Dosim. 2011;146(4):425–433.

[39] Berger MJ. Monte Carlo calculations of the penetration and diffusion of fast charged particles. vol. 1. B Alder MR S Fernbach, editor. New York: Academic Press; 1963.

[40] Goudsmit SA, Saunderson JL. Phys Rev. 1940;57:24.

[41] Bernal MA, Bordage MC, Brown JMC, Davídková M, Delage E, Bitar ZE, et al. Track structure modeling in liquid water: a review of the Geant4-DNA very low energy extension of the Geant4 Monte Carlo simulation toolkit. Phys Med. 2015;31:861–874.

[42] Incerti S, Baldacchino G, Bernal M, Capra R, Champion C, Francis Z, et al. The Geant4-DNA project. Int J Model Simul Sci Comput. 2010;1:157–178.

[43] Nath R, Andersson LL, Meli JA, Olch AJ, Stitt JA, Williamson JF. Code of practice for brachytherapy physics: Report of the AAPM Radiation Therapy Committee Task Group No. 56. Med Phys. 1997;24(10):1557–1598.

[44] Baltas D, Geramani K, Ioannidis GT, Hierholz K, Rogge B, Kolotas C, et al. Comparison of calibration procedures for ^{192}Ir high-dose-rate brachytherapy sources. Int J Radiat Oncol Biol Phys. 1999;43(3):653–661.

[45] IAEA. Radiation oncology physics: a handbook for teachers and students. Podgorsak EB, editor. Vienna, Austria; 2005.

[46] Devic S. Radiochromic film dosimetry: past, present, and future. Phys Med. 2011;27(3):122–134.

[47] Sorriaux J, Kacperek A, Rossomme S, Lee JA, Bertrand D, Vynckier S, et al. Evaluation of Gafchromic EBT3 films characteristics in therapy photon, electron and proton beams. Phys Med. 2013;29(6):599–606.

[48] Palmer A, Nisbet A, Bradley D. Verification of high dose rate brachytherapy dose distributions with EBT3 Gafchromic film quality control techniques. Phys Med Biol. 2013;58(3):497–511.

[49] Aldelaijan S, Devic S. Comparison of dose response functions for EBT3 model GafChromic film dosimetry system. Phys Med. 2018;49:112–118.

[50] Tomic N, Quintero C, Whiting BR, Aldelaijan S, Bekerat H, Liang L, et al. Characterization of calibration curves and energy dependence GafChromic^{TM} XR-QA2 model based radiochromic film dosimetry system. Med Phys. 2014;41(6):062105.

[51] Devic S, Tomic N, Lewis D. Reference radiochromic film dosimetry: Review of technical aspects. Med Phys. 2016;32(4):541–556.

[52] Micke A, Lewis DF, Yu X. Multichannel film dosimetry with nonuniformity correction. Med Phys. 2011;38(5):2523–2534.

[53] Devic S, Seuntjens J, Sham E, Podgorsak EB, Schmidtlein CR, Kirov AS, et al. Precise radiochromic film dosimetry using a flat-bed document scanner. Med Phys. 2005;32(7):2245–2253.

[54] Devic S, Aldelaijan S, Mohammed H, Tomic N, Liang L, DeBlois F, et al. Absorption Spectra Time Evolution of EBT-2 Model GAFCHROMIC^{TM} Film. Med Phys. 2010;37(5):2207–2214.

[55] Aldelaijan S, Alzorkany F, Moftah B, Buzurovic I, Seuntjens J, Tomic N, et al. Use of a control film piece in radiochromic film dosimetry. Phys Med. 2016;32(1):202–207.

[56] Beaulieu L, Goulet M, Archambault L, Beddar S. Current status of scintillation dosimetry for megavoltage beams. J Phys: Conf Ser. 2013;444:012013.

[57] Beddar AS, Suchowerska N, Law SH. Plastic scintillation dosimetry for radiation therapy: minimizing capture of Cerenkov radiation noise. Phys Med Biol. 2004;49(5):783–790.

[58] Archambault L, Briere TM, Pönisch F, Beaulieu L, Kuban DA, Lee A, et al. Toward a real-time in vivo dosimetry system using plastic scintillation detectors. Int J Radiat Oncol Biol Phys. 2010;78(1):280–287.

[59] Archambault L, Beddar AS, Gingras L, Roy R, Beaulieu L. Measurement accuracy and cerenkov removal for high performance, high spatial resolution scintillation dosimetry. Med Phys. 2006;33(1):128–135.

[60] Therriault-Proulx F, Archambault L, Beaulieu L, Beddar S. Development of a novel multipoint plastic scintillation detector with a single optical transmission line for radiation dose measurement. Phys Med Biol. 2012;57:7417.

[61] Therriault-Proulx F, Beddar S, Beaulieu L. On the use of a single-fiber multipoint plastic scintillation detector for ^{192}Ir high-dose-rate brachytherapy. Phys Med Biol. 2012;40:062101.

[62] Linares Rosales HM, Duguay-Drouin P, Archambault L, Beddar S, Beaulieu L. Optimization of a multipoint plastic scintillator dosimeter for high dose rate brachytherapy. Med Phys. 2019;46(5):2412–2421.

[63] Archambault L, Therriault-Proulx F, Beddar S, Beaulieu L. A mathematical formalism for hyperspectral, multipoint plastic scintillation detectors. Phys Med Biol. 2012;57(21):7133.

[64] Low DA, Harms WB, Mutic S, Purdy JA. A technique for the quantitative evaluation of dose distributions. Med Phys. 1998;25(5):656–661.

[65] Low DA, Dempsey JF. Evaluation of the gamma dose distribution comparison method. Med Phys. 2003;30(9):2455–2464.

[66] Ezzell GA, Burmeister JW, Dogan N, LoSasso TJ, Mechalakos JG, Mihailidis D, et al. IMRT commissioning: multiple institution planning and dosimetry comparisons, a report from AAPM Task Group 119. Med Phys. 2009;36(11):5359–5373.

[67] Yoosuf ABM, Jeevanandam P, Whitten G, Workman G, , McGarry CK. Verification of high-dose-rate brachytherapy treatment planning dose distribution using liquid-filled ionization chamber array. J Contemp Brachytherapy. 2018;10(2):142–154.

[68] Hussein M, Rowshanfarzad P, Ebert MA, Nisbet A, Clark CH. A comparison of the gamma index analysis in various commercial IMRT/VMAT QA systems. Radiother Oncol. 2013;109(3):370–376.

[69] DeWerd LA, Ibbott GS, Meigooni AS, Mitch MG, Rivard MJ, Stump KE, et al. A dosimetric uncertainty analysis for photon-emitting brachytherapy sources: Report of AAPM Task Group No. 138 and GEC-ESTRO. Med Phys. 2011;38(2):782–801.

[70] NUDAT 2.8, National Nuclear Data Center, Brookhaven National Laboratory, Upton, NY, USA;. Last accessed January 29, 2020. https://www.nndc.bnl.gov/nudat2/.

[71] Rivard MJ, Granero D, Perez-Calatayud J, Ballester F. Influence of photon energy spectra from brachytherapy sources on Monte Carlo simulations of kerma and dose rates in water and air. Med Phys. 2005;37(2):869–876.

[72] Ali A, Spencer B, McEwen MR, Rogers DWO. Towards a quantitative, measurement-based estimate of the uncertainty in photon mass attenuation coefficients at radiation therapy energies. Phys Med Biol. 2016;60:1641–1645.

[73] Kirisits C, Rivard MJ, Baltas D, Ballester F, De Brabandere M, van der Laarse R, et al. Review of clinical brachytherapy uncertainties: Analysis guidelines of GEC-ESTRO and the AAPM. Radiother Oncol. 2014;110(1):199–212.

[74] Elfrink RJ, Kolkman-Deurloo IK, van Kleffens HJ. Determination of the accuracy of implant reconstruction and dose delivery in brachytherapy in The Netherlands and Belgium. Radiother Oncol. 2001;59(3):297–306.

[75] Rickey DW, Sasaki D, Bews J. A quality assurance tool for high-dose-rate brachytherapy. Med Phys. 2010;37(6):2525–2532.

[76] Wong TP, Fernando W, Johnston PN, Bubb IF. Transit dose of an Ir-192 high dose rate brachytherapy stepping source. Phys Med Biol. 2001;46(2):323–331.

[77] Awunor O, Berger D, Kirisits C. A multicenter study to quantify systematic variations and associated uncertainties in source positioning with commonly used HDR afterloaders and ring applicators for the treatment of cervical carcinomas. Med Phys. 2015;42(8):4472–4483.

[78] Hrinivich WT, Morcos M, Viswanathan A, Lee J. Automatic tandem and ring reconstruction using MRI for cervical cancer brachytherapy. Med Phys. 2019;46(10):4324–4332.

[79] Tanderup K, Hellebust TP, Lang S, Granfeldt J, Pötter R, Lindegaard JC, et al. Consequences of random and systematic reconstruction uncertainties in 3D image based brachytherapy in cervical cancer. Radiother Oncol. 2008;89(2):156–163.

[80] Arnesen MR, Bruheim K, Malinen E, Hellebust TP. Spatial dosimetric sensitivity of contouring uncertainties in gynecological 3D-based brachytherapy. Radiother Oncol. 2014;113(3):414–419.

[81] Mizowaki T, Cohen GN, Fung AY, Zaider M. Towards integrating functional imaging in the treatment of prostate cancer with radiation: the registration of the MR spectroscopy imaging to ultrasound/CT images and its implementation in treatment planning. Int J Radiat Oncol Biol Phys. 2002;54(5):1558–1564.

[82] Nesvacil N, Tanderup K, Hellebust TP, De Leeuw A, Lang S, Mohamed S, et al. A multicentre comparison of the dosimetric impact of inter- and intra-fractional anatomical variations in fractionated cervix cancer brachytherapy. Radiother Oncol. 2013;107(1):20–25.

Chapter 5

Microdosimetric evaluation of current and alternative brachytherapy sources - a Geant4-DNA simulation study

Abstract

Purpose: Radioisotopes such as ^{75}Se, ^{169}Yb and ^{153}Gd have photon energy spectra and half-lives that make them excellent candidates as alternatives to ^{192}Ir for high dose rate brachytherapy. The aim of this study was to evaluate the relative biological effectiveness (RBE) of current (^{192}Ir, ^{125}I, ^{103}Pd) and alternative (^{75}Se, ^{169}Yb, ^{153}Gd) brachytherapy radionuclides using Monte Carlo simulations of lineal energy distributions.

Materials and methods: Brachytherapy sources (microSelectron v2 [^{192}Ir, ^{75}Se, ^{169}Yb, ^{153}Gd], SelectSeed [^{125}I], and TheraSeed [^{103}Pd]) were placed in the center of a spherical water phantom with a radius of 40 cm using the Geant4 Monte Carlo simulation toolkit. The kinetic energy of all primary, scattered and fluorescence photons interacting in a scoring volume were tallied at various depths from the source. Electron tracks were generated by sampling the photon interaction spectrum, and tracking all the interactions down to 10 eV using the event-by-event capabilities of the Geant4-DNA models. The dose mean lineal energy ($\bar{y}_D$) values were obtained through random sampling of transfer points and overlaying spherical scoring volumes within the associated volume of the tracks. The scoring volume diameter was determined by fitting the $\bar{y}_D$ ratio for ^{125}I to its observed RBE.

Results: $\bar{y}_D$ increased with increasing distance from the source for ^{192}Ir, ^{75}Se, and ^{169}Yb, remained constant for ^{153}Gd and ^{125}I, and decreased for ^{103}Pd. The diameter at which the $\bar{y}_D$ ratio coincided with the RBE of 1.15-1.20 for ^{125}I was $\sim$25 to 40 nm. The RBE (reference 1 MeV photons) at high doses and dose rates for ^{192}Ir, ^{75}Se, ^{169}Yb, ^{153}Gd, ^{125}I, and ^{103}Pd were 1.028-1.034, 1.05-1.07, 1.12-1.15, 1.16-1.21, 1.15-1.20, and 1.17-1.22, respectively.
Conclusions: The radiation quality of the radionuclides under investigation was greater than that of high-energy photons. The present study has provided a set of values to modify the prescription doses for brachytherapy to account for the variation in radiation quality among radionuclides.

5.1 Introduction

5.1.1 Brachytherapy radiation sources

Brachytherapy can be administrated using gamma emitting radionuclides with low energies ($E_{\gamma,avg}$ < 50 keV), intermediate energies (50 keV < $E_{\gamma,avg}$ < 200 keV) or high energies ($E_{\gamma,avg}$ > 200 keV), where $E_{\gamma,avg}$ is the average energy of the emitted gamma spectra [1]. ^{192}Ir is a widely used isotope for high dose rate (HDR) brachytherapy, but has the disadvantage of emitting high-energy gamma radiation, which can negatively affect organs at risk (OARs) outside the target volume and requires the treatment room to be sufficiently shielded.

Recent studies have identified and proposed gamma-emitting radionuclides with lower gamma energies than ^{192}Ir, which can provide radiobiological advantages, optimal depth-dose profiles, sufficient specific activities, acceptable half-lives, low production costs and minimal shielding requirements compared to ^{192}Ir [2, 3]. ^{75}Se has been investigated as an alternative to ^{192}Ir in industrial radiography [4] and in brachytherapy [5], owing to its softer gamma emission spectrum and significantly longer half-life. ^{169}Yb has been proposed as an alternative to ^{125}I for permanent interstitial implants [6–12] and as an alternative to ^{192}Ir for temporary implants [6, 8, 13–15]. ^{153}Gd has theoretically and experimentally been investigated as a radionuclide for use in HDR brachytherapy and intensity modulated brachytherapy [16–18]. ^{75}Se, ^{169}Yb and ^{153}Gd have photon energy spectra and half-lives (Table 7.1) that make them excellent candidates for use as radionuclides in HDR brachytherapy.

Table 5.1: Physical properties of various radionuclides. Range refers to maximum range of secondary electrons.

Radionuclide	Half-life (days)	Mean photon energy (keV)	Maximum photon energy (keV)	Range (mm)
^{192}Ir	73.8	380	1378	6.5
^{75}Se	118.5	210	822	3.4
^{169}Yb	32.0	93	782	3.2
^{153}Gd	240.4	60	172	0.36
^{125}I	59.5	30	35.5	0.02
^{103}Pd	17.0	21	497	1.8

5.1.2 Relative biological effectiveness

Introducing new radiation sources for brachytherapy necessitates investigation of the differences in the biological effect between the new radiation sources relative to the sources already in use for which accumulated clinical data are available. The relative biological effectiveness (RBE) is defined as the ratio between the absorbed dose of a reference radiation, such as 250 kVp X-rays or ^{60}Co γ-rays, and that of a test radiation for a given biological endpoint. The RBE depends on many factors, including the absorbed dose, dose rate, fractionation, radiation quality, biological system, and endpoint.

Currently, an RBE of unity is applied to all photon-emitting sources [19], therefore the value of RBE has been ignored in brachytherapy clinical practice. However, experimental studies and calculations with X-ray sources, low-energy brachytherapy sources and electronic brachytherapy sources have shown that the RBE values vary among radiation sources and can be considerably greater than unity (ranging from 1 to 2.4) for different endpoints such as cell death [20–23], cell inactivation [24], micronuclei formation [25, 23], chromosome aberrations [26], microdosimetric endpoints [27, 7, 28–32], ionization cluster formation [31, 33] and induction of double strand breaks (DSBs) [34, 35]. Thus, the radiobiological effectiveness of the alternative HDR radionuclides could be substantially different from that of conventional high-energy sources (e.g. ^{60}Co, ^{192}Ir).

5.1.3 Evaluation of radiation quality using microdosimetry

Microdosimetry has been developed and used extensively to characterize radiation quality in radiation therapy and radiation protection [19]. Lineal energy (y) is a stochastic quantity describing the distribution of energy deposited by ionizing particle tracks in a microscopic region or domain. It is defined as the ratio of the energy imparted in a scoring volume and the mean chord length ($\bar{l}$) of the scoring volume [36]. The dose mean lineal energy ($\bar{y}_D$), the mean value of the lineal energy dose distribution, is a recommended quantity for the evaluation of biological effectiveness [37, 38]. In particular, the $\bar{y}_D$ in a volume of $\sim$10 nm was shown to be related to the RBE of various beam qualities at clinically relevant doses and dose rates [39–43].

5.1.4 Objectives

The aim of the present study was to evaluate the RBE of brachytherapy radionuclides ^{192}Ir, ^{75}Se, ^{169}Yb, ^{153}Gd, ^{125}I, and ^{103}Pd, using a combination of Monte Carlo track structure (MCTS) simulations and microdosimetry techniques.

5.2 Materials and methods

Monte Carlo simulations were performed in a two-step process using the Geant4 [44, 45] toolkit, version 10.2 (patch 02). In the first simulation, the photon interaction spectrum was determined as a function of depth for each source. In the second simulation, electron tracks were generated by sampling the interaction spectrum using the event-by-event capabilities of Geant4-DNA [46, 47]. The lineal energy distributions were then determined for each set of tracks by superimposing scoring spheres onto the electron tracks. The details of each simulation are described in the following sections (Table A.1).

5.2.1 Simulation of photon interaction spectrum

Brachytherapy sources (^{192}Ir, ^{75}Se, ^{169}Yb, ^{153}Gd, ^{125}I, ^{103}Pd) were placed in the center of a spherical water phantom with a radius of 40 cm. The ^{192}Ir, ^{75}Se, ^{169}Yb and ^{153}Gd sources were modelled according to the microSelectron v2 HDR source model (Elekta Brachytherapy, Stockholm, Sweden) [48]. The ^{125}I source was modelled according to the SelectSeed 130.002 source model (Elekta Brachytherapy, Stockholm, Sweden) [49]. The ^{103}Pd source was modeled according to the TheraSeed 200 source model (Theragenics Co., Buford, GA, USA) [50]. The 1-MeV monoenergetic photon source (surrogate for ^{60}Co) was simulated as an isotropic point source. The Geant4-DNA processes are only valid for photons and electrons with energies $\leq$1 MeV. The radioactive decay for brachytherapy sources was determined by explicit simulation of nuclear decay. Photons were tracked using the standard Livermore physics list with atomic deexcitation activated. The prestep kinetic energy of all primary, scattered, and fluorescence photons interacting in spherical shells, placed at a radial distance of 1, 3, 5, 10, and 15 cm from the source, were tallied. The shells had a thickness equivalent to the maximum continuous-slowing-down approximation range of the secondary electrons (Table 7.1). Electrons were not tracked during this phase. The schematic setup of the simulation and the geometry of the sources are presented in Figure 5.1. A minimum of 10^8 photon histories was simulated for each radiation source to ensure that the statistical uncertainty in each energy bin was <0.3% of the highest gamma peak.

5.2.2 Generation of electron tracks

In the next simulation, 10^4 electron tracks were generated by sampling the photon interaction spectrum and tracking all the interactions after the initial Compton or photoelectric interaction using the MCTS code Geant4-DNA. In this step, the source was simulated as a point source in an infinitely large water phantom. All electrons were tracked down to 10 eV, at which point their energy was deposited locally. All secondary photons, including fluorescent photons, were killed. Atomic deexcitation was activated to simulate Meitner-Auger electron emission.

5.2.3 Calculation of microdosimetric quantities

Lineal energy distributions were calculated for various radionuclides at radial distances of 1, 3, 5, 10, and 15 cm from the source, using spherical scoring volumes with diameters of 2 to 100 nm. The radii were chosen to cover a range of depths relevant to brachytherapy. The weighted sampling algorithm and scoring of $\bar{y}_D$ have been previously described in detail [51]. In brief, the method consists of randomly sampling energy deposition points and overlaying scoring volumes within the associated volume of the track. Each of the 10^4 tracks was sampled $\geq 10^3$ times to obtain standard errors of $\leq$0.1% for all the sources and scoring volumes investigated. The dose mean lineal energy ratios $\bar{y}_{D,X}/\bar{y}_{D,\gamma}$, where the subscript X represents the test radiation, were tallied at 1-cm depth using 1-MeV photons as the reference radiation. The scoring volume diameter, which was used to calculate the RBE, was determined by fitting the $\bar{y}_D$-ratio for ^{125}I to its observed RBE.

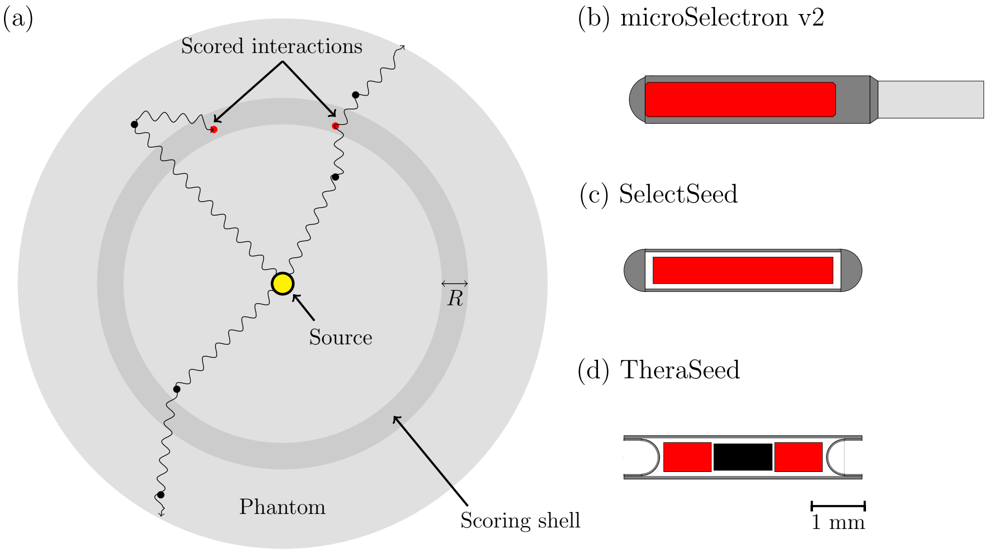

Figure 5.1: (a) Representation of brachytherapy source simulated in the center of a water phantom with a radius of 40 cm. The prestep kinetic energy of the photons at the interaction points within the scoring shell (dark shaded area) were tallied (red points), and those occurring outside the shell (light shaded area) were not (black points). The shell had a thickness equivalent to the maximum continuous-slowing-down approximation range (R) of the secondary electrons (Table 7.1). The cross-sections of the (b) microSelectron v2, (c) SelectSeed, and (d) TheraSeed source models are shown. Sources drawn to scale.

5.3 Results

The photon interaction spectra for ^{192}Ir, ^{75}Se, ^{169}Yb, ^{153}Gd, ^{125}I, and ^{103}Pd sources are presented in Figure 5.2, for a range of depths in water ($\leq$15 cm from the source). Although the photon interaction events for these radiation sources were largely dominated by primary photons near the source, the number of scattered photons that interacted within a volume increased with an increasing distance from the source. For ^{192}Ir, ^{75}Se, ^{169}Yb, and ^{153}Gd, this resulted in a lower average photon energy for the interaction events as the depth from the source increased. For ^{125}I, the average photon energy was about 28 keV over all depths. For ^{103}Pd, the contribution of higher-energy scattered photons (>25 keV) to the absorbed dose increased with depth at distances >5 cm.

The $\bar{y}_D$ values for the brachytherapy sources under investigation are presented as a function of depth from the source in Figure 5.3 for spherical scoring volume diameters of 2 nm, 10 nm, 40 nm, and 100 nm. In general, the $\bar{y}_D$ increased with an increasing distance from the

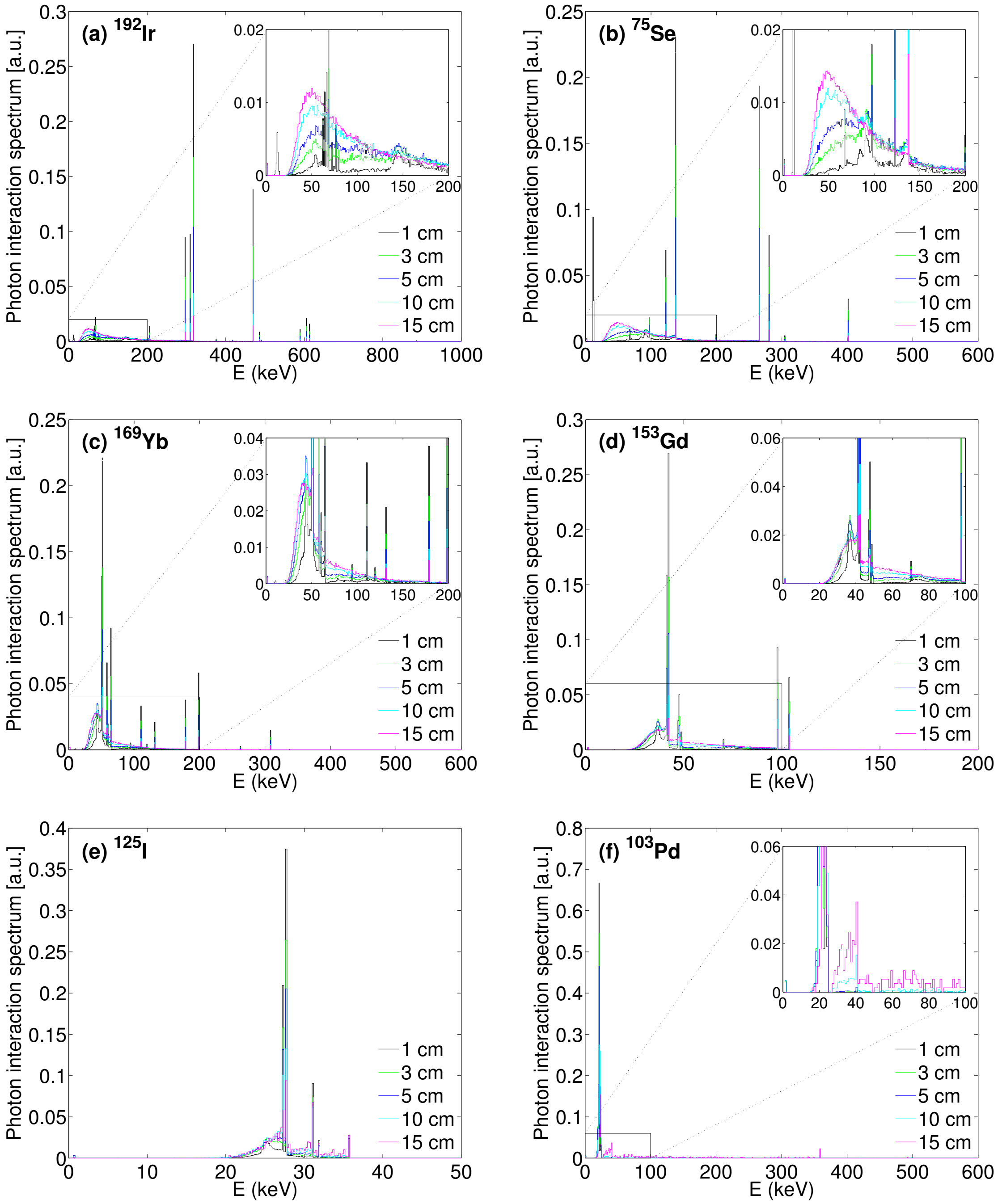

Figure 5.2: Photon interaction spectra at several radial distances from the source for (a) ^{192}Ir, (b) ^{75}Se, (c) ^{169}Yb, (d) ^{153}Gd, (e) ^{125}I, and (f) ^{103}Pd.

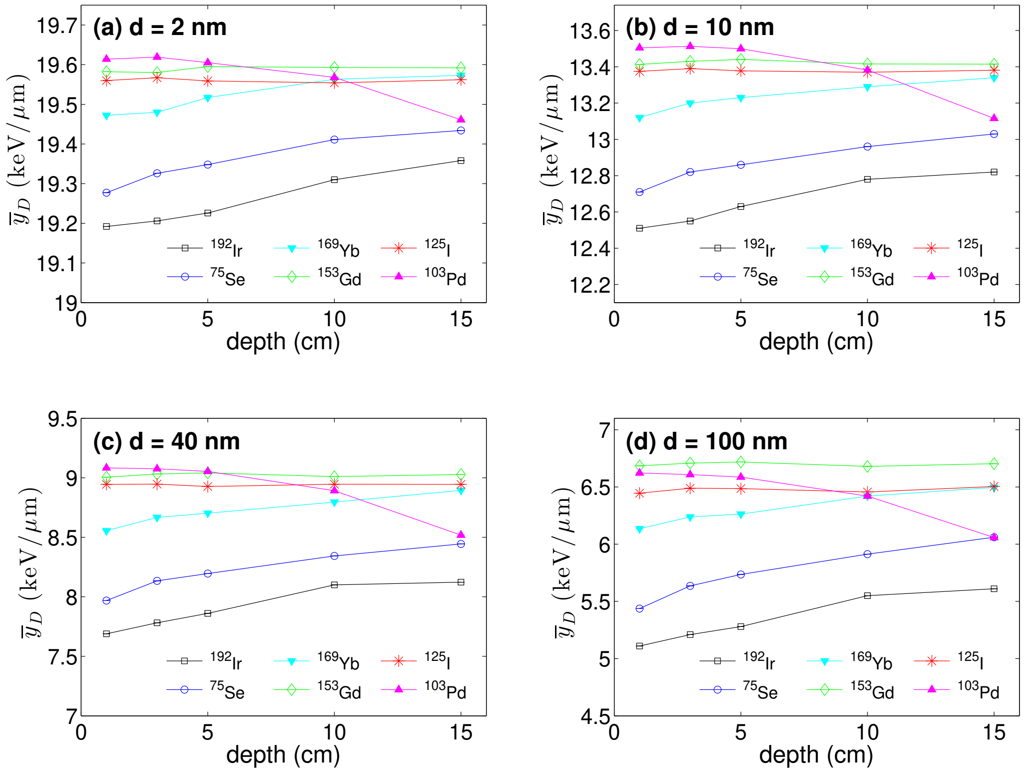

Figure 5.3: Dose mean lineal energy $\bar{y}_D$, calculated using (a) 2-nm, (b) 10-nm, (c) 40-nm, and (d) 100-nm spherical sites, at several radial distances from the source for various brachytherapy sources. The lines joining the successive points serve only as a guide to the eye.

source. For ^{192}Ir, ^{75}Se, and ^{169}Yb, the $\bar{y}_D$ increased by as much as 1%, 2%, 6%, and 10% for 2-, 10-, 40-, and 100-nm spherical sites, respectively, in the distance range of 1 to 15 cm. The $\bar{y}_D$ was relatively constant with depth (<1% variation) for ^{153}Gd and ^{125}I. The $\bar{y}_D$ decreased at distances >5 cm for ^{103}Pd.

The dose mean lineal energy ratios $\bar{y}_{D,X}/\bar{y}_{D,\gamma}$ for the sources are shown as a function of spherical diameter in Figure 5.4. For a given radionuclide, the $\bar{y}_D$ ratio increased with larger scoring volume sites. The $\bar{y}_D$ ratio for the 25- to 40-nm size volumes coincided with the experimentally determined RBE of 1.15-1.20 for ^{125}I [52]. The RBE of the various radionuclides, based on the $\bar{y}_D$ ratios in 25- to 40-nm scoring volumes, is presented in table 5.2.

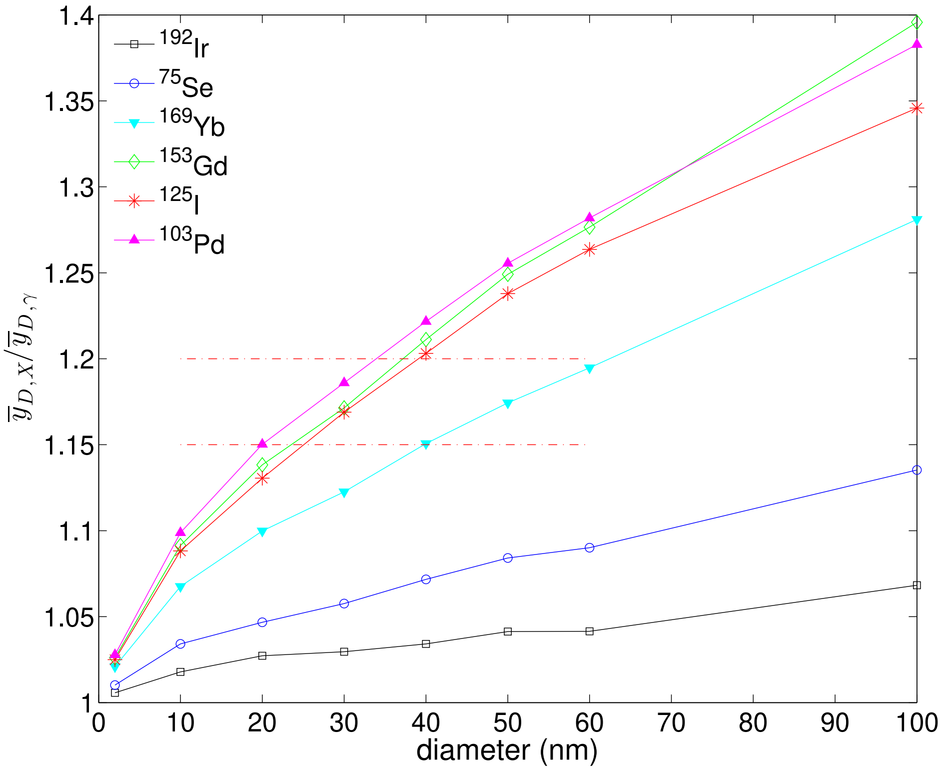

Figure 5.4: Dose mean lineal energy ratios $\bar{y}_{D,X}/\bar{y}_{D,\gamma}$ at different simulated spherical site diameters for various brachytherapy sources at 1-cm depth. The reference value refers to 1-MeV photons. The lines joining successive points serve only as a guide to the eye. The red dash-dotted lines correspond to the RBE range for ^{125}I.

5.4 Discussion

Simulations of the spatial patterns of energy deposition through MCTS simulations can provide insight into the RBE differences observed between different radiation sources. It has been suggested that biological effects result from clusters of energy deposition sites occurring close to or within the DNA molecule [53]. It is, therefore, of interest to study the energy deposition patterns in sites comparable to the size of DNA structures, such as DNA segments (∼2 nm), nucleosomes (∼10 nm), and chromatin fibres (∼30 nm). In the present study, the dose mean lineal energy values in nanometer-size targets were used to characterize the radiation quality of various radionuclides.

Table 5.2: Estimated relative biological effectiveness (RBE) of various radionuclides with 1-MeV photons and ^{192}Ir as reference radiation. Data presented as mean (range); range reflects the uncertainty in the high dose rate RBE for ^{125}I used to determine the diameter of the scoring volumes to calculate the dose mean lineal energy ratios.

Radionuclide	RBE	
	vs. 1 MeV photons	vs. ^{192}Ir
^{192}Ir	1.031 (1.028-1.034)	1.00
^{75}Se	1.062 (1.053-1.072)	1.032 (1.024-1.039)
^{169}Yb	1.134 (1.116-1.151)	1.101 (1.088-1.113)
^{153}Gd	1.184 (1.156-1.211)	1.148 (1.125-1.171)
^{125}I	1.176 (1.150-1.203)	1.144 (1.119-1.163)
^{103}Pd	1.195 (1.168-1.222)	1.159 (1.136-1.181)

For the high- and intermediate-energy brachytherapy sources, lineal energy tends to increase with depth from the source, because the contribution of scattered photons to dose deposition increases with distance from the source. This trend was not observed in a previous study [7] for ^{192}Ir and ^{169}Yb using micrometer-size volumes, although the uncertainties were too large to discern any patterns. On the other hand, for low energy sources such as ^{125}I, the radiation quality does not vary with the distance from the source owing to a lack of scattered photons, because the photoelectric effect dominates at these energies. This insensitivity of radiation quality with depth is in agreement with previous studies [31, 32, 54] for ^{125}I using 1-μm scoring volumes. Although ^{103}Pd is a low-energy source, it contains 3 minor high-energy gamma peaks at 295, 357, and 497 keV. Because the contribution of these higher energy photons to the dose is more important at >5 cm of depth, the lineal energy decreases at larger distances, in agreement with a previous study [54]. Overall, the trends seen for nanometer-size targets reproduced the measured and simulated trends obtained using micrometer-size volumes.

As photon energy decreases, the lineal energy generally increases. However, the $\bar{y}_D$ of ^{153}Gd is greater than that of ^{125}I, although the average photon energy decreases from 60 keV for ^{153}Gd to 28 keV for ^{125}I. While a softer spectrum would typically result in greater lineal energy, this is not the case in the 20 to 60 keV range [55, 35]. As photon energy decreases from 60 keV to 20 keV, the kinetic energy of the photoelectrons and Compton electrons also decreases. However, the proportion of photoelectrons increases, since the photoelectric cross-section is higher at lower energies. The overall effect is that the mean energy of the recoil electrons actually increases, because the photoelectrons tend to have higher kinetic energies. Consequently,

$\bar{y}_D$ decreases with decreasing photon energy in this energy range. An intermediate-energy brachytherapy source such as ^{153}Gd can therefore be expected to be at least as biologically effective as a low-energy source such as ^{125}I and to have an ideal radial dose function, similar to that of ^{192}Ir, for HDR brachytherapy applications [16].

Various computational and experimental studies [39–43] concluded that the dose mean lineal energy $\bar{y}_D$ in a volume of $\sim$10 nm was approximately proportional to the clinical RBE in fractionated radiation therapy for low linear energy transfer beams. However, the characteristic volume depends largely on the electron ionization, excitation, and elastic scattering models, which can differ considerably among MCTS codes [51]. We have included a low-energy source (^{125}I) in the present study owing to the substantial radiobiological data available to determine the sensitive volume that matches the $\bar{y}_D$ ratios to the clinical RBE values. The review by Scalliet and Wambersie [52] reported that RBE values for ^{125}I in the 1.15-1.20 range were, in general, observed for high doses and high-dose rates for different biological systems and endpoints. In the present study, the $\bar{y}_D$ ratio in the 25- to 40-nm volumes coincided with the experimentally determined RBE of 1.15-1.20 for ^{125}I. It is, therefore, expected that the results for 25- to 40-nm volumes can be used to evaluate the biological effectiveness for the sources with intermediate energies. Using the $\bar{y}_D$ values at 25 to 40 nm, the RBE for ^{192}Ir, ^{75}Se, ^{169}Yb, ^{153}Gd, ^{125}I, and ^{103}Pd sources was 1.028-1.034, 1.05-1.07, 1.12-1.15, 1.16-1.21, 1.15-1.20, and 1.17-1.22, respectively. Therefore, we expect that the ^{75}Se, ^{169}Yb, and ^{153}Gd sources would be 3%, 10%, and 15% more biologically effective than the current ^{192}Ir sources. Additional radiobiological data are needed to confirm these findings.

Prescription doses for HDR brachytherapy can vary substantially based on the type and severity of the disease, goal of treatment (boost vs. monotherapy), treatment site, risk group, patient geometry, radiation source, biochemistry test results, genetic factors, and so forth. The dose prescribed to individual patients is primarily a clinical decision and ideally should be established through clinical trials and confirmed by treatment outcome analysis. Typically, the prescribed dose will be limited such that the dose-volume constraints to organs at risk (OARs) are strictly met. These dose-volume constraints are carefully established from an accumulation of treatment outcome studies to avoid radiation-induced toxicity. If the prescribed dose is modified according to the ratios of the RBE values among different sources, this will ensure that the same biological effect is achieved [3]. For the currently used ^{192}Ir sources, an RBE of unity is applied, and the variation in radiation quality with depth is, in effect, ignored. To achieve the same biological effects with ^{75}Se, ^{169}Yb, or ^{153}Gd, one can simply use the effective clinical RBE values to modify the dose prescription. Alternatively, because radiation quality can vary by a few percentage points with distance, one can assign a weighting factor, variable with depth, to each voxel and calculate an RBE-weighted dose (RBE × dose) map. Regardless, if the current ^{192}Ir sources are eventually replaced with the alternative radionuclides under investigation, we believe the prescription doses for brachytherapy should be reduced to account for the changes in radiation quality.

In general, it has been assumed that the clinical RBE expresses the weighting of the dose to strive for the same biological effects when changing from one radiation quality to another. However, factors other than the clinical RBE can influence the achievable target dose, such as the dose distribution. If a given radiation quality provides a higher RBE-weighted dose to the OAR that exceeds the desired limits, the target dose may need to be reduced accordingly to ensure that the OAR constraints are met. Nevertheless, the dose distribution in water for high- and intermediate-energy brachytherapy sources is largely governed by the inverse-square law; thus, the effect of the dose distribution was not considered in the present study.

The RBE values provided for high doses and dose rates only accounted for differences in radiation quality. To assess the overall RBE for different irradiation conditions, one must account for the differences in the dose rate, total dose, fractionation, overall time, cell type, and biological endpoint using a metric such as the biologically effective dose, which is determined using linear-quadratic formalism [56]. The RBE values in the present study should be adjusted according to the biologically effective dose ratios to determine the overall RBE for a given set of irradiation conditions.

The method used in the present study consisted of randomly sampling a set of pregenerated particle tracks for a given photon interaction spectrum. Producing lineal energy distributions directly using track structure simulations and track sampling algorithms would eliminate the need to combine a data set of energy dependent $\bar{y}_D(E)$ for monoenergetic electrons (which must typically be interpolated for calculation purposes) with particle fluences or dose profiles. Directly simulating the particle tracks reduces the uncertainties related to the interpolation of values for various energies and scoring volumes. We suggest that tracks should be directly simulated in future microdosimetric studies using the most recent physics models and cross-sections available in the MCTS codes.

5.5 Conclusions

The radiation quality for current and alternative brachytherapy sources was evaluated by comparing the dose mean lineal energy values in nanometer-size volumes. The RBE of ^{192}Ir,

^{75}Se, ^{169}Yb, ^{153}Gd, ^{125}I, and ^{103}Pd was considerably greater than that of high-energy photons. Our results have provided a set of preliminary values to use as a guideline if the clinical dose prescriptions will eventually be modified to account for the RBE variations among radionuclides.

Acknowledgements: The authors would like to acknowledge support from the Natural Sciences and Engineering Research Council (NSERC) Discovery Grant (number 241018), Simone and Morris Fast Award for Oncology and NSERC CREATE Medical Physics Research Training Network Grant (number 432290).

Conflict of interest: None.

Supplementary material: Supplementary material for this article can be found in Appendix A.

References

[1] Beaulieu L, Carlsson Tedgren A, Carrier JF, Davis SD, Mourtada F, Rivard MJ, et al. Report of the Task Group 186 on model-based dose calculation methodsbin brachytherapy beyond the TG-43 formalism: current status and recommendations for clinical implementation. Med Phys. 2012;39(10):6208–6236.

[2] Meigooni AS, Nath R. A comparison of radial dose functions for 103Pd, 125I, 145Sm, 241Am, 169Yb, 192Ir, and 137Cs brachytherapy sources. Int J Radiat Oncol Biol Phys. 1992;22(5):1125–1130.

[3] Nath R, Rivard MJ, DeWerd LA, Dezarn WA, II HTH, Ibbott GS, et al. Guidelines by the AAPM and GEC-ESTRO on the use of innovative brachytherapy devices and applications: Report of Task Group 167. Med Phys. 2016;43(6):3178–3205.

[4] Grimm R, Kaftal T. Gamma radiography using selenium-75. Insight. 1996;38(9).

[5] Weeks KJ, Schulz RJ. Selenium-75: A potential source for use in high-activity brachytherapy irradiators. Med Phys. 1986;13(5):728–731.

[6] Mason DL, Battista JJ, Barnett RB, Porter AT. Ytterbium-169: calculated physical properties of a new radiation source for brachytherapy. Med Phys. 1992;19(3):695–703.

[7] Zellmer DL, Gillin MT, Wilson JF. Microdosimetric single event spectra of ytterbium-169 compared with commonly used brachytherapy sources and teletherapy beams. Radiat Res. 1992;23(3):627–632.

[8] Loft SM, Coles IP, Dale RG. The potential of ytterbium 169 in brachytherapy: A brief physical and radiobiological assessment. Br J Radiol. 1992;65:252–257.

[9] Piermattei A, Azario L, Rossi G, Soriano A, Arcovito G, Ragona R, et al. Dosimetry of ^{169}Yb seed model X1267. Phys Med Biol. 1995;40:1317–1330.

[10] MacPherson MS, Battista JJ. Radioactivity measurements of ytterbium-169 brachytherapy sources. Australas Phys Eng Sci Med. 1998;21(1):18–23.

[11] Leonard KL, DiPetrillo TA, Munro JJ, Wazer DE. A novel ytterbium-169 brachytherapy source and delivery system for use in conjunction with minimally invasive wedge resection of early-stage lung cancer. Brachytherapy. 2011;10:163–169.

[12] Currier B, Munro III JJ, Medich DC. Dosimetric characterization of the GammaClip$^{\text{TM}}$ ^{169}Yb low dose rate permanent implant brachytherapy source for the treatment of nonsmall cell lung cancer postwedge resection. Med Phys. 2013;40(8):080701.

[13] Lymperopoulou G, Papagiannis P, Sakelliou L, Milickovic N, Gianoulli S, Baltas D. A dosimetric comparison of 169Yb versus 192Ir for HDR prostate brachytherapy. Med Phys. 2005;32(12):3832–3842.

[14] Lymperopoulou G, Papagiannis P, Angelopoulos A, Karaiskos P, Georgiou E, Baltas D. A dosimetric comparison of ^{169}Yb and ^{192}Ir for HDR brachytherapy of the breast, accounting for the effect of finite patient dimensions and tissue inhomogeneities. Med Phys. 2006;33(12):4583–4589.

[15] Papagiannis P, Karaiskos P, Giorgiou E, Baltas D, Lymperopoulou G, Pantelis E, et al. On the use of high dose rate 192Ir and 169Yb sources with the MammoSite radiation therapy system. Med Phys. 2007;34(9):3614–3619.

[16] Enger SA, Fisher DR, Flynn RT. Gadolinium-153 as a brachytherapy source. Phys Med Biol. 2013;58(4):957–964.

[17] Adams QE, Xu J, Breitbach EK, Enger SA, Rockey WR, Kim Y, et al. Interstitial rotating shield brachytherapy for prostate cancer. Med Phys. 2014;41(5):051703.

[18] Famulari G, Urlich T, Armstrong A, Enger SA. Practical aspects of ^{153}Gd as a radioactive source for use in brachytherapy. Appl Radiat Isot. 2017;130:131–139.

[19] ICRP. The 2007 recommendations of the International Commission on Radiological Protection. ICRP publication 103. Ann ICRP. 2007;37(2-4):1–332.

[20] Barendsen GW, Walter HMD. Effect of different ionizing radiations on human cells in tissue cultures. III. Experiments with cyclotron accelerated particles and deuterons. Radiat Res. 1963;18:106–119.

[21] Zeitz L, Kim SH, Kim JH, Detko JF. Determination of RBE of soft x-rays. Radiat Res. 1977;70:552–563.

[22] Freeman M, Goldhagen H, Sierra E, Hall EJ. Studies with encapsulated ^{125}I sources: determination of the RBE using cultured mammalian cells. Int J Radiol Biol Phys. 1982;8:1355–1361.

[23] Lehnert A, Lessman E, Pawelke J, Dörr W. RBE of 25 kV x-rays for the survival and induction of micronuclei in the human mammary epithelial cell line MCF 12-A. Radiat Environ Biophys. 2006;45:253–260.

[24] Wambersie A, Dutreix J. Problèmes dosimétriques posés par la détermination de l'EBR dans un large domaine d'énergie. Biophysical Aspects of Radiation Quality. 1971;p. 261–272.

[25] Kwan DK, Kagan AR, Norman A. RBE of iode 125 in the induction of micronuclei in human peripheral blood lymphocytes. Radiother Oncol. 1985;4:163–166.

[26] Hill MA. The variation in biological effectiveness of low energy x-rays and gamma rays with energy. Radiat Prot Dosimetry. 2008;112:471–481.

[27] McDonald JC, Ma I, Zeitz L. Microdosimetric properties of encapsulated ^{125}I and other photon sources. Radiat Res. 1979;77:221–232.

[28] Wuu CS, Kliauga P, , Zaider M, Amols HI. Microdosimetric evaluation of relative biological effectiveness for ^{103}Pd, ^{125}I, ^{241}Am, and ^{192}Ir brachytherapy sources. Int J Radiat Oncol Biol Phys. 1996;36(3):689–697.

[29] Wuu CS, Zaider M. A calculation of the relative biological effectiveness of ^{125}I and ^{103}Pd brachytherapy sources using the concept of proximity function. Med Phys. 1998;25:2186–2189.

[30] Brenner DJ, Leu CS, Beatty JF, Shefer RE. Clinical relative biological effectiveness of low-energy x-rays emitted by miniature x-ray devices. Phys Med Biol. 1999;44:323–333.

[31] Reniers B, Vynckier S, Verhaegen F. Theoretical analysis of microdosimetric spectra and cluster formation for ^{103}Pd and 125I emitters. Phys Med Biol. 2004;49:3781–3795.

[32] Wuu CS, Chen J. Calculated microdosimetric characteristics of ^{125}I and ^{103}Pd brachytherapy seeds at different depths in water. Radiat Prot Dosimetry. 2006;122(1-4):506–508.

[33] Villegas F, Tilly N, Bäckström G, Ahnesjö A. Cluster pattern analysis of energy deposition sites for the brachytherapy sources ^{103}Pd, ^{125}I, ^{192}Ir, ^{137}Cs, and ^{60}Co. Phys Med Biol. 2014;59(18):5531–5543.

[34] Hsaio Y, Stewart RD. Monte Carlo simulation of DNA damage induction by X-rays and selected radioisotopes. Phys Med Biol. 2008;53(1):233–244.

[35] White SA, Reniers B, De Jong EEC, Rusch T, Verhaegen F. A comparison of the relative biological effectiveness of low energy electronic brachytherapy sources in breast tissue: a Monte Carlo study. Phys Med Biol. 2016;61:383–399.

[36] ICRU. Microdosimetry. vol. ICRU Report 36. Bethesda, MD: International Commission on Radiation Units & Measurements; 1983.

[37] Kellerer AM, Rossi HH. The theory of dual radiation action. Curr Top Radiat Res Q. 1972;8:85–158.

[38] Lindborg L, Nikjoo H. Microdosimetry and radiation quality determinations in radiation protection and radiation therapy. Radiat Prot Dosimetry. 2011;143(2-4):402–408.

[39] Grindborg JE, Olko P. A comparison of measured and calculated yD-values in the nanometre region for photon beams in dosimetry: an interdisciplinary approach. In: Goodhead DT, O'Neill P, Menzel HG, editors. 12th Symp. on Microdosimetry. Cornwall: Hartnolls Ltd; 1997. p. 387–390.

[40] Lindborg L, Grindborg JE. Nanodosimetry results and radiotherapy beams: a clinical application? Radiat Prot Dosimetry. 1997;70(1-4):541–546.

[41] Lillhök JE, Grindborg JE, Lindborg L, Gudowska I, Alm Carlsson G, Söderberg J, et al. Nanodosimetry in a clinical neutron therapy beam using the variance-covariance method and Monte Carlo simulation. Phys Med Biol. 2007;52(16):4953–4966.

[42] Lindborg L, Hultqvist M, Tedgren AC, Nikjoo H. Lineal energy and radiation quality in radiation therapy: model calculations and comparison with experiment. Phys Med Biol. 2013;58(1):3089–3105.

[43] Lindborg L, Hultqvist M, Tedgren AC, Nikjoo H. Nanodosimetry and RBE values in radiotherapy. Radiat Prot Dosimetry. 2015;166(1-4):339–342.

[44] Agostinelli S, Allison J, al Amako K, Apostolakis J, Araujo H, Arce P, et al. Geant4 - a simulation toolkit. Nucl Inst Meth Phys Res A. 2003;506(3):250–303.

[45] Allison J, Amako K, Apostolakis J, Araujo H, Dubois PA, Asai M, et al. Geant4 developments and applications. IEEE Trans Nucl Sci. 2006;53(1):270–278.

[46] Incerti S, Baldacchino G, Bernal M, Capra R, Champion C, Francis Z, et al. The Geant4-DNA project. Int J Model Simul Sci Comput. 2010;1:157–178.

[47] Bernal MA, Bordage MC, Brown JMC, Davídková M, Delage E, Bitar ZE, et al. Track structure modeling in liquid water: a review of the Geant4-DNA very low energy extension of the Geant4 Monte Carlo simulation toolkit. Phys Med. 2015;31:861–874.

[48] Daskalov GM. Monte Carlo-aided dosimetry of a new high dose-rate brachytherapy source. Med Phys. 1998;25:2200–2208.

[49] Karaiskos P, Papagiannis P, Sakelliou L, Anagnostopoulos G, Baltas D. Monte Carlo dosimetry of the selectSeed ^{125}I interstitial brachytherapy seed. Med Phys. 2001;28:1753–1760.

[50] Monroe JI, Williamson JF. Monte Carlo-aided dosimetry of the Theragenics TheraSeed Model 200 ^{103}Pd interstitial brachytherapy seed. Med Phys. 2002;29:609–621.

[51] Famulari G, Pater P, Enger SA. Microdosimetry calculations for monoenergetic electrons using Geant4-DNA combined with a weighted track sampling algorithm. Phys Med Biol. 2017;62:4295–5508.

[52] Scalliett P, Wambersie A. Which RBE for iodine 125 for clinical application. Radiother Oncol. 1987;9:221–230.

[53] Goodhead DT, Thacker J, Cox R. Effects of radiations of different qualities on cells: molecular mechanisms of damage and repair. Int J Radiat Biol. 1993;63:543–556.

[54] Reniers B, Verhaegen F. Microdosimetry of low-energy photons in radiotherapy. Radiat Prot Dosimetry. 2006;122(1-4):401–403.

[55] Shani G. Radiation Dosimetry: Instrumentation and Methods. 2nd ed. CRC Press; 2001.

[56] Fowler J. A review: The linear-quadratic formula and progress in fractionated radiotherapy. Br J Radiol. 1989;62(740):679–694.

Chapter 6

RapidBrachyMCTPS: a Monte Carlo-based treatment planning system for brachytherapy applications

Abstract

Despite being considered the gold standard for brachytherapy dosimetry, Monte Carlo (MC) has yet to be implemented into a software for brachytherapy treatment planning. The purpose of this work is to present RapidBrachyMCTPS, a novel treatment planning system (TPS) for brachytherapy applications equipped with a graphical user interface (GUI), optimization tools and a Geant4-based MC dose calculation engine, RapidBrachyMC. Brachytherapy sources and applicators were implemented in RapidBrachyMC and made available to the user via a source and applicator library in the GUI. To benchmark RapidBrachyMC, TG-43 parameters were calculated for the microSelectron v2 (^{192}Ir) and SelectSeed (^{125}I) source models and were compared against previously validated MC brachytherapy codes. The performance of RapidBrachyMC was evaluated for a prostate HDR case. To assess the accuracy of RapidBrachyMC in a heterogeneous setup, dose distributions with a cylindrical shielded/unshielded applicator were validated against film measurements in a Solid Water$^{\text{TM}}$ phantom. TG-43 parameters calculated using RapidBrachyMC generally agreed within 1%-2% of the results obtained in previously published work. For the prostate case, clinical dosimetric indices showed general agreement with Oncentra TPS within 1%. Simulation times were on the order of minutes on a single core to achieve uncertainties below 2% in voxels within the prostate. The calculation

time was decreased further using the multithreading features of Geant4. In the comparison between MC-calculated and film-measured dose distributions, at least 95% of points passed the 3%/3 mm gamma index criteria in all but one case. RapidBrachyMCTPS can be used as a post-implant dosimetry toolkit, as well as for MC-based brachytherapy treatment planning. This software is especially well suited for the development of new source and applicator models.

6.1 Introduction

Brachytherapy is a radiation therapy modality whereby sealed radioactive sources are placed within or close to the tumour. The seeds can be implanted either temporarily in the case of high dose rate (HDR) remote afterloading brachytherapy or permanently in the case of low dose rate (LDR) brachytherapy. Dosimetry plans in brachytherapy are routinely calculated according to the original [1] or updated [2] Task Group 43 (TG-43 or TG-43U1) formalism by the American Association of Physicists in Medicine (AAPM). This formalism assumes that the patient consists entirely of water with uniform mass density (0.998 g cm^{-3}). In this protocol, dose distributions around a seed are calculated in large phantoms providing sufficient scattering conditions (15 cm radius sphere for LDR sources, 40 cm radius sphere for HDR sources) and superimposed onto the patient geometry at each dwell position. The TG-43 formalism ignores important factors that can impact dose distributions, such as tissue and applicator heterogeneities (elemental composition and density), finite patient dimensions and interseed attenuation.

Recent studies have shown that clinical dose parameters can be over- or under-estimated using the TG-43 formalism. Several studies [3–7] have reported differences in PTV D_{90} between 2%-13% for prostate and 4%-35% for breast LDR brachytherapy. White et al. [8] reported differences in PTV D_{90} between 4%-40% for accelerated partial breast irradiation. Dose to critical structures were over- or under-estimated by up to 15% for esophageal [9], 10% for breast [10], and 23% for endorectal [11] HDR brachytherapy.

Model-based dose calculation algorithms (MBDCAs), such as the collapsed cone convolution superposition (CCS) method [12–14], grid-based Boltzmann solver (GBBS) [15, 16] and Monte Carlo (MC) methods [17], have been developed to provide more accurate dosimetry for brachytherapy applications. The AAPM Task Group 186 (TG-186) [18] provides guidance on the use of MBDCAs for brachytherapy dose calculations.

Front end MC software tools compatible with the DICOM-RT file format have been presented in the literature, such as BrachyGUI [19], based on PTRAN_CT [20], ALGEBRA [21], based on Geant4 [22, 23], BrachyDose [24] and egs_brachy [25], based on EGSnrc [26, 27], and

AMIGOBrachy [28] and BrachyGUIDE [29], based on MCNP [30]. These software packages are used in retrospective post-implant brachytherapy dosimetry studies. To our knowledge, MC-based treatment planning systems (TPSs) are not currently available to the brachytherapy community.

The purpose of the present study is to introduce RapidBrachyMCTPS, a novel and comprehensive MC-based TPS for brachytherapy applications. RapidBrachyMCTPS is equipped with a graphical user interface (GUI), optimization tools and a MC-based dose calculation engine, RapidBrachyMC, that takes into account various heterogeneities (tissue, source, applicator, shield) present in brachytherapy dosimetry. RapidBrachyMC is based on Geant4 and was specifically designed as a tool for the development of new source and applicator models. While other softwares contain a limited list of existing radionuclides with the emission spectra hard coded, RapidBrachyMC has the capability to investigate new radionuclides for brachytherapy applications without exception. There is no hard coding in RapidBrachyMC and the user does not need to be familiar with Geant4 or programming. The simulations are run through the interactive GUI of RapidBrachyMCTPS. The dose calculation engine of RapidBrachyMCTPS was validated against other MC codes and measurements.

6.2 Materials and methods

6.2.1 RapidBrachyMCTPS software

RapidBrachyMCTPS runs through a comprehensive GUI. The GUI is used to display the patient DICOM-RT data, and outline the brachytherapy catheters. The DICOM-RT image data and structure set are imported and scaled using the Visualization ToolKit (VTK) Grassroots DICOM (GDCM) data reader. The contours are drawn onto the slice views. A user-specified density and material table is required in order to convert the Hounsfield unit (HU) in the patient CT-based DICOM-RT image set to mass density and material for each voxel. This file is unique per CT scanner. Mass densities are interpolated using linear interpolation. From the GUI, the user is given several options to segment the patient data. The mass density and material assignment can be performed voxel-by-voxel via the HU-to-density curve described above. The segmentation can also be performed based on the patient's structure set. The user may override the mass density and material information from the HU-to-density curve and assign a uniform mass density and material in a structure. For this to take place, the structures are sorted from largest volume to smallest, so that material overrides applied to smaller volumes that overlap large

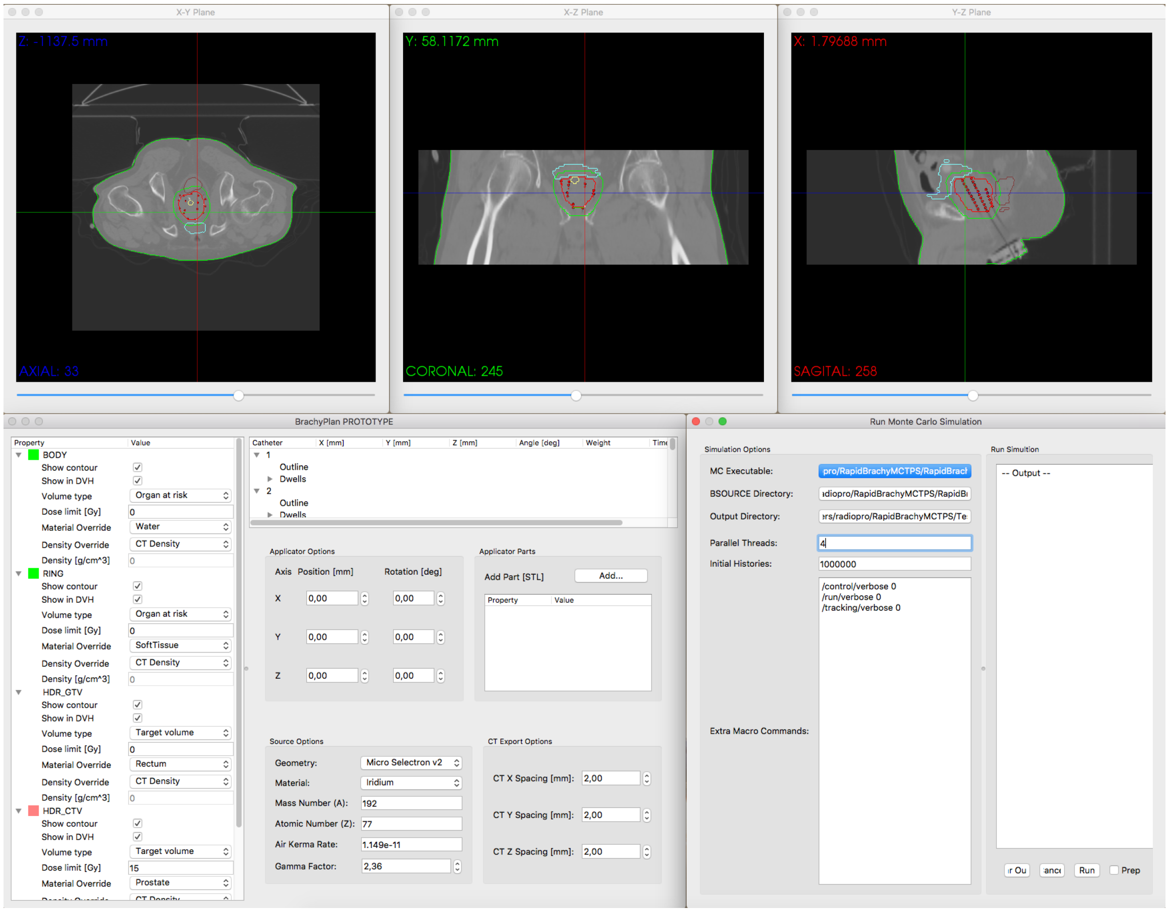

Property	Value
▼ 🟩 BODY	
Show contour	☑
Show in DVH	☑
Volume type	Organ at risk
Dose limit [Gy]	0
Material Override	Water
Density Override	CT Density
Density [g/cm^3]	0
▼ 🟩 RING	
Show contour	☑
Show in DVH	☑
Volume type	Organ at risk
Dose limit [Gy]	0
Material Override	SoftTissue
Density Override	CT Density
Density [g/cm^3]	0
▼ HDR_GTV	
Show contour	☑
Show in DVH	☑
Volume type	Target volume
Dose limit [Gy]	0
Material Override	Rectum
Density Override	CT Density
Density [g/cm^3]	0
▼ 🟥 HDR_CTV	
Show contour	☑
Show in DVH	☑
Volume type	Target volume
Dose limit [Gy]	15
Material Override	Prostate

Catheter	X [mm]	Y [mm]	Z [mm]	Angle [deg]	Weight	Time
▼ 1						
Outline						
▶ Dwells						
▼ 2						
Outline						
▶ Dwells						

Applicator Options

Axis	Position [mm]	Rotation [deg]
X	0,00	0,00
Y	0,00	0,00
Z	0,00	0,00

Applicator Parts

Add Part [STL]

Property	Value

Source Options

Geometry: Micro Selectron v2
Material: Iridium
Mass Number (A): 192
Atomic Number (Z): 77
Air Kerma Rate: 1.149e-11
Gamma Factor: 2,36

CT Export Options

CT X Spacing [mm]: 2,00
CT Y Spacing [mm]: 2,00
CT Z Spacing [mm]: 2,00

Simulation Options

MC Executable: pro/RapidBrachyMCTPS/RapidBrach
BSOURCE Directory: ıdiopro/RapidBrachyMCTPS/RapidBı
Output Directory: ərs/radiopro/RapidBrachyMCTPS/Te
Parallel Threads: 4
Initial Histories: 1000000
Extra Macro Commands:

```
/control/verbose 0
/run/verbose 0
/tracking/verbose 0
```

Run Simultion

Figure 6.1: A print screen of the RapidBrachyMCTPS interface.

volumes are possible. All voxels which are within the bounds of the structure are set to the override density and material as specified. It is possible to just override the mass density, or the material, or both. In the GUI, the user also chooses the voxel size for the simulation. The patient data is saved using the egsphant file format [31] and exported to RapidBrachyMC. The egsphant file contains information about material composition and mass density in each voxel. The setup of the GUI is shown in Figure 6.1.

RapidBrachyMC is a new Geant4-based calculation engine for brachytherapy dosimetry. RapidBrachyMC contains a set of mandatory (detector construction, physics list, primary generator action, run action) and optional (event action, stacking action, stepping action, track length estimator) user class bases. The roles of each of these classes are described in Figure 6.2. The user can change various simulation settings such as the source model, applicators, active core material, source characteristics (air kerma, reference activity, total dwell times), primary

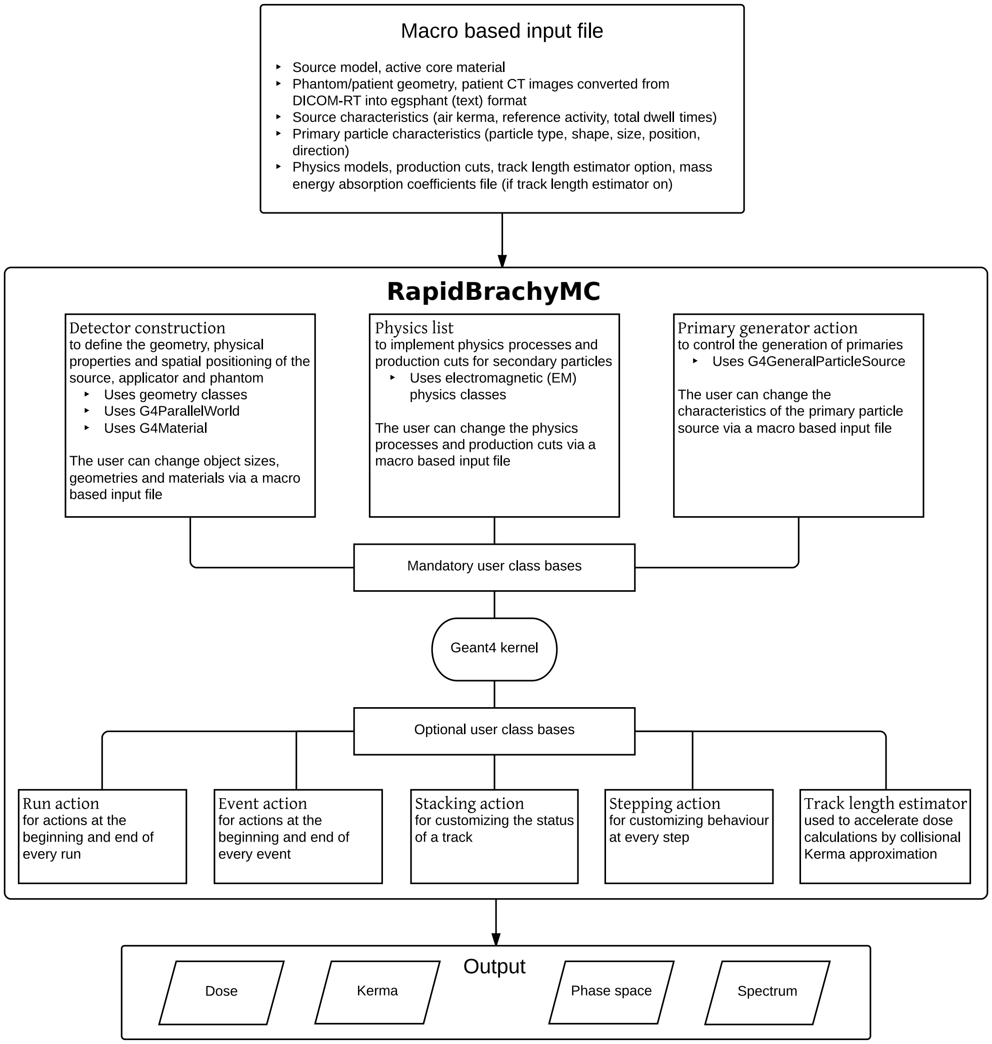

Figure 6.2: Schematic diagram for RapidBrachyMC.

particle characteristics (particle type, shape, size, position, direction), scoring mesh geometry, physics options (physics model, production cuts), and scoring options (absorbed dose, kerma, energy spectrum, phase space file) via the interactive GUI described above.

Radiation source and applicator geometry

Commercial brachytherapy source models were obtained from the literature [32] and implemented in RapidBrachyMC's source library. The sources can be accessed through a drop down menu in the GUI. The source models can also be imported via STereoLithography (STL) file in ASCII format. The sources are superimposed over the patient geometry using the layered mass geometry concept in Geant4 [33] which implements mass-containing parallel worlds. In addition, the user has the option to change the active core of the source to a desirable radionuclide. The radioactive decay for brachytherapy sources is handled through explicit simulation of nuclear decay. The radioactive decay data comes from the Evaluated Nuclear Structure Data File (ENSDF) (Brookhaven National Laboratory, National Nuclear Data Centre). This eliminates the need to include hard coded decay spectra files for each radionuclide and enables the user to change the active core of the source easily via the GUI.

The applicator geometry is specified as an STL file in ASCII format. The VTK STL file reader is used to load the file. It is possible to support other file formats, as the geometry is simply loaded as a triangular mesh. The material and mass density of the applicator are specified by the user in the GUI. The assigned material must be available in RapidBrachyMC's material table or in the Geant4 material database. Applicators consisting of different materials can be exported in different STL files. The user can than assign a unique material and mass density to each component. The applicator is exported as a macro file to be read in by RapidBrachyMC and superimposed over patient geometry similar to the radiation source, in a mass-containing parallel world.

Treatment plan

RapidBrachyMCTPS can either function as a post-implant dosimetry package by importing a DICOM-RT plan file or as a TPS by creating a new plan. Planning tools were integrated within the platform. Currently, dose optimization is performed using column generation-based optimization [34]. The objective is to minimize the total treatment time, that is the sum of the dwell times. The constraints are so that all points in the target (organ at risk) are above (below) the dose limit for that volume. Target volume doses and normal tissue constraints can be specified on the GUI for each contour. Contouring tools are under development and will be integrated in a future version of the software.

Transport and scoring options

RapidBrachyMC can score the collision kerma per history in voxels via a track length estimator. Collision kerma is assumed to equal dose, due to the low photon energies and short electron ranges involved. The track length estimator options can be selected in the macro based input file. If the track length estimator option is turned on, mass energy-absorption coefficients are

Table 6.1: Simulation parameters for dose calculations in water. The voxel size depends on the radial distance r from the center of the active core.

Source	Phantom	Distance	Voxel size
microSelectron v2 (^{192}Ir)	Water	$r \leqslant 1$ cm	(0.1 mm)^3
	(80 cm)^3	1 cm $< r \leqslant 5$ cm	(0.5 mm)^3
		5 cm $< r \leqslant 10$ cm	(1.0 mm)^3
		10 cm $< r \leqslant 20$ cm	(2.0 mm)^3
SelectSeed 130.002 (^{125}I)	Water	$r \leqslant 1$ cm	(0.1 mm)^3
	(30 cm)^3	1 cm $< r \leqslant 5$ cm	(0.5 mm)^3
		5 cm $< r \leqslant 10$ cm	(1.0 mm)^3

required for all the simulated material. Three transport/scoring options are available: dose to water in water ($D_{w,w}$), dose to water in medium ($D_{w,m}$), and dose to medium in medium ($D_{m,m}$). Using the parallel world formalism of Geant4, the resolution of the scoring mesh can be set independently of the physical geometry grid. RapidBrachyMC is implemented using the multithreading capabilities of Geant4 [35]. The code can run in parallel on the maximum number of cores available.

6.2.2 TG-43 parameters

TG-43 parameters for microSelectron v2 HDR (^{192}Ir) (Elekta Brachytherapy, Stockholm, Sweden) and selectSeed 130.002 (^{125}I) (Elekta Brachytherapy, Stockholm, Sweden) were benchmarked against BrachyDose, which has been extensively validated in the past, as well as other published values [36, 37, 24, 32, 38, 25]. Dose calculations were performed with the source positioned at the centre of a water phantom. The radial dose function $g(r)$ and 2D anisotropy functions $F(r, \theta)$ were calculated using a similar methodology as Chamberland et al. [25]. Different voxel sizes were implemented depending on the radial distance r from the center of the active core. The simulation parameters are listed in Table 6.1.

The dose rate constants Λ were calculated as in the studies of Taylor et al. [24] and Taylor and Rogers [38] for low energy (^{125}I) and high energy (^{192}Ir) source models, respectively. For the ^{192}Ir source, Λ was determined using the air kerma strength calculated in a large voxel ($10\times10\times0.05$ cm^3) at 100 cm from the source and corrected to give the air kerma strength at a point. For the ^{125}I source, Λ was determined using the air kerma strength at 10 cm from the source calculated in a small voxel ($0.1\times0.1\times0.05$ cm^3) and in a large voxel ($2.7\times2.7\times0.05$ cm^3). The former represents a point on the transverse axis. The latter represents a region

Table 6.2: Simulation parameters for air kerma calculations.

Source	Method	Distance	Voxel size
microSelectron v2 (^{192}Ir)	point	r = 100 cm	$10\times10\times0.05$ cm^3
SelectSeed 130.002 (^{125}I)	WAFAC	r = 10 cm	$2.7\times2.7\times0.05$ cm^3
	point	r = 10 cm	$0.1\times0.1\times0.05$ cm^3

covering the same solid angle subtended by the primary collimator of the wide-angle free air chamber (WAFAC) at the National Institute of Standards and Technology (NIST). The simulation parameters for the air kerma calculations are summarized in table 6.2. Air kerma per history was calculated *in vacuo* to avoid the need to correct for attenuation by air. Low energy characteristic x-rays were suppressed by discarding all photons with energies less than 10 keV for the ^{192}Ir source and 5 keV for the ^{125}I source.

In all calculations, photons were tracked using the standard Penelope physics list with atomic deexcitation activated. The production cut for photons was set to 0.1 mm (equivalent to an energy cut of 1.11 keV in liquid water). Electrons were not explicitly transported. In each case, 10^8 photons were simulated to obtain standard deviations below 0.2%. The statistical uncertainties in each voxel were calculated using the history-by-history method.

6.2.3 Patient study

The dose distribution and dose-volume histograms (DVHs) were calculated for a prostate HDR brachytherapy case. The patient was treated with a single fraction of 15 Gy, using a 17-catheter implant (source model: microSelectron v2). Two MC protocols were performed: (1) TG-43 MC ($D_{w,w}$): patient anatomy is modeled as uniform density water (0.998 g cm^{-3}) and (2) TG-186 MC ($D_{m,m}$): patient anatomy is modeled using elemental composition of tissues taken from ICRU 46 [39] and mass densities obtained using the HU values from CT scan. Tissue composition assignment was based on contours. The dose grid resolution was set using a voxel size of (1 mm)^3, (2 mm)^3 and (3 mm)^3.

6.2.4 Experimental validation

In order to validate RapidBrachyMC with experimental data, 2D dose distributions of an ^{192}Ir brachytherapy source were obtained using EBT3 Gafchromic$^{\text{TM}}$ film (Ashland Specialty Ingredients, Wayne, NJ). Films were scanned with an Epson Expression 11000XL flatbed

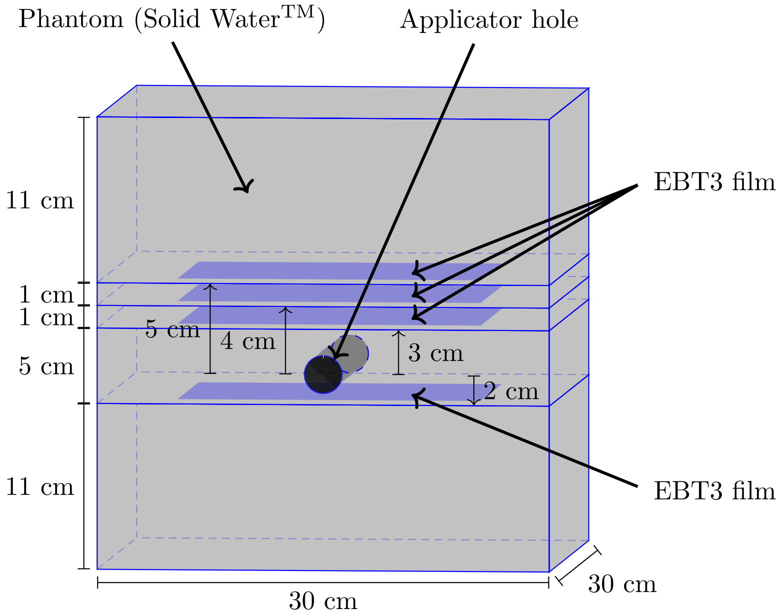

Figure 6.3: Schematic drawing of the irradiation setup. Film dimensions are not to scale.

document scanner (Epson, Nagano, Japan) and analyzed according to the dosimetry protocol described by Devic et al. [40, 41]. The resulting triple-channel TIFF images with 127 dpi resolution and 48-bit colour depth were analyzed using an in-house film analysis software in Matlab (The Mathworks, Natick, MA, USA).

The film calibration was performed using 6 MV photons on a Truebeam$^{\text{TM}}$ linear accelerator (Varian Medical Systems, Palo Alto, CA, USA) at 1.5 cm depth in Solid Water$^{\text{TM}}$ (Gammex-RMI, a Sun Nuclear Company, Middleton, WI, USA). Calibration data was obtained using 14 pieces of EBT3 film (3.25"×2.125") for the following nominal dose levels (cGy): 0, 50, 100, 150, 200, 250, 300, 400, 500, 600, 800, 1000, 1500 and 2000. A 20×20 cm^2 field size at source-surface distance (SSD) of 100 cm was used. The plan was created using the Eclipse TPS (Varian Medical Systems, Palo Alto, CA, USA).

A phantom (30×30×29 cm^3) was assembled using slabs of Solid Water$^{\text{TM}}$. A standard vaginal cylinder applicator with 25 mm diameter (Elekta Brachytherapy, Stockholm, Sweden) was placed inside an applicator hole drilled within a slab. This applicator comes with static tungsten shields which can produce shield combinations of 0° (none), 90°, 180°, and 270°. Pieces of EBT3 film (6.5"×4.25") were placed at 2 cm, 3 cm, 4 cm, and 5 cm from the center of the microSelectron v2 source. The schematic of the irradiation setup is shown in figure 6.3. The

Table 6.3: Air kerma strength per unit source activity S_K/A and statistical uncertainties calculated in this study and in previous studies. MC codes: ^{1}RapidBrachyMC, ^{2}FLURZnrc, ^{3}FLURZ, ^{4}MCPT.

Source	Authors	Method	S_K/A (10^{-8} U Bq^{-1})
microSelectron v2 (^{192}Ir)	This study^1	point	9.762 ± 0.002
	Anwarul Islam *et al.* [42]^2	point	9.698 ± 0.005
	Hong *et al.* [43]^2	point	9.737 ± 0.009
	Borg and Rogers [44]^3	point	9.730 ± 0.010
selectSeed 130.002 (^{125}I)	This study^1	WAFAC	2.073 ± 0.003
	This study^1	point	2.091 ± 0.003
	Sahoo *et al.* [45]^2	point	2.130 ± 0.003
	Karaiskos *et al.* [37]^4	point	2.170 ± 0.010

larger side of the film was positioned parallel to the source axis. A dose of 2 Gy was delivered at a point 5 cm away from the longitudinal axis of the source, using a single dwell position (130 mm from the phantom surface). The dwell time to deliver the dose was calculated using the Oncentra TPS (Elekta Brachytherapy, Stockholm, Sweden). Measurements were performed for the 0° and 180° shield combinations. The dwell time was identical in each case.

The dose distributions were generated using RapidBrachyMC and compared with the experimental distributions. The simulation was performed using the elemental composition (8.1% H, 67.2% C, 2.4% N, 19.9% O, 0.1% Cl, 2.3% Ca) and nominal density (1.04 g cm^{-3}) of Solid Water$^{\mathrm{TM}}$. We accounted for the added thickness of each film layer (280 μm) and included surrounding air gaps. Dose to film was reported as $D_{w,m}$. The dose distribution was calculated in $1.0 \times 1.0 \times 0.5$ mm^3 voxels. The source was shifted by 0.35 mm towards the ground to reflect the most likely position of the source within the catheter due to gravity. A total of 10^8 particles were simulated to obtain standard deviations below 1% in the central region (8×8 cm^2) of the films. The dose grid was resampled to match the resolution of the TIFF images (0.2 mm). The 2D gamma indices were determined for 3%/3 mm and 2%/2 mm acceptance criteria using an in-house Matlab routine.

Table 6.4: Dose rate constants Λ and statistical uncertainties calculated in this study and in previous studies. MC codes: ^{1}RapidBrachyMC, ^{2}egs_brachy, ^{3}BrachyDose, ^{4}MCPT.

Source	Authors	Method	Λ (cGy h^{-1} U^{-1})
microSelectron v2 (^{192}Ir)	This study^1	point	1.110 ± 0.002
	Chamberland *et al.* [25]^2	point	1.108 ± 0.002
	Taylor and Rogers [38]^3	point	1.109 ± 0.002
	Daskalov *et al.* [36]^4	extrap	1.108 ± 0.001
selectSeed 130.002 (^{125}I)	This study^1	WAFAC	0.931 ± 0.002
	This study^1	point	0.938 ± 0.002
	Taylor and Rogers [32]^3	WAFAC	0.917 ± 0.002
	Taylor and Rogers [32]^3	point	0.944 ± 0.003
	Karaiskos *et al.* [37]^4	point	0.954 ± 0.005

6.3 Results

6.3.1 TG-43 parameters

The air kerma strength per unit source activity S_K/A are presented in table 6.3. For the microSelectron v2 source model, the value calculated in this study agreed with previously published results within 1%. For the SelectSeed source model, the results for the point method showed agreement with the most recent published value by Sahoo *et al.* [45] within 2%.

The dose rate constants Λ are presented in Table 9.1. For the microSelectron v2 source model, the results from RapidBrachyMC agreed with those obtained in previous studies, within statistical uncertainties. For the SelectSeed source model, the results for the point and WAFAC methods were within 2% from those obtained in previous studies.

Figure 6.4 presents the radial dose function $g(r)$ calculated with RapidBrachyMC and BrachyDose for both source models. The agreement between the two codes was within 1% at distances $r < 10$ cm for the SelectSeed source model and $r < 20$ cm for the microSelectron v2 source model. Deviation averages were 0.17% and 0.36% for the microSelectron v2 and SelectSeed source models, respectively.

The 2D anisotropy functions $F(r,\theta)$ at a radial distance $r = 1.0$ cm are presented in Figure 6.5. The agreement between RapidBrachyMC and BrachyDose was within 1.5% for $10° < \theta < 170°$. The relative differences were larger in regions of high dose gradients (closer to 0° and 180°). Deviation averages were 0.19% and 0.45% for the microSelectron v2 and SelectSeed source models, respectively.

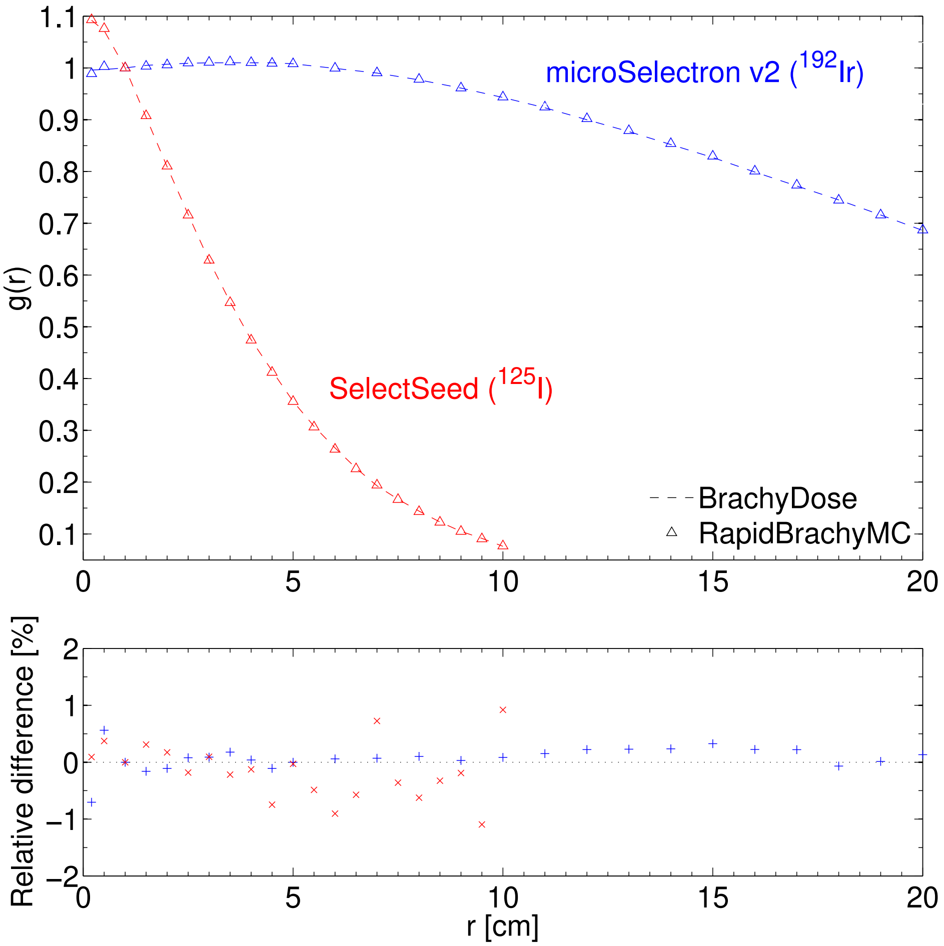

Figure 6.4: Radial dose function $g(r)$ for the microSelectron v2 (^{192}Ir) and SelectSeed 130.002 (^{125}I) source models, obtained using RapidBrachyMC (this study) and BrachyDose.

6.3.2 Patient study

Differences in dose-volume metrics between the Oncentra TPS and RapidBrachyMC calculations in water for a prostate case are shown in Table 6.5. The difference in the planning target volume (PTV) D_{90} was less than 0.1 Gy (0.7%). Differences in the PTV V_{100}, V_{150}, and V_{200} were less than 0.8 cc (1%). Differences in the urethral D_{10} and D_{50} were within 0.4 Gy (2.7%) and 0.05 Gy (0.3%), respectively. The median dose deviation for voxels within the PTV and the urethra were 0.6 Gy (4%) and 0.2 Gy (1.3%), respectively.

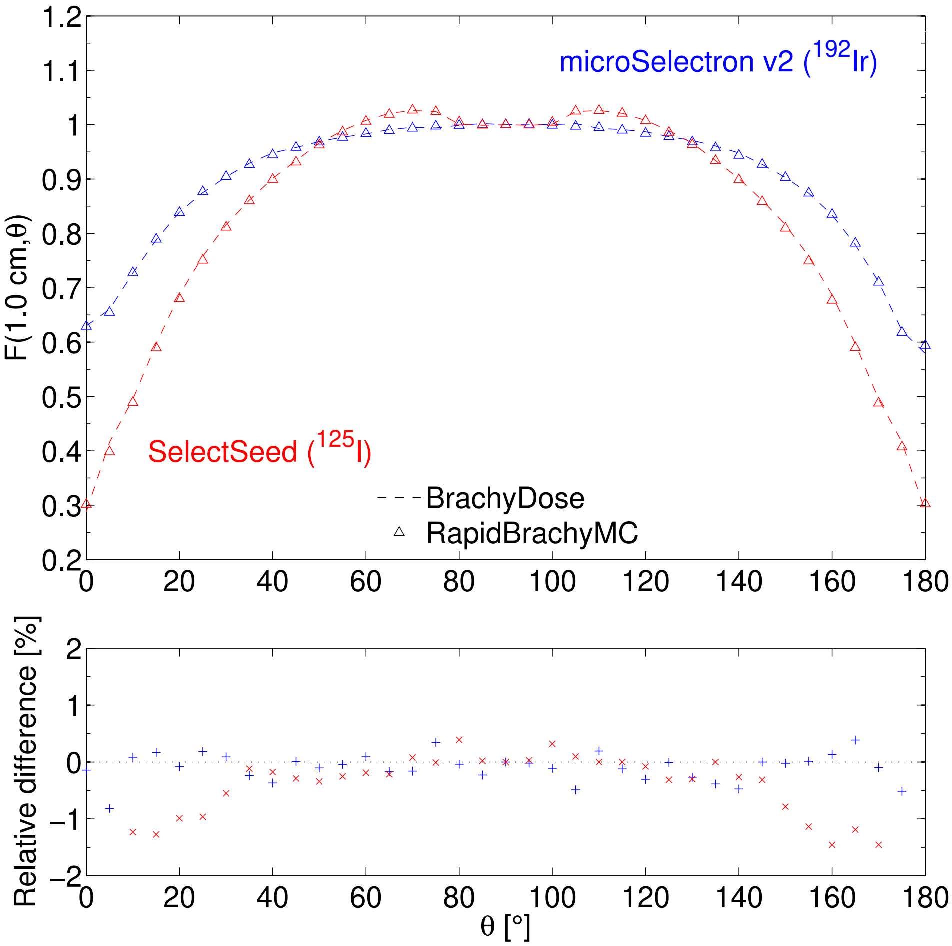

Figure 6.5: 2D anisotropy function $F(r,\theta)$ at $r = 1.0$ cm from the source for the microSelectron v2 (^{192}Ir) and SelectSeed 130.002 (^{125}I) source models, obtained using RapidBrachyMC (this study) and BrachyDose.

The DVH for the target and various organs at risk are presented in Figure 6.6. The DVH comparison between RapidBrachyMC calculations in water ($D_{w,w}$) and in realistic tissue ($D_{m,m}$) showed that the TG-43 protocol generally overestimated the dose given to the prostate, bladder, rectum, and urethra.

Table 6.5: Differences in dose-volume metrics between Oncentra TPS and TG-43 MC calculations for the PTV and urethra. The doses are expressed as a percentage of the prescription dose.

	PTV				Urethra	
Model	D_{90} (%)	V_{100} (%)	V_{150} (%)	V_{200} (%)	D_{10} (%)	D_{50} (%)
TG-43 TPS	100.25	90.32	19.00	7.50	110.01	102.77
TG-43 MC	99.66	89.85	19.81	8.46	112.58	103.00
TPS - MC	0.59	0.47	-0.81	-0.94	-2.57	-0.23

Table 6.6: The speed performance of RapidBrachyMC for a prostate HDR brachytherapy case using a 17-catheter implant and a total of 144 dwell positions. Both the simulation times and total times are reported for a single Intel core from a 2.6 GHz processor. A statistical uncertainty of less than 2% is achieved in all voxels within the prostate volume.

Model	Voxel size	Number of events	Simulation time (min)	Total time (min)
TG-43 MC ($D_{w,w}$)	$(3\text{ mm})^3$	6×10^5	0.9	1.0
	$(2\text{ mm})^3$	2×10^6	3.4	3.6
	$(1\text{ mm})^3$	8×10^6	15.6	15.9
TG-186 MC ($D_{m,m}$)	$(3\text{ mm})^3$	6×10^5	0.9	2.4
	$(2\text{ mm})^3$	2×10^6	3.3	5.1
	$(1\text{ mm})^3$	8×10^6	15.9	18.2

6.3.3 Simulation efficiency

The calculation times for the prostate case are shown in Table 6.6. The number of events were selected such that a statistical uncertainty of less than 2% was achieved in all voxels within the PTV. Both the simulation times and total times are reported for each voxel size. The simulation time refers to the time spent on radiation transport. The total time includes the time to initialize the geometry and output the results. For a given scoring mesh, simulation times for TG-43 MC ($D_{w,w}$) and TG-186 MC ($D_{m,m}$) were comparable. The total times were 1-3 min longer in heterogeneous media compared to homogeneous media. By increasing the number of threads/cores from 1 to 4, simulation times were reduced by a factor of 3.

6.3.4 Experimental validation

The uncertainty budget for the film measurements is summarized in Table 6.7. The sources of uncertainty regarding the film dosimetry system included the scanner reproducibility, scanner

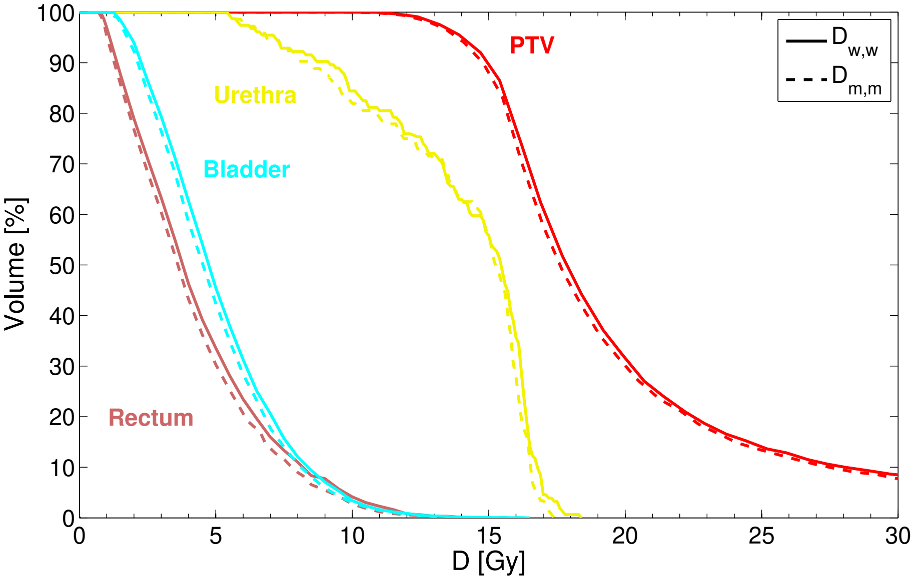

Figure 6.6: Comparison of dose-volumes histograms between TG-43 MC ($D_{w,w}$) and TG-186 MC ($D_{m,m}$) for the PTV and organs at risk (rectum, bladder, urethra) for a prostate HDR brachytherapy case.

homogeneity, calibration curve fit, and reproducibility of the net optical density (netOD) measurements. This resulted in a film dosimetry uncertainty of 2.3% (k=1). Additional sources of uncertainties regarding the treatment delivery were also considered. The uncertainty from the S_K measurement traceable to the primary standards lab was included for a high energy source [46]. The positional uncertainty was divided into two components: the source-to-film distance and the source dwell position. The source-to-film distance uncertainty of ±0.35 mm refers to the position offset of the source from the central axis of the channel. The source dwell position uncertainty of ±1 mm expresses the precision of the source positioning along the central axis for HDR afterloaders [47]. The total standard uncertainty (k=1) varied between 4.9% at $r = 2$ cm and 3.2% at $r = 5$ cm. The distance to agreement (DTA) corresponding to the point dose difference (DD) varied between 2.5 mm at $r = 2$ cm and 3.2 mm at $r = 5$ cm, based on the average dose gradient in each film (ranging from 2.0%/mm at $r = 2$ cm to 1.0%/mm at $r = 5$ cm). The uncertainty analysis suggests that the DD/DTA criteria of 3%/3 mm may be better suited for the gamma analysis, while the 2%/2 mm may be too stringent.

The 2D dose distributions within the films placed at various distances from the 25 mm cylindrical applicator are shown in Figure 6.7 and Figure 6.8 for the unshielded and shielded

Table 6.7: Total uncertainty budget for EBT3 film dosimetry measurements using the proposed experimental setup. Calculation of uncertainty is for absolute dose difference.

		Uncertainty (%)			
Source of uncertainty	Type	r = 2 cm	r = 3 cm	r = 4 cm	r = 5 cm
Scanner reproducibility	A	0.1			
Scanner homogeneity	B	0.2			
Calibration curve fit	B	2.2			
netOD measurement	A	0.7			
Film dosimetry uncertainty (k=1)		**2.3**			
S_K measurement	A	1.5			
Source-to-film distance (±0.35 mm)	B	3.5	2.3	1.8	1.4
Source dwell position (±1 mm)	B	2.0	1.5	1.2	1.0
Total standard uncertainty (k=1)		**4.9**	**3.9**	**3.5**	**3.2**
Expanded uncertainty (k=2)		**9.8**	**7.8**	**7.0**	**6.4**

Table 6.8: Summary of gamma parameters for 25 mm cylindrical applicator with no shielding and 180° shielding.

		Gamma passing rate (%)			
Configuration	DD/DTA	r = 2 cm	r = 3 cm	r = 4 cm	r = 5 cm
Shield 0° (none)	3%/3 mm	99.4	99.8	96.8	98.3
	2%/2 mm	92.0	97.9	77.8	89.1
Shield 180°	3%/3 mm	99.9	99.4	96.4	91.0
	2%/2 mm	90.5	91.3	79.1	69.1

applicator, respectively. The gamma index distributions are also shown for each case, and the gamma parameters are summarized in Table 6.8. At least 95% of points passed the 3%/3 mm gamma index criteria in most cases, except in the case with 180° shielding at r = 5 cm. Disagreement between calculated and measured dose were largest in regions of high dose gradients corresponding to the placement of the edges of the shielding material. Discrepancies were largely attributed to the high sensitivity of the location and shape of the edge gradient to the positioning of the source within the channel. In addition, a mismatch in the orientation of the film (<1°) resulted in a significant number of failing points along the high dose gradient.

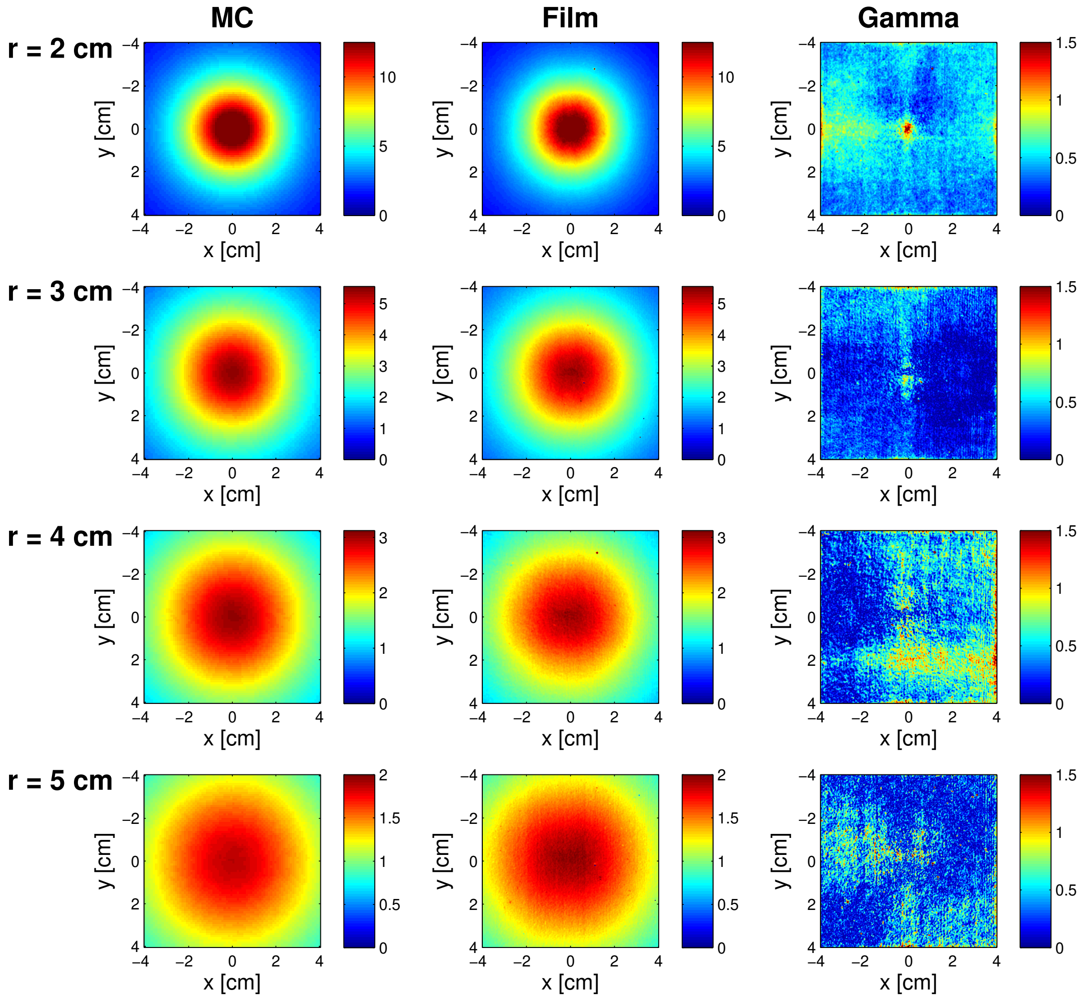

Figure 6.7: Comparison between Monte Carlo (MC) calculated (left) and film-measured (middle) dose distributions (in Gy) from the unshielded 25 mm cylindrical applicator placed at various distances from the source (2 cm, 3 cm, 4 cm, 5 cm). 2D gamma maps for the 3%/3 mm acceptance criteria are shown (right).

6.4 Discussion

In this study, a fast MC-based software, RapidBrachyMCTPS, was developed for brachytherapy applications. The 3D geometries of the radioactive sources, encapsulation and applicators with the correct mass density and material compositions are modeled in the software's dose

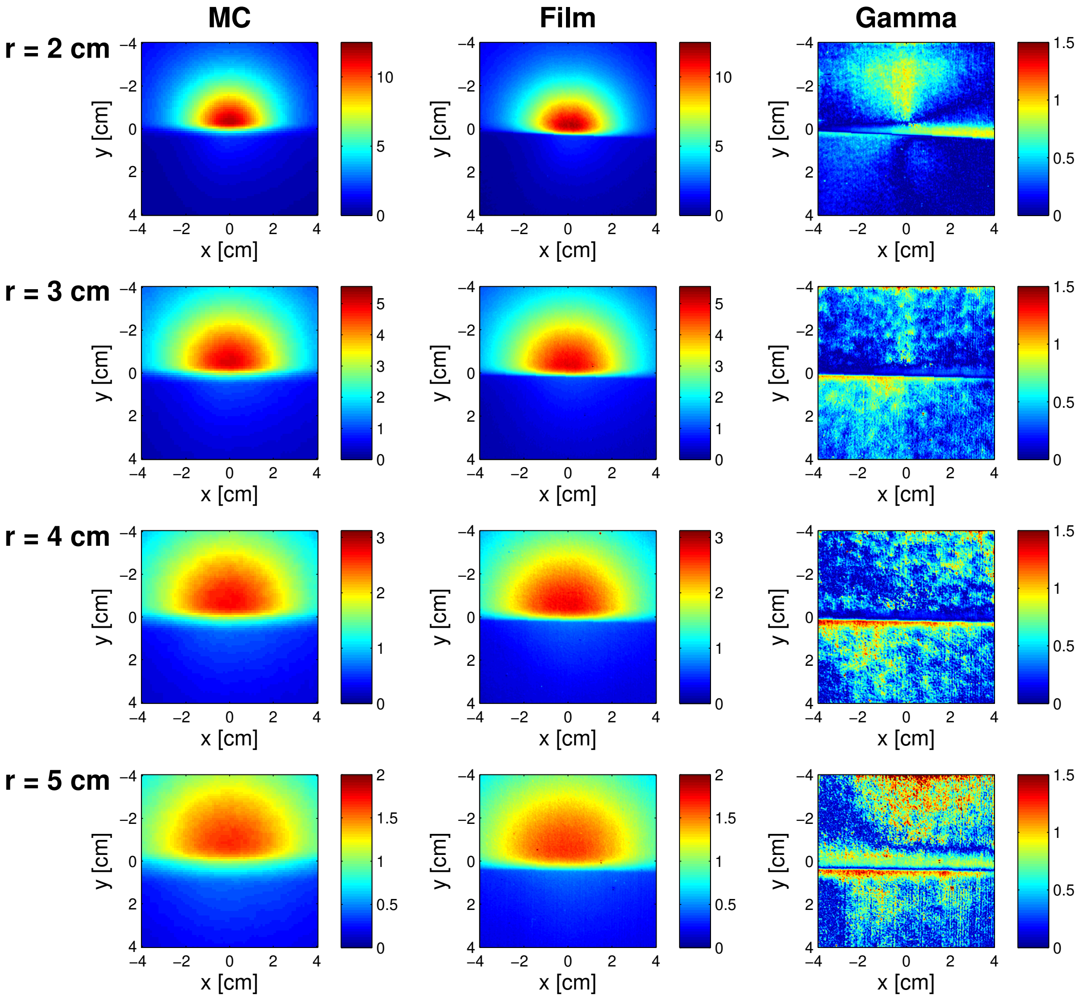

Figure 6.8: Comparison between Monte Carlo (MC) calculated (left) and film-measured (middle) dose distributions (in Gy) from the shielded 25 mm cylindrical applicator placed at various distances from the source (2 cm, 3 cm, 4 cm, 5 cm). 2D gamma maps for the 3%/3 mm acceptance criteria are shown (right).

calculation engine, RapidBrachyMC. The 3D patient geometry is obtained via DICOM-RT files. The DICOM-RT files are converted into egsphant files with tissue densities and material compositions assigned to each contour and imported as input into RapidBrachyMC via an interactive GUI. Using the GUI, the user can vary important simulation parameters such as the source models, source characteristics, applicator models, scoring options, tracking options, and physics models. In addition, the source code can easily be modified to adapt the simulation settings to the specific needs required by the user.

TG-43 parameters calculated using RapidBrachyMC generally agreed within 1%-2% of the results obtained with previously benchmarked MC codes. For the prostate case, the dosimetric endpoints considered (PTV D_{90}, V_{100}, V_{150}, V_{200}; urethra D_{10}, D_{50}) calculated with TG-43 MC agreed within 1% of those calculated using the clinical TPS in all but one case. These are within acceptable uncertainties for brachytherapy dose calculation softwares [47]. The dose distributions for a cylindrical shielded/unshielded applicator were also validated against film measurements in a Solid Water$^{\mathrm{TM}}$ phantom. In all but one case, at least 95% of the points passed the 3%/3 mm gamma index acceptance criteria.

Simulation times for a prostate case were on the order of minutes to achieve reasonable uncertainties ($<2\%$ in voxels within PTV) and increased with higher resolution of the scoring mesh. The total times were higher to perform heterogeneous dose calculations, due to the additional time required to initialize the geometry and read and write files. The computational efficiency can be improved by running calculations in parallel on several cores. Overall, the simulation times were reasonable to compute MC dose distributions in realistic patient geometries.

The main advantage of RapidBrachyMC is the ability to easily modify the active core of the source for any given source model, and to import any applicator model in STL format, assign material and mass density from the GUI, and superimpose over the patient geometry. The platform is suited for testing and developing new source/applicator models and radionuclides for brachytherapy applications. The code is also well suited to calculate dose distributions around applicators that are partially shielded with high-Z materials. RapidBrachyMC can be adopted as a quality assurance tool to validate the dose distributions exported from clinical TPS. The MC toolkit can also be used to benchmark clinically available MBDCAs. Although RapidBrachyMC was evaluated for a prostate HDR case, it is equally applicable for use in HDR and LDR applications.

6.5 Conclusions

A novel, comprehensive MC-based treatment planning platform, RapidBrachyMCTPS, was developed for brachytherapy applications. The software can be used as a retrospective post-implant dosimetry package, as well as for brachytherapy treatment planning for research purposes. The accuracy of the dose calculation engine, RapidBrachyMC, was assessed by comparing the results to other MC calculation codes and film measurements. Calculation times were on the order of minutes for typical brachytherapy applications using a single core, and can be reduced to below 1 min using the multithreading capabilities of Geant4. The software is well suited for the development of new radionuclides and source/applicator models for use in brachytherapy.

Acknowledgements: This work was supported by the Natural Sciences and Engineering Research Council (NSERC) Discovery Grant (number 241018) and RI-MUHC Merck Grant Award for Junior Investigators. G.F. would like to acknowledge financial support by the NSERC Alexander Graham Bell Canada Graduate Scholarship, Schulich Graduate Fellowship, and NSERC CREATE Medical Physics Research Training Network Grant (number 432290). The authors would like to thank Joe Larkin for machining of the phantom, Monica Serban for data transfer between Eclipse and Oncentra, and Saad Aldelaijan and Russell Ruo for fruitful discussions regarding film dosimetry.

Conflict of interest: None.

References

[1] Nath R, Andersson LL, Luxton G, Weaver KA, Williamson JF, Meigooni AS. Dosimetry of interstitial brachytherapy sources: Recommendations of the AAPM Radiation Therapy Committee Task Group No. 43. Med Phys. 1995;22(1):209–234.

[2] Rivard MJ, Coursey BM, DeWerd LA, Hanson WF, Huq MS, Ibbott GS, et al. Update of AAPM Task Group No. 43 Report: A revised AAPM protocol for brachytherapy dose calculations. Med Phys. 2004;31(3):633–674.

[3] Chibani O, Williamson JF, Todor D. Dosimetric effects of seed anisotropy and interseed attenuation for ^{103}Pd and ^{125}I prostate implants. Med Phys. 2005;32(8):2557–2566.

[4] Carrier JF, Beaulieu L, Therriault-Proulx F, Roy R. Impact of interseed attenuation and tissue composition for permanent prostate implants. Med Phys. 2006;33(3):595–604.

[5] Afsharpour H, Pignol JP, Keller B, Carrier JF, Reniers B, Verhaegen F, et al. Influence of breast composition and interseed attenuation in dose calculations for post-implant

assessment of permanent breast 103Pd seed implant. Phys Med Biol. 2010;55(16):4547–4561.

[6] Landry G, Reniers B, Murrer L, Lutgens L, Bloemen-Van Gurp E, Pignol JP, et al. Sensitivity of low energy brachytherapy Monte Carlo dose calculations to uncertainties in human tissue composition. Med Phys. 2010;37(10):5188–5198.

[7] Mason J, Al-Qaisieh B, Bownes P, Henry A, Thwaites D. Investigation of interseed attenuation and tissue composition effects in ^{125}I seed implant prostate brachytherapy. Brachytherapy. 2014;13(6):603–610.

[8] White SA, Landry G, Fonseca GP, Holt R, Rusch T, Beaulieu L, et al. Comparison of TG-43 and TG-186 in breast irradiation using a low energy electronic brachytherapy source. Med Phys. 2014;41(6):061701.

[9] Anagnostopoulos G, Baltas D, Pantelis E, Papagiannis P, Sakelliou L. The effect of patient inhomogeneities in oesophageal ^{192}Ir HDR brachytherapy: A Monte Carlo and analytical dosimetry study. Phys Med Biol. 2004;49:2675–2685.

[10] Lymperopoulou G, Papagiannis P, Angelopoulos A, Karaiskos P, Georgiou E, Baltas D. A dosimetric comparison of ^{169}Yb and ^{192}Ir for HDR brachytherapy of the breast, accounting for the effect of finite patient dimensions and tissue inhomogeneities. Med Phys. 2006;33(12):4583–4589.

[11] Poon E, Williamson JF, Vuong T, Verhaegen F. Patient-specific Monte Carlo dose calculations for high-dose-rate endorectal brachytherapy with shielded intracavitary applicator. Int J Radiat Oncol Biol Phys. 2008;72:1259–1266.

[12] Mackie TR, Scrimger JW, Battista JJ. A convolution method of calculating dose for 15-MV x rays. Phys Med Biol. 1985;12:188–196.

[13] Ahnesjö A. Collapsed cone convolution of radiant energy for photon dose calculation in heterogenous media. Med Phys. 1989;16:577–592.

[14] Carlsson AK, Ahnesjö A. The collapsed cone superposition algorithm applied to scatter dose calculations in brachytherapy. Med Phys. 2000;27(10):2320–2332.

[15] Gifford KA, Horton JL, Wareing TA, Failla G, Mourtada F. Comparison of a finite-element multigroup discrete-ordinates code with Monte Carlo for radiotherapy calculations. Phys Med Biol. 2006;51:2253–2265.

[16] Vassiliev ON, Wareing TA, McGhee J, Failla G, Salehpour MR, Mourtada F. Validation of a new grid-based Boltzmann equation solver for dose calculation in radiotherapy with photon beams. Phys Med Biol. 2010;55:581–598.

[17] Rogers DWO. Fifty years of Monte Carlo simulations for medical physics. Phys Med Biol. 2006;51:R287–R301.

[18] Beaulieu L, Carlsson Tedgren A, Carrier JF, Davis SD, Mourtada F, Rivard MJ, et al. Report of the Task Group 186 on model-based dose calculation methodsbin brachytherapy beyond the TG-43 formalism: current status and recommendations for clinical implementation. Med Phys. 2012;39(10):6208–6236.

[19] Poon E, Le Y, Williamson JF, Verhaegen F. BrachyGUI: an adjunct to an accelerated Monte Carlo photon transport code for patient-specific brachytherapy dose calculations and analysis. J Phys: Conf Ser. 2008;102(1):12–18.

[20] Le Y, Chibani O, Todor D, Siebers J, Williamson JF. An integrated CT-based monte carlo dose-evaluation system for brachytherapy and its application to permanent prostate implant postprocedure dosimetric analysis. Med Phys. 2005;32(6):2068.

[21] Afsharpour H, Landry G, D'Amours M, Enger S, Reniers B, Poon E, et al. ALGEBRA: ALgorithm for the heterogeneous dosimetry based on GEANT4 for BRAchytherapy. Phys Med Biol. 2012;57(11):3273–3280.

[22] Agostinelli S, Allison J, al Amako K, Apostolakis J, Araujo H, Arce P, et al. Geant4 - a simulation toolkit. Nucl Inst Meth Phys Res A. 2003;506(3):250–303.

[23] Allison J, Amako K, Apostolakis J, Araujo H, Dubois PA, Asai M, et al. Geant4 developments and applications. IEEE Trans Nucl Sci. 2006;53(1):270–278.

[24] Taylor REP, Yegin G, Rogers DWO. Benchmarking BrachyDose: Voxel based EGSnrc Monte Carlo calculations of TG-43 dosimetry parameters. Med Phys. 2007;34(2):445–457.

[25] Chamberland MJP, Taylor REP, Rogers DWO, Thomson RM. egs_brachy: a versatile and fast Monte Carlo code for brachytherapy. Phys Med Biol. 2016;61(23):8214–8231.

[26] Kawrakow I. Accurate condensed history Monte Carlo simulation of electron transport. I. EGSnrc, the new EGS4 version. Med Phys. 2000;27(3):485–498.

[27] Kawrakow I, Mainegra-Hing E, Rogers DWO, Tessier F, Walters BRB. The EGSnrc code system: Monte Carlo simulation of electron and photon transport. Ottawa, Canada: National Research Council of Canada; 2011. PIRS-701.

[28] Fonseca G, Reniers B, Landry G, White S, Bellezzo M, Antunes PC, et al. A medical image-based graphical platform - features, applications and relevance for brachytherapy. Brachytherapy. 2014;13(6):632–639.

[29] Pantelis E, Peppa V, Lahanas V, Pappas E, Papagiannis P. BrachyGuide: a brachytherapy-dedicated DICOM RT viewer and interface to Monte Carlo simulation software. J Appl Clin Med Phys. 2015;16(1):208–218.

[30] Goorley T, James M, Booth T. Initial MCNP6 release overview. Nucl Technol. 2012;180(3):298–315.

[31] Walters BRB, Kawrakow I, Rogers DWO. DOSXYZnrc Users Manual. Ottawa, Canada: National Research Council of Canada; 2015. PIRS-794 (revB).

[32] Taylor REP, Rogers DWO. An EGSnrc Monte Carlo-calculated database of TG-43 parameters. Med Phys. 2008;35(11):4228–4241.

[33] Enger SA, Landry G, D'Amours M, Verhaegen F, L LB, Asai M, et al. Layered mass geometry: a novel technique to overlay seeds and applicators onto patient geometry in Geant4 brachytherapy simulations. Phys Med Biol. 2012;57(19):6269–6277.

[34] Renaud M, Famulari G, Seuntjens J, Enger SA. OC-0256: Column generation-based Monte Carlo treatment planning for rotating shield brachytherapy. Radiother Oncol. 2016;119:S118.

[35] Dong X, Cooperman G, Apostolakis J. Multithreaded Geant4: semi-automatic transformation into scalable thread-parallel software. In: D'Ambra P, Guarracino M, Talia D, editors. Euro-Par 2010 - Parallel Processing. Berlin, Heidelberg: Springer; 2010. p. 287–303.

[36] Daskalov GM. Monte Carlo-aided dosimetry of a new high dose-rate brachytherapy source. Med Phys. 1998;25:2200–2208.

[37] Karaiskos P, Papagiannis P, Sakelliou L, Anagnostopoulos G, Baltas D. Monte Carlo dosimetry of the selectSeed ^{125}I interstitial brachytherapy seed. Med Phys. 2001;28:1753–1760.

[38] Taylor REP, Rogers DWO. EGSnrc Monte Carlo calculated dosimetry parameters for ^{192}Ir and ^{169}Yb brachytherapy sources. Med Phys. 2008;35(11):4933–4944.

[39] ICRU. Photon, electron, proton and neutron interaction data for body tissues. vol. ICRU report 46. Bethesda, MD: International Commission on Radiation Units & Measurements; 1992.

[40] Devic S, Seuntjens J, Sham E, Podgorsak EB, Schmidtlein CR, Kirov AS, et al. Precise radiochromic film dosimetry using a flat-bed document scanner. Med Phys. 2005;32(7):2245–2253.

[41] Devic S, Tomic N, Lewis D. Reference radiochromic film dosimetry: Review of technical aspects. Med Phys. 2016;32(4):541–556.

[42] Anwarul Islam M, Akramuzzaman MM, Zakaria GA. Dosimetric comparison between the microSelectron HDR ^{192}Ir v2 source and the BEBIG ^{60}Co source for HDR brachytherapy using the EGSnrc Monte Carlo transport code. J Med Phys. 2012;35(4):219–225.

[43] Hong L, Zakaria GA, Hartmann GH. EGSnrc Monte Carlo-aided dosimetric studies of the ^{192}Ir microSelectron v2 HDR brachytherapy source. In: Doessel O, Schlegel W, editors. WC, IFMBE Proceeding I/25; 2009. p. 341–4.

[44] Borg J, Rogers DW. Spectra and air-kerma strength for encapsulated ^{192}Ir sources. Med Phys. 1999;26(11):2441–2444.

[45] Sahoo S, Palani Selvam T, Vishwakarma RS, Chourasiya G. Monte Carlo modeling of ^{60}Co HDR brachytherapy source in water and in different solid water phantom materials. J Med Phys. 2010;35:15–22.

[46] DeWerd LA, Ibbott GS, Meigooni AS, Mitch MG, Rivard MJ, Stump KE, et al. A dosimetric uncertainty analysis for photon-emitting brachytherapy sources: Report of AAPM Task Group No. 138 and GEC-ESTRO. Med Phys. 2011;38(2):782–801.

[47] Kirisits C, Rivard MJ, Baltas D, Ballester F, De Brabandere M, van der Laarse R, et al. Review of clinical brachytherapy uncertainties: Analysis guidelines of GEC-ESTRO and the AAPM. Radiother Oncol. 2014;110(1):199–212.

Chapter 7

Can intermediate-energy sources result in elevated bone doses for prostate and head & neck high dose rate brachytherapy?

Abstract

Purpose: Several radionuclides with high (^{60}Co, ^{75}Se) and intermediate (^{169}Yb, ^{153}Gd) energies have been investigated as alternatives to ^{192}Ir for high dose rate (HDR) brachytherapy. The purpose of this study was to evaluate the impact of tissue heterogeneities for these five high-to-intermediate energy sources in prostate and head & neck brachytherapy.
Materials and methods: Treatment plans were generated for a cohort of prostate (*n*=10) and oral tongue (*n*=10) patients. Dose calculations were performed using RapidBrachyMCTPS, an in-house Geant4-based Monte Carlo treatment planning system. Treatment plans were generated using ^{60}Co, ^{192}Ir, ^{75}Se, ^{169}Yb and ^{153}Gd as the active core of the microSelectron v2 source. Two dose calculation scenarios were presented: (1) dose to water in water ($D_{w,w}$), and (2) dose to medium in medium ($D_{m,m}$).
Results: $D_{w,w}$ overestimates PTV coverage compared to $D_{m,m}$, regardless of photon energy. The average PTV D_{90} reduction was $\sim$1% for high energy sources, while larger differences were observed for intermediate energy sources (1%-2% for prostate and 4%-7% for oral tongue). Dose differences were not clinically significant (<5%) for soft tissues in general. Going from $D_{w,w}$ to $D_{m,m}$, bone doses were increased two- to three-fold for ^{169}Yb and four- to five-fold for ^{153}Gd, while the ratio was close to $\sim$1 for high energy sources.

Conclusions: $D_{w,w}$ underestimates the dose to bones and, to a lesser extent, overestimates the dose to soft tissues for radionuclides with average energies lower than ^{192}Ir. Further studies regarding bone toxicities are needed before intermediate energy sources can be adopted in cases where bones are in close vicinity to the tumor.

7.1 Introduction

Brachytherapy can be administrated by gamma emitting radionuclides with low energies ($E_{\gamma,avg}$ $<$ 50 keV), intermediate energies (50 keV $< E_{\gamma,avg} <$ 200 keV) or high energies ($E_{\gamma,avg}$ $>$ 200 keV), where $E_{\gamma,avg}$ is the average energy of the emitted photon spectra [1]. Several gamma emitting radionuclides, such as ^{60}Co, ^{75}Se, ^{169}Yb, and ^{153}Gd, have been investigated as alternatives to the widely adopted ^{192}Ir for high dose rate (HDR) brachytherapy [2–12]. ^{60}Co offers logistic and economic advantages due to its very long half-life [8]. A ^{75}Se source is an interesting alternative to lower shielding requirements and allow for fewer source exchanges due to its longer half-life [2]. Intermediate energy sources such as ^{169}Yb and ^{153}Gd are desirable to reduce shielding requirements for the treatment room and/or to enable collimation of the radiation emissions to spare healthy tissues [13–15]. From these alternatives, only ^{60}Co sources are commercially available and clinically used. An ^{169}Yb source was also recently made available for brachytherapy applications [16]. In addition, the American Association of Physicists in Medicine (AAPM) recently accepted a new Task Group No. 337 (TG-337) on Intensity Modulated and Anisotropic Brachytherapy Sources (IMABS) indicating that low and intermediate energy brachytherapy sources combined with high-Z metallic shields are emerging technology that will enter the clinical practice in a near future.

Currently, brachytherapy dosimetry is based on the TG-43 [17, 18] formalism, which assumes that the patient consists of uniform density water. Model-based dose calculation algorithms (MBDCAs) have been developed to provide more accurate dosimetry for brachytherapy applications [1]. The impact of tissue heterogeneities and finite patient dimensions on clinically relevant parameters was investigated for the high energy sources ^{60}Co and ^{192}Ir for cervical [19], esophageal [19, 20], breast [19, 21, 22], rectal [23], prostate[24], lung [25] and skin cancers [26]. Tissue heterogeneity effects have been investigated for ^{169}Yb in breast cancer patients [27, 28]. However, several studies investigating intermediate energy sources in combination with dynamically controlled high-Z shields for prostate [13, 14] and cervical [15] cancers have ignored the impact of patient heterogeneities on the resulting dose distributions, which can become substantial for high-density materials such as bony structures.

The aim of this study was to evaluate the effect of tissue heterogeneities for a range of high-to-intermediate energy sources for prostate and head & neck HDR brachytherapy. These treatment sites were selected to examine the role of proximity to the tissue-bone interfaces on the resulting dose distributions.

7.2 Materials and methods

7.2.1 Patient cohorts

This retrospective study received approval from our institutional review board (2019). In this work, dose calculations were performed for a cohort of 10 prostate and 10 oral tongue cancer patients treated with HDR brachytherapy. For the prostate cases, the brachytherapy planning aim was a single fraction of 15 Gy (boost) [29] or 21 Gy (monotherapy) [30]. For the oral tongue cases, the planning aim was 10 fractions of 3 Gy delivered twice daily with a minimum interval of 6 h [31]. The prostate cancer patients were treated with 17 plastic 6-French (6F) catheters. The tongue cases were treated using 4-5 plastic 6F catheters. Each case had post-implant CT images used for treatment planning. Contours were imported from DICOM-RT Structure Set files. Dwell positions were extracted from DICOM-RT Plan files. The orientation of the source at dwell position $P(i)$ was defined by the vector between the previous dwell position $P(i-1)$ and the next dwell position $P(i+1)$. The orientation of the first and last dwell positions were defined by the vector between the first two and last two successive points, respectively.

7.2.2 Source model

The microSelectron v2 source (Elekta Brachytherapy, Stockholm, Sweden) [32] was modeled in this study. The active core of the source was modified according to the selected radionuclide. The physical properties of the photon-emitting radionuclides under investigation are displayed in Table 7.1. The maximum activity of these radionuclides within the active core volume of the microSelectron v2 source were calculated using the practical specific activities achieved at Oak Ridge National Laboratory [33]. For ^{60}Co, ^{75}Se and ^{169}Yb, it is possible to produce a source equivalent to 370 GBq of ^{192}Ir. For ^{153}Gd, however, the maximum activity that can fit inside the active core (26 GBq) corresponds to a dose rate of 0.6% relative to 370 GBq of ^{192}Ir, due to its lower achievable specific activity [10].

Table 7.1: Physical properties of various radionuclides. β-: Beta minus decay. EC: Electron capture. CFSA: Carrier-free specific activity. PSA: Practical specific activity. A_{max}: Maximum achievable activity that can be fit within the active core of the microSelectron v2 source model. A_{eq}: Activity equivalent to 370 GBq of ^{192}Ir. RBE: Relative biological effectiveness.

Radionuclide	Decay mode	Half-life	Mean photon energy (MeV)	CFSA (GBq g^{-1})	PSA (GBq g^{-1})	A_{max} (GBq)	A_{eq} (GBq)	RBE
^{60}Co	β-	5.27 y	1.25	4.1×10^5	3.7×10^5	3.9×10^2	1.3×10^2	1.00
^{192}Ir	β- (95%), EC (5%)	73.8 d	0.38	3.4×10^5	1.4×10^5	3.9×10^3	3.7×10^2	1.03
^{75}Se	EC	118.5 d	0.21	5.5×10^5	2.1×10^5	1.2×10^3	6.3×10^2	1.06
^{169}Yb	EC	32.0 d	0.093	8.9×10^5	1.5×10^5	1.3×10^3	1.0×10^3	1.13
^{153}Gd	EC	240.4 d	0.060	1.3×10^5	2.9×10^3	2.6×10^1	4.4×10^3	1.18

7.2.3 Treatment planning

Dwell times were re-optimized for the various radionuclides using an in-house column generation-based optimizer [34] and normalized to match the PTV V_{100} coverage of the original clinical plan. The dose-volume constraints were taken from the Radiation Therapy Oncology Group (RTOG) 0321 protocol [35] for prostate cancer and the Head & Neck Working Group of the Groupe Européen de Curiethérapie - European SocieTy for Radiotherapy and Oncology (GEC-ESTRO) [31, 36] for oral cavity cancer. The plans were optimized in TG-43 conditions since this is the current clinical standard in brachytherapy dosimetry.

7.2.4 Tissue properties assignment schemes

Two tissue properties assignment schemes were performed to calculate: (1) dose to water in homogeneous water ($D_{w,w}$) based on the recommendations of TG-43, and (2) dose to medium in medium ($D_{m,m}$). For $D_{m,m}$, the elemental compositions of tissues were assigned according to the recommendations of TG-186 [1] and ICRU 46 [37] (Table B.1) and mass densities were obtained using the Hounsfield unit (HU) values from the CT scan (Table B.2). The tissue properties assignment schemes for the contours are presented in Table B.3 and Table B.4 for the prostate and oral tongue cases, respectively.

High density metal objects, such as dental fillings, radiopaque markers for catheter visualization and buttons for catheter stabilization, can cause artifacts in CT images. In order to reduce the impact of imaging artifacts on dose distributions, a simple threshold algorithm was applied. In regions of voxels where the density values were above the maximum threshold for a given structure (1.14 g cm^{-3} [38] for soft tissues), the medium was overridden to that of the surrounding tissue with nominal density (Table B.1).

7.2.5 Monte Carlo simulations

Dose calculations were performed using RapidBrachyMCTPS [39], a previously validated in-house Monte Carlo (MC) dose calculation engine. RapidBrachyMCTPS is based on the Geant4 [40, 41] MC radiation transport toolkit. Radioactive decay was simulated using photon decay spectra from the Evaluated Nuclear Structure Data File (ENSDF) [42]. Particle transport was performed using the standard Penelope low-energy electromagnetic physics list. Cross section data were taken from the EPDL97 [43], EEDL97 [44] and EADL97 [45] cross-section libraries. Using the parallel world formalism implemented in Geant4, the resolution of the scoring grid (1 mm^3) was set independently of the CT grid resolution. Due to the low photon energies and short electron ranges (with the exception of ^{60}Co), dose was approximated by the collisional kerma [1]. The collision kerma in voxels was scored using a track length estimator [46]. Mass energy-absorption coefficients were obtained for various materials using the methodology described by Mann-Krzisnik et al. [47]. Electron transport was simulated for ^{60}Co since charged particle equilibrium was not implicitly assumed. A total of 10^8 photons were simulated to obtain type A uncertainties less than 0.2% in voxels within the planning target volume (PTV). The type A uncertainties at points 10 mm, 30 mm and 50 mm distal to the PTV surface were below 0.3%, 0.5% and 0.8%, respectively. The MC simulation methods are summarized in Table B.5 according to the recommendations of TG-268 [48]. A detailed uncertainty analysis is presented in Table B.6.

7.2.6 Dose-volume metrics

Dose distributions and dose-volume histograms (DVHs) were extracted for visualization using RapidBrachyMCTPS. For the prostate cases, the dose-volume parameters were reported for the PTV (D_{90}, V_{100}, V_{150} and V_{200}), urethra (D_{10}), bladder (D_{2cc}), rectum (D_{2cc}), and left (Femur_L) and right (Femur_R) femoral heads (D_{max}). For the tongue cases, the dose-volume parameters were reported for the PTV (D_{90}, V_{100}, V_{150} and V_{200}), and mandible (D_{mean} and D_{max}). Relative differences and ratios in dose-volume parameters were reported as $100 * (D_{m,m} - D_{w,w})/D_{w,w}$ and $D_{m,m}/D_{w,w}$, respectively.

7.3 Results

7.3.1 Prostate cases

The clinical DVH metrics are presented for the various radionuclides calculated using $D_{w,w}$ and $D_{m,m}$ (Table B.7). All plans calculated with $D_{w,w}$ maintained compliance with the recommended RTOG protocol dosimetric guidelines. Figure 7.1 compares $D_{w,w}$ and $D_{m,m}$ distributions for a prostate case for the various radionuclides. Dose differences were more pronounced in bony structures and in distal soft tissues than within the prostate, rectum, bladder and urethra. For high energy sources, the dose to the pelvic bone and femoral heads were kept below $<30\%$ and $<15\%$ of the prescribed dose, respectively. For intermediate energy sources, there was an elevated $D_{m,m}$ dose to the high-density regions within the pelvic bones (up to 60% for ^{169}Yb and 90% for ^{153}Gd) and femoral heads (up to 30% for ^{169}Yb and 50% for ^{153}Gd).

Figure 7.2 shows the relative differences in dosimetric indices between $D_{w,w}$ and $D_{m,m}$. Going from $D_{w,w}$ to $D_{m,m}$ leads to a decrease of the various dosimetric indices of the PTV, urethra and rectum. $D_{w,w}$ underestimates the bladder D_{2cc} for high energy sources, but overestimates the bladder D_{2cc} for intermediate energy sources. The impact of tissue heterogeneities on clinical DVH metrics generally increased with decreasing photon energy. While $D_{w,w}$ underestimates PTV coverage, mean differences between $D_{w,w}$ and $D_{m,m}$ for all radionuclides were limited to $<2\%$ for the PTV D_{90}, $<2\%$ (or <1.5 cm^3) for the PTV V_{100}, $<4\%$ (or <1.0 cm^3) for the PTV V_{150} and $<4\%$ (or <0.4 cm^3) for the PTV V_{200}. The mean differences for the urethra D_{10}, bladder D_{2cc} and rectum D_{2cc} were $<5\%$ in all cases. The ratios of $D_{m,m}/D_{w,w}$ for the femoral heads D_{max} were about 0.9, 1.1, 1.5, 2.8 and 4.0 for ^{60}Co, ^{192}Ir, ^{75}Se, ^{169}Yb and ^{153}Gd, respectively.

7.3.2 Tongue cases

The clinical DVH metrics are presented for the various radionuclides calculated using $D_{w,w}$ and $D_{m,m}$ (Table B.8). All plans calculated with $D_{w,w}$ maintained compliance with the recommended GEC-ESTRO dosimetric guidelines. Figure 7.3 shows the $D_{w,w}$ and $D_{m,m}$ dose distributions for a tongue case. In general, for all the studied sources, dose differences were small inside the PTV and larger in the mandible and in soft tissues outside the PTV. For high energy sources, the mandible received $<110\%$ of the prescribed dose. Given similar target coverage, the mandible D_{max} was $\sim$250% of the prescribed dose for ^{169}Yb and $\sim$400% for ^{153}Gd, while the proportion

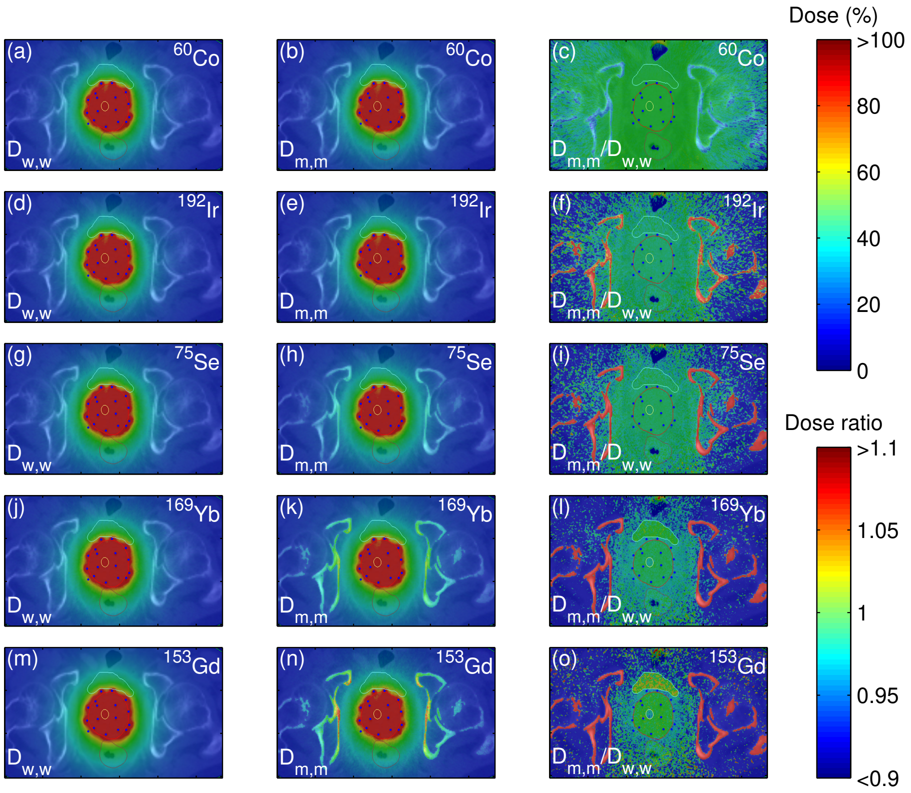

Figure 7.1: Axial CT slice for a prostate brachytherapy case with contours for the PTV (red), urethra (yellow), bladder (cyan), rectum (brown) and body (green). Dose distributions ($D_{w,w}$ and $D_{m,m}$) and dose ratio maps are overlaid over the patient geometry for (a-c) ^{60}Co, (d-f) ^{192}Ir, (g-i) ^{75}Se, (j-l) ^{169}Yb, and (m-o) ^{153}Gd. Catheter positions are indicated (blue).

of the mandible receiving at least 100% of the prescribed dose (V_{100}) was ∼30% and ∼50%, respectively.

Figure 7.4 shows the relative differences in dosimetric indices between $D_{w,w}$ and $D_{m,m}$. The mean PTV D_{90} reduction was larger for intermediate energy sources (4%-7%) than for high energy sources (∼1%). Similarly, mean differences for the PTV V_{100} (<6% or <1.5 cm^3), V_{150} (<15% or <2.0 cm^3) and V_{200} (<10% or <0.6 cm^3) increased with decreasing source energy. The ratios of $D_{m,m}/D_{w,w}$ for the mandible D_{mean} and D_{max} were about 0.9, 1.0 and 1.2 for ^{60}Co, ^{192}Ir and ^{75}Se, respectively. The ratios for the mandible D_{mean} (D_{max}) were 2.1 (2.5) for ^{169}Yb and 3.2 (4.4) for ^{153}Gd, respectively.

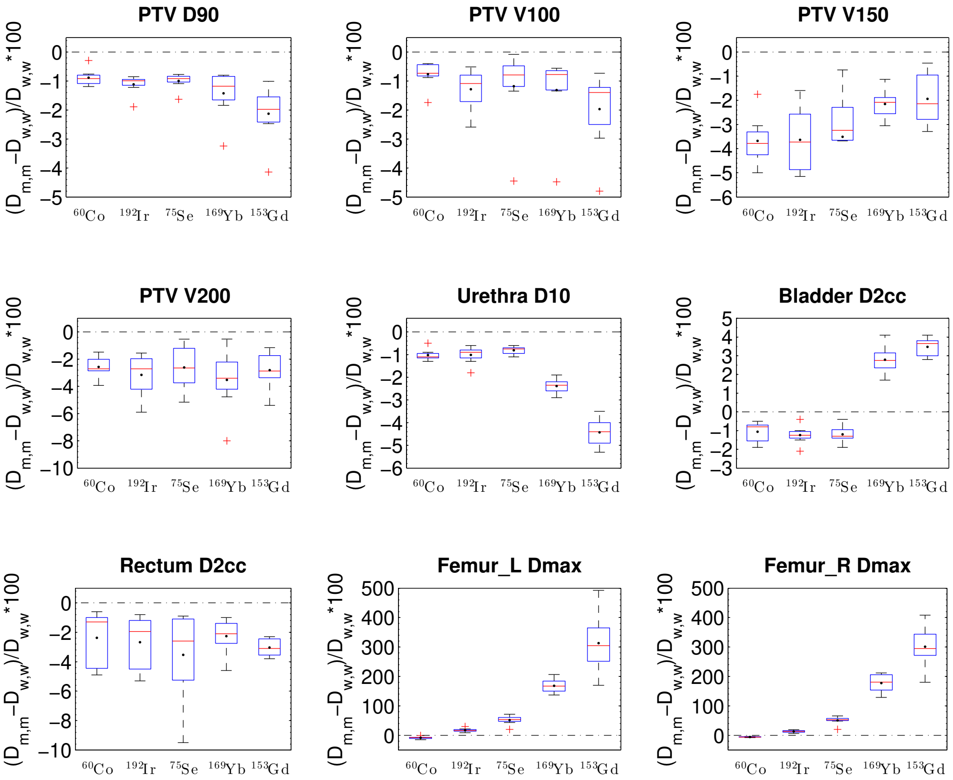

Figure 7.2: Boxplots of the relative differences in dosimetric indices between $D_{w,w}$ and $D_{m,m}$ for the prostate brachytherapy cases, reported for ^{60}Co, ^{192}Ir, ^{75}Se, ^{169}Yb, and ^{153}Gd sources. The mean (black dot), median (red line), first and third quartiles (box), maximum (minimum) value within 1.5 interquartile range from top (bottom) of box (whiskers) and outliers (red '+' symbol) are indicated.

7.4 Discussion

For the prostate and oral tongue sites, $D_{w,w}$ overestimates dose to soft tissues and, as a result, PTV coverage. On average, the PTV D_{90} was reduced by ~1% for high-energy sources. These results were consistent with those reported in previous studies for prostate (0.9%) [24] and oral tongue (1.3%) [49] ^{192}Ir HDR brachytherapy. For the intermediate-energy sources, the mean PTV D_{90} reduction between $D_{w,w}$ and $D_{m,m}$ was greater for the tongue (4%-7%) than the prostate (1%-2%) cases due to the lower absorption in mean soft tissue compared to prostatic tissue for photons with energies less than 100 keV [47]. The differences were not clinically

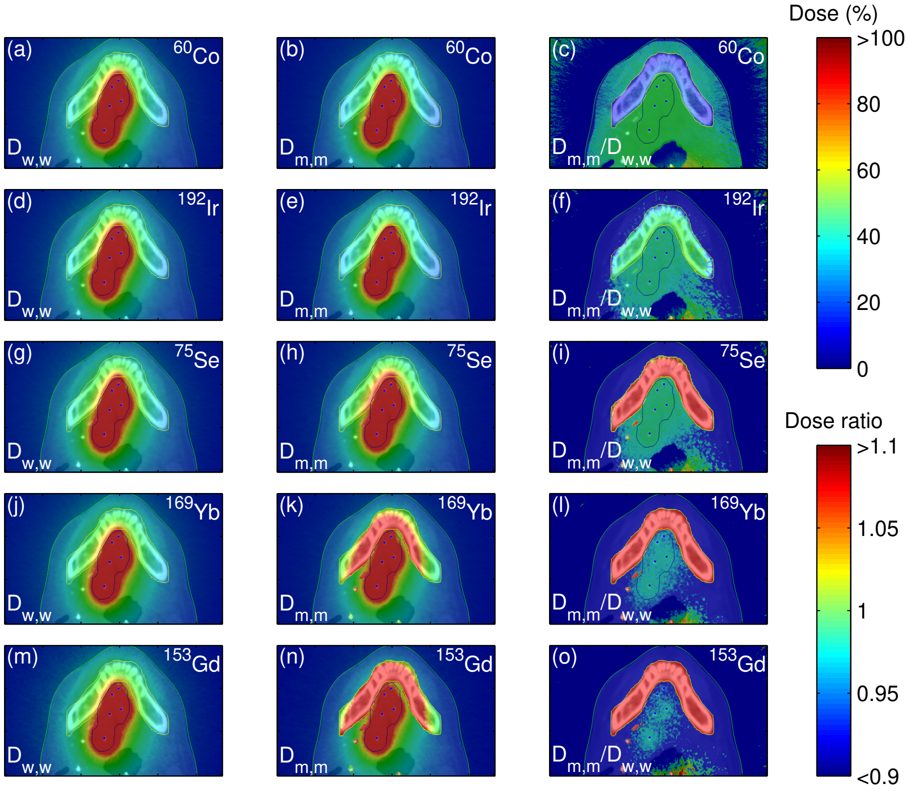

Figure 7.3: Axial CT slice for an oral tongue brachytherapy case with contours for the PTV (blue), mandible (yellow) and body (green). Dose distributions ($D_{w,w}$ and $D_{m,m}$) and dose ratio maps are overlaid over the patient geometry for (a-c) ^{60}Co, (d-f) ^{192}Ir, (g-i) ^{75}Se, (j-l) ^{169}Yb, and (m-o) ^{153}Gd. Catheter positions are indicated (blue).

relevant for the high energy sources, as they were small compared to the combined dosimetric uncertainties in brachytherapy dosimetry including source positioning uncertainties, changes in anatomy and contouring uncertainties, which can be as high as 10% (k=2) [50]. The differences may be clinically significant in some cases for intermediate energy sources. While type B uncertainties due to source modeling, physics implementation and cross sections cancel out to some extent when reporting the ratios or relative differences between $D_{w,w}$ and $D_{m,m}$ [51], it cannot be assumed that they are strongly correlated and will essentially cancel out; thus, differences smaller than $\sim$1% may not be statistically significant due to the estimated combined uncertainties (Table B.6).

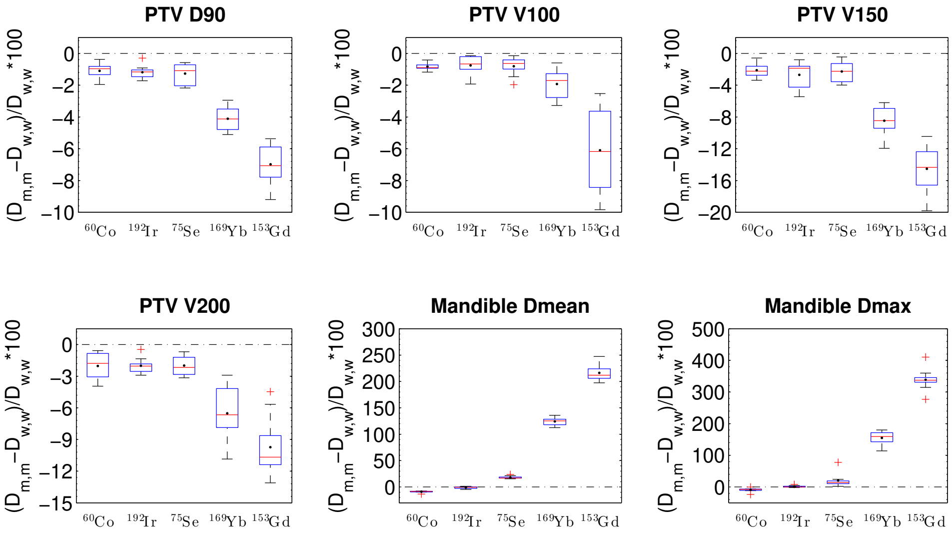
PTV D90

PTV V100

PTV V150

PTV V200

Mandible Dmean

Mandible Dmax

Figure 7.4: Boxplots of the relative differences in dosimetric indices between $D_{w,w}$ and $D_{m,m}$ for the oral tongue brachytherapy cases, reported for ^{60}Co, ^{192}Ir, ^{75}Se, ^{169}Yb, and ^{153}Gd sources. The mean (black dot), median (red line), first and third quartiles (box), maximum (minimum) value within 1.5 interquartile range from top (bottom) of box (whiskers) and outliers (red '+' symbol) are indicated.

Compton scattering, which is the dominant photon interaction for primary and scattered photons generated from high-energy brachytherapy sources, is proportional to the electron density of the tissue. For high photon energies (e.g. ^{60}Co), $D_{w,w}$ overestimates the dose to bone by ∼10% compared to $D_{m,m}$, since bone has fewer number of electrons per unit gram than water (3.00×10^{23} vs. 3.34×10^{23}, respectively) [52]. Although Compton scattering is the dominating interaction for primary photons emitting from intermediate-energy brachytherapy sources, the photoelectric effect is the dominating interaction for the low-energy single and multiple scattered photons. For these sources, $D_{w,w}$ underestimates the absorbed dose to bony structures compared to $D_{m,m}$. The lower-energy scattered photons result in an elevated dose to the high-density regions in the bony structures [26, 53]. Going from $D_{w,w}$ to $D_{m,m}$, dose to bones were increased two- to three-fold for ^{169}Yb and four- to five-fold for ^{153}Gd, while the ratio was close to ∼1 for high energy sources. The effect was of greater importance for oral tongue cases than for prostate cases, due to the closer proximity of the bone from the tumor. For the prostate cases, this resulted in elevated doses within the pelvic bone and femoral heads. For

Table 7.2: Calculation of maximum dose to the femoral head in 2 Gy equivalent fractions (EQD2) with an α/β ratio of 3 Gy for external beam radiotherapy (EBRT) combined with high dose rate (HDR) brachytherapy boost and HDR brachytherapy as a monotherapy.

Radionuclide	EBRT (15×2.5 Gy)	HDR boost (1×15 Gy)	EBRT+HDR boost	HDR monotherapy (1×21 Gy)
^{60}Co	20	2	22	3
^{192}Ir	20	2	22	3
^{75}Se	20	3	23	4
^{169}Yb	20	7	27	12
^{153}Gd	20	16	36	28

the tongue cases, this resulted in a significant portion of the mandible receiving a dose greater than the prescription dose.

While radiation-induced side effects for the bones are not generally observed for prostate HDR brachytherapy, external beam radiotherapy (EBRT) for prostate cancer has been associated with fractures of the femur and necrosis of the hip [54]. To avoid such complications, the maximum dose limits to the hottest 5% of the femoral heads are kept below 50 Gy in 2 Gy equivalent fractions (EQD2) [55]. As shown in Table 7.2, the combined femoral head dose for HDR monotherapy and HDR boost with EBRT for prostate cases is below the required threshold for all studied radionuclides. To put into perspective, Georg et al. [56] calculated that femoral head doses were ∼2 Gy EQD2 for low dose rate (LDR) brachytherapy monotherapy (145 Gy) with ^{125}I seeds, which, when converted from $D_{w,w}$ to $D_{m,m}$ (mass-energy absorption coefficient ratio of ∼7), results in ∼14 Gy EQD2 (well below the threshold). On another note, Trindade et al. [57] showed that high doses on the order of 100% of the prescription dose (145 Gy) were found on the interface between pelvic bone and soft tissue for ^{125}I when calculated using $D_{m,m}$, which results in ∼80 Gy EQD2 to a region within the pelvic bone. However, pelvic bone complications are rarely reported for LDR brachytherapy. In this study, the pelvic bone received less than the prescription dose for all the radionuclides considered for HDR brachytherapy, suggesting that the dose burden to the pelvic bone should also be well tolerated. While bone complications are generally not expected for prostate cases, dose to bony structures are considerably higher for intermediate-energy sources than high-energy sources and can be reported with a more accurate estimate using MBDCAs.

On the other hand, osteonecrosis of the mandible is the most serious complication for oral cancer after radiotherapy treatments [58, 59]. Associated radiological changes of osteonecrosis include decreased bone density with fractures, cortical destruction and loss of spongiosa trabeculation. With intermediate-energy sources, the dose delivered to the mandible would exceed that delivered to the tumor which results in a plan with poor conformity. This may lead to increased occurrence and severity of side effects and would be unacceptable according to current treatment planning guidelines [36].

Intermediate- and low-energy brachytherapy sources are associated with higher relative biological effectiveness (RBE) than high-energy brachytherapy sources and EBRT. A lower physical dose with intermediate-energy brachytherapy sources might deliver the same biological effect as a higher physical dose from ^{192}Ir or ^{60}Co. Currently, all photon-emitting sources are assigned an RBE of unity [60]. However, the RBE of the radionuclides considered in this study were calculated previously [61] based on the differences in their dose deposition patterns at the nanometer scale. For the high doses and dose rates delivered with HDR brachytherapy, the RBE is expected to vary between 1.00 (^{60}Co) and 1.18 (^{153}Gd) depending on the photon energy as presented in Table 7.1. It is therefore important to consider that, given the same physical dose, the biological effect is expected to be greater for sources with lower energies as described above. To achieve the same biological effect, prescription doses may need to be adjusted using the ratio of RBE values to account for the change in radiation quality between alternative radionuclides.

7.5 Conclusions

The TG-43 formalism underestimates the dose absorbed in bones and, to a lesser extent, overestimates the dose in soft tissues for radionuclides with average energies lower than ^{192}Ir. Our results also suggest that TG-186-based dosimetry should be used in combination with intermediate-energy brachytherapy sources such that patient tissue heterogeneity is taken into account enabling reporting of bone doses. The combined dose from all treatment modalities should be considered to evaluate whether the use of an alternative source presents an increased risk of complications. Further studies regarding bone toxicities are needed before intermediate-energy sources can be used in clinical cases where bones are directly adjacent to the tumor such as the oral tongue cases. While this study has focused on prostate and oral tongue brachytherapy, it is expected that these results can be extended to any site in the pelvic or head & neck region treated with HDR brachytherapy.

Acknowledgements: This work was supported by Collaborative Health Research Projects [grant number 523394-18] and the Natural Sciences and Engineering Research Council of Canada [grant number 241018].

Conflict of interest: None.

Supplementary material: Supplementary material for this article can be found in Appendix B.

References

[1] Beaulieu L, Carlsson Tedgren A, Carrier JF, Davis SD, Mourtada F, Rivard MJ, et al. Report of the Task Group 186 on model-based dose calculation methodsbin brachytherapy beyond the TG-43 formalism: current status and recommendations for clinical implementation. Med Phys. 2012;39(10):6208–6236.

[2] Weeks KJ, Schulz RJ. Selenium-75: A potential source for use in high-activity brachytherapy irradiators. Med Phys. 1986;13(5):728–731.

[3] Mason DL, Battista JJ, Barnett RB, Porter AT. Ytterbium-169: calculated physical properties of a new radiation source for brachytherapy. Med Phys. 1992;19(3):695–703.

[4] Loft SM, Coles IP, Dale RG. The potential of ytterbium 169 in brachytherapy: A brief physical and radiobiological assessment. Br J Radiol. 1992;65:252–257.

[5] MacPherson MS, Battista JJ. Radioactivity measurements of ytterbium-169 brachytherapy sources. Australas Phys Eng Sci Med. 1998;21(1):18–23.

[6] Lymperopoulou G, Papagiannis P, Sakelliou L, Milickovic N, Gianoulli S, Baltas D. A dosimetric comparison of 169Yb versus 192Ir for HDR prostate brachytherapy. Med Phys. 2005;32(12):3832–3842.

[7] Papagiannis P, Karaiskos P, Giorgiou E, Baltas D, Lymperopoulou G, Pantelis E, et al. On the use of high dose rate 192Ir and 169Yb sources with the MammoSite radiation therapy system. Med Phys. 2007;34(9):3614–3619.

[8] Strohmaier S, Zwierzchowski G. Comparison of ^{60}Co and ^{192}Ir sources in HDR brachytherapy. J Contemp Brachytherapy. 2011;3:199–208.

[9] Enger SA, Fisher DR, Flynn RT. Gadolinium-153 as a brachytherapy source. Phys Med Biol. 2013;58(4):957–964.

[10] Famulari G, Urlich T, Armstrong A, Enger SA. Practical aspects of ^{153}Gd as a radioactive source for use in brachytherapy. Appl Radiat Isot. 2017;130:131–139.

[11] Safigholi H, Meigooni AS, Song WY. Comparison of ^{192}Ir, ^{169}Yb, and ^{60}Co high-dose rate brachytherapy sources for skin cancer treatment. Med Phys. 2017;44(12):4426–4436.

[12] Flynn RT, Adams QE, Hopfensperger KM, Wu X, Xu W, Kim Y. Efficient ^{169}Yb high-dose-rate brachytherapy source production using reactivation. Med Phys. 2019;46:2935–2943.

[13] Adams QE, Xu J, Breitbach EK, Enger SA, Rockey WR, Kim Y, et al. Interstitial rotating shield brachytherapy for prostate cancer. Med Phys. 2014;41(5):051703.

[14] Dadkhah H, Hopfensperger KM, Kim Y, Wu X, Flynn RT. Multisource rotating shield brachytherapy apparatus for prostate cancer. Int J Radiat Oncol Biol Phys. 2017;99(3):719–728.

[15] Safigholi H, Han DY, Mashouf S, Soliman A, Meigooni AS, Owrangi A, et al. Direction modulated brachytherapy (DMBT) for treatment of cervical cancer: A planning study with 192Ir, 60Co, and 169Yb HDR sources. Med Phys. 2017;44(12):6538–6547.

[16] Reynoso FJ, Munro III JJ, Sho SH. Technical note: Monte Carlo calculations for the AAPM TG-43 brachytherapy dosimetry parameters for the titanium-encapsulated Yb-169 source. Med Phys. 2017;18:193–199.

[17] Nath R, Andersson LL, Luxton G, Weaver KA, Williamson JF, Meigooni AS. Dosimetry of interstitial brachytherapy sources: Recommendations of the AAPM Radiation Therapy Committee Task Group No. 43. Med Phys. 1995;22(1):209–234.

[18] Rivard MJ, Coursey BM, DeWerd LA, Hanson WF, Huq MS, Ibbott GS, et al. Update of AAPM Task Group No. 43 Report: A revised AAPM protocol for brachytherapy dose calculations. Med Phys. 2004;31(3):633–674.

[19] Fotina I, Zourari K, Lahanas V, Pantelis E, Papagiannis P. A comparative assessment of inhomogeneity and finite patient dimension effects in ^{60}Co and ^{192}Ir high-dose-rate brachytherapy. J Contemp Brachytherapy. 2018;10:73–84.

[20] Anagnostopoulos G, Baltas D, Pantelis E, Papagiannis P, Sakelliou L. The effect of patient inhomogeneities in oesophageal ^{192}Ir HDR brachytherapy: A Monte Carlo and analytical dosimetry study. Phys Med Biol. 2004;49:2675–2685.

[21] Pantelis E, Papagiannis P, Karaiskos P, Angelopoulos A, Anagnostopoulos G, Baltas D, et al. The effect of finite patient dimensions and tissue inhomogeneities on dosimetry planning of ^{192}Ir HDR breast brachytherapy: a Monte Carlo dose verification study. Int J Radiat Oncol Biol Phys. 2015;61(5):1596–1602.

[22] Yazdi HS, Shamsaei M, Jaberi R, Shabani HR, Allahverdi M, Vaezzadeh SA. The effect of rib and lung heterogeneities on the computed dose to lung in Ir-192 high-dose-rate breast brachytherapy: Monte Carlo versus a treatment planning system. J Cancer Res Ther. 2012;8:394–398.

[23] Poon E, Verhaegen F. MO-D-AUD B01: An analytical approach to account for shielding, anatomical heterogeneities and patient dimensions for ^{192}Ir high dose rate brachytherapy applications. Med Phys. 2008;35:2864.

[24] Ma Y, Lacroix F, Lavellée MC, Beaulieu L. Validation of the Oncentra Brachy Advanced Collapsed cone Engine for a commercial ^{192}Ir source using heterogeneous geometries. Brachytherapy. 2015;14:939–952.

[25] Gialousis G, Dimitriadis A, Yakoumakis E. Monte Carlo estimation of dose difference in lung from 192Ir brachytherapy due to tissue inhomogeneity. Radiat Prot Dosimetry. 2011;147:287–290.

[26] Safigholi H, Song WY, Meigooni AS. Optimum radiation source for radiation therapy of skin cancer. J Appl Clin Med Phys. 2015;16:219–227.

[27] Lymperopoulou G, Papagiannis P, Angelopoulos A, Karaiskos P, Georgiou E, Baltas D. A dosimetric comparison of ^{169}Yb and ^{192}Ir for HDR brachytherapy of the breast, accounting for the effect of finite patient dimensions and tissue inhomogeneities. Med Phys. 2006;33(12):4583–4589.

[28] Cazeca MJ, Medich DC, Munro III JJ. Monte Carlo characterization of a new Yb-169 high dose rate source for brachytherapy application. Med Phys. 2010;37(3):1129–1136.

[29] Hoskin PJ, Rojas AM, Bownes PJ, Lowe GJ, Ostler PJ, Bryant L. Randomised trial of external beam radiotherapy alone or combined with high-dose-rate brachytherapy boost for localised prostate cancer. Radiother Oncol. 2012;103:207–222.

[30] Gay HA, Michalski JM, Baumann B, DeWees T. A Phase I/II Study Evaluating the Safety and Efficacy of 21 Gy for High Dose Rate (HDR) Prostate Brachytherapy. Identifier No. NCT03424850;. Retrieved from https://clinicaltrials.gov/ct2/show/NCT03424850.

[31] Mazeron JJ, Ardiet JM, Haie-Méder C, Kovács G, Levendag P, Peiffert D, et al. GEC-ESTRO recommendations for brachytherapy for head and neck squamous cell carcinomas. Radiother Oncol. 2009;91:150–156.

[32] Daskalov GM. Monte Carlo-aided dosimetry of a new high dose-rate brachytherapy source. Med Phys. 1998;25:2200–2208.

[33] Reynolds SA. Theoretical and practical specific activities and other properties of common radionuclides. Oak Ridge, TN: Oak Ridge National Laboratory; 1973. ORNL-TN-4167.

[34] Renaud M, Famulari G, Seuntjens J, Enger SA. OC-0256: Column generation-based Monte Carlo treatment planning for rotating shield brachytherapy. Radiother Oncol. 2016;119:S118.

[35] Hsu IC, Bae K, Shinohara K, Pouliot J, Purdy J, Ibbott G, et al. Phase II trial of combined high-dose-rate brachytherapy and external beam radiotherapy for adenocarcinoma of the prostate: preliminary results of RTOG 0321. Int J Radiat Oncol Biol Phys. 2010;78(3):751–758.

[36] Kovács R, Martinez-Monge R, Budrukkar A, Guinot JL, Johansson B, Strnad V, et al. GEC-ESTRO ACROP recommendations for head & neck brachytherapy in squamous cell carcinomas: 1st update - Improvement by cross sectional imaging based treatment planning and stepping source technology. Radiother Oncol. 2017;122:248–254.

[37] ICRU. Photon, electron, proton and neutron interaction data for body tissues. vol. ICRU report 46. Bethesda, MD: International Commission on Radiation Units & Measurements; 1992.

[38] Miksys N, Vigneault E, Martin AG, Beaulieu L, Thomson RM. Large-scale retrospective Monte Carlo dosimetric study for permanent implant prostate brachytherapy. Int J Radiat Oncol Biol Phys. 2017;97:606–615.

[39] Famulari G, Renaud M, Poole CM, Evans MDC, Seuntjens J, Enger SA. RapidBrachyMCTPS: a Monte Carlo-based treatment planning system for brachytherapy applications. Phys Med Biol. 2018;63(17):175007.

[40] Agostinelli S, Allison J, al Amako K, Apostolakis J, Araujo H, Arce P, et al. Geant4 - a simulation toolkit. Nucl Inst Meth Phys Res A. 2003;506(3):250–303.

[41] Allison J, Amako K, Apostolakis J, Araujo H, Dubois PA, Asai M, et al. Geant4 developments and applications. IEEE Trans Nucl Sci. 2006;53(1):270–278.

[42] Tuli JK. Evaluated nuclear structure data file, a manual for preparation of data sets. Lawrence Berkeley National Laboratory, Berkeley, CA; 1987.

[43] Cullen DE, Hubbell JH, Kissel L. EPDL97: the evaluated photo data library '97 version. LLNL Report No. UCRL-50400. Lawrence Livermore National Laboratory, Livermore, CA; 1997.

[44] Perkins ST, Cullen DE, Seltzer MN. Tables and graphs of electron-interaction cross sections derived from the LLNL Evaluated Electron Data Library (EEDL), Z = 1-100. LLNL Report No. UCRL-50400-v-31. Lawrence Livermore National Laboratory, Livermore, CA; 1997.

[45] Perkins ST, Cullen DE, Chen MH, Hubell JH, Rathkopf J, Scofeld J. Tables and graphs of atomic subshell and relaxation data derived from the LLNL Evaluated Atomic Data Library (EADL), Z = 1-100. LLNL Report No. UCRL-50400-v-30. Lawrence Livermore National Laboratory, Livermore, CA; 1997.

[46] Williamson JF. Monte Carlo evaluation of kerma at a point for photon transport problems. Med Phys. 1987;14:567–576.

[47] Mann-Krzisnik D, Verhaegen F, Enger SA. The influence of tissue composition uncertainty on dose distributions in brachytherapy. Radiother Oncol. 2018;126:394–410.

[48] Sechopoulos I, Rogers DWO, Bazalova-Carter M, Bolch WE, Heath EC, McNitt-Gray MF, et al. RECORDS: improved Reporting of MontE CarlO RaDiation transport Studies: Report of the AAPM Research Committee Task Group 268. Med Phys. 2017;45:e1–e5.

[49] Peppa V, Pappas E, Major T, Takácsi-Nagy Z, Pantelis E, Papagiannis P. On the impact of improved dosimetric accuracy on head and neck high dose rate brachytherapy. Radiother Oncol. 2016;120(1):92–97.

[50] DeWerd LA, Ibbott GS, Meigooni AS, Mitch MG, Rivard MJ, Stump KE, et al. A dosimetric uncertainty analysis for photon-emitting brachytherapy sources: Report of AAPM Task Group No. 138 and GEC-ESTRO. Med Phys. 2011;38(2):782–801.

[51] Andreo P, Burns DT, Salvat F. On the uncertainties of photon mass energy-absorption coefficients and their ratios for radiation dosimetry. Phys Med Biol. 2012;57:2117–2136.

[52] Khan FM, Gibbons JP, Pine JW. Khan's the physics of radiation therapy. Philadelphia, PA: Lipincott Williams & Wilkins/Wolters Kluwer; 2014.

[53] Fonseca G, Carlsson Tedgren A, Reniers B, Nilsson J, Persson M, Yoriyaz H, et al. Dose specification for ^{192}Ir high dose rate brachytherapy in terms of dose-to-water-in-medium and dose-to-medium-in-medium. Phys Med Biol. 2015;60:4565–4579.

[54] Elliott SP, Jarosek SL, Alanee SR, Konety BR, Dusenbery KE, Virnig BA. Three-dimensional external beam radiotherapy for prostate cancer increases the risk of hip fracture. Cancer. 2011;117:4557–4565.

[55] Lawton CAF, Michalski J, El-Naqa I, Buyyounouski MK, Lee WR, Menard C, et al. RTOG GU Radiation oncology specialists reach consensus on pelvic lymph node volumes for high-risk prostate cancer. Int J Radiat Oncol Biol Phys. 2009;74:383–387.

[56] Georg D, Hopfgartner J, Gòra J, Kuess P, Kragl G, Berger D, et al. Dosimetric considerations to determine the optimal technique for localized prostate cancer among external photon, proton, or carbon-ion therapy and high-dose-rate or low-dose-rate brachytherapy. Int J Radiat Oncol Biol Phys. 2014;88:715–722.

[57] Trindade BM, Christovao MT, Trindade DFM, Falcao PL, de Campos TPR. Comparative dosimetry of prostate brachytherapy with I-125 and Pd-103 seeds vis SISCODES/MCNP. Radiol Bras. 2012;45:267–272.

[58] Lozza L, Cerrotta A, Gardani G, De Marie M, Di Russo A, Kenda R, et al. Analysis of risk factors for mandibular bone radionecrosis after exclusive low dose-rate brachytherapy for oral cancer. Radiother Oncol. 1997;44(2):143–147.

[59] Jereczek-Fossa BA, Orecchia R. Radiotherapy-induced mandibular bone complications. Cancer Treat Rev. 2002;28(1):65–74.

[60] ICRP. The 2007 recommendations of the International Commission on Radiological Protection. ICRP publication 103. Ann ICRP. 2007;37(2-4):1–332.

[61] Famulari G, Pater P, Enger SA. Microdosimetric evaluation of current and alternative brachytherapy sources - a Geant4-DNA simulation study. Int J Radiat Oncol Biol Phys. 2018;100(1):270–277.

Chapter 8

A novel ^{169}Yb-based dynamic-shield intensity modulated brachytherapy system for prostate cancer

Abstract

Purpose: Intensity modulated brachytherapy (IMBT) is a novel high dose rate brachytherapy (HDR BT) technique which incorporates static or dynamic shielding to increase tumor coverage and/or spare healthy tissues. The purpose of this study is to present a novel delivery system (AIM-Brachy) design that can enable dynamic-shielded IMBT for prostate cancer.

Materials and methods: The AIM-Brachy system dynamically controls the rotation of platinum shields, placed within interstitial catheters, which partially collimate the radiation emitted from an ^{169}Yb source. Conventional HDR BT and IMBT plans were generated using an in-house column generation-based optimizer, coupled to a Geant4-based dose calculation engine, RapidBrachyMC. Treatment plans were normalized to match the same PTV D_{90} coverage as the clinical plan. A sensitivity analysis was performed to evaluate the dosimetric impact of longitudinal source positioning errors (±1 mm, ±2 mm and ±3 mm) and rotational errors (±5°, ±10° and ±15°) on clinically relevant parameters (PTV D_{90} and urethra D_{10}).

Results: The platinum shield reduced the dose on the shielded side at 1 cm off-axis to 18.1% of the dose on the unshielded side. For equal PTV D_{90} coverage, the urethral D_{10} was reduced by 13.3%±4.7%, without change to other plan quality indices. Delivery times for HDR BT and IMBT were 9.2±1.6 mins and 18.6±4.0 mins, respectively. In general, the PTV D_{90} was more

sensitive to source positioning errors than rotational errors, while the urethral D_{10} was more sensitive to rotational errors than source positioning errors. For a typical range of positioning errors (±1 mm, ±5°), the overall tolerance was less than 2%.

Conclusions: The AIM-Brachy system was proposed to deliver dynamic-shielded IMBT for prostate cancer with the potential to create a low dose tunnel within the urethra. The urethra-sparing properties are desirable to minimize the occurrence and severity of urethral strictures or, alternatively, to provide a method for dose escalation.

8.1 Introduction

High dose rate brachytherapy (HDR BT) for prostate cancer is an effective therapy delivered either as a monotherapy or as a boost in combination with external beam radiotherapy (EBRT) [1, 2]. The HDR BT boost is a recommended method of dose escalation for intermediate- and high-risk prostate cancer [3, 4]. Several studies have reported a higher disease-free survival in patients treated with HDR BT combined with EBRT compared to those treated with EBRT alone [5, 6]. While late grade 3 gastrointestinal (GI) toxicity is rare, the rate of late grade 3 genitourinary (GU) toxicity for patients treated with a HDR BT boost ranges from 1% to 14% [7–11]. Urethral stricture is the most common late grade 3 GU toxicity from the combined HDR BT and EBRT treatments. The brachytherapy dose to the urethra is the most important predictor of long-term GU morbidity [12–14]. The low rate of toxicity for HDR BT monotherapy delivered in a single fraction of 19 Gy suggests that dose escalation may be beneficial, since local control rates are too low [2]. Further dose escalation to 21 Gy or more is currently limited by urethral dose constraints.

Radiation sources used in HDR BT have conventionally provided radially symmetric dose distributions. While HDR BT can deliver very high doses to tumours with good conformity in general, many available dwell positions in close proximity to organs at risk are limited in their overall contribution to the dose distribution due to the radially symmetric emission constraint. Intensity modulated brachytherapy (IMBT) is a novel brachytherapy technique which incorporates static or dynamic shields inside needles or applicators to direct the radiation towards the tumor and away from healthy tissues [15–17]. IMBT has been investigated for prostate [18–20], cervical [21–25] and rectal cancers [26, 27]. In the case of prostate cancer, IMBT has the capability to reduce the dose delivered to nearby radiation sensitive healthy tissues, such as the urethra, or allow for dose escalation without an associated increase in urethral dose for monotherapy [20]. However, its application in clinical practice has been limited due to lack of a commercially available radiation source and delivery system.

A multisource apparatus was proposed for the angular and linear positioning of partially shielded ^{153}Gd sources for prostate cancer [18, 19]. The proposed system could generate treatment plans which reduced the urethra D_{10} by 20.2%-26.0% on average without affecting target coverage using a 3 mm margin around the urethra to provide a dose gradient [20]. Due to the low maximum specific activity of ^{153}Gd [28, 29], the system was designed to handle multiple sources simultaneously to improve treatment times. Still, the financial and logistic issues related to implementing up to 20 sources and the long treatment times ($\sim$2 h) limits the clinical feasibility of the technique. Delivering IMBT within clinically acceptable treatment times requires a radiation source with a high specific activity, long half-life and appropriate energy spectrum.

^{169}Yb has been investigated as a source for brachytherapy applications [30–35]. ^{169}Yb has a half-life of 32.0 days and primarily emits photons with energies in the 50-308 keV range with an average energy of 93 keV [30]. The tenth-value layer (TVL) is 1.0 mm of platinum, which suggests a partially attenuating shield can be inserted within an interstitial catheter to collimate the radiation source. The lower energy also reduces the shielding requirements for treatment rooms. The availability of Yb_2O_3 powder highly enriched in ^{168}Yb (82%-88%) enables manufacturing of ^{169}Yb sources with high activities ($\sim$30 Ci), fitted inside capsules appropriate for HDR BT [35].

The purpose of this work is to present the concept and design of the anisotropic intensity modulated brachytherapy (AIM-Brachy) device, a novel delivery system that can enable ^{169}Yb-based dynamic-shield IMBT for prostate cancer, and to evaluate the potential urethra-sparing advantages of IMBT delivered with AIM-Brachy relative to HDR BT. The AIM-Brachy system was designed to be compatible with commercial afterloaders by incorporating an ^{169}Yb HDR source and a compact rotating mechanism that can be directly connected to the afterloader through the transfer tubes. Compared to previous designs [18, 19], the solution is cost-effective and does not require a custom afterloader for source translation. A prototype was developed to validate the functionality of the system design.

8.2 Materials and methods

8.2.1 Source and shield design

An ^{169}Yb source model was designed specifically for the AIM-Brachy system (Figure 8.1). The source has an active core which consists of Yb_2O_3 (6.9 g cm^{-3}). The active core has a diameter of 0.4 mm and a length of 3.2 mm, and is enclosed in an AISI 306 stainless steel capsule (7.8 g cm^{-3}) with an outer diameter of 0.6 mm and a wall thickness of 0.1 mm. The core material is compressed into the pellet with a density of 4.54 g cm^{-3} and sintered to a density of 7.5 g cm^{-3} before irradiation. An Yb_2O_3 target enriched to 20% ^{168}Yb irradiated in a reactor with a thermal neutron flux of 1×10^{14} n cm^{-2} s^{-1} can produce an ^{169}Yb source with a specific activity of $\sim$1400 Ci g^{-1} Yb_2O_3 [36]. For an Yb_2O_3 target with an enrichment level of 85%, this corresponds to a specific activity of $\sim$6000 Ci g^{-1} Yb_2O_3. With the proposed source dimensions, this results in an ^{169}Yb source with a total initial activity of 18 Ci. The source can be adapted to handle more activity to lower treatment times, if needed, by increasing the length of the active core. For a highly enriched precursor, the ^{175}Yb impurities levels are sufficiently low after activation and additional cooling is not required [35, 37]. To modulate the intensity profile of the source, thin platinum shields are inserted within the catheters, using a similar approach as Adams et al. [18]. Platinum was selected due to its high density (21.45 g cm^{-3}), high atomic number (Z=78) and ferromagnetic properties. The shield partially fills the hollow portion of a 6 French (2 mm) plastic catheter with a wall thickness of 0.25 mm (Figure 8.1bc). The platinum shield has a maximum thickness of 0.8 mm, an outer diameter of 1.45 mm and a total length that covers the entire needle. The platinum shield contains an emission window of 180° and a groove which guides the motion of the source through the catheter. The emission window is filled with air. The source is offset from the central axis of the catheter to maximize the amount of shielding that can be fit within the catheter. To account for this offset, the shield will provide a smooth transition for the source to travel through as it enters the catheter (Figure 8.1b). The presence of a 25 μm air gap between the shield, source and catheter allows the source to translate and the shield to rotate freely within the catheter. However, the current system does not allow insertion of shields into curved catheters. In practice, any curved catheter will be straightened when the shield is inserted into the catheter.

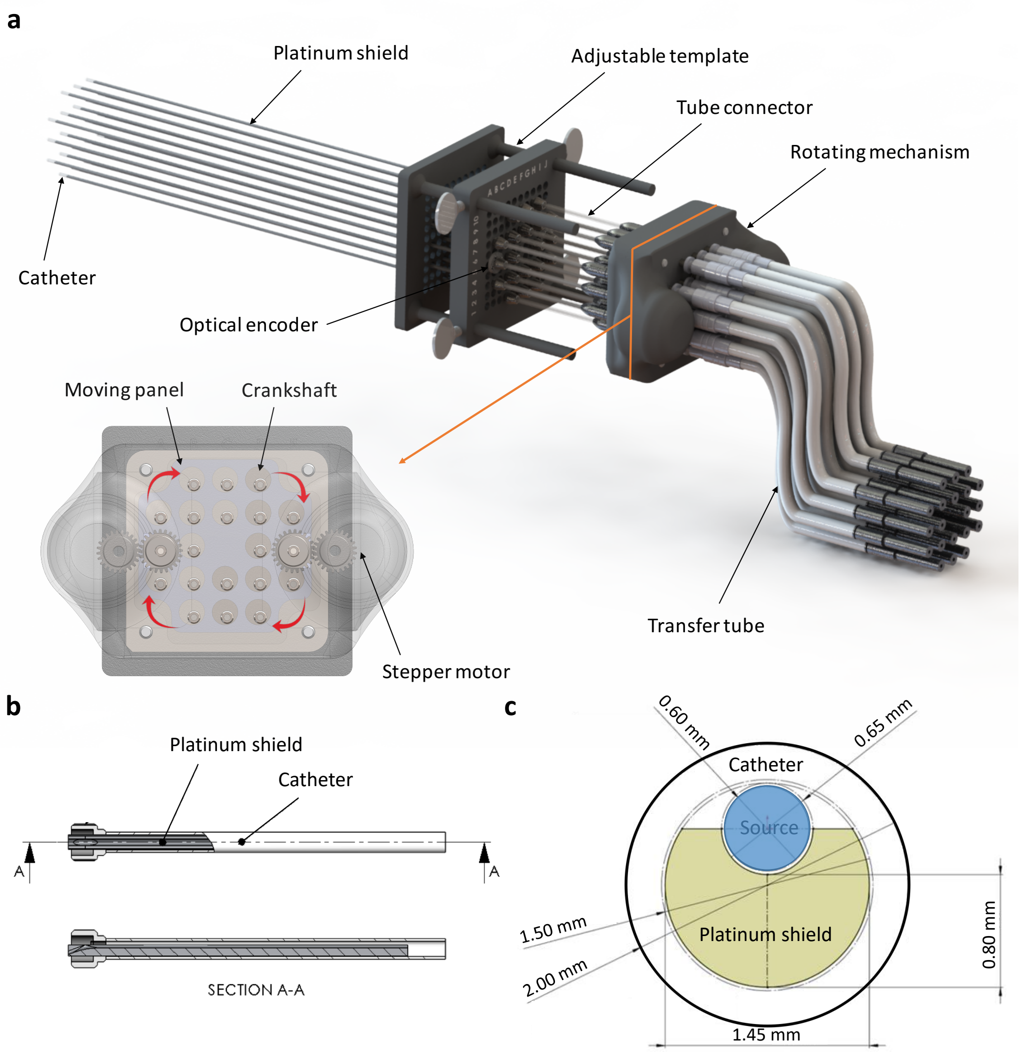

Figure 8.1: (a) Isometric view of the AIM-Brachy system. The device dynamically controls the orientation of platinum shields inserted within interstitial catheters. A cross section of the rotating mechanism is shown to illustrate the moving panel concept. Rotational motion of the stepper motor drives the rotation of the primary gear, illustrated with white center, which initiates the translational motion of the moving panel in a circular pattern (see Supplementary File 1 for animation). The crankshaft system converts the circular motion of the moving panel into rotational motion of the shields. For a dual source delivery (optional), a second stepper motor drives a second moving panel layer (see Supplementary File 2) such that each stepper motor only drives a subset of the shields. Side view is shown in Figure C.3. Cross section of rotating mechanism with dimensions in mm are displayed in Figure C.4. (b) Longitudinal and (c) transverse cross sections of the shield and catheter with dimensions.

8.2.2 System overview

AIM-Brachy is a portable device that dynamically controls the rotation of platinum shields placed inside interstitial catheters for prostate HDR BT. The rotating mechanism transmits the rotation of a stepper motor to the shields through a crankshaft system using a moving panel concept (Figure 8.1a). The crankshaft system converts the rotational motion of the stepper motor into circular motion of a moving panel. The crankshaft system then converts the circular motion of the moving panel into rotational motion of the male connectors on the outside of the rotating mechanism, which drive the rotation of the shields. The male connectors, moving panel and crankshafts are composed of stainless steel. The shields are connected to the rotating panel through flexible tube connectors. The tube connectors consist of stainless steel (AISI 316L) assembled with flexible nylon tubing. Flexible nylon has excellent dimensional stability, which ensures that the rotation on the proximal end is transmitted to the distal end. The flexibility of the tube connectors allows catheters to be positioned in various configurations. Shields are oriented at a known angle through a keying mechanism machined onto the male connectors on rotating mechanism. Therefore, the shields are oriented in the same direction at any given time. A second stepper motor and panel are included to ensure compatibility with a dual-source afterloader that can drive two radiation sources simultaneously. For a dual source delivery, each shield would be connected to one of the panels such that each stepper motor independently drives a different set of shields. An adjustable double-layered 3D-printed template modulates the depth of insertion of the shields and catheters. The proximal ends of the shields line up with the proximal face of the adjustable template (see Figure C.3). The distance between the template layers can be adjusted for a given patient. The prototype contains a dual L6470PD stepper motor driver (1.8° full step with up to 1/128 microstepping) which allows for a rotational accuracy of 0.014°. Optical encoders read the actual orientation of the shield and provide feedback to the stepper motor system. The encoders are placed at the entry of the shield, against the proximal template layer. The prototype uses a custom encoder with 10 mm diameter (Applied Image, Inc., Rochester, NY, USA).

8.2.3 Treatment delivery

Clinical IMBT delivery using the AIM-Brachy system will occur as follows. Following catheter implantation under transrectal ultrasound (TRUS) guidance, the planning images (either TRUS, CT, or MRI) will be acquired using the same patient positioning as will be used during treatment delivery. Once contouring is performed and catheter positions are identified, an optimized plan will be generated using inverse planning. The shields will be inserted within the catheters through the template axis. The shields will then be connected to the rotating mechanism through the tube connectors. The keying mechanism will ensure that the shields are initially placed in a known orientation. Once all the components of the delivery system are fixed as illustrated in Figure 8.1a, the transfer tubes will be connected to the rotating mechanism and the optimized treatment plan will be delivered. As in conventional HDR BT, the dwell position of the source will be controlled by a commercial remote afterloader. For a given dwell position, the shield will spend a required amount of time at each rotational angle, as determined by the treatment plan. Thus, for a given dwell position, one full rotation of all shields on the panel associated with the dwell position is required. Once the source will have spent the required dwell time at each planned dwell position and shield angle combination, the source will retract back into the safe. The current prototype coordinates rotation with positioning using a timer and an OPB911 slotted optical switch (TT Electronics) to determine the entrance and exit times of the source through the catheter.

8.2.4 Patient cohort

The patient dataset consisted of 12 prostate HDR BT cases. All patients received EBRT followed by HDR BT boost. The prescribed dose was a single fraction of 15 Gy. The patients were treated with a microSelectron v2 ^{192}Ir source (Elekta Brachytherapy, Stockholm, Sweden). Catheters were placed under TRUS guidance. The CT-based HDR BT plans were generated using the Oncentra treatment planning system (TPS) (Elekta Brachytherapy, Stockholm, Sweden). Every plan had at least the planning target volume (PTV), urethra, rectum, bladder and external body contoured.

8.2.5 Monte Carlo treatment planning

Conventional HDR BT and IMBT plans were generated using an in-house column generation-based optimizer [38]. Dose calculations were performed using RapidBrachyMC [39], a previously validated Monte Carlo code for brachytherapy applications based on the Geant4 toolkit [40, 41]. The microSelectron v2 ^{192}Ir source (10 Ci) and shielded ^{169}Yb source (18 Ci) were modelled for HDR BT and IMBT, respectively. The PENELOPE electromagnetic physics list was used to transport photons. Dose was approximated by collision kerma and was scored using a track length estimator [42]. Tissue composition assignment was based on the recommendations of TG-186 [43]. The elemental compositions of tissues were taken from ICRU

46 [44] and mass densities were derived from the Hounsfield unit (HU) values from CT scan. The dose rate distributions were calculated for each beamlet (dwell position and shield angle combination) directly onto the patient geometry. The beamlet dose distributions were then used as inputs into the optimization algorithm. For HDR BT and IMBT optimization, dose distributions were generated for the same activated dwell positions as the delivered plan. In the case of IMBT optimization, 16 dose distributions were generated for each dwell position, corresponding to equally spaced shield angles of 22.5°. Intershield attenuation was explicitly taken into account by overlaying all shields in the patient geometry. The orientation of the various shields was modeled for each dwell position and shield angle combination. Assuming a single source delivery, all shields were oriented in the same direction at the same time. Dose was scored using a 1 mm^3 voxel grid. The number of photon histories per beamlet was set to 2×10^7 to achieve statistical uncertainties per beamlet of 0.5%, 0.8% and 2.5% at the 200%, 100% and 10% isodose levels, respectively.

Treatment plans were normalized to match the same PTV D_{90} coverage as the original clinical plan. The dose-volume constraints were taken from the Radiation Therapy Oncology Group (RTOG) 0321 protocol [45]. The PTV V_{100}, V_{150} and V_{200} were constrained to >90%, <35% and <12%, respectively. The rectum V_{75}, bladder V_{75} and urethral D_{10} were limited to <1 cm^3, <1 cm^3 and <120% (18.0 Gy), respectively. Dose-volume constraints and weights were chosen to maximize urethral sparing while satisfying the RTOG 0321 protocol recommendations. The homogeneity index (HI) [46] and conformity index (COIN) [47] were reported in addition to the dose-volume metrics mentioned. Dose distributions and dose-volume histograms (DVHs) were extracted for visualization. Differences in dose-volume metrics were evaluated for statistical significance using a paired sampled Wilcoxon signed rank test with a criterion of $p < 0.05$.

8.2.6 Uncertainty tolerance

There are a number of uncertainties related to the delivery of IMBT using the AIM-Brachy system. The most important sources include: (1) the uncertainty in the source positioning with a commercial afterloader and (2) the uncertainty in the orientation of the shields, (3) the uncertainty in digitization, (4) the uncertainty in patient/applicator relative movement and (5) the uncertainty in applicator length. Setup uncertainties occurring during treatment can degrade target coverage and increase the dose to organs at risk. To evaluate the uncertainty tolerance of the proposed delivery system, systematic longitudinal source positioning shifts of ±1 mm, ±2 mm and ±3 mm and systematic angular orientation shifts of ±5°, ±10° and ±15° were applied.

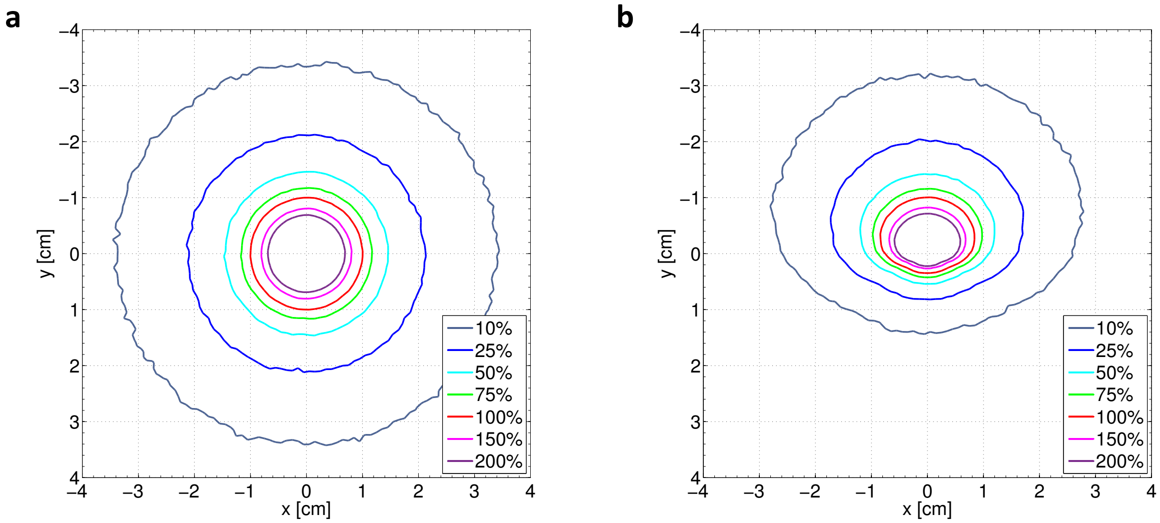

Figure 8.2: Relative dose distribution in the transverse plane of (a) an ^{192}Ir source for conventional high dose rate brachytherapy (HDR BT) and (b) a shielded ^{169}Yb source for intensity modulated brachytherapy (IMBT), normalized to 100% at a radial distance of 1 cm from the source on the unshielded side.

The PTV D_{90} and urethral D_{10} were evaluated in each case to estimate the dosimetric impact of the setup errors on plan quality indices.

8.3 Results

The relative dose distributions of an ^{192}Ir source and a shielded ^{169}Yb source are shown in Figure 8.2. The dose rate at 1 cm per unit activity of the ^{192}Ir source and the ^{169}Yb source were 4.01±0.01 cGy h^{-1} mCi^{-1} and 12.95±0.04 cGy h^{-1} mCi^{-1}, respectively. The dose rate for ^{169}Yb was in reasonable agreement with other reported values for ^{169}Yb source models: 1.31±0.03 cGy h^{-1} mCi^{-1} [31], 1.22±0.03 cGy h^{-1} mCi^{-1} [32], 1.67±0.03 cGy h^{-1} mCi^{-1} [33], and 1.37±0.02 cGy h^{-1} mCi^{-1} [34]. The platinum shield partially collimates the radiation emitted from the ^{169}Yb source to produce a highly anisotropic dose distribution. The platinum shield reduced the dose rate at a radial distance of 1 cm from the source on the shielded side down to 18.1% of the dose rate on the unshielded side.

The average DVH comparison between conventional HDR BT and IMBT treatments is shown in Figure 8.3. Table 8.1 lists the dosimetric indices obtained with both conventional

Table 8.1: Comparison in dose-volume metrics between conventional high dose rate brachytherapy (HDR BT) and intensity modulated brachytherapy (IMBT) treatment plans for prostate cancer. The p-values are derived from a paired sampled Wilcoxon signed rank test.

Structure	Dosimetric index	HDR BT	IMBT	p-value
PTV	D_{90} (Gy)	15.9±0.8	15.9±0.8	-
	V_{100} (%)	94.4±3.7	93.7±4.1	0.126
	V_{150} (%)	28.3±5.9	29.9±6.2	0.064
	V_{200} (%)	11.3±2.0	11.8±2.3	0.222
	HI	0.70±0.05	0.68±0.06	0.057
	COIN	0.76±0.05	0.75±0.05	0.477
Urethra	D_{10} (Gy)	16.7±0.7	14.5±1.2	0.002
Rectum	V_{75} (cm^3)	0.5±0.5	0.4±0.3	0.208
Bladder	V_{75} (cm^3)	0.6±0.4	0.3±0.3	0.147

HDR BT and IMBT. For equal PTV D_{90} coverage, the IMBT plans achieved a significantly lower urethral D_{10} than the conventional HDR BT plans, without significantly affecting other plan quality indices. The IMBT plans were able to improve the urethral D_{10} in all cases. The urethral D_{10} was reduced by 13.3%±4.7%. The minimum and maximum decrease for a single case were 4.1% and 20.6%, respectively. A moderate positive correlation between PTV volume and urethral D_{10} reduction was observed (R = 0.54). The low dose tunnel generated in the urethra is illustrated in Figure 8.4. For the simulated cohort of patients, the delivery times (total dwell times) for conventional HDR BT (10 Ci ^{192}Ir source) and IMBT (18 Ci ^{169}Yb source) were 9.2±1.6 mins and 18.6±4.0 mins, respectively.

The intershield attenuation caused an overall reduction in the delivered dose to the PTV and healthy tissues. The PTV D_{90}, urethra D_{10}, bladder D_{2cc} and rectum D_{2cc} were reduced on average by 7.5%, 6.5%, 11.0% and 11.9%, respectively, due to intershield attenuation. Dose differences were greatest in regions of high dose close to the dwell positions.

The impact of source positioning errors and shield orientation errors on plan quality indices are shown in Figure 8.5 and Figure 8.6, respectively. In general, systematic errors led to a decrease in PTV coverage and an increase in dose to the urethra. Source positioning shifts of ±1 mm, ±2 mm and ±3 mm correspond to average deviations of 0.7%, 2.0% and 4.0% for the PTV D_{90} and 0.6%, 1.2% and 2.0% for the urethral D_{10}. Angular shifts of ±5°, ±10° and ±15° resulted in deviations of 0.4%, 0.9% and 1.5% for the PTV D_{90} and 1.1%, 2.8% and 6.2% for the urethral D_{10}.

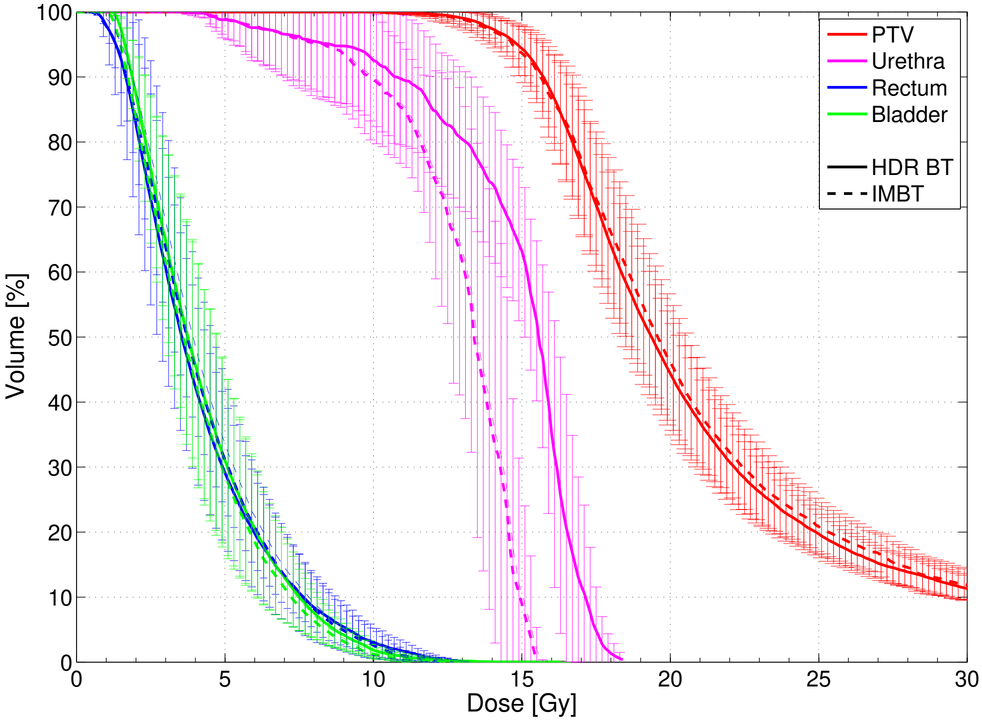

Figure 8.3: Average dose-volume histogram (DVH) for prostate cancer treated with conventional high dose rate brachytherapy (HDR BT) and intensity modulated brachytherapy (IMBT). Error bars represent standard deviations.

8.4 Discussion

In conventional HDR BT, a single source delivers a radially symmetric dose distribution. High-Z shields can attenuate the radiation in a given direction to spare healthy tissues. Dynamic motion of shields provides additional degrees of freedom that can improve plan quality. Compared to HDR BT, dynamic-shielded IMBT allows the possibility to create a low dose tunnel (region receiving less than prescription dose) within the urethra, which runs through the center of the prostate. Given equal PTV coverage, IMBT has the potential to reduce the urethra D_{10} by 13.3%±4.7% (range: 4.1%-20.6%), without affecting other plan quality indices. Patients with larger PTV volume were more likely to experience a larger reduction, with a further inter-catheter spacing and catheter-urethra distance allowing an opportunity for intensity modulation to provide a more conformal dose distribution. The urethra-sparing properties of IMBT are desirable to minimize the occurrence and severity of urethral strictures and acute/late GU

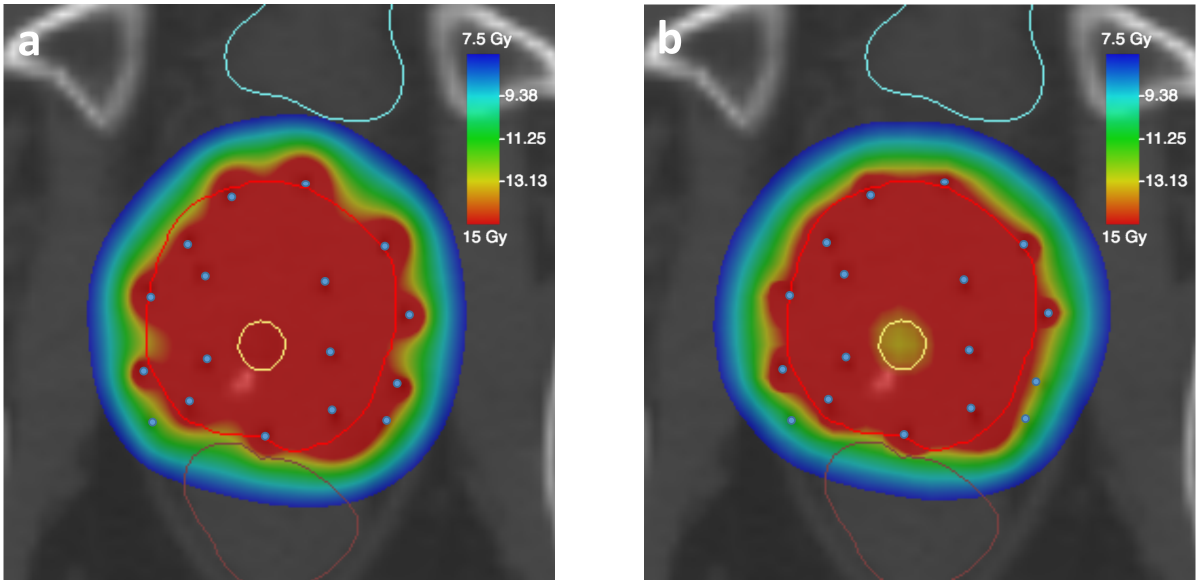

Figure 8.4: Dose colorwash comparison between (a) high dose rate brachytherapy (HDR BT) and (b) intensity modulated brachytherapy (IMBT) for a prostate cancer case. Contours are shown for the PTV (red), urethra (yellow), bladder (cyan), and rectum (brown).

toxicities in general. Alternatively, IMBT could provide a method to escalate the monotherapy dose from 19 Gy to 21 Gy or more without increasing the urethral dose, which could increase the effectiveness of brachytherapy as a monotherapy [20]. IMBT also has potential for delivering focal therapy, where an inhomogeneous dose distribution is desired to specifically treat areas within the prostate where recurrent disease is present [2].

Delivery times for IMBT with an 18 Ci ^{169}Yb source are about twice as long as those for HDR BT with a 10 Ci ^{192}Ir source, but roughly equivalent to those obtained with a 2 Ci ^{60}Co source [48]. Nevertheless, IMBT treatments can be delivered in a reasonable timeframe ($\sim$20 mins) with the proposed system, relative to the total time (multiple hours) required for needle implantation, imaging, treatment planning, treatment delivery and recovery. Due to the lower half-life of ^{169}Yb compared to ^{192}Ir (32.0 days vs. 73.8 days), source exchanges may need to be performed every month instead of every 3-4 months, to ensure delivery times are kept under 40 mins. Mass production techniques are currently under development to achieve higher specific activities which can reduce the delivery times and the frequency of source exchanges [49]. Treatment times with the proposed system can be reduced by manufacturing a source with a longer active core. While the source length was designed to match the length of most commercially available HDR BT sources, the AIM-Brachy system can accommodate

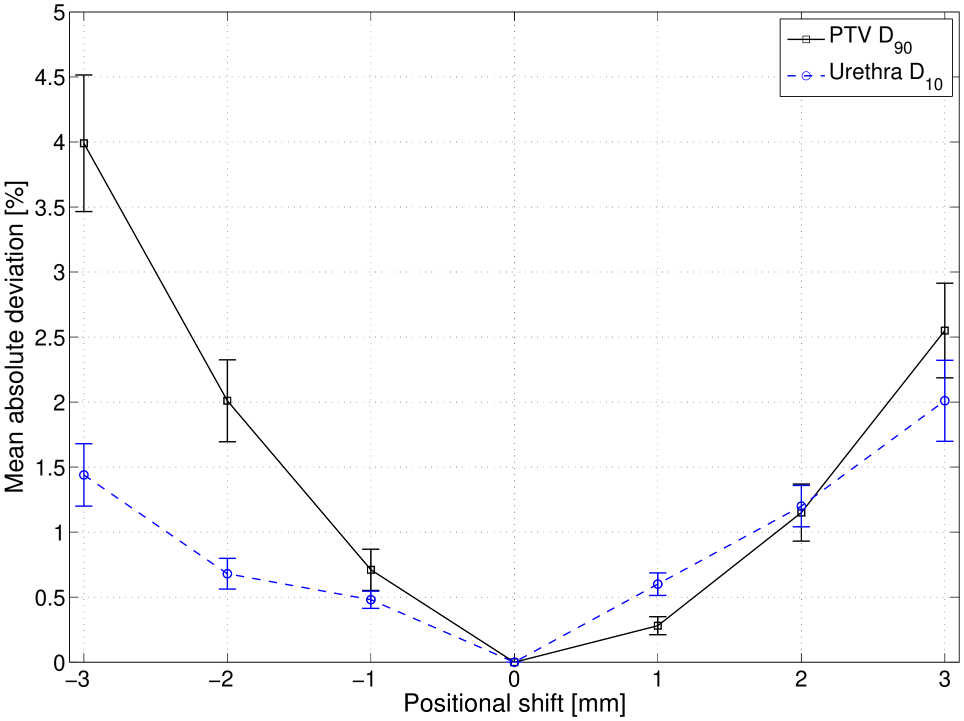

Figure 8.5: Impact of source position errors on plan quality indices. Error bars represent standard deviations. The lines joining successive points serve only as a guide to the eye.

source models of variable length as long as the source diameter is respected. Alternatively, treatment times can be reduced by combining shielded catheters with unshielded catheters in cases where IMBT is not necessarily advantageous. Delivery times can also be reduced by a factor of ∼2 using a dual source delivery, which in theory is possible with the Flexitron (Elekta Brachytherapy, Stockholm, Sweden) afterloader.

The intershield attenuation may be important to consider in the dose calculation algorithm when high-Z shielding is introduced in the patient geometry during the treatment delivery process. With multiple platinum shields present at once with a dynamically varying orientation, it was important to account for the intershield attenuation effect for the proposed system. Given the design feature that all shields are oriented in the same direction at the same time, we have developed a method to account for intershield attenuation in the dose calculation algorithm. Ignoring intershield attenuation with the proposed delivery system can result in an overestimation (6.5%-11.9%) of clinically relevant plan quality indices.

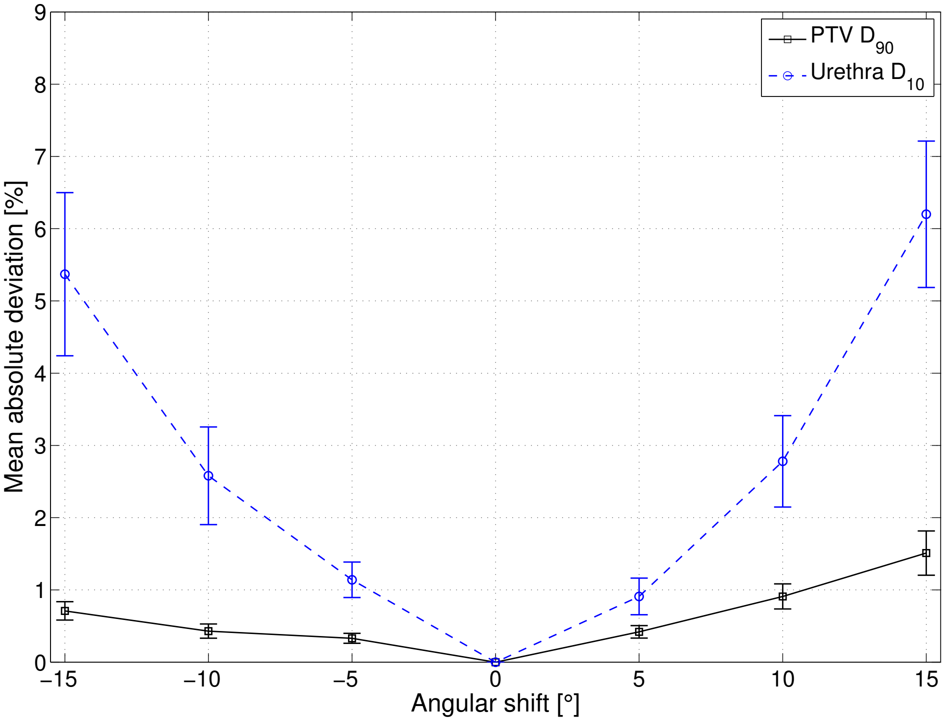

Figure 8.6: Impact of rotational shield errors on plan quality indices. Error bars represent standard deviations. The lines joining successive points serve only as a guide to the eye.

A sensitivity analysis was performed to determine the dosimetric impact of positioning errors on plan quality indices. While translational and rotational errors contain both systematic and random components, only systematic errors were considered here to provide a worst case scenario. Systematic translational and rotational shifts led to a decrease in PTV coverage and an increase in dose to the urethra. In general, the PTV D_{90} was more sensitive to systematic source positioning errors, while the urethral D_{10} was more sensitive to rotational errors. Commercial afterloaders have an uncertainty in source positioning of ± 1 mm. The orientation uncertainty of the emission angle with respect to the patient anatomy is estimated to be less than 5°. This misalignment includes both patient motion relative to the catheter [50, 51] and setup errors for the proposed delivery system (alignment of shield at calibration, deviation between motor and shield angle). For these ranges of uncertainties, the combined tolerance due to positioning errors is expected to be less than 2%. These results suggest that the IMBT treatment plans generated with the proposed system are robust with respect to setup errors. However, positional and rotational uncertainties can also be incorporated into the optimization algorithm. This may reduce the plan quality but in exchange provide robustness to delivery errors. The application of robust optimization for IMBT will be examined in a future study.

There exists a tradeoff between plan conformity and treatment time, which are directly affected by the transmission through the shielded side and the collimation angle. When IMBT was first conceptualized, Ebert [15, 16] found that a collimation angle of 22.5°-45° and a transmission of $<10\%$ were needed to maximize the benefit of IMBT. However, the study did not consider any practical limitations of IMBT delivery. With the proposed system, the small diameter ($\sim$2 mm) of interstitial catheters sets a lower limit for the transmission and collimation angle. The source was offset to maximize the amount of shielding material, limiting the collimation angle to 180°. Thus, for interstitial HDR BT, the advantages of IMBT are limited by the geometric constraints of the catheters. It would be possible to optimize these parameters, i.e. minimum transmission and collimation angle, for cancer sites treated with intracavitary applicators, since additional shielding could be packed within the applicators.

In this study, catheter positions were not optimized for IMBT, since available dwell positions were imported from the original clinical plans. However, the catheter arrangements were consistent for both techniques and clinically feasible, demonstrating the superiority of IMBT over HDR BT given identical, realistic setup conditions. While alternative configurations could be tested to find optimal catheter positions for IMBT, this was beyond the scope of this work and will be investigated in a future study.

Differences in relative biological effectiveness (RBE) between ^{192}Ir and ^{169}Yb were not taken into account in this work, since all photon-emitting sources are assigned an RBE of unity in the clinic. However, a previous study showed that ^{169}Yb has an RBE of $\sim$1.1 relative to ^{192}Ir for HDR BT applications [52]. Prescription doses, and thus delivery times, may need to be adjusted to account for the differences in RBE values.

The main advantage of the AIM-Brachy system is its compatibility with existing commercial remote afterloaders that can support a 0.6 mm diameter wire within the shielded catheters. However, additional software needs to be integrated into the current remote afterloading systems to control the rotation of the shields. Current optimization algorithms in commercial treatment planning systems will also need to be updated to incorporate both dwell position and shield angle as degrees of freedom. More importantly, future clinical implementation of interstitial IMBT hinges on the availability of a commercial ^{169}Yb source with the proposed diameter. Clinical adoption of dynamic-shield IMBT will ultimately depend on whether the expected clinical benefits outweigh the increased costs for source production and exchange, hardware and software development, workflow and quality assurance.

8.5 Conclusions

The AIM-Brachy system was developed in combination with a ^{169}Yb source to deliver dynamic-shield IMBT for prostate cancer with reasonable treatment times. Treatment plans were robust with respect to delivery errors. IMBT delivered with the AIM-Brachy system has the potential to create a low dose tunnel within the urethra without affecting other plan quality indices. The urethra-sparing properties are desirable to minimize the occurrence and severity of urethral strictures and acute/late GU toxicities in general or, alternatively, provide a method for dose escalation.

Acknowledgements: This work was supported by the Natural Sciences and Engineering Research Council of Canada (grant number 241018) and Collaborative Health Research Projects (grant number 523394-18). G.F. acknowledges financial support by a CGS D scholarship from the Natural Sciences and Engineering Research Council of Canada.

Conflict of interest: None.

Supplementary material: Supplementary material for this article can be found in Appendix C.

References

[1] Morton GC. High-dose-rate brachytherapy boost for prostate cancer: rationale and technique. J Contemp Brachytherapy. 2014;6:323–330.

[2] Mendez LC, Morton GC. High dose-rate brachytherapy in the treatment of prostate cancer. Transl Androl Urol. 2018;7(3):357–370.

[3] Wojcieszek J, Bialas B. Prostate cancer brachytherapy: guidelines overview. J Contemp Brachytherapy. 2012;4(2):116–120.

[4] Chin J, Rumble RB, Kollmeier M, Heath E, Efstathiou J, Dorff T, et al. Brachytherapy for Patients With Prostate Cancer: American Society of Clinical Oncology/Cancer Care Ontario Joint Guideline Update. J Clin Oncol. 2017;35:1737–1743.

[5] Hoskin PJ, Rojas AM, Bownes PJ, Lowe GJ, Ostler PJ, Bryant L. Randomised trial of external beam radiotherapy alone or combined with high-dose-rate brachytherapy boost for localised prostate cancer. Radiother Oncol. 2012;103:207–222.

[6] Spratt DE, Zumsteg ZS, Ghadjar P, Kollmeier MA, Pei X, Cohen G, et al. Comparison of high-dose (86.4 Gy) IMRT vs combined brachytherapy plus IMRT for intermediate-risk prostate cancer. BJU Int. 2014;114(3):360–367.

[7] Agoston P, Major T, Fröhlich G, Szabó Z, Lövey J, Fodor J, et al. Moderate dose escalation with single-fraction high-dose-rate brachytherapy boost for clinically localized intermediate- and high-risk prostate cancer: 5-year outcome of the first 100 consecutively treated patients. Brachytherapy. 2011;10:376–384.

[8] Aluwini S, van Rooij PH, Kirkels WJ, Jansen PP, Praag JO, Bangma CH, et al. High-dose-rate brachytherapy and external-beam radiotherapy for hormone-naive low- and intermediate-risk prostate cancer: a 7-year experience. Int J Radiat Oncol Phys Biol. 2012;83:1480–1485.

[9] Kaprealian T, Weinberg V, Speight JL, Gottschalk AR, Roach 3rd M, Shinohara K, et al. High-dose-rate brachytherapy boost for prostate cancer: comparison of two different fractionation schemes. Int J Radiat Oncol Biol Phys. 2012;82(1):222–227.

[10] Neviani CB, Miziara MA, de Andrade Carvalho H. Results of high dose-rate brachytherapy boost before 2D or 3D external beam irradiation for prostate cancer. Radiother Oncol. 2011;98(2):169–174.

[11] Zwahlen DR, Andrianopoulos N, Matheson B, Duchesne GM, Millar JL. High-dose-rate brachytherapy in combination with conformal external beam radiotherapy in the treatment of prostate cancer. Brachytherapy. 2012;9(1):27–35.

[12] Ishiyama H, Kitano M, Satoh T, Kotani S, Uemae M, Matsumoto K, et al. Genitourinary toxicity after high-dose-rate (HDR) brachytherapy combined with hypofractionated

external beam radiotherapy for localized prostate cancer: an analysis to determine the correlation between dose-volume histogram parameters in HDR brachytherapy and severity of toxicity. Int J Radiat Oncol Biol Phys. 2009;75:23–28.

[13] Hsu IC, Hunt D, an J Pouliot WS, Cunha A, Krishnamurthy D, Sandler H. Dosimetric analysis of radiation therapy oncology group 0321: the importance of urethral dose. Pract Radiat Oncol. 2014;4(1):27–34.

[14] Morton GC, Loblaw DA, Chung H, Tsang G, Sankreacha R, Deabreu A, et al. Health-related quality of life after single-fraction high-dose-rate brachytherapy and hypofractionated external beam radiotherapy for prostate cancer. Int J Radiat Oncol Biol Phys. 2011;80:1299–1305.

[15] Ebert MA. Possibilities for intensity-modulated brachytherapy: technical limitations on the use of non-isotropic sources. Phys Med Biol. 2002;47:2459–2509.

[16] Ebert MA. Potential dose-conformity advantages with multi-source intensity-modulated brachytherapy (IMBT). Australas Phys Eng Sc Med. 2006;29(2):165–171.

[17] Shi C, Guo B, Cheng CY, Esquivel C, Eng T, Papanikolaou N. Three dimensional intensity modulated brachytherapy (IMBT): dosimetry algorithm and inverse treatment planning. Med Phys. 2010;37(7):3725–3737.

[18] Adams QE, Xu J, Breitbach EK, Enger SA, Rockey WR, Kim Y, et al. Interstitial rotating shield brachytherapy for prostate cancer. Med Phys. 2014;41(5):051703.

[19] Dadkhah H, Hopfensperger KM, Kim Y, Wu X, Flynn RT. Multisource rotating shield brachytherapy apparatus for prostate cancer. Int J Radiat Oncol Biol Phys. 2017;99(3):719–728.

[20] Adams QE, Hopfensperger KM, Kim Y, Wu X, Xu W, Shukla H, et al. Effectiveness of rotating shield brachytherapy for prostate cancer dose escalation or urethra sparing. Int J Radiat Oncol Biol Phys. 2018;102(5):1543–1550.

[21] Yang W, Kim Y, Wu X, Song Q, Liu Y, Bhatia SK, et al. Rotating-shield brachytherapy for cervical cancer. Phys Med Biol. 2013;58(11):3931–3941.

[22] Dadkhah H, Kim Y, Wu X, Flynn RT. Multihelix rotating shield brachytherapy for cervical cancer. Int J Radiat Oncol Biol Phys. 2014;72(11):6579–6588.

[23] Han DY, Webster MJ, Scanderbeg DJ, Yashar C, Choi D, Song B, et al. Direction-modulated brachytherapy for high-dose-rate treatment of cervical cancer. I: theoretical design. Int J Radiat Oncol Biol Phys. 2014;89(3):666–673.

[24] Han DY, Safigholi H, Soliman A, Ravi A, Leung E, Scanderbeg DJ, et al. Direction modulated brachytherapy for treatment of cervical cancer. II: comparative planning study with intracavitary and intracavitary-interstitial techniques. Int J Radiat Oncol Biol Phys. 2016;96(2):440–448.

[25] Safigholi H, Han DY, Mashouf S, Soliman A, Meigooni AS, Owrangi A, et al. Direction modulated brachytherapy (DMBT) for treatment of cervical cancer: A planning study with 192Ir, 60Co, and 169Yb HDR sources. Med Phys. 2017;44(12):6538–6547.

[26] Webster MJ, Devic S, Vuong T, Han DY, Park JC, Scanderbeg D, et al. Dynamic modulated brachytherapy (DMBT) for rectal cancer. Med Phys. 2013;40(1):011718.

[27] Webster MJ, Devic S, Vuong T, Han DY, Scanderbeg D, Choi D, et al. HDR brachytherapy of rectal cancer using a novel grooved-shielding applicator design. Med Phys. 2013;40(1):091704.

[28] Enger SA, Fisher DR, Flynn RT. Gadolinium-153 as a brachytherapy source. Phys Med Biol. 2013;58(4):957–964.

[29] Famulari G, Urlich T, Armstrong A, Enger SA. Practical aspects of ^{153}Gd as a radioactive source for use in brachytherapy. Appl Radiat Isot. 2017;130:131–139.

[30] Mason DL, Battista JJ, Barnett RB, Porter AT. Ytterbium-169: calculated physical properties of a new radiation source for brachytherapy. Med Phys. 1992;19(3):695–703.

[31] Medich DC, Tries MA, Munro III JJ. Monte Carlo characterization of an ytterbium-169 high dose rate brachytherapy source with analysis of statistical uncertainty. Med Phys. 2006;33(1):163–172.

[32] Cazeca MJ, Medich DC, Munro III JJ. Monte Carlo characterization of a new Yb-169 high dose rate source for brachytherapy application. Med Phys. 2010;37(3):1129–1136.

[33] Currier B, Munro III JJ, Medich DC. Dosimetric characterization of the GammaClip$^{\text{TM}}$ ^{169}Yb low dose rate permanent implant brachytherapy source for the treatment of nonsmall cell lung cancer postwedge resection. Med Phys. 2013;40(8):080701.

[34] Reynoso FJ, Munro III JJ, Sho SH. Technical note: Monte Carlo calculations for the AAPM TG-43 brachytherapy dosimetry parameters for the titanium-encapsulated Yb-169 source. Med Phys. 2017;18:193–199.

[35] Flynn RT, Adams QE, Hopfensperger KM, Wu X, Xu W, Kim Y. Efficient ^{169}Yb high-dose-rate brachytherapy source production using reactivation. Med Phys. 2019;46:2935–2943.

[36] Hetherington ELR, Wood NR. The production of ytterbium-169 radiography sources in a high flux reactor. Lucas Heights, Australia: Australian Atomic Energy Commission; 1974.

[37] IAEA. Manual for reactor produced radioisotopes. Technical Reports Series No. 1340. Vienna, Austria; 2008.

[38] Renaud M, Famulari G, Seuntjens J, Enger SA. OC-0256: Column generation-based Monte Carlo treatment planning for rotating shield brachytherapy. Radiother Oncol. 2016;119:S118.

[39] Famulari G, Renaud M, Poole CM, Evans MDC, Seuntjens J, Enger SA. RapidBrachyMCTPS: a Monte Carlo-based treatment planning system for brachytherapy applications. Phys Med Biol. 2018;63(17):175007.

[40] Agostinelli S, Allison J, al Amako K, Apostolakis J, Araujo H, Arce P, et al. Geant4 - a simulation toolkit. Nucl Inst Meth Phys Res A. 2003;506(3):250–303.

[41] Allison J, Amako K, Apostolakis J, Araujo H, Dubois PA, Asai M, et al. Geant4 developments and applications. IEEE Trans Nucl Sci. 2006;53(1):270–278.

[42] Williamson JF. Monte Carlo evaluation of kerma at a point for photon transport problems. Med Phys. 1987;14:567–576.

[43] Beaulieu L, Carlsson Tedgren A, Carrier JF, Davis SD, Mourtada F, Rivard MJ, et al. Report of the Task Group 186 on model-based dose calculation methodsbin brachytherapy beyond the TG-43 formalism: current status and recommendations for clinical implementation. Med Phys. 2012;39(10):6208–6236.

[44] ICRU. Photon, electron, proton and neutron interaction data for body tissues. vol. ICRU report 46. Bethesda, MD: International Commission on Radiation Units & Measurements; 1992.

[45] Hsu IC, Bae K, Shinohara K, Pouliot J, Purdy J, Ibbott G, et al. Phase II trial of combined high-dose-rate brachytherapy and external beam radiotherapy for adenocarcinoma of the prostate: preliminary results of RTOG 0321. Int J Radiat Oncol Biol Phys. 2010;78(3):751–758.

[46] Wu A, Ulin K, Sternick ES. A dose homogeneity index for evaluating 192Ir interstitial breast implants,. Med Phys. 1988;15(1):104–107.

[47] Baltas D, Kolotas C, Geramani K, Mould RF, Ioannidis G, Kekchidi M, et al. A conformal index (COIN) to evaluate implant quality and dose specification in brachytherapy. Int J Radiat Oncol Biol Phys. 1998;40(2):515–524.

[48] Andrássy M, Niatsetsky Y, Pérez-Calatayud J. Co-60 versus Ir-192 in HDR brachytherapy: Scientific and technological comparison. Rev Phys Med. 2012;13:125–130.

[49] Akulinichev SV, Antanovich AA, Derzhiev VI, Zibrov IP, Semakina TS, Filonenko VP, et al. Production of ytterbium ceramic for medical radioactive sources. Glass Ceram. 2018;75(1-2):47–50.

[50] Palombarini M, Mengoli S, Fantazzini P, Cadioli C, Degli Esposti C, Frezza GP. Analysis of inter-fraction setup errors and organ motion by daily kilovoltage cone beam computed tomography in intensity modulated radiotherapy of prostate cancer. Radiat Oncol. 2012;7:56.

[51] Zhou J, Uhl B, Dewit K, Young M, Taylor B, Fei DY, et al. Analysis of daily setup variation with tomotherapy megavoltage computed tomography. Med Phys. 2010;35(1):31–37.

[52] Famulari G, Pater P, Enger SA. Microdosimetric evaluation of current and alternative brachytherapy sources - a Geant4-DNA simulation study. Int J Radiat Oncol Biol Phys. 2018;100(1):270–277.

Chapter 9

Monte Carlo dosimetric characterization of a new high dose rate ^{169}Yb brachytherapy source and independent verification using a multipoint plastic scintillator detector

Abstract

Purpose: A prototype ^{169}Yb source was developed in combination with a dynamic rotating platinum shield system (AIM-Brachy) to deliver intensity modulated brachytherapy (IMBT). The purpose of this study was to evaluate the dosimetric characteristics of the bare/shielded ^{169}Yb source using Monte Carlo (MC) simulations and perform an independent dose verification using a dosimetry platform based on a multipoint plastic scintillator detector (mPSD).

Materials and methods: The TG-43U1 dosimetric parameters were calculated for the source model using RapidBrachyMCTPS. Real-time dose rate measurements were performed in a water tank for both the bare/shielded source using a custom remote afterloader. For each dwell position, the dose rate was independently measured by the three scintillators (BCF-10, BCF-12, BCF-60). For the bare source, dose rate was measured at distances up to 3 cm away from the source over a range of 7 cm along the catheter. For the shielded source, measurements were performed with the mPSD placed at 1 cm from the source at four different azimuthal angles (0°, 90°, 180° and 270°).

Results: The dosimetric parameters were tabulated for the source model. For the bare source, differences between measured and calculated along-away dose rates were generally below 5%-10%. Along the transverse axis, deviations were, on average (range), 3.3% (0.6%-6.2%) for BCF-10, 1.7% (0.9%-2.9%) for BCF-12 and 2.2% (0.3%-4.4%) for BCF-60. The maximum dose rate reduction due to shielding at a radial distance of 1 cm was 88.8%±1.2%, compared to 83.5%±0.5% as calculated by MC.

Conclusions: The dose distribution for the bare/shielded ^{169}Yb source was independently verified using mPSD with good agreement in regions close to the source. The ^{169}Yb source coupled with the partial-shielding system is a promising technique to deliver IMBT.

9.1 Introduction

The ^{169}Yb radionuclide has been investigated as a viable source for brachytherapy applications [1–5]. Radioactive ^{169}Yb is produced in a nuclear reactor by neutron activation of ^{168}Yb and decays by electron capture to ^{170}Tm. It primarily emits photons with energies in the 50-308 keV range and has an average energy of 93 keV. The half-life of ^{169}Yb is 32.0 days, which is shorter than that of ^{192}Ir but sufficiently long for a high dose rate (HDR) temporary implant brachytherapy source. The lower energy reduces the amount of shielding required in brachytherapy suites. The ^{169}Yb source can be produced with a specific activity appropriate for HDR brachytherapy ($>$ 12 Gy h^{-1}), due to the high thermal neutron cross section of ^{168}Yb and the availability of ^{168}Yb in enriched form in Yb_2O_3 powder.

Intensity modulated brachytherapy (IMBT) is a brachytherapy technique that can be delivered using a shielded applicator or source to modulate the dose distribution [6]. Static and dynamic IMBT approaches can be used to modulate the dose distribution to the shape of the tumor, reduce the dose to organs at risk, provide a method for dose escalation or allow for fewer catheters to be implanted. Recently, an ^{169}Yb source was proposed to deliver dynamic-shield IMBT [7]. The source can be combined with a rotating platinum shield inside of an interstitial catheter to produce a highly anisotropic dose distribution. Platinum was selected as the shielding material due to its high density, high atomic number, machinability and ferromagnetic properties.

Current brachytherapy dose calculations are performed according to the guidelines from the update of the American Association of Physicists in Medicine (AAPM) Task Group Report No. 43 (TG-43U1) [8]. Monte Carlo (MC) simulations are widely adopted to accurately characterize the dosimetric parameters for brachytherapy sources [9]. In particular, model-based dose calculation algorithms should be adopted for accurate dosimetry in cases where heterogeneities from the shielded applicator or source have to be taken into account [10]. For IMBT treatment planning, MC-generated dose distributions are typically used as inputs for the optimization algorithm during inverse optimization [6].

Several detectors have been studied to assess the dose delivery during a brachytherapy treatment. Plastic scintillator detectors (PSDs) show promise for obtaining accurate dose measurements in brachytherapy [11–15]. Additionally, the use of PSDs in a multipoint configuration (mPSD) has been reported to be a suitable tool to asses the dose at multiple points simultaneously, thereby improving treatment quality and accuracy [16–19]. Among the advantages of using PSDs, we can find their high spatial resolution, linearity with dose, energy independence in the megavolt energy range, and water equivalence. However, a non-negligible fraction of the light collected by PSDs consists of Cherenkov light. Whether Cherenkov light requires removal in brachytherapy applications depends on the radioactive source used and the measurement geometry. In HDR brachytherapy with an ^{192}Ir source, Cherenkov radiation can cause significant errors in dose reporting if it is not taken into account [12, 12]. In this study, the stem effect is accounted for using the multi-hyperspectral filtering method proposed by Archambault et al. [16].

The purpose of this study is to evaluate the dosimetric characteristics of a new ^{169}Yb source using the TG-43U1 protocol and independently verify the dose distribution with an mPSD system.

9.2 Materials and methods

9.2.1 Source characteristics

Figure 9.1 shows the design of the ^{169}Yb source model (SPEC, St. Rose, LA, USA). The source has an active core which consists of Yb_2O_3 (6.9 g cm^{-3}). The active core has a diameter of 0.4 mm and a length of 3.2 mm. The active core is encapsulated in a 304 grade stainless steel

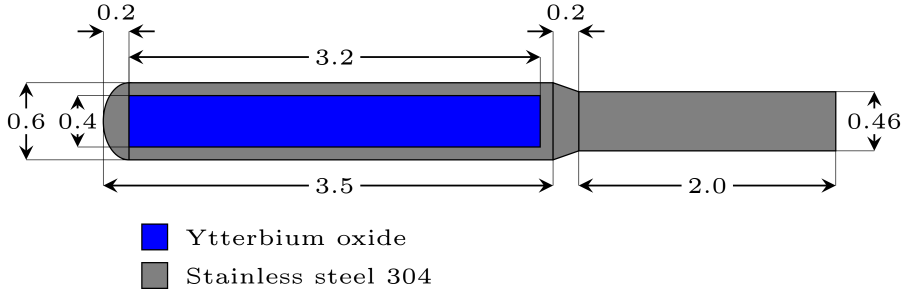

Figure 9.1: Materials and dimensions (mm) for the ^{169}Yb brachytherapy source.

cylinder (8.0 g cm^{-3}) with an outer diameter of 0.6 mm and a wall thickness of 0.1 mm. The tip of the encapsulation is a semi-spheroid (oblate) with a bisected axis of 0.2 mm and a major semi-axis of 0.3 mm. The tip is attached to a 3.2 mm long hollow cylindrical section followed by a 0.1 mm long solid cylindrical section. Following the solid cylindrical section is a conical section with a length of 0.2 mm. Attached to the conical section is a 2 mm section of a 304 grade stainless steel cable (8.0 g cm^{-3}) with a diameter of 0.46 mm.

9.2.2 Monte Carlo simulations

Simulations were performed using RapidBrachyMCTPS [20], an in-house MC code for brachytherapy applications based on the Geant4 simulation toolkit [21, 22]. The decay spectrum was taken from the National Nuclear Data Centre [23]. Photons were tracked using the standard Penelope physics list with atomic deexcitation activated. Cross section data were taken from the EPDL97 [24] and EADL97 [25] cross-section libraries. Dose was approximated by collisional kerma. Collisional kerma was calculated using a tracklength estimator [26]. Consequently, electrons were not explicitly transported. Collisional kerma underestimates dose by $<1\%$ for radial distances >1 mm for typical ^{169}Yb sources [27]. Mass-energy absorption coefficients were taken from the mass-energy coefficient library present in RapidBrachyMCTPS [28].

In a first simulation, the air kerma strength per unit contained activity S_K/A was calculated in a large voxel ($10\times10\times0.05$ cm^3) at 100 cm from the source and corrected by 0.22% to give the air kerma strength at a point [27]. S_K/A was calculated in vacuum to avoid the need to correct for attenuation by air. Low energy characteristic x-rays were suppressed by discarding the contribution from photons with energies less than 10 keV. The energy spectra of decay photons (including x-rays and gammas) and photons escaping the encapsulation were tabulated using a bin width of 0.1 keV. The photon yield was determined as the number of photons generated within the active core per decay.

In a second simulation, the source was placed in the center of a water phantom with a radius of 40 cm. The dose rate in water per unit contained activity $\dot{D}(r,\theta)/A$ was calculated in spherical shells divided in sections with a minimum resolution of 5°. The shell thickness varied with the radial distance r from the center of the active core as follows: 0.1 mm ($r \leq$1 cm), 0.5 mm (1 cm $< r \leq$ 5 cm), 1.0 mm (5 cm $< r \leq$ 10 cm), and 2.0 mm (10 cm $< r \leq$ 20 cm). Primary and scattered separated (PSS) dose data were tabulated according to the formalism developed by Russell et al. [29, 30]. The dose rate per unit air kerma strength was calculated along and away from the source axis using a grid of 1 mm^3 voxels. A total of 10^8 photons were simulated to obtain type A uncertainties below 0.2% for each simulation.

9.2.3 Experimental measurements

Dosimetry system

The dosimetry system consisted of a 1.0 mm-diameter core mPSD coupled to 15 m-long fiber-optic cable *Eska GH-4001* (Mitsubishi Rayon Co., Tokyo, Japan). The mPSD is composed by 3 mm of BCF-10, 6 mm of BCF-12 and 7 mm of BCF-60 crystals (Saint Gobain Crystals, Hiram, Ohio, USA). The size of the scintillators were optimized to balance the scintillation emission from each scintillator for optimal hyperspectral deconvolution and minimize variations in spatial resolution [19]. The mPSD's sensors and optical fiber were shielded from light using an opaque plastic tube. The outer diameter of the crystal and tube was 1.2 mm, which was thin enough to fit into most brachytherapy catheters including the plastic catheters used in this experiment. The optical fiber was connected to a data acquisition system consisting of photomultiplier tubes (PMTs) coupled to dichroic mirrors and filters that monitored the signal with a 100 kHz sample rate. A more detailed characterization of the mPSD system can be found in a previous study [19].

Real time dose rate measurements were performed under full scattering conditions [8]. The scintillation light generated inside the mPSD is deconvolved into different spectral bands in real time, converted to an electrical signal in the PMTs, and translated into dose rate without the contribution of the Cherenkov radiation. The mathematical formalism based on a linear regression proposed by Archambault et al. [16] was used as the stem removal technique. The calibration matrix and dose rate values were calculated according to the formulation published

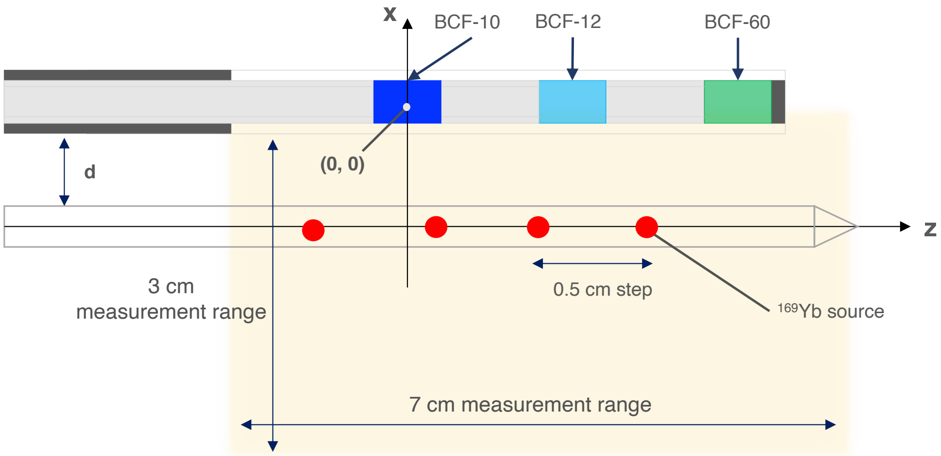

Figure 9.2: Schematic of the main parameters used for the along-away dose rate measurements from the bare ^{169}Yb source using the mPSD.

by Linares Rosales et al. [19] for a three-point mPSD configuration. Dose rate values provided by the scintillators were integrated over the scintillator volume to account for their finite size. A Python-based graphical user interface was used for system management and signal processing.

Dose rate measurements

Dose rate measurements were carried out using a custom-made afterloader (Worcester Polytechnic Institute and SPEC, Worcester, MA, USA). The distal end of a commercial guidewire (40 cm section) was replaced by a thinner diameter wire (0.46 mm). To ensure the accuracy and reproducibility of the source-to-detector distance, catheters were inserted into a custom-made polymethyl methacrylate (PMMA) holder [31, 19]. The holder ensures that catheters are placed parallel to each other with a minimum spacing of 0.5 cm. The afterloader unit was able to move the source to the desired position along the catheter with a positional accuracy (k=2) within ±2 mm. The mPSD was inserted into an additional catheter for use in real-time dose verification. The light collection system was independently controlled from the afterloader unit. The source air kerma strength (S_K) was 780 U at the onset of measurements.

Figure 9.2 shows a schematic of the parameters used for dose rate measurement as a function of distance to the source. Calculations were performed with a coordinate system, where the radial direction to the source is represented as x and the longitudinal direction as z. The coordinates' origin is considered at the effective center of the scintillator BCF-10. For the bare source, measurements in the x-direction were done with catheters positioned at 0.5, 1.0, 1.5, 2.0,

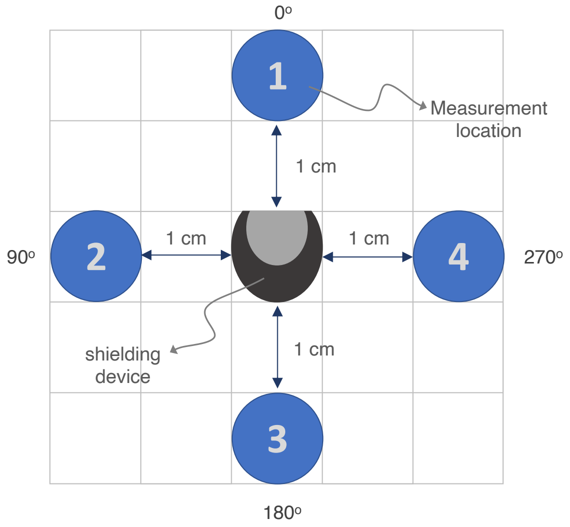

Figure 9.3: Schematic of the dose rate measurement setup around the platinum-shielded ^{169}Yb source. The mPSD was placed at a distance of 1 cm from the central catheter, containing the source and shield, at four different locations (indicated by 1-4). The source is offset from the central catheter's longitudinal axis by 0.4 mm. Figure not to scale.

2.5, and 3.0 cm. In the z-axis direction, the measurements covered a range of distances of 7.0 cm. The source dwelled along each needle with a 0.5 cm step, from -1.5 cm to 5.5 cm in the z-direction. A dwell time of 1 min was programmed at each dwell position. The mPSD calibration and measurements were carried out under the same experimental conditions. The formalism proposed by Johansen et al. [32] was used to correct for source-to-detector positioning errors. Based on the calculated dose rate distribution, we determined the average source shifts within catheters by minimizing the chi-square between the measured dwell position and the expected one. The dose rate measured by the mPSD were compared to the MC-calculated along-away dose data as the reference.

Figure 9.3 shows the setup for the dose rate measurements around the ^{169}Yb source in the presence of the platinum shield. The platinum shield was inserted into a catheter and the source was sent to a fixed position inside the shield. Measurements were taken with the mPSD placed at 1 cm at four different catheter positions, defined by their azimuthal angles with respect to the catheter containing the source and shield (0°, 90°, 180° and 270°). A dwell time of 1 min was programmed for each of the four positions. The dose rates measured by the mPSD were compared to MC-calculated data generated in a previous study [7] for this combined source and shield model. The dose distribution is centered along the catheter's longitudinal axis and considers a source offset of 0.4 mm.

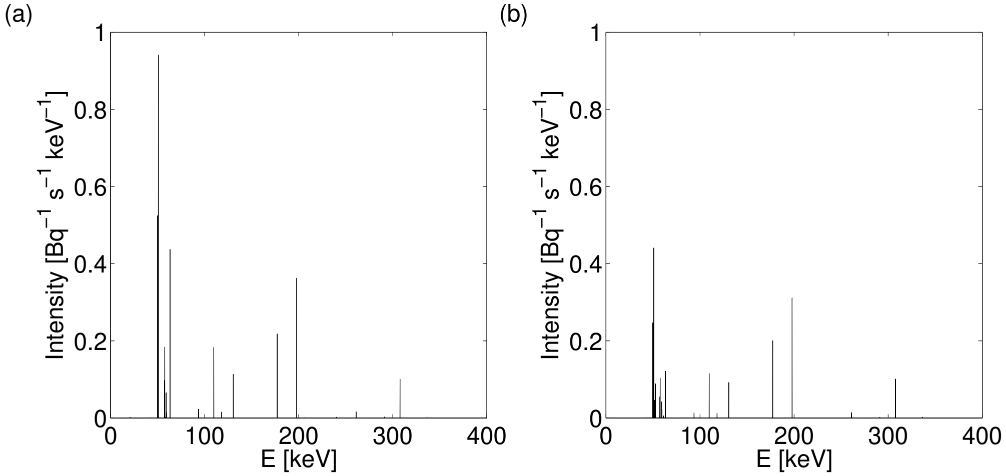

Figure 9.4: (a) Photon spectrum calculated from ^{169}Yb decay. (b) Photon spectrum exiting the stainless steel encapsulation. Photons with energies less than 10 keV were discarded. The bin width is 0.1 keV.

9.3 Results

9.3.1 TG-43U1 parameters

The photon decay spectrum and photon spectrum after exiting the encapsulation are shown in Figure 9.4. The average energy of the decay photons was 93.4 keV (excluding photons with energies less than 10 keV). The total photon yield from decay processes was 3.32±0.03 photons per disintegration. The average energy of the photons leaving the encapsulation was 108.8 keV. The air kerma strength per unit activity S_K/A was 1.24±0.03 U mCi^{-1}. The dose rate per unit activity $\dot{D}(r_0,\theta_0)/A$ at $r_0 = 1$ cm and $\theta_0 = 0$ was 1.50±0.03 cGy h^{-1} mCi^{-1}. The dose rate constant Λ was 1.21±0.03 cGy h^{-1} U^{-1}. Table 9.1 compares S_K/A and Λ for this source model with those for other published ^{169}Yb sources.

The relative uncertainties in the air kerma strength per unit activity S_K/A, dose rate per unit activity $\dot{D}(r_0,\theta_0)/A$ at r_0 = 1 cm and θ_0 = 90°, and dose rate constant Λ for the source model are displayed in Table 9.2. Type A statistical uncertainties were 0.2% for S_K/A and $\dot{D}(r_0,\theta_0)/A$. The uncertainty due to the source geometry was determined by varying the diameter of the capsule and active core assuming a rectangular distribution over a tolerance of ±0.06 mm [9]. These uncertainties were 1.9% for S_K/A, 1.6% for $\dot{D}(r_0,\theta_0)/A$ and 2.0% for Λ. The uncertainties due to the physics implementation in the radiation transport algorithm are about 0.2% [9] for high energy sources. The uncertainties in mass-attenuation coefficients

Table 9.1: Air kerma strength per unit activity S_K/A and dose rate constant Λ calculated for ^{169}Yb source models.

Source model	MC code	S_K/A (U mCi^{-1})	Λ (cGy h^{-1} U^{-1})
This model	Geant4	1.24±0.03	1.21±0.03
Ti capsule	MCNP5 [33]	1.15±0.03	1.19±0.03
GammaClip	MCNP5 [4]	1.37±0.03	1.22±0.03
M42	MCNP5 [3]	1.08±0.03	1.12±0.04
HDR 4140	MCNP5 [2]	1.10±0.03	1.19±0.03
Type 8	MCPT [34]		1.204±0.004
	EGS4 [35]		1.191±0.007
X1267	EGS4 [36]	1.33±0.04	1.21±0.03
	EGS4 [35]		1.17±0.01

Table 9.2: Total relative standard uncertainty budget (in %) for calculation of dosimetric parameters.

Source of uncertainty	Type	S_K/A	$\dot{D}(r_0,\theta_0)/A$	Λ
Statistics	A	0.2	0.2	0.3
Source geometry	B	1.9	1.6	2.0
MC radiation transport	B	0.2	0.2	0.3
Mass-attenuation coefficients (μ/ρ)	B	0.1	0.1	0.1
Mass-energy absorption coefficients (μ_{en}/ρ)	B	0.5	0.5	0.1
Source photon spectrum	B	0.1	0.1	0.1
Photon yield	B	0.8	0.8	
Combined standard uncertainty (k=1)		**2.1**	**1.9**	**2.1**
Expanded uncertainty (k=2)		**4.2**	**3.8**	**4.2**

(μ/ρ) and mass-energy absorption coefficients (μ_{en}/ρ) are about 0.5% [37] for photons with energies above 100 keV. The influence of the mass-attenuation coefficient uncertainties on S_K/A and $\dot{D}(r_0,\theta_0)/A$ were estimated to be no more than 0.1% [38]. The influence of the mass-energy absorption coefficient uncertainties on S_K/A and $\dot{D}(r_0,\theta_0)/A$ were set to 0.5%, since the calculations of S_K/A and $\dot{D}(r_0,\theta_0)/A$ are based on the product of photon energy fluence and (μ_{en}/ρ). The mass-energy absorption coefficient uncertainty on Λ was assigned based on the estimates from Andreo et al. [39] for the (water/air) ratios of mass-energy absorption coefficients. The uncertainty in the photon energy spectrum was separated into two components: the relative spectral contributions and the total photon yield per decay. The uncertainty due to the choice of photon spectrum was estimated as 0.1% [40] when total photon yield per decay is normalized to equal values. The uncertainty in photon yield was evaluated as the mean weighted

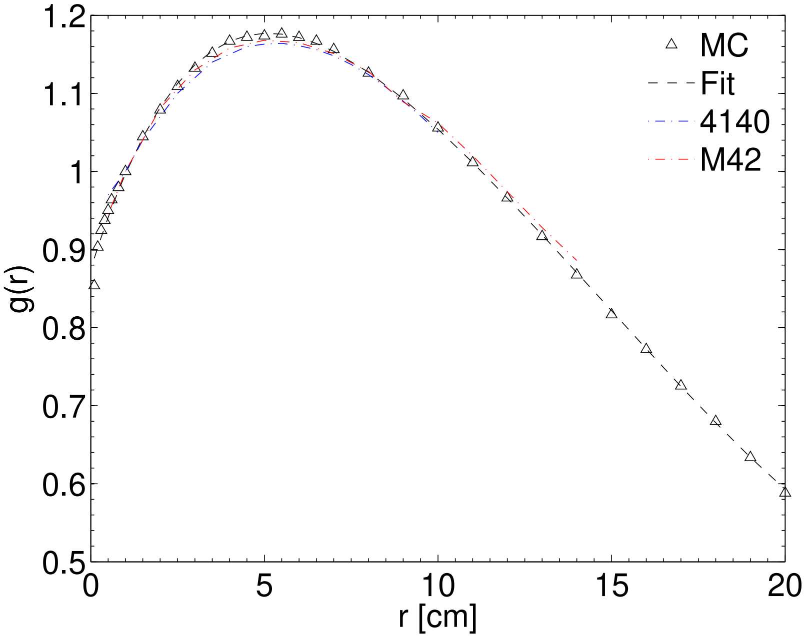

Figure 9.5: Radial dose function $g_L(r)$ calculated for the ^{169}Yb source model (L = 0.32 cm) and fifth order polynomial fit for $g_L(r)$. By definition, the uncertainty at r = 1 cm is 0. The relative uncertainty (k=1) is 2.1% otherwise. The results were compared to those for Implant Sciences Model HDR 4140 [2] and SPEC Model M42 [3].

uncertainty of the individual photon energies in the spectrum (0.8%) [4]. The uncertainties in photon yield largely cancel out when calculating Λ and were considered negligible. Unless stated otherwise, the uncertainties in Λ were determined using the quadrature sum of the uncertainties in S_K/A and $\dot{D}(r_0,\theta_0)/A$.

The radial dose function $g_L(r)$ based on a line source geometry function (L = 0.32 cm) is shown in Figure 9.5, with a maximum of 1.176±0.035 at r = 5.5 cm. Since $g_L(r)$ is a ratio of dose rate values, a standard uncertainty (k=1) of 2.1% was conservatively assumed (similar to Λ), using a similar methodology for uncertainty propagation as Medich et al. [2]. The $g_L(r)$ was fitted to a fifth order polynomial function for treatment planning purposes between 0.2 cm and 20 cm:

$$g_L(r) = a_0 + a_1 r + a_2 r^2 + a_3 r^3 + a_4 r^4 + a_5 r^5 \tag{9.1}$$

where a_0 = 0.8746, a_1 = 0.1433, a_2 = -2.236×10^{-2}, a_3 = 1.364×10^{-3}, a_4 = -4.433×10^{-5} and a_5 = 6.178×10^{-7} (R^2 = 0.9981). Deviations between fit and calculated values were within 1% over the entire range, with an average deviation of 0.43%.

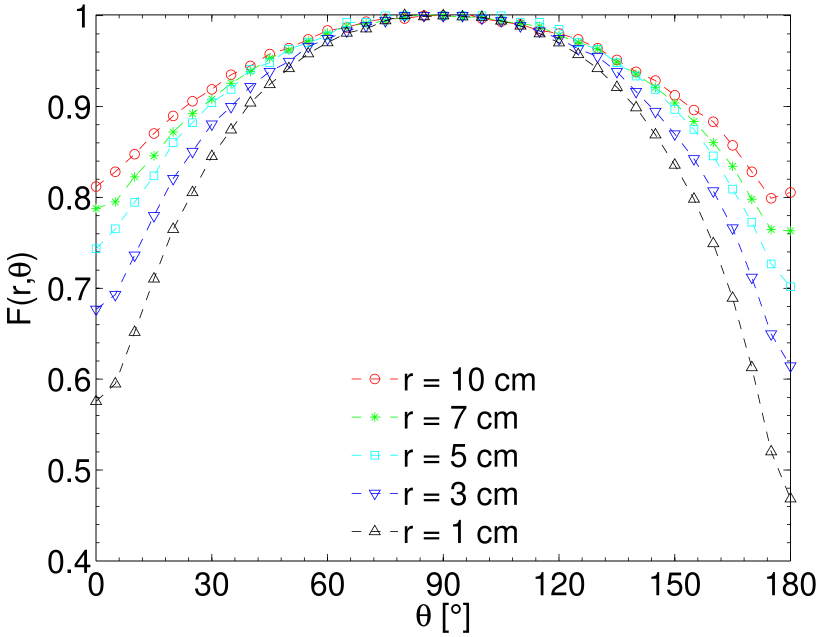

Figure 9.6: Two-dimensional (2D) anisotropy function $F(r,\theta)$ calculated for the ^{169}Yb source model. By definition, the uncertainty at θ = 90° is 0. The relative uncertainty (k=1) is 2.1% otherwise.

The two-dimensional (2D) anisotropy function $F(r,\theta)$ is shown for a few values of r in Figure 9.6 and tabulated with higher resolution in r in Table 9.3. $F(r,\theta)$ ranges between 0.47 and 1.0 over all polar angles at r = 1 cm. $F(r,\theta)$ decreases at low polar angles, and increases with increasing distance r from the source. Since $F(r,\theta)$ is also defined as a dose rate ratio, the standard uncertainty (k=1) on $F(r,\theta)$ was estimated as 2.1%.

The PSS dose data are presented in Figure 9.7. Scattered photons dominate the absorbed dose at radial distances greater than 3 cm. The majority of the dose at distances greater than 6 cm is delivered by multiple scattered photons, specifically. Since the PSS dose data is defined as a ratio of dose rate per unit of radiant photon energy, it is largely independent on photon yield, which results in a standard uncertainty (k=1) of 1.9%. The along-away dose data are shown in Table 9.4. Since the along-away distribution is defined as a ratio of dose rate per unit air kerma strength, the uncertainty in Λ was adopted.

Table 9.3: Two-dimensional (2D) anisotropy function $F(r,\theta)$ calculated for the ^{169}Yb source model. The source tip is oriented along θ = 0°. By definition, the uncertainty at θ = 90° is 0. The relative uncertainty (*k*=1) is 2.1% otherwise.

	r [cm]									
θ [°]	0.5	1.0	2.0	3.0	4.0	5.0	6.0	7.0	8.0	10.0
0	0.556	0.576	0.628	0.677	0.705	0.744	0.756	0.788	0.800	0.812
5	0.582	0.595	0.656	0.693	0.732	0.765	0.780	0.795	0.814	0.828
10	0.639	0.652	0.707	0.736	0.769	0.795	0.809	0.823	0.834	0.848
15	0.701	0.710	0.756	0.780	0.806	0.824	0.838	0.846	0.859	0.870
20	0.757	0.765	0.799	0.821	0.838	0.860	0.865	0.872	0.880	0.890
25	0.805	0.806	0.836	0.851	0.866	0.882	0.888	0.892	0.900	0.906
30	0.844	0.845	0.867	0.881	0.889	0.904	0.906	0.908	0.917	0.919
35	0.876	0.875	0.893	0.900	0.912	0.919	0.923	0.926	0.931	0.935
40	0.902	0.904	0.914	0.922	0.930	0.941	0.938	0.939	0.944	0.945
45	0.924	0.924	0.933	0.938	0.944	0.948	0.950	0.953	0.956	0.958
50	0.941	0.942	0.949	0.950	0.958	0.963	0.963	0.962	0.966	0.964
55	0.957	0.958	0.962	0.966	0.967	0.970	0.971	0.972	0.973	0.974
60	0.969	0.970	0.972	0.975	0.977	0.978	0.980	0.981	0.981	0.984
65	0.979	0.981	0.981	0.983	0.981	0.993	0.988	0.988	0.988	0.987
70	0.987	0.986	0.988	0.989	0.991	0.993	0.992	0.991	0.992	0.994
75	0.992	0.995	0.994	0.994	0.995	1.000	0.995	0.994	0.995	0.997
80	0.997	1.000	0.997	1.000	0.995	1.000	0.998	0.999	0.998	0.997
85	0.999	0.999	0.999	1.000	1.000	1.007	1.000	1.001	1.000	1.000
90	1.000	1.000	1.000	1.000	1.000	1.000	1.000	1.000	1.000	1.000
95	1.000	0.999	0.999	1.000	1.000	1.000	1.000	0.999	0.999	1.003
100	0.997	0.998	0.997	0.997	0.995	1.000	0.998	0.999	0.998	0.997
105	0.993	0.994	0.993	0.994	0.995	1.000	0.995	0.994	0.996	0.994
110	0.987	0.989	0.988	0.989	0.991	0.993	0.991	0.991	0.991	0.990
115	0.979	0.980	0.981	0.983	0.981	0.993	0.986	0.988	0.986	0.984
120	0.969	0.970	0.972	0.975	0.977	0.985	0.980	0.978	0.980	0.981
125	0.956	0.957	0.960	0.964	0.967	0.970	0.970	0.971	0.972	0.974
130	0.941	0.942	0.947	0.955	0.953	0.963	0.960	0.964	0.963	0.964
135	0.923	0.921	0.932	0.938	0.939	0.948	0.948	0.949	0.953	0.951
140	0.900	0.899	0.911	0.916	0.925	0.934	0.935	0.936	0.941	0.938
145	0.873	0.869	0.889	0.895	0.907	0.919	0.919	0.921	0.928	0.929
150	0.840	0.836	0.862	0.870	0.884	0.897	0.901	0.904	0.912	0.912
155	0.797	0.798	0.828	0.843	0.861	0.875	0.881	0.884	0.893	0.896
160	0.746	0.749	0.788	0.807	0.829	0.846	0.856	0.860	0.872	0.883
165	0.681	0.689	0.738	0.766	0.792	0.809	0.827	0.834	0.848	0.857
170	0.597	0.613	0.677	0.712	0.746	0.773	0.792	0.798	0.820	0.828
175	0.483	0.520	0.603	0.650	0.691	0.727	0.751	0.765	0.785	0.799
180	0.414	0.469	0.575	0.615	0.673	0.702	0.758	0.763	0.790	0.806

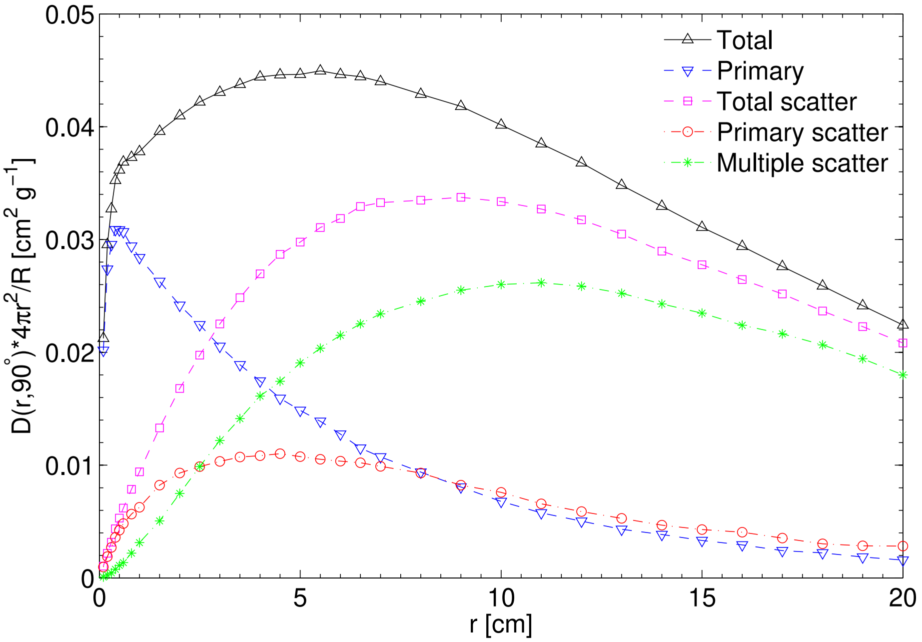

Figure 9.7: Primary and scattered separated (PSS) dose data along the transverse axis for the ^{169}Yb source model. The dose is normalized by the total radiant energy R of photons escaping the encapsulation. The relative uncertainty (k=1) is 1.9%.

9.3.2 Experimental measurements

The dose rate measurements and relative deviations are shown in Figure 9.8. The heat map colors in Figure 9.8 show the dose rate distribution for each scintillator in the mPSD as a function of x and z distances. The origin of coordinates was set at the center of BCF-10 as illustrated in Figure 9.2. The annotated values show the measurements' relative deviations from MC-based along-away dose data at each source dwell position.

Figure 9.9 shows the dose rate measured approximately along each scintillator's transverse axis (z = 0 cm for BCF-10, z = 2 cm for BCF-12, z = 3.5 cm for BCF-60). Mean differences between measured and calculated dose rates were, on average, 3.3% (0.6%-6.2%) for BCF-10, 1.7% (0.9%-2.9%) for BCF-12 and 2.2% (0.3%-4.4%) for BCF-60. However, these differences were generally within their combined uncertainties. The measurement uncertainty (k=1), including the statistical uncertainty as well as the uncertainty associated to all the components in the optical chain, increased with distance and varied between 2.9%-4.5%, 1.8%-3.5% and 1.1%-3.7% for BCF-10, BCF-12 and BCF-60, respectively. The signal-to-noise ratio (SNR) fell

Table 9.4: Along-away dose rate in water per unit of air kerma strength (cGy h^{-1} U^{-1}) calculated for the ^{169}Yb source model. The source is oriented along the z axis. The relative uncertainty (k=1) is 2.1%.

	Away x [cm]												
Along z [cm]	0	0.2	0.5	1.0	1.5	2.0	2.5	3.0	4.0	5.0	6.0	8.0	10.0
-10.0	0.011	0.009	0.010	0.009	0.011	0.010	0.011	0.010	0.010	0.008	0.009	0.007	0.006
-8.0	0.016	0.016	0.019	0.017	0.017	0.017	0.020	0.016	0.016	0.013	0.013	0.009	0.008
-6.0	0.030	0.028	0.032	0.030	0.031	0.030	0.031	0.030	0.024	0.021	0.017	0.014	0.008
-5.0	0.040	0.037	0.041	0.043	0.044	0.042	0.039	0.040	0.034	0.026	0.021	0.017	0.010
-4.0	0.059	0.058	0.063	0.069	0.065	0.061	0.062	0.052	0.043	0.033	0.027	0.017	0.012
-3.0	0.092	0.100	0.107	0.115	0.105	0.102	0.088	0.076	0.058	0.044	0.034	0.018	0.012
-2.5	0.126	0.137	0.160	0.162	0.145	0.126	0.109	0.090	0.064	0.049	0.035	0.019	0.013
-2.0	0.183	0.205	0.233	0.224	0.201	0.165	0.131	0.109	0.073	0.049	0.035	0.020	0.013
-1.5	0.290	0.344	0.394	0.362	0.282	0.215	0.162	0.126	0.081	0.055	0.041	0.020	0.013
-1.0	0.582	0.783	0.828	0.597	0.401	0.266	0.185	0.140	0.085	0.056	0.039	0.022	0.013
-0.5	2.39	3.35	2.26	0.985	0.530	0.320	0.212	0.148	0.092	0.058	0.040	0.022	0.013
-0.2	...	14.6	3.99	1.19	0.550	0.334	0.220	0.152	0.087	0.059	0.039	0.021	0.013
0	...	24.0	4.58	1.21	0.568	0.328	0.217	0.153	0.086	0.055	0.041	0.021	0.012
0.2	...	14.6	3.96	1.19	0.562	0.318	0.213	0.156	0.092	0.059	0.041	0.022	0.012
0.5	3.03	3.38	2.26	0.984	0.518	0.313	0.211	0.153	0.090	0.057	0.039	0.022	0.014
1.0	0.732	0.814	0.824	0.602	0.385	0.268	0.189	0.142	0.084	0.058	0.039	0.021	0.012
1.5	0.353	0.376	0.400	0.362	0.282	0.211	0.165	0.123	0.078	0.053	0.039	0.021	0.014
2.0	0.214	0.219	0.237	0.225	0.202	0.160	0.132	0.107	0.075	0.046	0.038	0.021	0.013
2.5	0.136	0.154	0.157	0.158	0.147	0.124	0.108	0.089	0.064	0.048	0.034	0.020	0.012
3.0	0.107	0.113	0.111	0.119	0.111	0.096	0.090	0.073	0.054	0.042	0.032	0.017	0.011
4.0	0.063	0.062	0.064	0.068	0.065	0.062	0.060	0.053	0.042	0.033	0.027	0.016	0.010
5.0	0.043	0.044	0.041	0.043	0.044	0.046	0.040	0.037	0.032	0.026	0.023	0.014	0.009
6.0	0.029	0.030	0.034	0.031	0.032	0.033	0.032	0.029	0.025	0.023	0.017	0.013	0.009
8.0	0.018	0.017	0.016	0.019	0.018	0.017	0.019	0.017	0.014	0.015	0.012	0.009	0.008
10.0	0.011	0.012	0.012	0.009	0.011	0.010	0.010	0.008	0.010	0.008	0.009	0.007	0.005

below 5 at a radial distance of 3.2 cm, 3.8 cm and 3.0 cm, respectively. Since the dwell position shift formalism corrected for positioning uncertainties, these were not included here.

The impact of the shield on the dose distribution is shown in Figure 9.10. The trend from the MC-calculated curve was well reproduced by the measurements. The dose rate at a radial distance of about 1 cm, measured by BCF-10, was reduced by up to 88.8%±1.2%, compared to the MC-calculated dose rate reduction of 83.5%±0.5%. The deviations in the maximum dose rate reduction were 5.3%, 7.0% and 1.4% (global relative to ϕ = 0°) in Figure 9.10a, 9.10b and 9.10c, respectively. The total uncertainty budget for the dose rate measurements is described in Table 9.5. In addition to type A uncertainties, uncertainties due to source-to-detector positioning, shield orientation and shield thickness were included in the budget. The dosimetric uncertainty due to source-to-detector positioning was based on the inverse square law effect for a ±0.2 mm shift. The dosimetric impact due to shield orientation uncertainty of ±5° was estimated using the gradient of the MC-calculated curve. The uncertainty due to shield thickness was based on the exponential attenuation expected from a ±0.025 mm variation in shield thickness. The

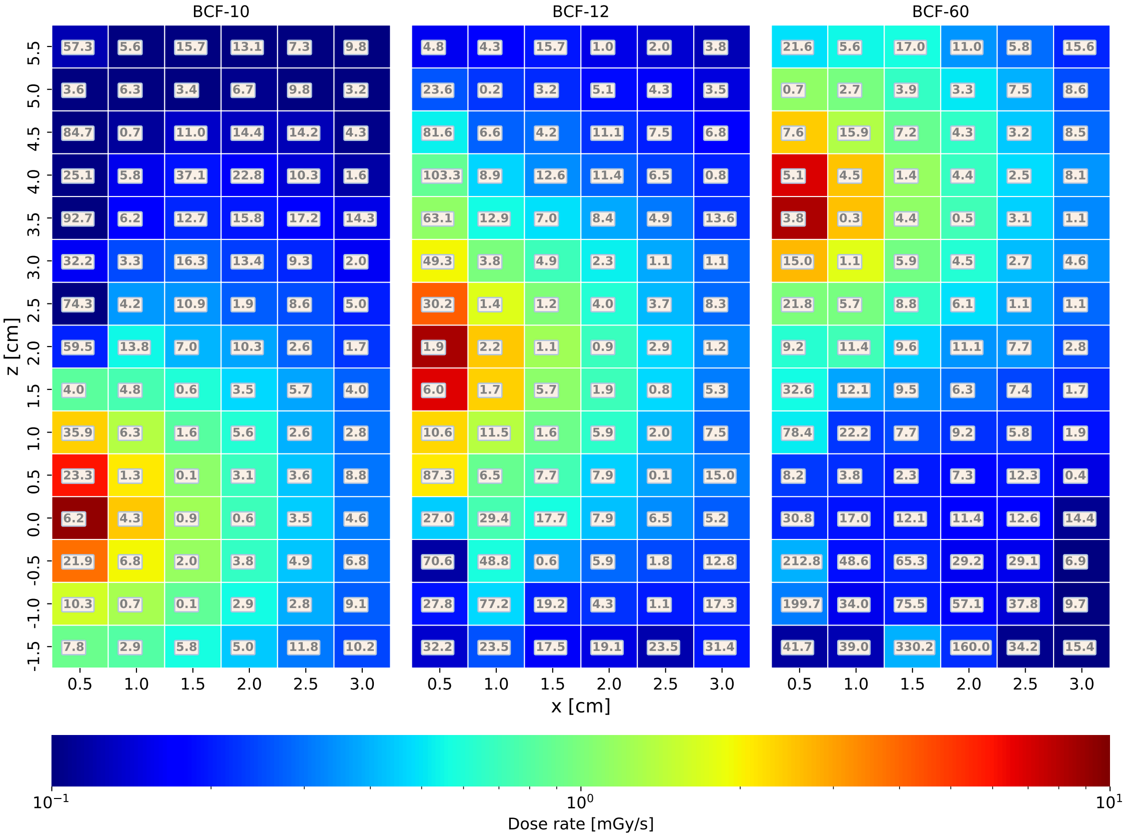

BCF-10

	0.5	1.0	1.5	2.0	2.5	3.0
5.5	57.3	5.6	15.7	13.1	7.3	9.8
5.0	3.6	6.3	3.4	6.7	9.8	3.2
4.5	84.7	0.7	11.0	14.4	14.2	4.3
4.0	25.1	5.8	37.1	22.8	10.3	1.6
3.5	92.7	6.2	12.7	15.8	17.2	14.3
3.0	32.2	3.3	16.3	13.4	9.3	2.0
2.5	74.3	4.2	10.9	1.9	8.6	5.0
2.0	59.5	13.8	7.0	10.3	2.6	1.7
1.5	4.0	4.8	0.6	3.5	5.7	4.0
1.0	35.9	6.3	1.6	5.6	2.6	2.8
0.5	23.3	1.3	0.1	3.1	3.6	8.8
0.0	6.2	4.3	0.9	0.6	3.5	4.6
-0.5	21.9	6.8	2.0	3.8	4.9	6.8
-1.0	10.3	0.7	0.1	2.9	2.8	9.1
-1.5	7.8	2.9	5.8	5.0	11.8	10.2

BCF-12

	0.5	1.0	1.5	2.0	2.5	3.0
5.5	4.8	4.3	15.7	1.0	2.0	3.8
5.0	23.6	0.2	3.2	5.1	4.3	3.5
4.5	81.6	6.6	4.2	11.1	7.5	6.8
4.0	103.3	8.9	12.6	11.4	6.5	0.8
3.5	63.1	12.9	7.0	8.4	4.9	13.6
3.0	49.3	3.8	4.9	2.3	1.1	1.1
2.5	30.2	1.4	1.2	4.0	3.7	8.3
2.0	1.9	2.2	1.1	0.9	2.9	1.2
1.5	6.0	1.7	5.7	1.9	0.8	5.3
1.0	10.6	11.5	1.6	5.9	2.0	7.5
0.5	87.3	6.5	7.7	7.9	0.1	15.0
0.0	27.0	29.4	17.7	7.9	6.5	5.2
-0.5	70.6	48.8	0.6	5.9	1.8	12.8
-1.0	27.8	77.2	19.2	4.3	1.1	17.3
-1.5	32.2	23.5	17.5	19.1	23.5	31.4

BCF-60

	0.5	1.0	1.5	2.0	2.5	3.0
5.5	21.6	5.6	17.0	11.0	5.8	15.6
5.0	0.7	2.7	3.9	3.3	7.5	8.6
4.5	7.6	15.9	7.2	4.3	3.2	8.5
4.0	5.1	4.5	1.4	4.4	2.5	8.1
3.5	3.8	0.3	4.4	0.5	3.1	1.1
3.0	15.0	1.1	5.9	4.5	2.7	4.6
2.5	21.8	5.7	8.8	6.1	1.1	1.1
2.0	9.2	11.4	9.6	11.1	7.7	2.8
1.5	32.6	12.1	9.5	6.3	7.4	1.7
1.0	78.4	22.2	7.7	9.2	5.8	1.9
0.5	8.2	3.8	2.3	7.3	12.3	0.4
0.0	30.8	17.0	12.1	11.4	12.6	14.4
-0.5	212.8	48.6	65.3	29.2	29.1	6.9
-1.0	199.7	34.0	75.5	57.1	37.8	9.7
-1.5	41.7	39.0	330.2	160.0	34.2	15.4

Figure 9.8: Along-away measurements of the dose rate from the bare ^{169}Yb source in a water tank (TG-43U1 conditions) using the mPSD. Relative deviations (%) from calculated along-away data indicated in boxes.

uncertainties in the normalized dose rate were calculated as the quadrature sum of the total uncertainties for each measurement.

9.4 Discussion

The TG-43U1 parameters were calculated using MC methods for the source model. The S_K/A was found comparable to other published values for ^{169}Yb source models: 1.33±0.04 U mCi^{-1} [36], 1.10±0.03 U mCi^{-1} [2], 1.08±0.03 U mCi^{-1} [3], 1.37±0.03 U mCi^{-1} [4], 1.15±0.03 U mCi^{-1} [33]. Deviations between source models were mostly attributed to the diameter of the active core and encapsulation. The Λ was in reasonable agreement with other reported values in the literature: 1.21±0.03 cGy h^{-1} U^{-1} [36], 1.204±0.004 cGy h^{-1} U^{-1} [34], 1.191±0.007

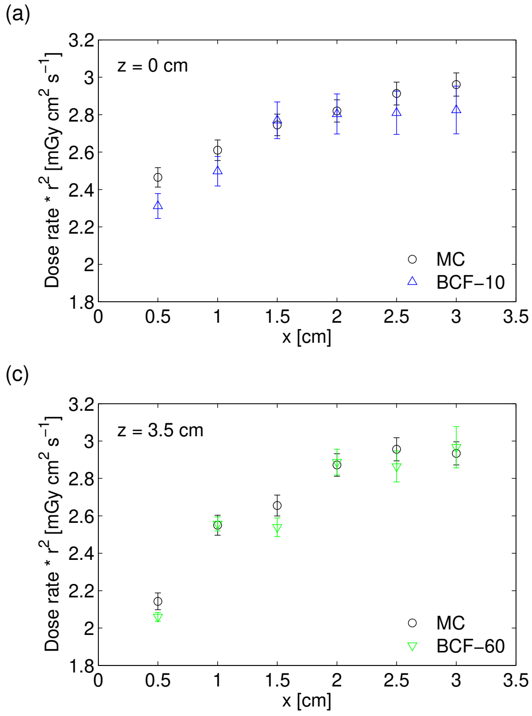

Figure 9.9: Comparison of the dose rate multiplied by radial distance squared (r^2) measured by mPSD and calculated using MC along (a) $z = 0$ cm for BCF-10, (b) $z = 2$ cm for BCF-12, and (c) $z = 3.5$ cm for BCF-60. The distances to the source are relative to each scintillator's effective center. Error bars represent standard deviations.

cGy h^{-1} U^{-1} [35], 1.17±0.01 cGy h^{-1} U^{-1} [35], 1.19±0.03 cGy h^{-1} U^{-1} [2], 1.12±0.04 cGy h^{-1} U^{-1} [3], 1.22±0.03 cGy h^{-1} U^{-1} [4], 1.19±0.03 cGy h^{-1} U^{-1} [33]. While the radial dose function $g_L(r)$ was in close agreement ($<$2% difference) with other HDR source models [2, 3] with larger diameter and length, the source model investigated in this study exhibited lower anisotropy closer to the longitudinal axis of the source, primarily due to the decreased attenuation within the active core volume and the encapsulation at the proximal and distal ends of the source. The increased contribution from scattered photons to dose deposition at depth (first mean free path of 3.0 cm) resulted in a dose falloff that is ideal for HDR brachytherapy in the therapeutic range.

The experimental verification of the dose distribution from the bare source was performed using the mPSD. Good agreement was achieved along the transverse axis for each scintillator, with deviations generally within their combined standard uncertainties. In the comparison of

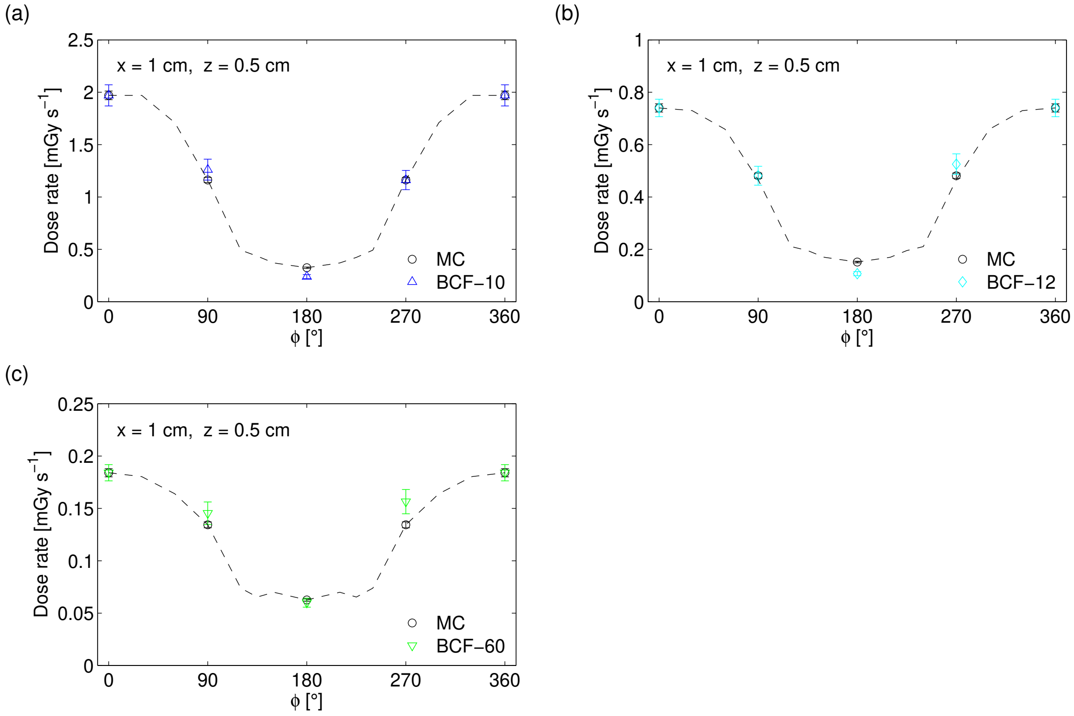

Figure 9.10: Comparison of the dose rate around the shielded ^{169}Yb source measured by (a) BCF-10, (b) BCF-12 and (c) BCF-60 and calculated with MC. Measurements were performed at x = 1 cm and z = 0.5 cm with a variable azimuthal angle ϕ. Error bars represent standard deviations.

the along-away dose data, deviations were largest for a detector-to-catheter distance of 0.5 cm, which was expected due to the relatively high positioning uncertainties that tend to dominate the total uncertainties at these short distances [41]. While the source-to-detector position was corrected according to the formalism published by Johansen et al. [32], the diameter of the source was thin (0.6 mm) compared to the inner diameter of the catheter (1.6 mm), which may have led to source displacements in the x-direction of ±0.5 mm (uniform distribution). These random source position fluctuations were more difficult to identify than the longitudinal offsets. Even if this effect could be observed at all the distances explored, the dosimetric impact was more significant at short distances. In addition, reliable measurements were not possible for distances greater than 3 cm (dose rate <0.3 mGy s^{-1}) due to the low SNR measured by the mPSD. Relative deviations generally increased as the radial distance r from each scintillator's center increased, likely due to the decreased SNR in this low dose rate range. Overall, the

Table 9.5: Total relative standard uncertainty budget (in %) for measurements of dose rate by mPSD at four different angles ϕ around the shielded ^{169}Yb source.

Source of uncertainty	Type	ϕ = 0°	ϕ = 90°	ϕ = 180°	ϕ = 270°
Measurement (BCF-10/BCF-12/BCF-60)	A	3.1/2.0/1.4	3.3/2.2/1.6	4.1/3.1/2.9	3.3/2.2/1.6
Source-to-detector distance (±0.2 mm)	B	4.0	4.0	4.0	4.0
Shield orientation (±5°)	B	0	6.0	1.0	6.0
Shield thickness (±0.025 mm)	B	0	0	5.5	0
Combined standard uncertainty (k=1)		**5.1/4.5/4.2**	**7.9/7.5/7.4**	**8.0/7.5/7.5**	**7.9/7.5/7.4**
Expanded uncertainty (k=2)		**10.2/9.0/8.4**	**15.8/15.0/14.8**	**16.0/15.0/15.0**	**15.8/15.0/14.8**

SNR was greater than 5 for values of radial distance r below 3 cm. According to the Rose criteria, proper detection of an object strongly depends on SNR, only becoming possible when SNR exceeds 5; detection performance degrades as SNR approaches zero [42, 19]. In the regions where both positioning uncertainties and SNR were acceptable ($x \geq 1$ cm, $r \leq 3$ cm), differences between measured and calculated dose rates were generally within 5%.

The dose rate measurements for the bare source had several limitations. First, the low activity source (0.64 Ci) impacted both the validation range over which reliable measurements could be performed and the level of agreement in the regions where the SNR was appropriate. Measurement uncertainties are directly affected by the air kerma strength of brachytherapy sources. As the distance to the source is directly related to the dose rate, a decrease in the dose rate leads to an increase in the measurement uncertainty, especially at long distances from the source. Thus, it is expected that additional dose verification over an extended distance range can be performed with a higher activity source. Second, the positioning uncertainties put a lower limit on the range of distances that could be evaluated. The thin diameter of the source and guidewire relative to the catheter diameter resulted in positioning uncertainties in both the radial and longitudinal directions that were relatively higher than for sources and guidewires with larger diameter commonly used in HDR brachytherapy. While the custom afterloader typically has a positional accuracy (k=2) of ±1 mm for larger diameter sources and guidewires, the positioning was less accurate (±2 mm) for this experimental setup due to the increased bending and torsion of the cable. A commercial afterloader with a thin catheter may be able to ensure source positioning with better reproducibility for this source model, and eliminate the need to estimate the source path and correct for source-to-detector positioning errors. Despite the limitations in the dose rate measurements, the experimental verification with a multipoint dosimeter was useful for the purpose of this study. Three synchronized, independent sets of measurements were obtained for each dwell position explored, which allowed for real-time source localization. Source localization would have been difficult to achieve using independent single point dosimeters without the influence of additional sources of uncertainty.

The overall trend of the MC-calculated azimuthal anisotropy curve for the shielded source was reproduced by the measurements performed at four locations. MC calculations and mPSD measurements showed that the dose distribution around the shielded source is highly anisotropic. For the case where SNR was most reliable for all measurement locations (BCF-10), there was strong agreement at 0°, 90° and 270°, with differences within their combined uncertainties, while the difference in the maximum dose rate reduction was just above 5%. Discrepancies between measurements and calculations were likely due to greater than expected positioning errors due to the non-uniformity or deformation of the shield and limitations in SNR for low dose rate regions. While this study demonstrated a proof of concept of the shielding capabilities of the partial platinum shield, the next step is to perform a full verification of the dose distribution over a larger range of distances using a high-activity ^{169}Yb source developed in collaboration with a medical device manufacturer and integrated into a commercial afterloader.

9.5 Conclusions

This study demonstrated the feasibility of producing an experimental ^{169}Yb source model and evaluated its dosimetric characteristics through MC calculations and mPSD measurements. Due to the low activity of the ^{169}Yb source and SNR limitations, the measurements using the mPSD system were limited to a short spatial range. However, within this range, the agreement between measurements and MC calculations was within their combined uncertainties. In combination with previous findings regarding the suitability of the practical source properties, the dosimetric properties also indicate that the ^{169}Yb source coupled with the partial-shielding system is a promising technique to deliver IMBT. Additional verification at further distances would be required before a reference data set is established for this source model.

Acknowledgements: The authors would like to acknowledge Doug Leonardi for machining work and general aid with the experimental setup. This work was supported by the Natural Sciences and Engineering Research Council (NSERC) (grant numbers 241018, 484144-15 and RGPIN-2019-05038), Collaborative Health Research Projects (grant number 523394-18) and Canadian Foundation for Innovation (CFI) JR Evans Leader Funds grant number 35633. G.F. would like to acknowledge support by the NSERC Alexander Graham Bell Canada Graduate Scholarship. H.M.L.R. further acknowledges support from Fonds de Recherche du Quebec -

Nature et Technologies (FRQNT).

Conflict of interest: None.

References

[1] Mason DL, Battista JJ, Barnett RB, Porter AT. Ytterbium-169: calculated physical properties of a new radiation source for brachytherapy. Med Phys. 1992;19(3):695–703.

[2] Medich DC, Tries MA, Munro III JJ. Monte Carlo characterization of an ytterbium-169 high dose rate brachytherapy source with analysis of statistical uncertainty. Med Phys. 2006;33(1):163–172.

[3] Cazeca MJ, Medich DC, Munro III JJ. Monte Carlo characterization of a new Yb-169 high dose rate source for brachytherapy application. Med Phys. 2010;37(3):1129–1136.

[4] Currier B, Munro III JJ, Medich DC. Dosimetric characterization of the GammaClip$^{\text{TM}}$ ^{169}Yb low dose rate permanent implant brachytherapy source for the treatment of nonsmall cell lung cancer postwedge resection. Med Phys. 2013;40(8):080701.

[5] Flynn RT, Adams QE, Hopfensperger KM, Wu X, Xu W, Kim Y. Efficient ^{169}Yb high-dose-rate brachytherapy source production using reactivation. Med Phys. 2019;46:2935–2943.

[6] Callaghan CM, Adams Q, Flynn RT, Wu X, Xu W, Kim Y. Systematic review of intensity-modulated brachytherapy (IMBT): static and dynamic techniques. Int J Radiat Oncol Biol Phys. 2019;105(1):206–221.

[7] Famulari G, Duclos M, Enger SA. A novel ^{169}Yb-based dynamic-shield intensity modulated brachytherapy delivery system for prostate cancer. Med Phys. 2020;47(3):859–868.

[8] Rivard MJ, Coursey BM, DeWerd LA, Hanson WF, Huq MS, Ibbott GS, et al. Update of AAPM Task Group No. 43 Report: A revised AAPM protocol for brachytherapy dose calculations. Med Phys. 2004;31(3):633–674.

[9] DeWerd LA, Ibbott GS, Meigooni AS, Mitch MG, Rivard MJ, Stump KE, et al. A dosimetric uncertainty analysis for photon-emitting brachytherapy sources: Report of AAPM Task Group No. 138 and GEC-ESTRO. Med Phys. 2011;38(2):782–801.

[10] Beaulieu L, Carlsson Tedgren A, Carrier JF, Davis SD, Mourtada F, Rivard MJ, et al. Report of the Task Group 186 on model-based dose calculation methodsbin brachytherapy beyond the TG-43 formalism: current status and recommendations for clinical implementation. Med Phys. 2012;39(10):6208–6236.

[11] Lambert J, McKenzie DR, Law S, Elsey J, Suchowerska N. A plastic scintillation dosimeter for high dose rate brachytherapy. Phys Med Biol. 2006;51(21):5505–5516.

[12] Therriault-Proulx F, Beddar S, Briere TM, Archambault L, Beaulieu L. Technical Note: Removing the stem effect when performing Ir-192 HDR brachytherapy in vivo dosimetry using plastic scintillation detectors: A relevant and necessary step. Med Phys. 2011;38(4):2176–2179.

[13] Therriault-Proulx F, Briere TM, Mourtada F, Aubin S, Beddar S, Beaulieu L. A phantom study of an in vivo dosimetry system using plastic scintillation detectors for real-time verification of ^{192}Ir HDR brachytherapy. Med Phys. 2011;38(5):2542–2551.

[14] Liu PZY, Suchowerska N, Abolfathi P, McKenzie DR. Real-time scintillation array dosimetry for radiotherapy: The advantages of photomultiplier detectors. Med Phys. 2012;39(4):1688–1695.

[15] Therriault-Proulx F, Beaulieu L, Beddar S. Validation of plastic scintillation detectors for applications in low-dose-rate brachytherapy. Brachytherapy. 2017;16(4):903–909.

[16] Archambault L, Therriault-Proulx F, Beddar S, Beaulieu L. A mathematical formalism for hyperspectral, multipoint plastic scintillation detectors. Phys Med Biol. 2012;57(21):7133.

[17] Therriault-Proulx F, Archambault L, Beaulieu L, Beddar S. Development of a novel multipoint plastic scintillation detector with a single optical transmission line for radiation dose measurement. Phys Med Biol. 2012;57:7417.

[18] Duguay-Drouin P. Caractérisation et optimisation d'un détecteur à scintillation à 2 points. Université Laval; 2016.

[19] Linares Rosales HM, Duguay-Drouin P, Archambault L, Beddar S, Beaulieu L. Optimization of a multipoint plastic scintillator dosimeter for high dose rate brachytherapy. Med Phys. 2019;46(5):2412–2421.

[20] Famulari G, Renaud M, Poole CM, Evans MDC, Seuntjens J, Enger SA. RapidBrachyMCTPS: a Monte Carlo-based treatment planning system for brachytherapy applications. Phys Med Biol. 2018;63(17):175007.

[21] Agostinelli S, Allison J, al Amako K, Apostolakis J, Araujo H, Arce P, et al. Geant4 - a simulation toolkit. Nucl Inst Meth Phys Res A. 2003;506(3):250–303.

[22] Allison J, Amako K, Apostolakis J, Araujo H, Dubois PA, Asai M, et al. Geant4 developments and applications. IEEE Trans Nucl Sci. 2006;53(1):270–278.

[23] Tuli JK. Evaluated nuclear structure data file, a manual for preparation of data sets. Lawrence Berkeley National Laboratory, Berkeley, CA; 1987.

[24] Cullen DE, Hubbell JH, Kissel L. EPDL97: the evaluated photo data library '97 version. LLNL Report No. UCRL-50400. Lawrence Livermore National Laboratory, Livermore, CA; 1997.

[25] Perkins ST, Cullen DE, Seltzer MN. Tables and graphs of electron-interaction cross sections derived from the LLNL Evaluated Electron Data Library (EEDL), Z = 1-100. LLNL Report No. UCRL-50400-v-31. Lawrence Livermore National Laboratory, Livermore, CA; 1997.

[26] Williamson JF. Monte Carlo evaluation of kerma at a point for photon transport problems. Med Phys. 1987;14:567–576.

[27] Taylor REP, Rogers DWO. EGSnrc Monte Carlo calculated dosimetry parameters for ^{192}Ir and ^{169}Yb brachytherapy sources. Med Phys. 2008;35(11):4933–4944.

[28] Mann-Krzisnik D, Verhaegen F, Enger SA. The influence of tissue composition uncertainty on dose distributions in brachytherapy. Radiother Oncol. 2018;126:394–410.

[29] Russell KR, Ahnesjö A, Carlsson Å K. Derivation of dosimetry data for brachytherapy sources using Monte Carlo for primary and scatter dose separation. In: Schlegel W, Bortfeld T, editors. The Use of Computers in Radiation Therapy. Berlin, Heidelberg: Springer; 2000. p. 495–497.

[30] Russell KR, Ahnesjö A, Carlsson Å K. Brachytherapy source characterization for improved dose calculations using primary and scatter dose separation. Med Phys. 2005;32:2739–2752.

[31] Therriault-Proulx F, Beddar S, Beaulieu L. On the use of a single-fiber multipoint plastic scintillation detector for ^{192}Ir high-dose-rate brachytherapy. Phys Med Biol. 2012;40:062101.

[32] Johansen JG, Rylander S, Buus S, Bentzen L, Hokland SB, Søndergaard CS, et al. Time-resolved in vivo dosimetry for source tracking in brachytherapy. Brachytherapy. 2018;17(1):122–132.

[33] Reynoso FJ, Munro III JJ, Sho SH. Technical note: Monte Carlo calculations for the AAPM TG-43 brachytherapy dosimetry parameters for the titanium-encapsulated Yb-169 source. Med Phys. 2017;18:193–199.

[34] Das RK, Meigooni AS, Misha V, Langton MA, Williamson JF. Dosimetric characterstics of the Type 8 ytterbium-169 interstitial brachytherapy source. J Brachytherapy Int. 1997;13:219–234.

[35] Mainegra E, Capote R, Lopez E. Dose-rate-constants for ^{125}I, ^{103}Pd, ^{192}Ir and ^{169}Yb brachytherapy sources. Phys Med Biol. 1998;43:1557–1566.

[36] Piermattei A, Azario L, Rossi G, Soriano A, Arcovito G, Ragona R, et al. Dosimetry of ^{169}Yb seed model X1267. Phys Med Biol. 1995;40:1317–1330.

[37] Ali A, Spencer B, McEwen MR, Rogers DWO. Towards a quantitative, measurement-based estimate of the uncertainty in photon mass attenuation coefficients at radiation therapy energies. Phys Med Biol. 2016;60:1641–1645.

[38] Rivard MJ, Granero D, Perez-Calatayud J, Ballester F. Brachytherapy dosimetry parameters calculated for a ^{131}Cs source. Med Phys. 2007;34(2):754–762.

[39] Andreo P, Burns DT, Salvat F. On the uncertainties of photon mass energy-absorption coefficients and their ratios for radiation dosimetry. Phys Med Biol. 2012;57:2117–2136.

[40] Rivard MJ, Granero D, Perez-Calatayud J, Ballester F. Influence of photon energy spectra from brachytherapy sources on Monte Carlo simulations of kerma and dose rates in water and air. Med Phys. 2005;37(2):869–876.

[41] Andersen CE, Nielsen SK, Lindegaard JC, Tanderup K. Time-resolved in vivo luminescence dosimetry for online error detection in pulsed dose-rate brachytherapy. Med Phys. 2009;36(11):5033–5043.

[42] Bushberg JT, Sibert JA, Leidholdt EM, Boone JM. The Essential Physics of Medical Imaging. 3rd ed. Mitchell CW, editor. Philadelphia, PA: Lippincott Williams & Wilkins, Wolters Kluwer; 2012.

Chapter 10

Future directions and outlook

In this thesis, we demonstrated that IMBT has the potential to create a low dose tunnel within the urethra given similar PTV coverage for prostate cancer cases. For single-fraction HDR boost (15 Gy) or monotherapy (19 Gy), the change in absorbed dose of 13% on average corresponds to a change in BED on the order 25%-30%. The urethra-sparing properties of IMBT are desirable to minimize the occurrence and severity of late grade GU toxicities such as urethral strictures that are relatively common with prostate brachytherapy. Alternatively, IMBT could provide a method to escalate the single-fraction monotherapy prescription dose from 19 Gy (BED = 260 Gy) to 21 Gy (BED = 315 Gy) or higher without increased risk of GU complications. This has the potential to improve the long-term efficacy of HDR brachytherapy as a monotherapy for prostate cancer. Furthermore, the use of a single-fraction treatment is an interesting approach to reduce costs and resources associated with treatment of prostate cancer, which accounts for roughly 10% of all cancer types in Canada. While this work has focused on the improvement in dosimetric indices, clinical trials will eventually be necessary to demonstrate that the dosimetric improvements lead to significant improvements in TCP and NTCP.

In this work, we presented a prototype system that can dynamically control the rotation of platinum shields. As a first step, dose measurements were performed in static conditions to validate the dose distribution calculated through MC simulations. The stepper motor system in the current prototype is controlled by a software that reads in a plan containing shield angles and the times spent at each shield angle. However, the source dwell position and dwell time are independently controlled by an afterloading system. The next step for this project is to demonstrate that the prototype is able to deliver a dynamic-shield IMBT treatment plan. This will require the development of a control unit that simultaneously controls both source position and shield rotation. The control unit should be able to import an IMBT treatment plan containing three variables (dwell position, shield angle and dwell time) and deliver the plan accordingly. After this point, measurements in dynamic conditions can then be performed to validate the dose distribution calculated by treatment planning system.

The clinical implementation of interstitial dynamic-shield IMBT currently hinges on the availability of a commercial ^{169}Yb source with an appropriate diameter. While ^{169}Yb HDR sources have been commercially available in the past, such as the Model HDR 4140 (Implant Science Co., Wakefield, MA, USA) and Model M42 (Source Production and Equipment Co. [SPEC], St. Rose, LA, USA), the production of these sources have been discontinued. In chapter 9, we have demonstrated that it is possible to produce a low-activity, custom-designed source that fits with a platinum shield inside an interstitial catheter. Future work should focus on experimental work with ^{169}Yb, to determine the achievable specific activity, impurity levels, and production costs. These will depend on various parameters such as the form of the precursor, the shape of the target and the reactor flux. Efficient source reactivation as a means to improve the efficiency of ^{169}Yb production should also be investigated.

In chapter 5, we provided RBE estimates for various photon-emitting brachytherapy sources using $\bar{y}_D$ ratios in a specific scoring volume. The goal of this study was to demonstrate that there may exist a clinically relevant RBE difference (on the order of $\sim$1.1) between ^{169}Yb and ^{192}Ir for high dose rate applications. In clinical practice, the RBE of photon-emitting sources are rarely considered, since there remains considerable uncertainties in RBE estimates. The RBE is sensitive to variations in radiation quality, dose, dose rate, biological/physiological factors and clinical endpoints. Due to the large variability in the published data, the weighting factors are therefore conservatively set to unity to ensure adequate tumor control. Thus, there needs to be sufficient evidence demonstrating the RBE of ^{169}Yb before considering introducing a weighting factor in clinical practice. Moving forward, additional radiobiological data will be necessary to provide a better RBE estimate for various endpoints (e.g. clonogenic cell death) that are potentially relevant to TCP and NTCP. The range of RBE values provided by the data will give insight on whether adjustment in prescription doses may be necessary.

In chapter 7, we evaluated the impact of tissue heterogeneities on the dose distribution for various photon-emitting brachytherapy sources. The purpose of this study was to determine whether heterogeneity corrections should be considered for accurate dosimetry with ^{169}Yb. While the impact on soft tissues may not be clinically relevant, the main takeaway was that bones may be receiving a considerably elevated dose with ^{169}Yb compared to ^{192}Ir (up to 2-3 times higher). The clinical relevance of this relatively higher dose has yet to be determined and depends on many factors, including the proximity to bony structures, dose, fractionation scheme, and combination of treatment modalities. There remain considerable uncertainties related to the elemental composition of bony structures, since a given bone can demonstrate a high level of heterogeneity. The assigned material composition greatly influences the absorbed dose at intermediate energies due to increased contributions of photoelectric interactions. On the one hand, one can argue that the radiation sensitive tissues are located within the bone (e.g. bone marrow, spongiosa), and these are considerably closer in composition to soft tissues to compact bone (e.g. cortical bone). On the other hand, dose in compact bone can be used as a conservative estimate to ensure that toxicity is avoided. While additional clinical data is needed to demonstrate the need for tissue heterogeneity corrections in ^{169}Yb-based brachytherapy treatment planning, there are some important conclusions that can be inferred from this study. For prostate brachytherapy, the dose burden to the pelvic bone and femoral heads should be well tolerated in the worst-case assumption. However, the same cannot be said for head & neck brachytherapy, where the mandible (the dose-limiting organ) receives a dose that exceeds by far the target dose. These results provided insight on whether it is worthwhile to consider investigating ^{169}Yb-based IMBT for a given treatment site given the expected dose uptake in bone associated with ^{169}Yb.

This work involved some development towards a MC-based treatment planning software package for brachytherapy applications. The software package is a valuable tool for post-treatment MC-based dosimetric evaluation and retrospective treatment planning for research purposes. The software package is continuously being updated to deal with conventional and next-generation brachytherapy applications such as IMBT. The current version of RapidBrachyMCTPS includes updated applicator import and positioning, catheter reconstruction, dose optimization algorithms and three-plane contouring tools [1, 2]. In addition, the engine will be used to perform dose recalculations of test case plans for the AAPM Working Group on Model-Based Dose Calculation Algorithms in Brachytherapy.

In chapter 8, we showed that uncertainties in dwell position and shield angle can impact the clinically relevant dose-volume indices to a varying extent, depending on the magnitude of the uncertainties. These uncertainties mainly arise from setup uncertainties, delivery errors and patient motion relative to the applicator. It is important to identify and quantify the random and systematic errors that exist for this emerging brachytherapy modality. Such uncertainties could be built into the optimization process, reducing plan quality somewhat but building in robustness to delivery errors. The application of robust optimization for IMBT would be an interesting avenue to investigate in future work. Incorporating such an algorithm in the treatment planning engine may lead to plans that are less sensitive to these uncertainties.

The outlook for IMBT as a brachytherapy modality is very bright. IMBT techniques have been investigated for multiple treatment sites, such as prostate, breast, cervix, skin and rectum. Many static applicators are currently available as commercial products. The accurate delivery of static IMBT techniques depends on the wide-spread adoption of MBDCA as the gold standard in clinical practice. While MBDCA such as ACE (Elekta) and Acuros (Varian) are currently implemented in clinical TPS, dose reporting is still based on TG-43 in clinical practice. Dynamic techniques are considered as the next frontier for brachytherapy technology. The barrier to entry for dynamic techniques is typically higher than for static techniques, since these techniques may require substantial developments in treatment planning software, treatment delivery platform, radiation source production, workflow and quality assurance. Future development of dynamic IMBT will require extensive collaboration between academia and industry. The AAPM TG-337 is currently working on a report regarding Intensity Modulated and Anisotropic Brachytherapy Sources. The report aims to review IMBT techniques, address the resource requirements for these techniques (e.g. imaging modalities, treatment planning software, radiation source, delivery platform), and provide general recommendations on the necessary studies for acceptance testing, commissioning, periodic quality assurance and patient-specific quality control. This provides a strong indication that many of these emerging treatment techniques are expected to enter clinical practice in the next few years.

References

[1] Glickman H, Antaki M, Deufel C, Enger SA. RapidBrachyMCTPS 2.0: a comprehensive and flexible Monte Carlo-based treatment planning system for brachytherapy applications; 2020. arXiv:2007.02902.

[2] Antaki M, Deufel C, Enger SA. Fast mixed integer optimization (FMIO) for high dose rate brachytherapy. Phys Med Biol. 2020;65(21):215005.

Appendix A

Supplementary material of chapter 5

Table A.1: Geant4 MC simulation parameters.

	Step 1 Photon interaction spectrum	Step 2 Generation of electron tracks
Geometry	40 cm radius water phantom	Infinite water phantom
Source model	microSelectron v2 (^{192}Ir, ^{75}Se, ^{169}Yb, ^{153}Gd) SelectSeed 130.002 (^{125}I) TheraSeed 200 (^{103}Pd) Isotropic point source (1 MeV photons)	Isotropic point source
Particle source	Radioactive decay	Photon interaction spectrum
Physics constructor	Livermore	Geant4-DNA
Production cuts	250 eV	None
Tracking cuts	None	10 eV
Photon tracking	On	Secondary photons killed
Electron tracking	Secondary electrons killed	On
Atomic relaxation	On	On
Scoring event	Photon interaction events (pre-step kinetic energy)	Energy deposition events (x, y, z, dose)
Scoring voxels	Spherical shells radius: 1-15 cm thickness: 0.02-6.5 mm width: 5° polar, 360° azimuthal	

Appendix B

Supplementary material of chapter 7

Table B.1: Elemental composition and nominal densities of tissues.

Material	Element (% mass)												Mass density
	H	C	N	O	Na	Mg	P	S	Cl	Ar	K	Ca	(g cm^{-3})
Water	11.2			88.8									0.998
Air	0.1		75.0	23.6						1.3			0.0012
Prostate	10.5	8.9	2.5	77.4	0.2		0.1	0.2			0.2		1.04
Soft tissue	10.1	11.1	2.6	76.2									1.00
Mean male soft tissue	10.5	25.6	2.7	60.2	0.1		0.2	0.3	0.2		0.2		1.03
Bladder	10.5	9.6	2.6	76.1	0.2		0.2	0.2	0.3		0.3		1.04
Rectum	10.6	11.5	2.2	75.1	0.1		0.1	0.1	0.2		0.1		1.03
Cortical bone	3.4	15.5	4.2	43.5	0.1	0.2	10.3	0.3				22.5	1.92

Table B.2: Conversion from Hounsfield units (HU) to mass density.

Hounsfield unit (HU)	Mass density (g cm^{-3})
-1024	0.000
-1000	0.0012
-659	0.330
-516	0.480
-97	0.945
-57	0.980
0	1.000
14	1.052
69	1.094
217	1.155
220	1.157
456	1.335
809	1.561
1230	1.824
3000	2.874
5000	3.92
10000	3.92

Table B.3: Tissue properties assignment scheme for the prostate brachytherapy cases according to recommendations by TG-186 and ICRU 46.

Structure	Material	Mass density range (g cm^{-3})
PTV	Prostate	[0.0012, 1.14]
Urethra	Mean male soft tissue	[0.0012, 1.14]
Rectum	Air	[0.0012, 0.92]
	Rectum	[0.92, 1.14]
Bladder	Air	[0.0012, 0.92]
	Bladder	[0.92, 1.14]
Body	Air	[0.0012, 0.92]
	Mean male soft tissue	[0.92, 1.14]
	Cortical bone	[1.14, 3.92]

Table B.4: Tissue properties assignment scheme for the oral tongue brachytherapy cases according to recommendations by TG-186 and ICRU 46.

Structure	Material	Mass density range (g cm^{-3})
PTV	Soft tissue	[0.0012, 1.14]
Mandible	Cortical bone	[0.0012, 3.92]
Body	Air	[0.0012, 0.92]
	Mean male soft tissue	[0.92, 1.14]
	Cortical bone	[1.14, 3.92]

Table B.5: Monte Carlo simulation methods based on the recommendations of TG-268.

Item name	Description	Reference
Code, version	Geant4 10.2, RapidBrachyMCTPS	[38-40]
Validation	Previously validated	[38]
Timing	3-4 h on a single Intel core from a 2.6 GHz processor.	
Geometry	Voxelized geometry (egsphant) extracted from DICOM CT images and DICOM RT Structure Set files. CT grid interpolated to grid with voxel size 1×1×1 mm^3.	
Materials	a) Homogeneous water phantom (TG-43) or b) heterogeneous phantom (TG-186), with elemental composition of tissues, CT-to-density conversion, and tissue properties assignment schemes provided in Tables B.1-B.4.	[1, 16, 17, 36, 46]
Source description	MicroSelectron v2 source geometry (active core consists of ^{60}Co, ^{192}Ir, ^{75}Se, ^{169}Yb, or ^{153}Gd). Explicit simulation of radioactive decay using photon decay spectra from ENSDF. Source positions and orientations imported from DICOM RT Plan files. Dwell times imported from RapidBrachyMCTPS plan files.	[31, 41]
Cross sections	EPDL97, EEDL97, EADL97.	[42-44]
Transport parameters	PENELOPE low-energy electromagnetic physics list with default transport parameters. Electron transport off except for ^{60}Co). Production cut: 0.1 mm.	
Variance reduction technique	Tracklength estimator using mass-energy absorption coefficient library provided in RapidBrachyMCTPS.	[38, 45, 46]
Scored quantities	Absorbed dose (collisional kerma approximation) scored to a) water or b) medium. Voxel size: 1×1×1 mm^3.	
Histories/statistical uncertainty	10^8 photon histories. Type A uncertainties (k=1) <0.2% for voxels inside PTV, and <0.3%, <0.5%, and <0.8% at 10 mm, 30 mm, and 50 mm from PTV.	
Statistical methods	History-by-history method.	
Postprocessing	Dose to voxels converted into dose-volume parameters using RapidBrachyMCTPS.	[38]

Table B.6: Total uncertainty budget for the Monte Carlo (MC) simulations. A range of uncertainties is reported for a region of interest receiving between 100% and 10% of the prescription dose.

Source of uncertainty	Type	Uncertainty (%)	Reference
Statistics	A	0.2-0.6	
Source geometry	B	0.5	
Source photon spectrum	B	0.5	[49]
MC radiation transport	B	0.2	[49]
Interaction cross sections (μ/ρ)	B	0.1	[49]
Scoring cross sections (μ_{en}/ρ)	B	1.0	[49]
Tally volume averaging	B	0.2	
Standard uncertainty (k=1)		1.3-1.4	
Expanded uncertainty (k=2)		2.6-2.8	

Table B.7: Dosimetric indices for the prostate brachytherapy cases (n=10) calculated using dose to homogeneous water ($D_{w,w}$) and dose to medium in medium ($D_{m,m}$). Plans were generated using ^{60}Co, ^{192}Ir, ^{75}Se, ^{169}Yb, and ^{153}Gd sources. Doses are expressed as a percentage of the prescription dose. Uncertainties represent standard deviations for patient cohort.

Structure	Dosimetric index	Model	Radionuclide				
			^{60}Co	^{192}Ir	^{75}Se	^{169}Yb	^{153}Gd
PTV	D_{90} (%)	$D_{w,w}$	103.8±4.0	104.3±4.0	104.7±4.2	104.4±4.0	104.2±3.9
		$D_{m,m}$	102.9±3.9	103.1±4.2	103.6±4.2	102.9±4.4	102.0±4.3
	V_{100} (%)	$D_{w,w}$	93.4±3.4	93.5±3.9	93.7±3.9	93.5±3.9	93.4±3.5
		$D_{m,m}$	92.7±3.5	92.3±4.3	92.6±3.9	92.3±4.6	91.5±4.3
	V_{150} (%)	$D_{w,w}$	28.6±4.7	27.3±4.9	27.0±4.3	23.5±4.4	20.7±3.2
		$D_{m,m}$	27.5±4.6	26.3±4.8	26.0±4.0	22.9±4.3	20.3±3.1
	V_{200} (%)	$D_{w,w}$	12.2±2.0	11.2±1.9	11.2±1.9	9.6±1.6	8.6±1.5
		$D_{m,m}$	11.9±2.0	10.8±1.9	10.9±1.9	9.2±1.6	8.4±1.6
Urethra	D_{10} (%)	$D_{w,w}$	109.8±3.4	110.1±3.5	110.7±3.6	110.8±3.0	111.1±2.7
		$D_{m,m}$	108.7±3.4	109.0±3.5	109.8±3.6	108.2±3.1	106.0±2.9
Bladder	D_{2cc} (%)	$D_{w,w}$	62.0±9.0	61.5±8.6	62.4±9.6	62.5±8.6	62.1±8.6
		$D_{m,m}$	61.3±9.1	60.7±8.6	61.6±9.6	64.3±8.5	64.4±8.7
Rectum	D_{2cc} (%)	$D_{w,w}$	57.3±10.0	58.7±10.2	59.6±10.6	61.1±9.9	61.9±10.6
		$D_{m,m}$	56.0±10.2	57.2±10.5	57.4±10.7	59.6±9.5	60.0±10.5
Femur_L	D_{max} (%)	$D_{w,w}$	9.4±2.3	10.1±2.3	10.5±2.6	11.2±2.8	11.2±2.9
		$D_{m,m}$	8.6±2.4	11.8±2.5	15.7±3.1	30.6±6.8	47.3±11.8
Femur_R	D_{max} (%)	$D_{w,w}$	9.9±2.5	10.3±2.0	10.3±1.9	10.9±2.2	11.1±2.2
		$D_{m,m}$	9.3±2.4	11.7±2.3	15.5±3.0	30.6±6.0	45.1±9.9

Table B.8: Dosimetric indices for the oral tongue brachytherapy cases (n=10) calculated using dose to homogeneous water ($D_{w,w}$) and dose to medium in medium ($D_{m,m}$). Plans were generated using ^{60}Co, ^{192}Ir, ^{75}Se, ^{169}Yb, and ^{153}Gd sources. Doses are expressed as a percentage of the prescription dose. Uncertainties represent standard deviations for patient cohort.

Structure	Dosimetric index	Model	Radionuclide				
			^{60}Co	^{192}Ir	^{75}Se	^{169}Yb	^{153}Gd
PTV	D_{90} (%)	$D_{w,w}$	103.6±15.0	104.8±17.8	103.4±14.7	103.8±14.4	103.1±14.1
		$D_{m,m}$	102.4±14.9	103.6±17.7	102.2±14.9	99.5±13.5	96.0±13.8
	V_{100} (%)	$D_{w,w}$	91.4±8.8	91.5±8.3	91.4±8.7	91.4±8.7	91.3±9.0
		$D_{m,m}$	90.6±8.9	90.9±8.6	90.7±8.9	89.7±9.1	85.9±10.3
	V_{150} (%)	$D_{w,w}$	47.5±11.5	47.4±11.0	48.4±10.0	43.9±9.4	41.4±7.4
		$D_{m,m}$	46.6±11.6	46.1±10.6	47.3±9.8	40.2±8.9	35.4±6.3
	V_{200} (%)	$D_{w,w}$	24.3±4.1	24.6±7.6	23.7±5.0	20.9±4.2	19.9±2.9
		$D_{m,m}$	23.8±4.2	24.1±7.4	23.2±4.9	19.6±3.9	17.9±2.5
Mandible	D_{mean} (%)	$D_{w,w}$	25.7±6.4	26.7±6.7	26.8±6.2	28.7±6.6	29.3±7.1
		$D_{m,m}$	23.3±5.9	26.4±6.8	31.6±7.3	64.4±14.9	92.3±21.2
	D_{max} (%)	$D_{w,w}$	94.7±36.2	96.0±35.2	95.6±35.3	95.0±34.3	95.3±32.9
		$D_{m,m}$	86.4±34.5	97.8±38.8	111.9±39.5	237.9±71.5	412.5±119.4

Appendix C

Supplementary material of chapter 8

https://aapm.onlinelibrary.wiley.com/doi/abs/10.1002/mp.13959

Figure C.1: Animation of the moving panel concept. The crankshafts and moving panel rotate in unison.

https://aapm.onlinelibrary.wiley.com/doi/abs/10.1002/mp.13959

Figure C.2: Animation showing the various components for the rotating mechanism. For a dual-source delivery, two moving panel layers are independently controlled by two stepper motors. Each shield is connected to one panel such that each motor controls a subset of shields.

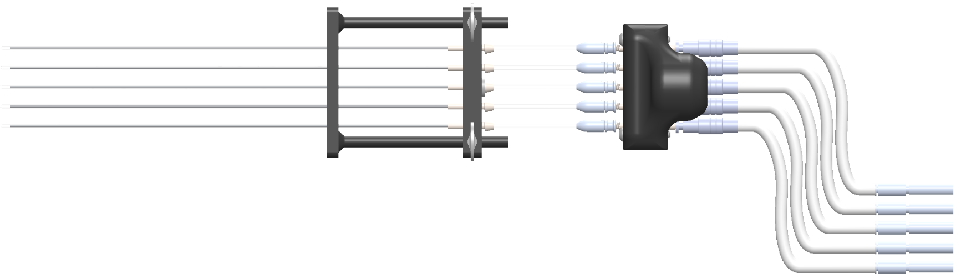

Figure C.3: Side view of the AIM-Brachy system.

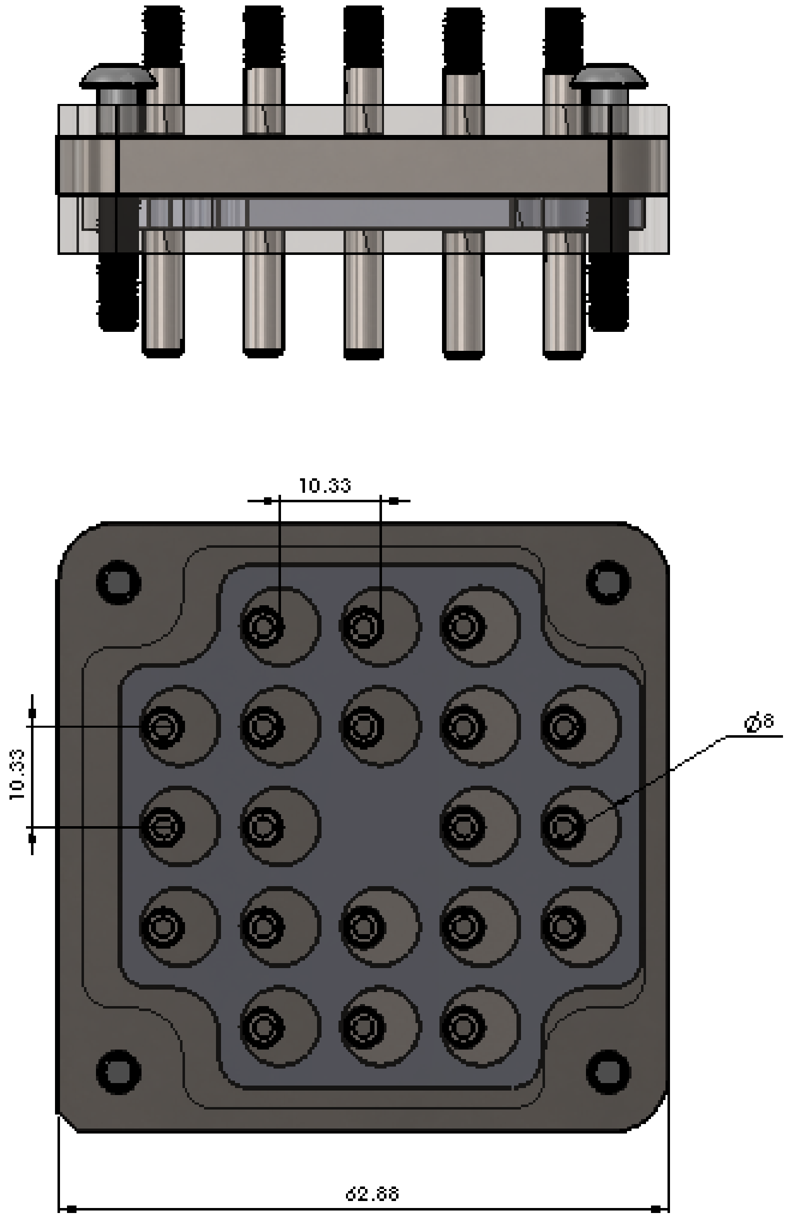

Figure C.4: Cross section of the rotating mechanism with dimensions (in mm).